Analysis of composite beam by taking into account inter-layer slip and uplift

Thaileng Oeng

COLLEGE DOCTORAL BRETAGNE SCIENCES POUR L'INGENIEUR

INSA INSTITUT NATIONAL DES SCIENCES APPLIQUÉES RENNES

THÈSE DE DOCTORAT DE

L'INSTITUT NATIONAL DES SCIENCES APPLIQUÉES DE RENNES

ÉCOLE DOCTORALE N° 647
Sciences pour l'Ingénieur
Spécialité : *Génie Civil*

Par
Thaileng OENG

Analysis of composite beam by taking into account inter-layer slip and uplift

Thèse présentée et soutenue à l'INSA Rennes, le 13/Juillet/2023
Unité de recherche : EA 3913 Laboratoire de génie civil et génie mécanique (LGCGM)
Thèse N° : 23ISAR 20 / D23 - 20

Rapporteurs avant soutenance :

Cristina CAMPIAN	Professeur des universités, Technical University of Cluj-Napoca
Abdelhamid BOUCHAIR	Professeur des universités, Clermont Auvergne INP
Sophy CHHANG	Enseignant-Chercheur, Institut de Technologie du Cambodge

Composition du Jury :

Attention, en cas d'absence d'un des membres du Jury le jour de la soutenance, la composition du jury doit être revue pour s'assurer qu'elle est conforme et devra être répercutée sur la couverture de thèse

Président :	Panagiotis KOTRONIS	Professeur des universités, Ecole Centrale de Nantes
Examinateurs :	Emmanuel FERRIER	Professeur des universités, Université Lyon 1
	Abdelhamid BOUCHAIR	Professeur des universités, Clermont Auvergne INP
	Cristina CAMPIAN	Professeur des universités, Technical University of Cluj-Napoca
	Sophy CHHANG	Enseignant-Chercheur, Institut de Technologie du Cambodge
Dir. de thèse :	Mohammed HJIAJ	Professeur des universités, INSA Rennes
Co-enc. de thèse :	Pisey KEO	Maître de Conférences, INSA Rennes
Co-dir. de thèse :	Sovanvichet LIM	Enseignant-Chercheur, Institut de Technologie du Cambodge

"To my home country: ***CAMBODIA****"*

"To my home institution: ***Institute of Technology of Cambodia****"*

"To my family"

Thaileng OENG

Abstract

This thesis presents a finite element approach for the analysis of composite (two-layers) beams by taking into account slip and uplift at the interface of the layers. Two models of connection are considered: the discrete bond and continuous bond model. The connector element consists of two-directional coupled springs. The horizontal spring parallel to the contact surface, captures the slip while the vertical spring, orthogonal to the contact surface, captures the uplift between the layers. The vertical spring is activated only if there is a separation between the layers, otherwise, the contact forces exist. This unilateral behavior complicates the problem and requires the implementation of a corresponding solution method. Two classical methods for solving the contact problem are evaluated: the penalty method and the augmented Lagrangian method. Besides, it is assumed that both slip and uplift are small, which corresponds to the observations made on composite beams.

A semi-analytical solution is proposed for the geometrically and materially linear case. In this formulation, the kinematic variables are interpolated exactly, and the node-to-node contact conditions are imposed for both connection models. The observation shows that the penalty method has a high convergence rate, while the augmented Lagrangian one fully respects the non-penetration condition. In the second task, the resolution methods of the contact problem are evaluated in geometrical nonlinearity (co-rotational approach). In nonlinear finite element analysis, displacement-based and two-field mixed formulations for the problem of geometrical and material nonlinearity are proposed. We adopt fiber discretization for the sections of the composite beam. A plastic flow rule considering the coupling between slip and uplift is adopted, which permits the modeling of the interaction between longitudinal shear forces and the tensile force of the connector. For both formulations, a corresponding algorithm is proposed to solve the contact problem. The treated numerical examples demonstrate the robustness of the proposed formulations.

Keywords : composite beam, co-rotational approach, finite elements, inter-layer slips and uplifts, penalty method, augmented Lagrangian method, coupled connector

Résumé

Dans ce travail, nous proposons une approche éléments finis pour l'analyse de poutres mixtes (bicouches) intégrant les phénomènes de glissement et le soulèvement à l'interface de la poutre bicouche. Deux modèles de connexion à l'interface sont considérés : connexion discrète et connexion continue. L'élément connecteur corresponds à 2 ressorts couplés. Le ressort tangent à l'interface décrit le glissement et celui, normal à l'interface, décrit le soulèvement. Ce dernier n'est activé que s'il y a séparation entre les deux éléments. Dans le cas contraire, une force de contact se développe. Ce comportement unilatéral complexifie le problème et nécessite de mettre en œuvre une méthode de résolutions ad hoc. Deux méthodes classiques de résolutions du problème de contact sont évaluées : la méthode pénalité, et la méthode Lagrangienne augmentée. Par ailleurs, on supposera que le glissement et le soulèvement sont petits, ce qui corresponds aux observations effectuées sur des poutres mixtes.

Une solution semi-analytique est proposée pour le cas géométriquement et matériellement linéaire. Dans cette formulation, les variables cinématiques sont interpolées de manière exacte et les conditions de contact sont imposées aux nœuds pour les deux modèles de connexion. On observe que la méthode de pénalité converge plus rapidement, tandis que la méthode Lagrangien augmentée respecte strictement la condition de non-pénétration. Dans une seconde phase, les méthodes de résolutions du problème de contact sont évaluées dans un contexte géométriquement non-linéaire (approche co-rotationnelle). Enfin, une formulation en déplacement et une formulation mixte à deux champs du problème géométriquement et matériellement non-linéaire sont également proposées. Nous adoptons la discrétisation par fibres pour les sections de la poutre mixte. Une loi d'écoulement plastique considérant le couplage entre glissement et soulèvement est adoptée, ce qui permet de modéliser l'interaction entre les efforts de cisaillement longitudinaux et ceux produits par le soulèvement. Pour ces deux formulations, on propose un algorithme ad hoc pour le traitement du problème du contact. Les exemples traités démontrent la robustesse des formulations proposées.

Mots-clés : poutres mixtes (bicouches), glissement, soulèvement, approche co-rotationnelle, méthode de pénalité, méthode Lagrangien augmentée, connecteur couplé

Acknowledgements

After nearly three years of intensive effort, I am pleased to have completed this doctoral thesis. I am deeply grateful to the individuals and organizations who have supported me throughout this rigorous and challenging research journey during the COVID-19 pandemic.

First and foremost, I express my heartfelt appreciation to **Prof. Mohammed HJIAJ**, my thesis director, whose expert guidance, mentorship, and unwavering dedication to excellence were vital to the successful completion of this thesis. He provided crucial support in helping me secure the financial supports to embark on my doctoral degree, and his contributions have been instrumental in shaping the direction and quality of my research.

Furthermore, I would like to extend my deepest gratitude to **Dr. Pisey KEO** , my co-supervisor, who has been a role model to me throughout my doctoral research. His insightful feedback and guidance have greatly enhanced the quality of my research work. His profound expertise in the field of structural engineering has been an ever-present source of inspiration, and has continuously aided in the development of my knowledge. I am deeply grateful for the opportunity to learn from him.

In addition, I would like to express the gratitude to my thesis co-director, **Dr. Sovanvichet LIM**, for his invaluable support and scientific advice throughout my research, particularly with regard to the administrative processes at ITC.

During my research, I spent a significant amount of time at the Laboratoire de Génie Civil et Génie Mécanique (**LGCGM**). I am deeply grateful to all of my colleagues there, whose support and encouragement made it easier for me to carry out my research. I would like to acknowledge also the French Government Scholarship (**BGF**) and The Government of Cambodia for providing me with the financial support that enabled me to pursue my doctoral studies.

Moreover, I would like to express my sincere appreciation to my dear seniors and friends: Vanthet OUCH, Lynita SAROU, Piseth HENG, Yassir WARDI, Mouad MADHOUNI, Adham AL RAHIM, Mael SONA, Murillo SANTANA, Davin SANG, Try MENG, Sounean HENG, Yeakleang MUY, Sokvisal MOM, Sela HOEUN, Loby HENG, etc. for their encouragement, support, and understanding throughout this demanding journey.

Lastly, I would like to express my deepest love and gratitude to my families, especially my sister Muyeng OENG and aunt Stella UNG LIM (my second mom) for their unconditional love, support, and encouragement. Their unwavering belief in me has been the foundation upon which I have built my academic pursuits. Without their love and support, this achievement would not have been possible.

Contents

List of Figures

List of Tables

List of Symbols

A	area of cross section	mm^2 , m^2
D	damage degradation	mm^2/N , m^2/kN
D_{sc}	shear force of connector	N , kN
D_u	shear strength of connector	N , kN
E	elastic modulus	N/mm^2 , kN/m^2
g	interface gap or penetration	mm , m
H_k	instant kinematic hardening parameter	N/mm^2 , kN/m^2
H_{nl}	Armstrong-Frederick hardening parameter	N/mm^2 , kN/m^2
h_a	half-height of layer a	mm , m
h_b	half-height of layer b	mm , m
I	moment of inertia	mm^4 , m^4
K	confined parameter	
k_h	horizontal stiffness in discrete bond model	N/mm^2 , kN/m^2
K_h	horizontal stiffness in continuous bond model	N/mm^2 , kN/m^2
k_v	vertical stiffness in discrete bond model	N/mm^2 , kN/m^2
K_v	vertical stiffness in continuous bond model	N/mm^2 , kN/m^2
M	bending moment	$N.mm^2$, $kN.m^2$
N	normal force	N , kN
q	displacement vector	mm , m
Q or Q_{int}	internal force vector	N , kN
Q_{ext}	external force vector	N , kN
s	inter-layer slip	mm , m
u	axial or horizontal displacement	mm , m
v	vertical displacement	mm , m
V_{sc}	tensile or uplift force of connector	N , kN
V_u	tensile strength of connector	N , kN
ε	axial strain	mm/mm , m/m
ε_0	initial strain	mm/mm , m/m

ε_e	elastic strain	mm/mm , m/m
ε_d	damaged strain	mm/mm , m/m
ε_p	plastic strain	mm/mm , m/m
ε_{pd}	plastic-damage strain	mm/mm , m/m
ε_y	yield strain	mm/mm , m/m
χ	back stress	N , kN
$\dot{\lambda}$	rate of plastic strain	
σ	stress	N/mm^2 , kN/m^2
σ_e	elastic stress	N/mm^2 , kN/m^2
σ_p	plastic stress	N/mm^2 , kN/m^2
σ_y	yield stress	N/mm^2 , kN/m^2
σ_{max}	maximum stress	N/mm^2 , kN/m^2
θ	rotation	rad
Π	total potential energy	N.mm , kN.m
Π_{int}	internal potential energy	N.mm , kN.m
Π_{ext}	external potential energy	N.mm , kN.m

List of Abbreviations

ALM	**A**ugmented **L**agrangian **M**ethod
DB	**D**isplacement **B**ased
DOF	**D**egree **O**f **F**reedom
FE	**F**inite **E**lement
FEA	**F**inite **E**lement **A**nalysis
FEM	**F**inite **E**lement **M**ethod
PM	**P**enalty **M**ethod

Chapter 1

Introduction

1.1 Overview of composite beam

For close to a hundred years, engineers have been utilizing composite members made of semi-rigidly connected layers in their structures. One of the most commonly used composite systems is the steel-concrete composite beam, which has proven to be an economical choice for both multi-story buildings and bridges. In some conceptions, other combinations such as timber-steel, timber-concrete and aluminum-composite materials are also commonly used in construction. A steel-concrete composite beam is a structural element that consists of a steel beam and a concrete slab, which are connected together to act as a single unit. In fact, the concrete slab acts as a flange and increases the rigidity and strength of the beam. Compared to steel or reinforced concrete structures, steel-concrete composite structures offer numerous technical, economical, and architectural benefits, including:

- Decreasing the weight of the structure with the same applied loads,
- Increasing the bending stiffness of the slab or beam,
- Increasing fire resistance,
- Providing the great stability against local and lateral-torsional buckling of steel profile,
- Decreasing the height of the slab; hence total height of the building for a common number of floors is reduced,
- Decreasing the duration of construction works.

The steel-concrete composite beam is made up of three main elements: the concrete slab, the steel beam and the shear connectors, typically in the form of shear studs. Other complementary components such as reinforcing bars in the slab and steel decking, may also be included, see Fig. 1.1. Reinforcing bars in the form of steel bars or wires are placed within the concrete slab to enhance its strength and ductility. This added reinforcement enables the concrete to endure more compressive stresses if the rebars are placed in the compression zone. If they are placed in the tension zone, the concrete may resist higher tensile stresses,

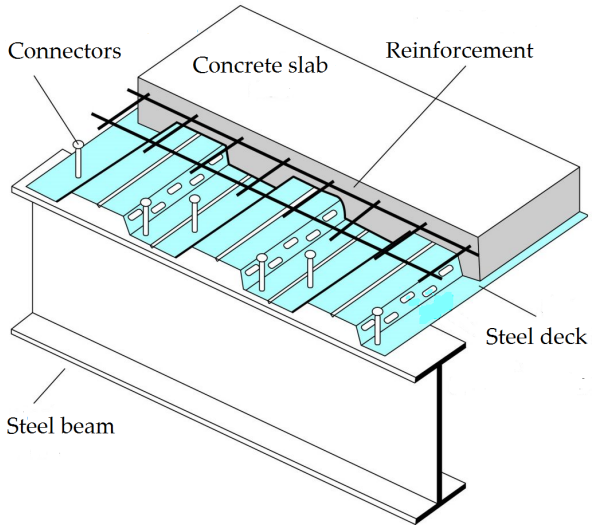

FIGURE 1.1: Composite concrete steel beam

which can increases the overall strength and ductility of the composite beam. Besides, the steel deck serves as a permanent form-work, providing support for the wet concrete during casting and curing, and also acts as a tensile reinforcement for the composite beam. The profiled shape of the steel deck improves the bond between the concrete slab and the steel section, resulting in a more efficient transfer of loads between the two materials.

The connection between the steel beam and concrete slab is usually made by shear connectors. The behavior of the composite members is heavily influenced by the type of shear connection used. If the latter is rigid, it allows for full composite action between the layers, and the conventional analysis principals for structural members can be applied. On the other hand, if the connectors are flexible, relative displacements may occur at the interface of the two layers, resulting in a so-called partial interaction. In this case, the behavior of composite beams is more complex and requires a specific analysis.

1.2 State of the art

Over the past century, the development of researches have focused on the behavior of connection in composite beam and its modeling, contact problem at layer interface, and advanced approaches for analyzing composite structures. The analysis of steel-concrete composite structures has followed two specific themes. Firstly, the researchers have tried to derive analytical solutions of the governing differential equation for general cases by adopting simple assumptions such as linear elastic material [1], which have provided simple equations for engineering design purposes that can also be used as benchmark solutions for evaluating numerical methods. Secondly, the focus has been on developing finite element models and numerical procedures, which offer better versatility compared with the generic

models and which can be used for analyzing large steel-concrete composite framed structures including material nonlinearity.

1.2.1 Modeling of connection between layers

The connection between the layers of a composite member is crucial as it influences all aspects of the member. The primary goal of this connection is to make the element act as a single (unified) body, thereby facilitating the transfer of loads and enhancing the ability to resist forces. Modeling the connection between the different layers is an important aspect of designing and analyzing the behavior of the composite beam. In order to accurately model the connection, several factors need to be considered. These include load transfer mechanisms, slip resistance, uplift resistance, durability, etc.

The shear force transfer between the layers is typically accomplished by two mechanism: the interactive mechanism provided by connector devises, and the friction which is assumed proportional to the normal force at the interface. The mechanical shear connection can be modeled by either concentrated springs at connector locations or by continuous distributed springs along the beam. The former model is called "discrete bond model" while the latter is denoted as "continuous bond model". A few authors have considered the discrete bond model to analyse the behavior of composite beam [2, 3, 4]. Otherwise, the shear connection is represented as continuous, despite its inherently discrete nature. The first contribution of composite beam model considering continuous bond is commonly attributed to Newmark, Siess, Viest, et al. [5]. It has been shown that the adoption of the distributed bond model greatly reduces the number of elements required for analysis. In fact, the equivalent distributed spring stiffness can be determined by dividing the stiffness of a single row of connectors by their distance along the length of the beam. However, when applying the continuous bond model to layered beams with substantial connector spacing, it may result in a significant underestimation of the transverse deflection.

1.2.2 Non-penetration between the layers

In a composite beam, uplift occurs when there is a difference in the vertical displacement of upper and lower layers due to various external factors such as loading conditions, temperature or moisture changes, etc, [6]. In some situations, both layers are stick together (bearing one on another without penetration between them). In this case, the efficiency of connector devise to resist uplift is inactive and the problem becomes "contact problem" which is highly nonlinear.

The contact problem has been studied for years. The algorithms such as penalty method, Lagrangian method, augmented Lagrangian method, and modified barrier method have been proposed to solve the contact problem. In most of the research works on modelling

composite beam taking into account uplift, penalty method is adopted explicitly by considering anisotropic constitutive law i.e. different connector stiffness in tension (positive uplift) and compression (negative uplift). In this case, the stiffness of the connector in compression becomes the penalty parameter. A part from penalty method, other methods are rarely implemented in composite beam model. In [3], the augmented Lagrangian method has been adopted to solve the contact problem at the steel-concrete interface and a new concept called "Flying Node Concept" is introduced. It is stated that this concept solves the problem of continuous contact at the interface that could sometimes occur along the beam especially in the case of distributed loads.

1.2.3 Elastic behavior of composite beam

As mentioning earlier, the first contribution of analytical analysis of elastic composite beam in partial interaction is commonly attributed to Newmark, Siess, Viest, et al. [5]. In their formulation, they adopted the Euler-Bernoulli kinematic assumptions for both concrete slab and steel profile and considered a linear relationship between the relative interface displacements and the corresponding interface shear stresses. However, the uplift between the two layers are neglected. In this model, basing on the equilibrium equations and the compatibility relation at the interface, they established a second order differential equation where the axial force in the concrete slab is the primary unknown. Then, they solved this equation analytically. The results of Newmark's works [5] are extensively used by many authors to formulate theoretical models for the static response of composite beam in linear elastic range [7, 8, 9, 10, 11, 12, 13, 14, 15]. Besides these analytical works, several numerical models, mostly FE formulations have been developed [16, 17, 18]. It has been shown that locking problems occur for a low order displacement-based finite element formulation of composite beam when the continuous connection is considered. This problem can be avoided by either introducing internal nodes [16], adopting a strain field formulation [18], or using exact stiffness matrix obtained from analytical solutions. Heinisuo [19] proposed a finite element formulation using exact stiffness matrix for uniform, straight, linearly elastic layered beams with two faces and one core and with three symmetric faces and two identical cores. Based on the analytical solution given in [20], Sousa Jr [21] derived the exact flexibility matrix for partially connected multi-layered beams with the assumption that both transverse displacement and rotation are the same for all layers.

Only a limited number of mathematical models proposed in the literature take into account both slip and uplift at the layer interface. The first attempt was made by Adekola [22] who considered the linear elastic behavior of simply supported composite beams accounting for both inter-layer slip and uplift. It is assumed that in regions where separation occurs the uplift force is proportional to the relative transverse displacement. When one layer bears against the other, normal contact forces develop. A constant stiffness coefficient is adopted considering compressibility of the layers. In addition, stiffness coefficients (longitudinal

and vertical) are assumed to be uncoupled. The governing system of differential equations is derived based on equilibrium conditions and solved numerically. However this model is applicable only to the analysis of determinate structures as the moment distribution along the beam needs to be known a priori. Later, Robinson and Naraine [23] revisited the problem of a simply supported composite steel-concrete beam subjected to a single point load applied either on the top of slab or to the steel beam (pull down). A closed form solution was derived for both load cases. Besides, finite element formulations have also been developed to analyze the effects of uplift on the behavior of composite beams. Aribert and Aziz [24] developed a discrete shear connection model to perform a state analysis of composite beams taking into account the effects of uplift at the steel-concrete interface. The vertical separation (positive uplift) and the compressibility (negative uplift) of one layer bearing on the other was considered in [24] by imposing inequality constraint on the transverse displacement. More recently, a displacement-based finite element model for the analysis of elastic composite beams with continuous shear connection has been developed by Gara, Ranzi, and Leoni [25]. They adopted a bi-linear constitutive relationship between the gap and the uplift force, i.e. different stiffness for positive and negative uplift.

1.2.4 Geometric nonlinearity

Several large displacement formulations for two-layer beams including slip at the interface have been proposed either within the total Lagrangian framework or using the co-rotational framework [26, 27, 28, 29]. Most papers on composite beams are focused on the effects of inter-layer slip while the relative vertical displacement referred to as uplift is assumed to be negligible. Only a few authors considered both slip and uplift in their nonlinear geometric model. Kroflič, Saje, and Planinc [30] proposed a geometrically and materially nonlinear two-layer beam model by adopting the Reissner beam model for each layer. To circumvent geometric constraints on the transverse displacement at the interface, a thin-connecting-layer made of soft material is inserted between the two layers. In their model, slip and uplift are considered in an average sense and related to the generalized shear-force and the generalized normal tensile force, respectively. Most recently, Schnabl and Planinc [31] developed a finite element model to predict the elastic critical buckling loads and the corresponding buckling modes of two-layer composite Reissner's columns considering inter-layer slip and uplift at the interface.

1.2.5 Material Nonlinearity

In the context of inelastic behavior analysis of structures, two main types of modeling approaches are commonly used: concentrated plasticity and distributed plasticity. Concentrated plasticity elements are designed to lump plasticity at their member ends, which is expected to occur for beam-columns subject to strong lateral forces. These elements range from simple one- or two-component models with nonlinear springs at the member ends [32],

to more sophisticated elements with fiber modeling at predetermined plastic hinge lengths [33, 34]. For distributed plasticity models, member cross-section is discretized into several material fibers along the element length. This approach provides a more accurate representation of member response by accounting for nonlinear interaction of internal forces along the entire element.

For the study of the nonlinear behavior of composite members, the existing models can be grouped into the following two categories: (1) Finite-element models utilizing beam, plate, shell, and/or brick finite elements to represent in great detail the constituents of composite structural elements. Such models are rather complex and very computationally intensive. (2) 1D beam elements that capture salient features of the nonlinear behavior of composite members within the framework of beam theory. Within the latter category, proposed models can be grouped into three categories: (i) Full composite action models based on displacement interpolation functions with fiber discretization of the cross section and uniaxial stress-strain relations of the constituent materials, as proposed by [35] for the analysis of composite columns under uniaxial bending and [36] under biaxial bending; (ii) models of the partial composite action between concrete and steel based on displacement interpolation functions [25, 20] and (iii) recent models that attempt to overcome the limitation of displacement-based model by the use of force interpolation function (flexibility formulation). Interest in this nonlinear model increased after the work of [37], who proposed a consistent implementation of the flexibility formulation of a nonlinear Bernoulli beam element within the framework of a general-purpose nonlinear analysis program. In view of limitations of the displacement formulation, and the difficulty of selecting force interpolation functions that strictly satisfy equilibrium for the problem with strong interaction between displacements and internal forces, Ayoub and Filippou [38] recently proposed a consistent mixed formulation of the anchored reinforcing bar problem with independent interpolation functions for the axial displacements and the reinforcing steel stress. This formulation combines the advantages of the displacement and force formulation while overcoming most of their limitations.

The finite element formulation can be cast within the framework of displacement-based, force-based or mixed methods. In the displacement-based finite element analysis of composite beams, the coupling of the transverse and longitudinal displacement fields may cause oscillations in the interlayer slip field and reduction in optimal convergence rate. This problem is known as slip-locking. To avoid slip-locking behavior for the stiff connection, Erkmen and Bradford [39] proposed the assumed strain formulation and the kinematic interpolation strategy while Dall'Asta and Zona [40] and [41] adopted the consistent interpolation strategy.

Mixed and flexibility-based formulations [42, 43, 44, 45, 46] provide good potential alternatives for alleviating the above problems. Instead of using displacements as independent quantities in the formulation, other variables can be also included as independent variables.

For example, in a first-order distributed plasticity analysis of framing members subjected to only end loads, the exact variation of moments along the element is linear. If a mixed element formulation based on a linear interpolation of the moments is used, then a model can be established in which the governing differential equations of equilibrium are satisfied section-by-section along the length of the element. An improved representation of curvatures along the inelastic element length is achieved by the use of this moment interpolation, and the resulting element provides a sufficient accuracy with a coarse mesh compared to displacement-based formulations. For composite beam element, the bond slip shear forces along the element can be approximated by a cubic interpolation function [42]. The formulation of the element, however, is rather complex and it does not satisfy the kinematic condition of shear slip continuity [42]. Although the displacement and force-based formulations have the same degree of approximation, the force-based formulations may lead to superior accuracy when compared with displacement-based formulations because of the exact fulfillment of the equilibrium equations.

1.3 Objectives and Scope

This thesis presents an in-depth numerical modeling for two-layer composite beam with partial interaction, taking into account longitudinal slip and vertical uplift. For accounting those factors, the connectors are modeled by the two-directional springs. The horizontal one is parallel to the contact surface at the interface of the two layers, while the vertical one is orthogonal to the contact surface. The horizontal and the vertical springs are used to capture slip and uplift effects in the composite beam, respectively. In practical term, the penetration between layers (negative uplift) is not permitted. This requirement is presented by contact conditions which is solved by using contact resolution algorithm. This work focuses on several key aspects, including:

- Material and geometrically linear analysis: the two bond models (discrete and continuous bond model) with the non-penetration condition will be presented.
- Geometrically nonlinear analysis: the two bond models with the non-penetration condition will be presented in large displacement analysis by adopting the co-rotational formulation.
- Material and geometrically nonlinear analysis: FE formulation will be conducted using displacement-based and mixed (stress-strain) formulation. The plastic-damaged model for concrete and the plastic model for steel will be used. Moreover, the connection model accounts for the interaction between the shear and tension force of the connector is proposed and used in the FE model.

This thesis is composed of six important chapters, as follows:

Chapter 1 is the introduction part, state of the art, the objective and scopes of the study.

Chapter 2 presents a geometrically linear finite element formulation for the analysis of planar two-layered beam taking into account interlayer slip and uplift. The two bond models are considered in the analysis: the discrete and continuous bond models. The exact stiffness matrix is derived from the governing equations for both models. To prevent penetration between the layers, contact resolution methods such as the penalty and augmented Lagrangian methods with Uzawa updating schemes are adopted. Finally, numerical applications and discussions are presented.

Chapter 3 presents a geometrically nonlinear finite element formulation for the analysis of planar two-layer beam while taking into account interlayer slip and uplift. The co-rotational method is adopted, in which the motion of the element is decomposed into two parts: the rigid body motion and the small deformational one. The performance of the proposed formulation is assessed through several numerical applications. The works presented in this chapter have been published as a research paper (Oeng et al. [47]) in an international journal.

Chapter 4 presents the constitutive laws of the components that constitute the composite beams, including steel, concrete and connectors. A nonlinear kinematic/linear isotropic hardening model is presented for the steel material. The numerical integration of this model is developed. Additionally, a coupled plastic-damaged model is presented for the concrete material, and a coupled/uncoupled plastic model is introduced for the connectors.

Chapter 5 deals with the two different finite element formulations: displacement based and mixed formulation to treat the nonlinear material problem in nonlinear FEA. A fiber model is used to simulate the cross-section behavior. The algorithm and numerical applications, specially, the comparison of the numerical results with experimental data will be presented.

Chapter 6 is general the conclusions and perspectives.

The complexity of the calculations, formulations, basic approaches adopted in this study, and the big-sized matrix will be shown in the appendix as:

Appendix A presents the formulation for deriving global inter-layer slip and uplift variations.

Appendix B describes the formulation for interpolating in the displacement-based formulation.

Appendix C recalls the basic approaches in numerical integration process.

Appendix D shows the big-sized vector and matrix used in analysis for Chapter 5.

Chapter 2

Geometrically linear elastic behavior of composite beams

2.1 Introduction

This chapter presents the analysis of composite beam with partial interaction (including both slip and uplift) in a linear elastic range. The discrete and continuous bond models of connection are considered. The inter-layer slips and uplifts are represented by a two-directional spring element. For discrete bond model, the two-directional forces of the connector are at the extremities, whereas for continuous bond model, they are continuously distributed along the contact surface (interface) of the element. The behavior of the connector is assumed to be elastic linear. Accordingly, the shear force between the interacting elements is assumed to be directly proportional to the inter-layer slips which correspond to the relative longitudinal displacements at the interface. Uplifts should be positive or null. For positive uplift, the uplift force is directly proportional to the uplift. Primarily, the non-penetrated condition (contact condition) is relaxed, i.e. uplifts can be positive or negative. In doing so, the two layers of composite beam can be treated as individual beam elements that are either locally connected to each other at its extremities where the connectors are located for discrete bond model, or continuously connected to each other for continuous bond model. Hence, the equilibrium equations and compatibility relations at the interface can be developed. As a result, the governing equation can be derived and solved analytically. Finally, the exact stiffness matrix can be obtained.

To address the uplift problem at the interface surface, particularly the condition of non-interpenetration between the layers, a contact resolution method is adopted. One of the methods that can be used is the penalty method, which is similar to using anisotropic constitutive relationships for vertical springs connecting the connected layers. For the compressibility (negative uplift) of one layer bearing on the other (represented by contact conditions) the stiffness of the vertical spring becomes the so-called penalty parameter. Increasing the latter to infinity would lead to the exact solution to the contact problem. Another resolution

method is Lagrange multiplier method. In this method, the contact constraints is fulfilled exactly by introducing additional unknowns in the form of Lagrange multipliers. A combination of the penalty and Lagrangian multiplier methods leads to the so-called augmented Lagrangian method (ALM).

This chapter is structured in the following manner. The fundamental equations that describe compatibility, constitutive relations and equilibrium states are highlighted in Section 2.2. Sections 2.3 and 2.4 present the closed-form solutions for continuous and discrete bond model, respectively. The contact resolution methods are recalled in Section 2.5. Several numerical analyses are performed in Section 2.6 in order to support the conclusions made in Section 2.7.

2.2 Fundamental equations

The field equations describing the behavior of a linear elastic two-layered beam with slip and uplift at the interface are presented in this section. In what follows, the subscript a and b denote the components of the displacement field in layer a (steel beam) and b (concrete beam), respectively. The superscripts i and j denote the positions at the start and the end of the element, respectively.

The presented model assumes the following:

- The composite beam is composed of two straight beams whose cross-sections are symmetric with respect to y-axis.
- The composite beam is deformed in (x, y) plan.
- Connected components are made out of elastic, homogeneous and isotropic materials.
- Euler-Bernoulli's kinematic assumptions are hold.
- Slip as well as uplift can develop at the slab/joist interface and are assumed to be small.

2.2.1 Compatibility

The displacement field of a planar composite beam consists of two axial translations u_a and u_b in x-direction, two vertical translations v_a and v_b in y-direction and two rotations θ_a and θ_b around z-axis. The degree of freedom of the planar composite beam element without rigid body mode is:

$$\mathbf{q} = \left[u_b^i, v_b^i, \theta_b^i, u_a^i, v_a^i, \theta_a^i, u_b^j, v_b^j, \theta_b^j, u_a^j, v_a^j, \theta_a^j\right]^{\mathrm{T}} \tag{2.1}$$

Considering Euler-Bernoulli beam kinematics by assuming the rotations are small at the

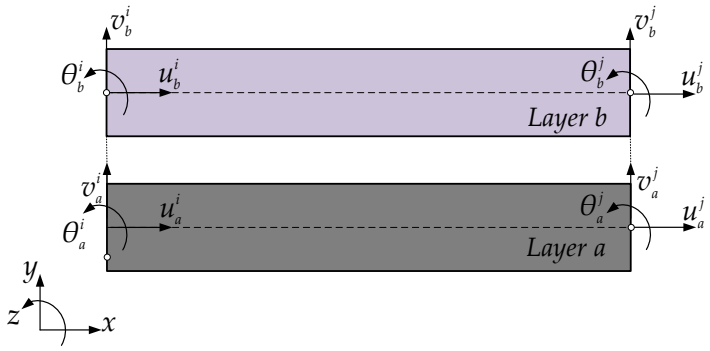

FIGURE 2.1: Unconnected beam in both layers

cross-section level, we have:

$$u_i(x,y) = u_i(x) - y_i\theta_i(x) \tag{2.2}$$

$$\theta_i(x) = v_{i,x}(x) \tag{2.3}$$

$$v_i(x,y) = v_i(x) \tag{2.4}$$

where $i = a,b$ and the subscript $(.)_{,x}$ denotes differentiation with respect to x.

The kinematic equations relating the displacement components (u_i, v_i, θ_i) to the corresponding strain component $(\epsilon_i, \theta_i, \kappa_i)$:

$$\epsilon_i = \partial u_i \tag{2.5}$$

$$\theta_i = \partial v_i \tag{2.6}$$

$$\kappa_i = \partial \theta_i \tag{2.7}$$

- $\partial = d/dx$
- ϵ_i , θ_i and κ_i are the axial strain, the cross-section rotation and the curvature of layer i, respectively.

It is worth mentioning that the slip is measured as the difference between the axial displacements of both layers at the contact surface and the uplift or gap is measured as the difference between the vertical displacement of both layers. As indicated in Fig. 2.2, the inter-layer slip s along the interface can be expressed as follows:

$$s = u_b - u_a + h_a \tan(\theta_a) + h_b \tan(\theta_b)$$

In which h_a and h_b are the distance between the centroid of both layers a and b, respectively to the contact surface. Since the cross-section rotations are small, we have $\tan(\theta_i) \approx \theta_i$. The

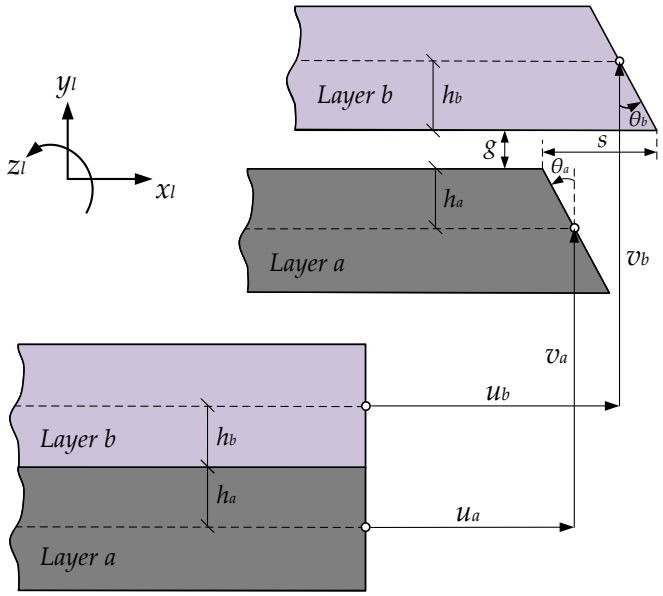

FIGURE 2.2: Representation of slip and uplift in deformed configuration

expression of slip s can be simplified as:

$$s = u_b - u_a + h_a\theta_a + h_b\theta_b \tag{2.8}$$

and the gap,

$$g = v_b - v_a \geq 0 \tag{2.9}$$

The difference between the vertical displacements of both layers must be positive and is known as uplift. In cases where the calculated gap is negative ($g < 0$), which is called penetration, for a certain loading condition, it must be adjusted by considering the non-penetrated condition.

2.2.2 Constitutive relationships

Constitutive relationship in beam

The generalized stress-strain relationships are simply obtained by integrating the appropriate uni-axial constitutive model over each cross-section. We adopt a linear stress-strain relationship at the material level and deduce the following constitutive law for the cross-section of each layer:

$$N_i = \int_{A_i} \sigma_i dA_i = E_i A_i \epsilon_i \tag{2.10}$$

$$M_i = -\int_{A_i} y_i \sigma_i dA_i = E_i I_i \kappa_i \tag{2.11}$$

in which N_i and M_i are normal force and bending moment of the layer i, respectively. E_i, A_i and I_i are the elastic modulus, the area of section, and the second moment of area of layer i, respectively.

Constitutive relationship in connection

The horizontal force, also known as the bond force, of connector elements is denoted by D_{sc}. This force represents the shear force transmitted between the layers through the connector element. The vertical force which is orthogonal to the bond force is denoted by V_{sc} and represents the normal force transmitted between layers through the connector element. These forces correspond to load transferring between the two layers of the composite beam.

A linear elastic relationship is adopted for both forces as follows:

- The bond force D_{sc}:

$$D_{sc} = K_h\, s \tag{2.12}$$

in which K_h is the horizontal or shear stiffness of connector and s is the slip at the interface calculated using Eq. (2.8)

- The uplift force V_{sc}:

$$V_{sc} = K_v\, g \tag{2.13}$$

in which K_v is the vertical or tensile stiffness of connector and g is the gap at the interface calculated using Eq. (2.9).

In case of discrete bond connection, both bond and uplift forces are evaluated at the extremities of the element.

2.2.3 Equilibrium

The composite beam element consists of two unconnected beam representing the two layers and a connector element at the interface. While the connector element is distributed along the beam at the interface, it results in a continuous connection between the layers. When the discrete bond model is considered, the connector elements are concentrated at both extremities.

The vertical displacements of the two unconnected beams are supposed to be different. In that case, uplift effects can be taken into account. The following presents the equilibrium equation, which serves as the basis for deriving the stiffness matrices of composite beam elements.

Equilibrium of continuous bond connection

A free body diagram of a differential element of composite beam subjected to a distributed transverse load q_y is considered in Fig. 2.3. The nodes are located at the centroid of both layers and at the extremities of the beam. The equilibrium conditions result in the following set of equations:

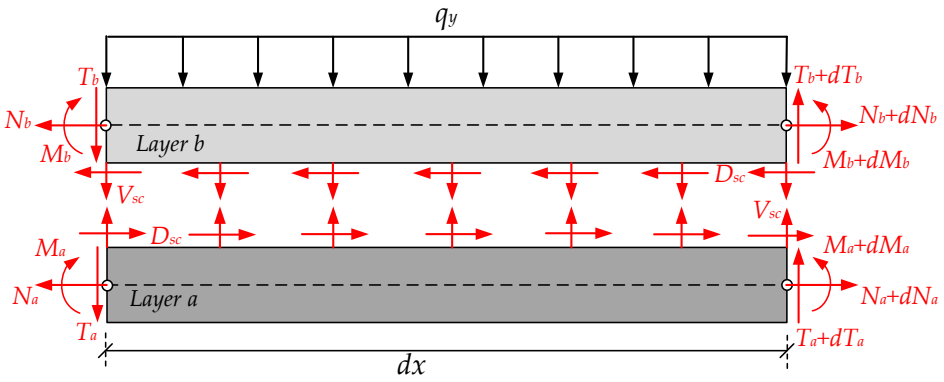

FIGURE 2.3: Equilibrium of the two-layered beam in continuous bond model

- For the layer a:

$$\partial N_a = -D_{sc} \tag{2.14}$$
$$\partial T_a = -V_{sc} \tag{2.15}$$
$$\partial M_a = -T_a + D_{sc} h_a \tag{2.16}$$

- For the layer b:

$$\partial N_b = D_{sc} \tag{2.17}$$
$$\partial T_b = q_y + V_{sc} \tag{2.18}$$
$$\partial M_b = -T_b + D_{sc} h_b \tag{2.19}$$

Equilibrium of discrete bond connection

- For the layer a:

$$\partial N_a = 0 \tag{2.20}$$
$$\partial T_a = 0 \tag{2.21}$$
$$\partial M_a = -T_a \tag{2.22}$$

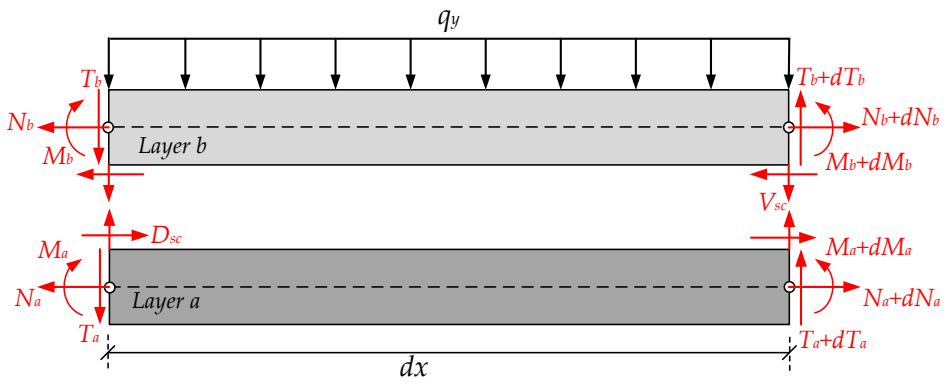

FIGURE 2.4: Equilibrium of the two-layered beam in discrete bond model

- For the layer b:

$$\partial N_b = 0 \tag{2.23}$$

$$\partial T_b = q_y \tag{2.24}$$

$$\partial M_b = -T_b \tag{2.25}$$

- Connector element:

  The equilibrium of a concentrated two-directional spring is illustrated in Fig. 2.5.

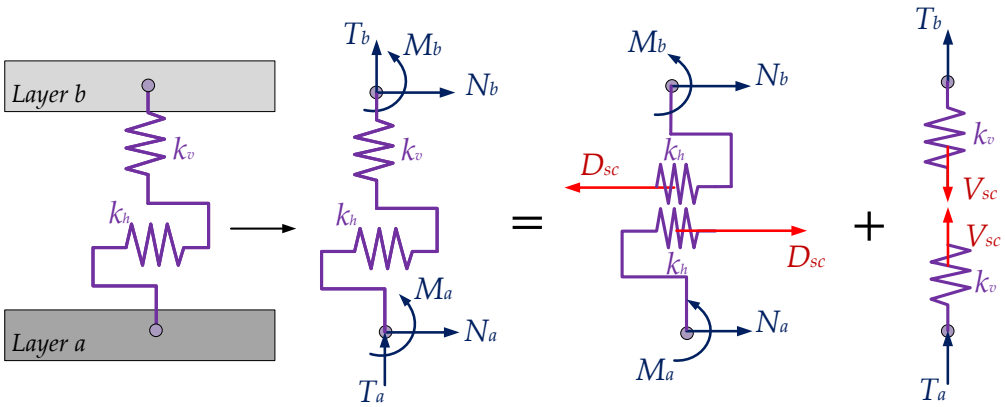

FIGURE 2.5: Schematic of internal force in the two-directional spring

In equilibrium with both layers, we obtain:

- With the layer a:

$$D_{sc} + N_a = 0 \tag{2.26}$$
$$V_{sc} + T_a = 0 \tag{2.27}$$
$$M_a - D_{sc} h_a = 0 \tag{2.28}$$

- With the layer b:

$$D_{sc} - N_b = 0 \tag{2.29}$$
$$-V_{sc} + T_b = 0 \tag{2.30}$$
$$M_b - D_{sc} h_b = 0 \tag{2.31}$$

2.3 Closed-form solution of the continuous bond model

In this section, we will determine analytically the displacement fields and internal forces as well as the exact stiffness matrix of an element in the continuous bond model.

2.3.1 Derivation of the governing equations

The relationship introduced in section 2.2.2 (using Eqs. (2.10) and (2.11)) are now combined to derive the equation governing the behavior of a two-layered beam in partial interaction. Combining the kinematic relations Eqs. (2.5-2.7) with the force-deformation relation Eqs. (2.10-2.11) and inserting the first derivation of the outcome and Eqs. (2.12) and (2.13) into the equilibrium equations, Eqs. (2.14-2.19), produce the following set of differential equations:

$$E_b A_b \partial^2 u_b = K_h s \tag{2.32}$$
$$E_a A_a \partial^2 u_a = -K_h s \tag{2.33}$$
$$E_b I_b \partial^3 v_b + E_a I_a \partial^3 v_a = -T + h K_h s \tag{2.34}$$

in which h is the distance between the centroids of both layers: $h = h_a + h_b$ and T is the total shear force. Inserting the first variation of the bond force Eq. (2.12) into the derivation of Eqs. (2.16) and (2.19), one obtains:

$$\partial^2 M_a = -\partial T_a + K_h h_a \partial s \tag{2.35}$$
$$\partial^2 M_b = -\partial T_b + K_h h_b \partial s \tag{2.36}$$

Making use of Eqs. (2.6), (2.7), (2.11), (2.13), (2.15) and (2.18), we obtain the fourth derivation of the vertical displacement for layer a and b as follows:

$$\partial^4 v_a = \frac{K_v g}{E_a I_a} + K_h h_a \frac{\partial s}{E_a I_a} \tag{2.37}$$

$$\partial^4 v_b = -\frac{q_y}{E_b I_b} - \frac{K_v g}{E_b I_b} + K_h h_b \frac{\partial s}{E_b I_b} \tag{2.38}$$

Substituting Eqs. (2.37) and (2.38) and the derivation of Eqs. (2.32) and (2.33) into the third derivation of the slip Eq. (2.8), we get:

$$\partial^3 s = A\partial s + Bg - \frac{h_b q_y}{E_b I_b} \tag{2.39}$$

where

$$A = \frac{K_h}{E_a A_a} + \frac{K_h}{E_b A_b} + \frac{K_h h_a^2}{E_a I_a} + \frac{K_h h_b^2}{E_b I_b}$$

$$B = K_v \left(\frac{h_a}{E_a I_a} - \frac{h_b}{E_b I_b} \right)$$

In practice, the horizontal stiffness of spring $K_h > 0$, we can say that A is always positive.

Taking the fourth derivation of the gap Eq. (2.9) and making use of Eq. (2.37) and Eq. (2.38), one gets the following equation:

$$\partial^4 g = Cg + D\partial s - \frac{q_y}{E_b I_b} \tag{2.40}$$

where

$$C = -K_v \left(\frac{1}{E_b I_b} + \frac{1}{E_a I_a} \right)$$

$$D = K_h \left(\frac{h_b}{E_b I_b} - \frac{h_a}{E_a I_a} \right)$$

In practice, the horizontal stiffness of spring $K_v > 0$, we can say that C is always negative.

Combining Eq. (2.40) and Eq. (2.39) by eliminate the slip s, we obtain the equation as follows:

$$\partial^6 g - A\partial^4 g - C\partial^2 g + (AC - DB)\, g = \frac{(A - Dh_b)}{E_b I_b} q_y \tag{2.41}$$

Let $\tilde{g} = \partial^2 g$; $\hat{g} = \partial^2 \tilde{g}$ and $E = \frac{(A - Dh_b)}{E_b I_b}$

We can write the system of equations as follows:

$$\begin{cases} \partial^2 g = \tilde{g} \\ \partial^2 \tilde{g} = \hat{g} \\ \partial^2 \hat{g} - A\hat{g} - C\tilde{g} + (AC - DB)\, g = Eq_y \end{cases} \tag{2.42}$$

Assuming $\mathbf{g}^* = [g, \quad \tilde{g}, \quad \hat{g}]^T$, one arrives at the following coupled second-order system of differential equations where the primary unknown variables are the gap distribution:

$$\partial^2 \mathbf{g}^* - \mathbf{M}\mathbf{g}^* = \mathbf{h} \tag{2.43}$$

in which

$$\mathbf{M} = \begin{bmatrix} 0 & 1 & 0 \\ 0 & 0 & 1 \\ -(AC - DB) & C & A \end{bmatrix}$$

and

$$\mathbf{h} = \begin{bmatrix} 0 & 0 & Eq_y \end{bmatrix}^T$$

Let $\mathbf{M}_\lambda$ and $\mathbf{M}_v$ respectively are the matrix collecting the eigenvalues and eigenvectors of $\mathbf{M}$. Then, we have the following relationship:

$$\mathbf{M}_\lambda = \mathbf{M}_v^{-1}\mathbf{M}\mathbf{M}_v \tag{2.44}$$

Subsequently, we insert the vector $\mathbf{g}^*$ obtained by pre-multiplying the vector $\bar{\mathbf{g}}$ by the matrix collecting the eigenvector:

$$\mathbf{g}^* = \mathbf{M}_v \bar{\mathbf{g}} \tag{2.45}$$

into Eq. (2.43) and make use of Eq. (2.44) to produce an uncoupled differential equation system:

$$\partial^2 \bar{\mathbf{g}} - \mathbf{M}_\lambda \bar{\mathbf{g}} = \bar{\mathbf{h}} \tag{2.46}$$

where

$$\bar{\mathbf{h}} = \mathbf{M}_v^{-1}\mathbf{h} \tag{2.47}$$

2.3.2 Solution of the governing equations

In this section, we provide only the analytical solution of the governing equations for the general case of the interface connection (which means that $0 < K_h, K_v < \infty$). Turning back to solve analytically Eqs. (2.39) and (2.40), we need to consider two cases depending on the

value of α:

$$\alpha = \frac{h_a}{E_a I_a} - \frac{h_b}{E_b I_b}$$

In cases of $\alpha \neq 0$, the governing second order differential equation Eq. (2.46) can be used and involves the single unknown variable $\bar{\mathbf{g}}$. The eigenvalue λ can be real or complex number depending on the matrix $\mathbf{M}$.

Nevertheless, in case $\alpha = 0$, the Eqs. (2.39) and (2.40) will becomes as follows:

$$\begin{cases} \partial^3 s = A\partial s - \dfrac{h_b q_y}{E_b I_b} \\ \partial^4 g = Cg - \dfrac{q_y}{E_b I_b} \end{cases} \tag{2.48}$$

which are uncoupled.

Case 1: $\alpha \neq 0$

When $\alpha \neq 0$, there are two subcases to consider with respect to the eigenvalue of $\mathbf{M}$. These subcases distinguish between real and complex eigenvalues, since elements of the matrix $\mathbf{M}$ can sometimes be negative.

- Case: Real eigenvalues

The homogenous solution $\bar{\mathbf{g}}$ is examined in three distinct cases of λ, wherein λ may be a positive, negative, or zero value.

- For $\lambda_i > 0$

$$\bar{\mathbf{g}}_i = \bar{C}_{2i-1} e^{\sqrt{\lambda_i} x} + \bar{C}_{2i} e^{-\sqrt{\lambda_i} x} - \frac{E q_y}{\lambda_i} \tag{2.49}$$

- For $\lambda_i = 0$

$$\bar{\mathbf{g}}_i = C_{2i-1} + C_{2i} x - \frac{E q_y}{\lambda_i} \tag{2.50}$$

- For $\lambda_i < 0$

$$\bar{\mathbf{g}}_i = C_{2i-1} \cos(\sqrt{-\lambda_i} x) + C_{2i} \sin(\sqrt{-\lambda_i} x) - \frac{E q_y}{\lambda_i} \tag{2.51}$$

The solution of $\bar{\mathbf{g}}_i$ in case $\lambda_i > 0$ invloves exponential terms which may take a very large value. To avoid numerical ill-conditioning of the stiffness matrix, we replace the actual expression of the constants of integration with the following ones:

$$\begin{cases} \bar{C}_{2i-1} = e^{-\sqrt{\lambda_i} L} C_{2i-1} \\ \bar{C}_{2i} = C_{2i-1} \end{cases} \tag{2.52}$$

By the dimension of matrix $\mathbf{M}$ is 3×3, the the subsprition i is the set of = $\{1,2,3\}$ and L is the length of the element. All $\bar{\mathbf{g}}_i$ are collected in a vector so the analytical solution can be written in a matrix form as follows:

$$\bar{\mathbf{g}} = \mathbf{X}_{\bar{g}}\mathbf{C} + \mathbf{Z}_{\bar{g}} \tag{2.53}$$

in which

$$\mathbf{C} = \begin{bmatrix} C_1 & C_1 & ... & C_{12} \end{bmatrix}^T$$

The component of matrix $\mathbf{X}_{\bar{g}}$ and $\mathbf{Z}_{\bar{g}}$ are dependent on the eigenvalues of $\mathbf{M}$ and the external load q_y, respectively. In case $\mathbf{M}$ is positive definite i.e. $\lambda_i > 0$, we obtain the following expression for $\mathbf{X}_{\bar{g}}$ and $\mathbf{Z}_{\bar{g}}$.

$$\mathbf{X}_{\bar{g}} = \begin{bmatrix} e^{\sqrt{\lambda_1}(x-L)} & e^{-\sqrt{\lambda_1}x} & 0 & 0 & 0 & 0 & 0 & 0 & 0 & 0 & 0 & 0 \\ 0 & 0 & e^{\sqrt{\lambda_2}(x-L)} & e^{-\sqrt{\lambda_2}x} & 0 & 0 & 0 & 0 & 0 & 0 & 0 & 0 \\ 0 & 0 & 0 & 0 & e^{\sqrt{\lambda_3}(x-L)} & e^{-\sqrt{\lambda_3}x} & 0 & 0 & 0 & 0 & 0 & 0 \end{bmatrix}$$

and

$$\mathbf{Z}_{\bar{\mathbf{g}}} = \begin{bmatrix} 0 & 0 & \dfrac{Eq_y}{\lambda_3} \end{bmatrix}^T$$

- Case: Complex eigenvalues

In some cases, the element of the matrix $\mathbf{M}$ can be negative. The matrix has one real eigenvalue λ_1 and two complex conjugate eigenvalues $\lambda_{re} + i\lambda_{im}$ and $\lambda_{re} - i\lambda_{im}$.

Here, λ_{re} and λ_{im} denote the real and imaginary parts of the complex eigenvalues, respectively. For the first real eigenvalue λ_1, $\bar{\mathbf{g}}_1$ can be expressed using Eqs. (2.49) to (2.51). As for the conjugate eigenvalue, there are three cases for the real part of the eigenvalue λ_{re}, as follows:

Assume that $\mathbf{M}_v^{-1}\mathbf{h} = \begin{bmatrix} v_1' \\ v_{re}' + iv_{im}' \\ v_{re}' - iv_{im}' \end{bmatrix}$

Let v_1' denote the initial component of vector $\mathbf{M}_v^{-1}\mathbf{h}$, and let v_{re}' and v_{im}' denote the real and complex values of the second component of the vector, respectively. In this scenario, the third component of $\mathbf{M}_v^{-1}\mathbf{h}$ is consistently conjugated complex with the second component.

- For $\lambda_{re} > 0$

$$\begin{aligned} \bar{\mathbf{g}}_2 = {} & C_3 e^{\sqrt{\lambda_{re}}(x-L)} \left(\cos(\sqrt{\lambda_{im}}x) + i\sin(\sqrt{\lambda_{im}}x) \right) \\ & + C_4 e^{-\sqrt{\lambda_{re}}(x)} \left(\cos(\sqrt{\lambda_{im}}x) - i\sin(\sqrt{\lambda_{im}}x) \right) - Eq_y \left(\frac{v_{re}' + iv_{im}'}{\lambda_{re} + i\lambda_{im}} \right) \end{aligned} \tag{2.54}$$

$$\begin{aligned}\bar{\mathbf{g}}_3 &= C_5 e^{\sqrt{\lambda_{re}}(x-L)}\left(\cos(\sqrt{\lambda_{im}}x) - i\sin(\sqrt{\lambda_{im}}x)\right) \\ &+ C_6 e^{-\sqrt{\lambda_{re}}(x)}\left(\cos(\sqrt{\lambda_{im}}x) + i\sin(\sqrt{\lambda_{im}}x)\right) - Eq_y\left(\frac{v'_{re} - iv'_{im}}{\lambda_{re} - i\lambda_{im}}\right)\end{aligned} \tag{2.55}$$

- For $\lambda_{re} = 0$

$$\begin{aligned}\bar{\mathbf{g}}_2 &= C_3\left(\cos(\sqrt{\lambda_{im}}x) + i\sin(\sqrt{\lambda_{im}}x)\right) \\ &+ C_4 x\left(\cos(\sqrt{\lambda_{im}}x) - i\sin(\sqrt{\lambda_{im}}x)\right) - Eq_y\left(\frac{v'_{re} + iv'_{im}}{\lambda_{re} + i\lambda_{im}}\right)\end{aligned} \tag{2.56}$$

$$\begin{aligned}\bar{\mathbf{g}}_3 &= C_5\left(\cos(\sqrt{\lambda_{im}}x) - i\sin(\sqrt{\lambda_{im}}x)\right) \\ &+ C_6 x\left(\cos(\sqrt{\lambda_{im}}x) + i\sin(\sqrt{\lambda_{im}}x)\right) - Eq_y\left(\frac{v'_{re} - iv'_{im}}{\lambda_{re} - i\lambda_{im}}\right)\end{aligned} \tag{2.57}$$

- For $\lambda_{re} < 0$

$$\begin{aligned}\bar{\mathbf{g}}_2 &= C_3\left(\cos(\sqrt{-\lambda_{re}}x)\right)\left(\cos(\sqrt{\lambda_{im}}x) + i\sin(\sqrt{\lambda_{im}}x)\right) \\ &+ C_4\left(\sin(\sqrt{-\lambda_{re}}x)\right)\left(\cos(\sqrt{\lambda_{im}}x) - i\sin(\sqrt{\lambda_{im}}x)\right) - Eq_y\left(\frac{v'_{re} + iv'_{im}}{\lambda_{re} + i\lambda_{im}}\right)\end{aligned} \tag{2.58}$$

$$\begin{aligned}\bar{\mathbf{g}}_3 &= C_5\left(\cos(\sqrt{-\lambda_{re}}x)\right)\left(\cos(\sqrt{\lambda_{im}}x) - i\sin(\sqrt{\lambda_{im}}x)\right) \\ &+ C_6\left(\sin(\sqrt{-\lambda_{re}}x)\right)\left(\cos(\sqrt{\lambda_{im}}x) + i\sin(\sqrt{\lambda_{im}}x)\right) - Eq_y\left(\frac{v'_{re} - iv'_{im}}{\lambda_{re} - i\lambda_{im}}\right)\end{aligned} \tag{2.59}$$

Substituting Eq. (2.53) into Eq. (2.45), we obtain:

$$\mathbf{g}^* = \mathbf{X}_{g^*}\mathbf{C} + \mathbf{Z}_{g^*} \tag{2.60}$$

where

$$\mathbf{X}_{g^*} = \begin{bmatrix}\mathbf{X}_{\mathbf{g}} \\ \mathbf{X}_{\tilde{\mathbf{g}}} \\ \mathbf{X}_{\hat{\mathbf{g}}}\end{bmatrix} = \mathbf{M}_v\mathbf{X}_{\bar{g}} \qquad ; \qquad \mathbf{Z}_{g^*} = \begin{bmatrix}\mathbf{Z}_{\mathbf{g}} \\ \mathbf{Z}_{\tilde{\mathbf{g}}} \\ \mathbf{Z}_{\hat{\mathbf{g}}}\end{bmatrix} = \mathbf{M}_v\mathbf{Z}_{\bar{g}}$$

The matrix $\mathbf{X}_{g^*}$ as well as the vector $\mathbf{Z}_{g^*}$ are decomposed into two sub-matrices and sub-vectors, respectively in order to separate the distribution of gap $\mathbf{g}$, the second derivation of gap $\tilde{\mathbf{g}}$ and fourth derivation of gap $\hat{\mathbf{g}}$.

Substituting $\mathbf{g}^* = [\mathbf{g}, \quad \tilde{\mathbf{g}}, \quad \hat{\mathbf{g}}]^T$ to Eq. (2.60), one obtains:

$$\mathbf{g} = \mathbf{X}_g \mathbf{C} + \mathbf{Z}_g \tag{2.61}$$

$$\tilde{\mathbf{g}} = \mathbf{X}_{\tilde{g}} \mathbf{C} + \mathbf{Z}_{\tilde{g}} \tag{2.62}$$

$$\hat{\mathbf{g}} = \mathbf{X}_{\hat{g}} \mathbf{C} + \mathbf{Z}_{\hat{g}} \tag{2.63}$$

Case 2: $\alpha = 0$

In this study case, the supposed value B in Eq. (2.39) and D in Eq. (2.40) are equal to zeros. With $B = 0$, the differential equation Eq. (2.39) will become:

$$\partial s^3 = A \partial s - \frac{h_b q_y}{E_b I_b} \tag{2.64}$$

As mentioning above $A = \frac{K_h}{E_a A_a} + \frac{K_h}{E_b A_b} + \frac{K_h h_a^2}{E_a I_a} + \frac{K_h h_b^2}{E_b I_b}$ cannot be negative.

$$\begin{cases} A > 0 \rightarrow & \partial s = \bar{C}_1 e^{\sqrt{A}x} + \bar{C}_2 e^{-\sqrt{A}x} + \dfrac{h_b q_y}{A E_b I_b} \\ \text{or} & \partial s = C_1 e^{\sqrt{A}(x-L)} + C_2 e^{-\sqrt{A}x} + \dfrac{h_b q_y}{A E_b I_b} \\ A = 0 \rightarrow & \partial s = C_1 + C_2 x + \dfrac{h_b q_y}{A E_b I_b} \end{cases} \tag{2.65}$$

It is able to write the first derivation of function slip, ∂s in form of:

$$\partial s = \mathbf{X}_{\partial s} \mathbf{C} + \mathbf{Z}_{\partial s} \tag{2.66}$$

We note that $\mathbf{X}_{\partial s}$ and $\mathbf{Z}_{\partial s}$ can be computed from Eq. (2.65). For example, in case of $A > 0$:

$$\mathbf{X}_{\partial s} = \begin{bmatrix} e^{\sqrt{\lambda_1}(x-L)} & e^{-\sqrt{\lambda_1}x} & 0 & 0 & 0 & 0 & 0 & 0 & 0 & 0 & 0 & 0 \end{bmatrix}$$

and

$$\mathbf{Z}_{\partial s} = \frac{h_b q_y}{A E_b I_b}$$

With $D = 0$, the differential equation Eq. (2.40) will become:

$$\partial g^4 = C g - \frac{q_y}{E_b I_b} \tag{2.67}$$

We recall that $C = -K_v\left(\frac{1}{E_b I_b} + \frac{1}{E_a I_a}\right) < 0$, for any positive value of vertical spring stiffness. The solution of this fourth differential equation is expressed by:

$$g = C_3 e^{\sqrt[4]{-C}(x-L)} + C_4 e^{-\sqrt[4]{-C}x} + C_5\cos(\sqrt[4]{-C}x) + C_6\sin(\sqrt[4]{-C}x) + \frac{q_y}{CE_bI_b} \tag{2.68}$$

We can write the gap function as following:

$$\mathbf{g} = \mathbf{X_g C} + \mathbf{Z_g}$$

$$\mathbf{X}_g = \begin{bmatrix} 0 & 0 & e^{\sqrt[4]{-C}(x-L)} & e^{-\sqrt[4]{-C}x} & \cos(\sqrt[4]{-C}x) & \sin(\sqrt[4]{-C}x) & 0 & 0 & 0 & 0 & 0 & 0 \end{bmatrix}$$

and

$$\mathbf{Z}_g = \frac{q_y}{CE_bI_b}$$

2.3.3 Determination of displacement fields

To solve the Eq. (2.34), it requires the distribution of the total shear force $T(x)$ to be known. In order to simplify the development of the solution, we assume that the external distributed load on the element is uniform. As a result, the distribution of the shear force must be linear to ensure the overall transverse equilibrium:

$$T(x) = q_y x + C_{12} \tag{2.69}$$

in which C_{12} is the shear force at the left hand side of the beam and be considered to be a 12^{th} constant of integration. To compute the axial displacement, the deflections and rotations of both layers, we use the relationships in which the kinematic variables are expressed as a function of slip and gap. Combining Eq. (2.9) and Eq. (2.34), one obtains the function of third derivation of vertical displacement in both layers:

$$\partial^3 v_b = \frac{-(q_y x + C_{12}) + (h_a + h_b)k_h s + E_a I_a \partial^3 g}{E_a I_a + E_b I_b} \tag{2.70}$$

$$\partial^3 v_a = \frac{-(q_y x + C_{12}) + (h_a + h_b)k_h s - E_b I_b \partial^3 g}{E_a I_a + E_b I_b} \tag{2.71}$$

Inserting Eqs. (2.32) and (2.33) to the second derivation of the slip function Eq. (2.8), one can possibly compute the slip function in a new form as:

$$s = \frac{\partial^2 s - (h_a \partial^3 v_a + h_b \partial^3 v_b)}{F k_h} \tag{2.72}$$

in which, we have

$$\partial s = D^{-1}\partial^4 g - D^{-1} C g + D^{-1}\frac{q_y}{E_b I_b} \tag{2.73}$$

and

$$F = \frac{1}{E_a A_a} + \frac{1}{E_b A_b} \tag{2.74}$$

Replacing Eq. (2.72) into Eq. (2.70), one obtains:

$$\partial^3 v_b = \mathbf{X}_{\partial^3 v_b}\mathbf{C} + \mathbf{Z}_{\partial^3 v_b} \tag{2.75}$$

in which,

$$\mathbf{X}_{\partial^3 v_b} = \frac{-\mathbf{I}_{12} + (h_a + h_b)\dfrac{\mathbf{X}_{\partial^2 s}}{F} + \mathbf{X}_{\partial^3 g}\left(E_a I_a + \dfrac{h h_a}{F}\right)}{f} \tag{2.76}$$

$$\mathbf{Z}_{\partial^3 v_b} = \frac{-q_y x + (h_a + h_b)\dfrac{\mathbf{Z}_{\partial^2 s}}{F} + \mathbf{Z}_{\partial^3 g}\left(E_a I_a + \dfrac{h h_a}{F}\right)}{f} \tag{2.77}$$

where

$$f = E_a I_a + E_b I_b + \frac{h^2}{F}$$

$$\mathbb{I}_i = \begin{bmatrix} 0 & 0 & 0 & 0 & 0 & 0 & \delta_{i7} & \delta_{i8} & \delta_{i9} & \delta_{i10} & \delta_{i11} & \delta_{i12} \end{bmatrix}$$

δ_{ij} is the Kronecker delta, where $\delta_{ij} = \begin{cases} 0 & \text{if} \quad i \neq j \\ 1 & \text{if} \quad i = j \end{cases}$

and

$$\mathbf{X}_{\partial^2 s} = \partial^2 \mathbf{X}_s \tag{2.78}$$

$$\mathbf{Z}_{\partial^2 s} = \partial^2 \mathbf{Z}_s \tag{2.79}$$

$$\mathbf{X}_{\partial^3 g} = \partial^3 \mathbf{X}_g \tag{2.80}$$

$$\mathbf{Z}_{\partial^3 g} = \partial^3 \mathbf{Z}_g \tag{2.81}$$

The vertical displacement of layer b, v_b is computed by:

$$v_b = \mathbf{X}_{v_b}\mathbf{C} + \mathbf{Z}_{v_b} \tag{2.82}$$

where

$$\mathbf{X}_{v_b} = \int \mathbf{X}_{\theta_b} dx + \mathbb{I}_9 \quad ; \quad \mathbf{Z}_{v_b} = \int \mathbf{Z}_{\theta_b} dx \tag{2.83}$$

$$\mathbf{X}_{\theta_b} = \int \mathbf{X}_{\kappa_b} dx + \mathbb{I}_8 \quad ; \quad \mathbf{Z}_{\theta_b} = \int \mathbf{Z}_{\kappa_b} dx \tag{2.84}$$

$$\mathbf{X}_{\kappa_b} = \int \mathbf{X}_{\partial^3 v_b} dx + \mathbb{I}_7 \quad ; \quad \mathbf{Z}_{\kappa_b} = \int \mathbf{Z}_{\partial^3 v_b} dx \tag{2.85}$$

Substituting Eqs. (2.61) and (2.83) to the gap function Eq. (2.9), one obtains the vertical displacement of layer a:

$$v_a = \mathbf{X}_{v_a}\mathbf{C} + \mathbf{Z}_{v_a} \tag{2.86}$$

in which,

$$\mathbf{X}_{v_a} = \mathbf{X}_{v_b} - \mathbf{X}_g \tag{2.87}$$
$$\mathbf{Z}_{v_a} = \mathbf{Z}_{v_b} - \mathbf{Z}_g \tag{2.88}$$

The rotations of both layers are expressed by:

$$\theta_b = \mathbf{X}_{\theta_b}\mathbf{C} + \mathbf{Z}_{\theta_b} \tag{2.89}$$
$$\theta_a = \mathbf{X}_{\theta_a}\mathbf{C} + \mathbf{Z}_{\theta_a} \tag{2.90}$$

in which,

$$\mathbf{X}_{\theta_a} = \mathbf{X}_{\theta_b} - \mathbf{X}_{\partial g} \tag{2.91}$$
$$\mathbf{Z}_{\theta_a} = \mathbf{Z}_{\theta_b} - \mathbf{Z}_{\partial g} \tag{2.92}$$
$$\mathbf{X}_{\partial g} = \partial \mathbf{X}_g \tag{2.93}$$
$$\mathbf{Z}_{\partial g} = \partial \mathbf{Z}_g \tag{2.94}$$

The axial displacement of layer b can be determined by integrating its second derivation Eq. (2.32). This gives

$$u_b = \mathbf{X}_{u_b}\mathbf{C} + \mathbf{Z}_{u_b} \tag{2.95}$$

where

$$\mathbf{X}_{\partial u_b} = \int \mathbf{X}_{\partial^2 u_b} + \mathbb{I}_{10} \tag{2.96}$$
$$\mathbf{Z}_{\partial u_b} = \int \mathbf{Z}_{\partial^2 u_b} \tag{2.97}$$
$$\mathbf{X}_{u_b} = \int \mathbf{X}_{\partial u_b} + \mathbb{I}_{11} \tag{2.98}$$
$$\mathbf{Z}_{u_b} = \int \mathbf{Z}_{\partial u_b} \tag{2.99}$$

Once the axial displacement of the first layer is known, Eq. (2.8) is used to derive the axial displacement as follows:

$$u_a = \mathbf{X}_{u_a}\mathbf{C} + \mathbf{Z}_a \tag{2.100}$$

where:

$$\mathbf{X}_{u_a} = \mathbf{X}_{u_b} - \mathbf{X}_s + h_a\mathbf{X}_{\theta_a} + h_b\mathbf{X}_{\theta_b} \tag{2.101}$$
$$\mathbf{Z}_{u_a} = \mathbf{Z}_{u_b} - \mathbf{Z}_s + h_a\mathbf{Z}_{\theta_a} + h_b\mathbf{Z}_{\theta_b} \tag{2.102}$$

2.3.4 Determination of internal forces vector

After defining the displacement fields, the force fields can be obtained using the linear elastic relationship given by Eqs. (2.10-2.11).

- For layer b

$$N_b = \mathbf{Y}_{N_b}\mathbf{C} + \mathbf{R}_{N_b} \tag{2.103}$$
$$M_b = \mathbf{Y}_{M_b}\mathbf{C} + \mathbf{R}_{M_b} \tag{2.104}$$
$$T_b = \mathbf{Y}_{T_b}\mathbf{C} + \mathbf{R}_{T_b} \tag{2.105}$$

where

$$\mathbf{Y}_{N_b} = E_b A_b \mathbf{X}_{\partial u_b} \tag{2.106}$$
$$\mathbf{Y}_{M_b} = E_b I_b \mathbf{X}_{\kappa_b} \tag{2.107}$$
$$\mathbf{Y}_{T_b} = -E_b I_b \mathbf{X}_{\partial^3 v_b} + h_b K_h \mathbf{X}_s \tag{2.108}$$

and

$$\mathbf{R}_{N_b} = E_b A_b \mathbf{Z}_{\partial u_b} \tag{2.109}$$
$$\mathbf{R}_{M_b} = E_b I_b \mathbf{Z}_{\kappa_b} \tag{2.110}$$
$$\mathbf{R}_{T_b} = -E_b I_b \mathbf{Z}_{\partial^3 v_b} + h_b K_h \mathbf{Z}_s \tag{2.111}$$

- For layer a

$$N_a = \mathbf{Y}_{N_a}\mathbf{C} + \mathbf{R}_{N_a} \tag{2.112}$$
$$M_a = \mathbf{Y}_{M_a}\mathbf{C} + \mathbf{R}_{M_a} \tag{2.113}$$
$$T_a = \mathbf{Y}_{T_a}\mathbf{C} + \mathbf{R}_{T_a} \tag{2.114}$$

where

$$\mathbf{Y}_{N_a} = E_a A_a \mathbf{X}_{\partial u_a} \tag{2.115}$$
$$\mathbf{Y}_{M_a} = E_a I_a \mathbf{X}_{\theta_a} \tag{2.116}$$
$$\mathbf{Y}_{T_a} = -E_a I_a \mathbf{X}_{\partial^3 v_a} + h_a K_h \mathbf{X}_s \tag{2.117}$$

and

$$\mathbf{R}_{u_a} = E_a A_a \mathbf{Z}_{\partial u_a} \tag{2.118}$$

$$\mathbf{R}_{M_a} = E_a I_a \mathbf{Z}_{\theta_a} \tag{2.119}$$

$$\mathbf{R}_{T_a} = -E_a I_a \mathbf{Z}_{\partial^3 v_a} + h_a K_h \mathbf{Z}_s \tag{2.120}$$

The direct stiffness method is used to derive the exact stiffness of the two-layered beam. Applying the kinematic boundary conditions at $x = 0$ and $x = L$ leads to the relationship between the vector of constants of integration $\mathbf{C}$ and the vector of displacement $\mathbf{q}$, where L is the length of beam element. The vector of nodal displacements $\mathbf{q}$ can be derived:

$$\mathbf{q} = \mathbf{X_c C} + \mathbf{Z_c} \tag{2.121}$$

The nodal forces vector can be expressed in compact form as:

$$\mathbf{Q} = \mathbf{Y_c C} + \mathbf{R_c} \tag{2.122}$$

in which,

$$\mathbf{q} = \begin{bmatrix} u_b(0) \\ v_b(0) \\ \theta_b(0) \\ u_a(0) \\ v_a(0) \\ \theta_a(0) \\ u_b(L) \\ v_b(L) \\ \theta_b(L) \\ u_a(L) \\ v_a(L) \\ \theta_a(L) \end{bmatrix} \quad ; \quad \mathbf{X_c} = \begin{bmatrix} \mathbf{X}_{u_b}(0) \\ \mathbf{X}_{v_b}(0) \\ \mathbf{X}_{\theta_b}(0) \\ \mathbf{X}_{u_a}(0) \\ \mathbf{X}_{v_a}(0) \\ \mathbf{X}_{\theta_a}(0) \\ \mathbf{X}_{u_b}(L) \\ \mathbf{X}_{v_b}(L) \\ \mathbf{X}_{\theta_b}(L) \\ \mathbf{X}_{u_a}(L) \\ \mathbf{X}_{v_a}(L) \\ \mathbf{X}_{\theta_a}(L) \end{bmatrix} \quad ; \quad \mathbf{Z_c} = \begin{bmatrix} \mathbf{Z}_{u_b}(0) \\ \mathbf{Z}_{v_b}(0) \\ \mathbf{Z}_{\theta_b}(0) \\ \mathbf{Z}_{u_a}(0) \\ \mathbf{Z}_{v_a}(0) \\ \mathbf{Z}_{\theta_a}(0) \\ \mathbf{Z}_{u_b}(L) \\ \mathbf{Z}_{v_b}(L) \\ \mathbf{Z}_{\theta_b}(L) \\ \mathbf{Z}_{u_a}(L) \\ \mathbf{Z}_{v_a}(L) \\ \mathbf{Z}_{\theta_a}(L) \end{bmatrix} \tag{2.123}$$

and

$$\mathbf{Q} = \begin{bmatrix} -N_b(0) \\ -T_b(0) \\ -M_b(0) \\ -N_a(0) \\ -T_a(0) \\ -M_a(0) \\ N_b(L) \\ T_b(L) \\ M_b(L) \\ N_a(L) \\ T_a(L) \\ M_a(L) \end{bmatrix} \quad ; \quad \mathbf{Y_c} = \begin{bmatrix} -\mathbf{Y}_{N_b}(0) \\ -\mathbf{Y}_{T_b}(0) \\ -\mathbf{Y}_{M_b}(0) \\ -\mathbf{Y}_{N_a}(0) \\ -\mathbf{Y}_{T_a}(0) \\ -\mathbf{Y}_{M_a}(0) \\ \mathbf{Y}_{N_b}(L) \\ \mathbf{Y}_{T_b}(L) \\ \mathbf{Y}_{M_b}(L) \\ \mathbf{Y}_{N_a}(L) \\ \mathbf{Y}_{T_a}(L) \\ \mathbf{Y}_{M_a}(L) \end{bmatrix} \quad ; \quad \mathbf{R_c} = \begin{bmatrix} -\mathbf{R}_{N_b}(0) \\ -\mathbf{R}_{T_b}(0) \\ -\mathbf{R}_{M_b}(0) \\ -\mathbf{R}_{N_a}(0) \\ -\mathbf{R}_{T_a}(0) \\ -\mathbf{R}_{M_a}(0) \\ \mathbf{R}_{N_b}(L) \\ \mathbf{R}_{T_b}(L) \\ \mathbf{R}_{M_b}(L) \\ \mathbf{R}_{N_a}(L) \\ \mathbf{R}_{T_a}(L) \\ \mathbf{R}_{M_a}(L) \end{bmatrix} \tag{2.124}$$

2.3.5 Exact stiffness matrix

The nodal displacements are independent, and thus, the matrix $\mathbf{X}_c$ is invertible. Consequently, the set of constants $\mathbf{C}$ are obtained as a function of the nodal displacements $\mathbf{q}$. The constants $\mathbf{C}$ can be computed using Eq. (2.121), depending on the specific formulation and assumptions used in the beam analysis.

$$\mathbf{C} = \mathbf{X_c}^{-1}(\mathbf{q} - \mathbf{Z_c}) \tag{2.125}$$

Substituting the Eq. (2.125) into Eq. (2.122), one obtains:

$$\mathbf{Kq} = \mathbf{Q} + \mathbf{Q}_{ext} \tag{2.126}$$

where

$$\mathbf{K} = \mathbf{Y_c}\mathbf{X_c}^{-1} \tag{2.127}$$

represented the exact stiffness of the element, and

$$\mathbf{Q}_{ext} = \mathbf{K}\mathbf{Z_c} - \mathbf{R_c} \tag{2.128}$$

represented the nodal force due to the uniform external load q_y.

2.4 Closed-form solution of the discrete bond model

In contrast to the continuous bond model, the stiffness matrix of the composite beam element can be easily derived in the discrete bond model. In fact, it requires only the individual stiffness of the unconnected beam and of the connector element. Once derived, the

stiffnesses are assembled in a consistent position.

The compatibility introduced in Section 2.2.1 is now combined with force-deformation relation in Section 2.2.2 for layer i, we obtain:

$$N_i(x) = E_i A_i \frac{du_i(x)}{dx} \tag{2.129}$$

$$M_i(x) = E_i I_i \frac{d^2 v_i(x)}{dx^2} \tag{2.130}$$

By making uses of the Eqs. (2.20), (2.22), (2.23) and (2.25), the second variation of axial displacement and fourth variation of vertical displacement are expressed by:

For layer b,

$$\partial^2 u_b(x) = 0 \tag{2.131}$$

$$\partial^4 v_b(x) = -\frac{q_y}{EI} \tag{2.132}$$

For layer a,

$$\partial^2 u_a(x) = 0 \tag{2.133}$$

$$\partial^4 v_a(x) = 0 \tag{2.134}$$

The solution of non-homogeneous differential equations for Eqs. (2.131) to (2.134) are as follows:

For layer b,

$$v_b(x) = C_1 x^3 + C_2 x^2 + C_3 x + C_4 + v_{q_y}(x) \tag{2.135}$$

$$\theta_b(x) = 3C_1 x^2 + 2C_2 x + C_3 + \partial v_{q_y}(x) \tag{2.136}$$

$$u_b(x) = C_5 x + C_6 \tag{2.137}$$

For layer a,

$$v_a(x) = C_7 x^3 + C_8 x^2 + C_9 x + C_{10} \tag{2.138}$$

$$\theta_a(x) = 3C_7 x^2 + 2C_8 x + C_9 \tag{2.139}$$

$$u_a(x) = C_{11} x + C_{12} \tag{2.140}$$

where $C_1, C_2, \ldots, C_{12}$ are constants.

2.4.1 Determination of displacement fields

In general, the displacement field is characterized by its components as expressed in Eq. (2.1). However, through the discrete bond model, it becomes feasible to calculate the analogous

components on layer b and a. The start and end of extremities can be defined at $x = 0$ and $x = L$, respectively.

Hence, with respect to layer b, the relationships can be computed by making uses Eqs. (2.135-2.137) as follows:

$$\begin{bmatrix} u_b(0) \\ v_b(0) \\ \theta_b(0) \\ u_b(L) \\ v_b(L) \\ \theta_b(L) \end{bmatrix} = \begin{bmatrix} 0 & 0 & 0 & 0 & 0 & 1 \\ 0 & 0 & 0 & 1 & 0 & 0 \\ 0 & 0 & 1 & 0 & 0 & 0 \\ 0 & 0 & 0 & 0 & L & 1 \\ L^3 & L^2 & L & 1 & 0 & 0 \\ 3L^2 & 2L & 1 & 0 & 0 & 0 \end{bmatrix} \begin{bmatrix} C_1 \\ C_2 \\ C_3 \\ C_4 \\ C_5 \\ C_6 \end{bmatrix} + \begin{bmatrix} 0 \\ v_{q_y}(0) \\ \partial v_{q_y}(0) \\ 0 \\ v_{q_y}(L) \\ \partial v_{q_y}(L) \end{bmatrix} \tag{2.141}$$

Or

$$\mathbf{q} = \mathbf{X_d C} + \mathbf{Z_d} \tag{2.142}$$

It is noticeable that the displacement field $\mathbf{q}$ in Eq. (2.142) considers only layer b and $\mathbf{C}$ are $C_1, C_2, \ldots, C_6$.

2.4.2 Determination of internal forces vector

To compute the internal force vector, only the displacement field in layer b, as represented in Section 2.4.1, is taken into account. Upon combining the relationships presented in Eqs. (2.10-2.11) with the displacement fields, the following expression is obtained:

$$\begin{bmatrix} N_b(0) \\ T_b(0) \\ M_b(0) \\ N_b(L) \\ T_b(L) \\ M_b(L) \end{bmatrix} = \begin{bmatrix} 0 & 0 & 0 & 0 & -(EA)_b & 0 \\ 6(EI)_b & 0 & 0 & 0 & 0 & 0 \\ 0 & -2(EI)_b & 0 & 0 & 0 & 0 \\ 0 & 0 & 0 & 0 & (EA)_b & 0 \\ -6(EI)_b & 0 & 0 & 0 & 0 & 0 \\ 6L(EI)_b & 2(EI)_b & 0 & 0 & 0 & 0 \end{bmatrix} \begin{bmatrix} C_1 \\ C_2 \\ C_3 \\ C_4 \\ C_5 \\ C_6 \end{bmatrix} + \begin{bmatrix} 0 \\ (EI)_b \partial^3 v_{q_y}(0) \\ -(EI)_b \partial^2 v_{q_y}(0) \\ 0 \\ -(EI)_b \partial^3 v_{q_y}(L) \\ (EI)_b \partial^2 v_{q_y}(L) \end{bmatrix}$$

Or,

$$\mathbf{Q} = \mathbf{Y_d C} + \mathbf{Z_d} \tag{2.143}$$

2.4.3 Exact stiffness matrix

The exact stiffness matrix for the discrete bond model can be obtained by performing an analogous calculation as the ones in Section 2.3.5. The constants $\mathbf{C}$ can be computed using Eq. (2.142), depending on the specific formulation and assumptions used in the beam analysis.

$$\mathbf{C} = \mathbf{X}_d^{-1} (\mathbf{q} - \mathbf{Z_d}) \tag{2.144}$$

Substituting the Eq. (2.144) into Eq. (2.143), one obtains:

$$\mathbf{K}_b\mathbf{q} = \mathbf{Q} + \mathbf{Q}_{ext} \tag{2.145}$$

where

$$\mathbf{K}_b = \mathbf{Y_d}\mathbf{X_d}^{-1} \tag{2.146}$$

represents the exact stiffness of the element for layer b.

The rigidity matrix of the unconnected beam element for layer b is as follows:

$$\mathbf{K}_b = \begin{bmatrix} E_bA_b/l & 0 & 0 & -E_bA_b/l & 0 & 0 \\ 0 & 12E_bI_b/l^3 & 6E_bI_b/l^2 & 0 & -12E_bI_b/l^3 & 6E_bI_b/l^2 \\ 0 & 6E_bI_b/l^2 & 4E_bI_b/l & 0 & -6E_bI_b/l^2 & 2E_bI_b/l \\ -E_bA_b/l & 0 & 0 & E_bA_b/l & 0 & 0 \\ 0 & -12E_bI_b/l^3 & -6E_bI_b/l^2 & 0 & 12E_bI_b/l^3 & -6E_bI_b/l^2 \\ 0 & 6E_bI_b/l^2 & 2E_bI_b/l & 0 & -6E_bI_b/l^2 & 4E_bI_b/l \end{bmatrix} \tag{2.147}$$

and

$$\mathbf{Q}_{ext} = \mathbf{K}_b\mathbf{Z_d} - \mathbf{R_d} \tag{2.148}$$

represented the nodal force due to the uniform external load q_y.

The observation can be made that the stiffness matrix $\mathbf{K}_b$ is associated with the displacement field $\mathbf{q}_b = \begin{bmatrix} u_b^i & v_b^i & \theta_b^i & u_b^j & v_b^j & \theta_b^j \end{bmatrix}$. It is worth noting that a similar calculation procedure can be applied to layer a.

The combination of beam elements for both layers a and b with connector elements at their extremities results in a connected composite beam element. The matrix of rigidity of the latter is as follows:

$$\mathbf{K} = \begin{bmatrix} \mathbf{K}_{ue}^{(13)} + \mathbf{K}_{ce}^{i} & \mathbf{K}_{ue}^{(46)} \\ \mathbf{K}_{ue}^{(46),\mathrm{T}} & \mathbf{K}_{ue}^{(31)} + \mathbf{K}_{ce}^{j} \end{bmatrix} \tag{2.149}$$

where

- $\mathbf{K}_{ue}^{(13)}$ is the stiffness corresponding to displacement vector $\begin{bmatrix} u_b^i & v_b^i & \theta_b^i & u_a^i & v_a^i & \theta_a^i \end{bmatrix}$,
- $\mathbf{K}_{ue}^{(31)}$ is the stiffness corresponding to displacement vector $\begin{bmatrix} u_b^j & v_b^j & \theta_b^j & u_a^j & v_a^j & \theta_a^j \end{bmatrix}$,
- $\mathbf{K}_{ce}^{i}$ is the stiffness matrix of connector at node i,
- $\mathbf{K}_{ce}^{j}$ is the stiffness matrix of connector at node j.

In order to derive the matrices $\mathbf{K}_{ue}^{(13)}$, $\mathbf{K}_{ue}^{(31)}$, and $\mathbf{K}_{ue}^{(46)}$, the properties of the element matrix

with respect to the individual layer, as well as the displacement vector, are derived accordingly.

$$\mathbf{K}_{ue}^{(13)} = \begin{bmatrix} E_b A_b/l & 0 & 0 & 0 & 0 & 0 \\ 0 & 12E_b I_b/l^3 & 6E_b I_b/l^2 & 0 & 0 & 0 \\ 0 & 6E_b I_b/l^2 & 4E_b I_b/l & 0 & 0 & 0 \\ 0 & 0 & 0 & E_a A_a/l & 0 & 0 \\ 0 & 0 & 0 & 0 & 12E_a I_a/l^3 & 6E_a I_a/l^2 \\ 0 & 0 & 0 & 0 & 6E_a I_a/l^2 & 4E_a I_a/l \end{bmatrix}$$

$$\mathbf{K}_{ue}^{(46)} = \begin{bmatrix} -E_b A_b/l & 0 & 0 & 0 & 0 & 0 \\ 0 & -12E_b I_b/l^3 & 6E_b I_b/l^2 & 0 & 0 & 0 \\ 0 & -6E_b I_b/l^2 & 2E_b I_b/l & 0 & 0 & 0 \\ 0 & 0 & 0 & -E_a A_a/l & 0 & 0 \\ 0 & 0 & 0 & 0 & -12E_a I_a/l^3 & 6E_a I_a/l^2 \\ 0 & 0 & 0 & 0 & -6E_a I_a/l^2 & 2E_a I_a/l \end{bmatrix}$$

$$\mathbf{K}_{ue}^{(31)} = \begin{bmatrix} E_b A_b/l & 0 & 0 & 0 & 0 & 0 \\ 0 & 12E_b I_b/l^3 & -6E_b I_b/l^2 & 0 & 0 & 0 \\ 0 & -6E_b I_b/l^2 & 4E_b I_b/l & 0 & 0 & 0 \\ 0 & 0 & 0 & E_a A_a/l & 0 & 0 \\ 0 & 0 & 0 & 0 & 12E_a I_a/l^3 & -6E_a I_a/l^2 \\ 0 & 0 & 0 & 0 & -6E_a I_a/l^2 & 4E_a I_a/l \end{bmatrix}$$

To obtain the rigidity matrix of a connector element $\mathbf{K}_{ce}$, Eq. (2.12) and Eq. (2.13) are introduced into equations such as Eqs. (2.26) to (2.31).

$$\mathbf{K}_{ce}^{i} = \begin{bmatrix} k_h^i & 0 & h_b k_h^i & -k_h^i & 0 & h_a k_h^i \\ 0 & k_v^i & 0 & 0 & -k_v^i & 0 \\ h_b k_h^i & 0 & h_b^2 k_h^i & -h_b k_h^i & 0 & h_b h_a k_h^i \\ -k_h^i & 0 & -h_b k_h^i & k_h^i & 0 & -h_a k_h^i \\ 0 & -k_v^i & 0 & 0 & k_v^i & 0 \\ h_a k_h^i & 0 & h_a h_b k_h^i & -h_a k_h^i & 0 & h_a^2 k_h^i \end{bmatrix}$$

$$\mathbf{K}_{ce}^{j} = \begin{bmatrix} k_h^j & 0 & h_b k_h^j & -k_h^j & 0 & h_a k_h^j \\ 0 & k_v^j & 0 & 0 & -k_v^j & 0 \\ h_b k_h^j & 0 & h_b^2 k_h^j & -h_b k_h^j & 0 & h_b h_a k_h^j \\ -k_h^j & 0 & -h_b k_h^j & k_h^j & 0 & -h_a k_h^j \\ 0 & -k_v^j & 0 & 0 & k_v^j & 0 \\ h_a k_h^j & 0 & h_a h_b k_h^j & -h_a k_h^j & 0 & h_a^2 k_h^j \end{bmatrix}$$

2.5 Treatment of non-interpenetration between the layers

The governing equations of the problems are obtained by minimization of the total potential energy defined as the difference of the initial strain energy $W_{int}(\mathbf{q}_g)$ and the work performed by the external loads $W_{ext}(\mathbf{q}_g)$ i.e.:

$$\Pi(\mathbf{q}_g) = W_{int}(\mathbf{q}_g) - W_{ext}(\mathbf{q}_g) \tag{2.150}$$

which is formed by the difference of the internal and external virtual work, $W_{int}(\mathbf{q}_g)$ and $W_{ext}(\mathbf{q}_g)$, respectively. $\mathbf{q}$ is a vector of displacements and the subscript g denotes the global coordinate system.

The principle of the stationary potential energy reads:

$$\delta\Pi(\mathbf{q}_g) = \delta W_{int}(\mathbf{q}_g) - \delta W_{ext}(\mathbf{q}_g) = 0 \tag{2.151}$$

The variational forms of the internal and external virtual works for discretized problem are given by:

$$\delta W_{int}(\mathbf{q}_g) = \delta \mathbf{q}_g^{\mathrm{T}} \mathbf{Q}_{int}(\mathbf{q}_g) \tag{2.152}$$

$$\delta W_{ext}(\mathbf{q}_g) = \delta \mathbf{q}_g^{\mathrm{T}} \mathbf{Q}_{ext} \tag{2.153}$$

in which $\mathbf{Q}_{int}(\mathbf{q}_g)$ and $\mathbf{Q}_{ext}$ are internal and external force, respectively.

The non-interpenetration condition between the layers imposes that:

$$\mathbf{G}(\mathbf{q}_g) \geq 0 \tag{2.154}$$

where $\mathbf{G}(\mathbf{q}_g)$ is actual gap in composite beam. The constrained problem is now written as:

$$\begin{cases} \text{Minimize } \Pi(\mathbf{q}_g) \\ \text{subjected to } \mathbf{G}(\mathbf{q}_g) \geq 0 \end{cases} \tag{2.155}$$

In the following, we will highlight the methods that can be used to solve Eq. (2.155).

2.5.1 Penalty method

Optimization problems that involve constraints, such as those presented in Eq. (2.155), can be solved using the penalty method by adding a penalty term to Eq. (2.151) in which the gaps, $\mathbf{g}$, violate the constraint condition as follows:

$$\Pi'(\mathbf{q}_g, \lambda) = \Pi(\mathbf{q}_g) + \frac{p}{2}\mathbf{g}^{\mathrm{T}}(\mathbf{q}_g)\mathbf{g}(\mathbf{q}_g) \tag{2.156}$$

where p is the penalty parameter and $p > 0$.

Taking the first variation of Eq. (2.156) with respect to displacement and making use of Eq. (2.152) and Eq. (2.153), we obtain:

$$\delta \mathbf{q}_g^{\mathrm{T}} \mathbf{Q}_{int}(\mathbf{q}_g) - \delta \mathbf{q}_g^{\mathrm{T}} \mathbf{Q}_{ext} + p\, \delta \mathbf{g}^{\mathrm{T}}(\mathbf{q}_g)\, \mathbf{g}(\mathbf{q}_g) = 0 \tag{2.157}$$

With

$$\mathbf{C}(\mathbf{q}_g) = \frac{\partial \mathbf{g}(\mathbf{q}_g)}{\partial \mathbf{q}_g}, \tag{2.158}$$

we can rewrite Eq. (2.157) as follow:

$$\delta \mathbf{q}_g^{\mathrm{T}} \left[\mathbf{Q}_{int}(\mathbf{q}_g) - \mathbf{Q}_{ext} + p\, \mathbf{C}^{\mathrm{T}}(\mathbf{q}_g)\, \mathbf{g}(\mathbf{q}_g) \right] = 0 \tag{2.159}$$

which is fulfilled for an arbitrary virtual displacement $\delta \mathbf{q}_g$. We have then:

$$\mathbf{Q}_{int}(\mathbf{q}_g) - \mathbf{Q}_{ext} + p\, \mathbf{C}^{\mathrm{T}}(\mathbf{q}_g)\, \mathbf{g}(\mathbf{q}_g) = 0 \tag{2.160}$$

To solve Eq. (2.160), Newton-Raphson method may be used. By replacing $\mathbf{Q}_{int}(\mathbf{q}_g) = \mathbf{K}\mathbf{q}_g$, Eq. (2.160) becomes,

$$\left[\mathbf{K} + p\, \mathbf{C}^{\mathrm{T}}(\mathbf{q}_g)\, \mathbf{g}(\mathbf{q}_g) \right] \mathbf{q} = \mathbf{Q}_{ext} \tag{2.161}$$

2.5.2 Lagrange multiplier method

Lagrange multiplier method is also the classical method used to solve the contact problem. In this method, the total potential energy function Eq. (2.151) is modified by affixing an additional Lagrange multiplier term:

$$\Pi'(\mathbf{q}_g, \boldsymbol{\lambda}) = \Pi(\mathbf{q}_g) + \boldsymbol{\lambda}^{\mathrm{T}} \mathbf{g}(\mathbf{q}_g) \tag{2.162}$$

in which $\boldsymbol{\lambda}$ is Lagrange multiplier and $\boldsymbol{\lambda} < 0$. Variation of Eq. (2.162) with respect to displacement and Lagrange multipliers gives the following system of nonlinear equations:

$$\mathbf{Q}_{int}(\mathbf{q}_g) - \mathbf{Q}_{ext} + \mathbf{C}^{\mathrm{T}}(\mathbf{q}_g)\boldsymbol{\lambda} = 0 \tag{2.163}$$

$$\mathbf{g}(\mathbf{q}_g) = 0 \tag{2.164}$$

in which Eq. (2.158) is used. It can be seen that the number of unknown has increased in Lagrange multiplier method since $\boldsymbol{\lambda}$ is an additional variable in the system of equations. Thus, the size of the system of equations needs to be re-ordered during the solution of the system according to the violation to the constrained condition. However, this method allows to fulfill exactly the contact condition.

2.5.3 Augmented Lagrangian method

The penalty method has solutions that are highly dependent on the penalty parameter p. The classical Lagrange method requires the resulting larger system of equations to be effectively reordered during the solution of the system. A combination of penalty and Lagrange multiplier method leads to a so-called augmented Lagrangian method. In this method, the penalty and Lagrange multiplier terms are added to the total potential energy Eq. (2.151). We obtain then:

$$\Pi'(\mathbf{q}_g, \boldsymbol{\lambda}) = \Pi(\mathbf{q}_g) + \boldsymbol{\lambda}^{\mathrm{T}}\mathbf{g}(\mathbf{q}_g) + \frac{p}{2}\mathbf{g}^{\mathrm{T}}(\mathbf{q}_g)\mathbf{g}(\mathbf{q}_g) \tag{2.165}$$

The advantage of using this method is that the penalty factor value does not need to be large in order to obtain the convergence of the iterative process. Besides, by coupling this method with Uzawa updating scheme, the Lagrange multipliers can be isolated from the system of equations. The number of unknown in the system of equations is then conserved.

Assuming that Lagrange multiplier $\boldsymbol{\lambda}$ is known as $\bar{\boldsymbol{\lambda}}$, the variation of Eq. (2.165) with respect to displacement yields the following system of nonlinear equations:

$$\mathbf{Q}_{int}(\mathbf{q}_g) - \mathbf{Q}_{ext} + \mathbf{C}^{\mathrm{T}}(\mathbf{q}_g)\bar{\boldsymbol{\lambda}} + p\,\mathbf{C}^{\mathrm{T}}(\mathbf{q}_g)\mathbf{g}(\mathbf{q}_g) = 0 \tag{2.166}$$

Newton-Raphson method may be used to solve nonlinear equation Eq. (2.166) for a fixed known Lagrange multiplier $\bar{\boldsymbol{\lambda}}$. The solution of Eq. (2.166) is then used to verified the contact condition. If it is violated, the Lagrange multiplier can be updated by:

$$\bar{\boldsymbol{\lambda}}_{k+1} = \bar{\boldsymbol{\lambda}}_k + p\,\mathbf{g}(\mathbf{q}_g) \tag{2.167}$$

For dealing with the contact problem, increasing the penalty factor p to infinity would lead the exact solution to the contact problem. However, in the computational application, it is not possible to use a very high penalty factor since it may lead to numerically ill-conditioning of the system. Nevertheless, it requires a good start of penalty parameter to facilitate the convergence. It has been shown in [48] that the optimal convergence is achieved with the penalty parameter equal to:

$$p_{opt} = \frac{2}{\lambda_m + \lambda_M} \tag{2.168}$$

in which λ_m and λ_M denote the smallest and the largest nonzero eigenvalue of matrix $\mathbf{C}\left(\dfrac{\partial \mathbf{Q}_{int}}{\partial \mathbf{q}_g}\right)^{-1}\mathbf{C}^{\mathrm{T}}$, respectively.

The penalty parameter p is then recommended between 0 and p_{opt}.

2.6 Numerical Applications

In this study, we will begin by performing a validation of the numerical model through comparison with an existing beam model. Following this, we will proceed to examine the discrete bond and continuous bond models, focusing on the effect of connection stiffness. Additionally, we will investigate the penetration problem with distinct value of vertical stiffness of connection with/without the contact algorithm.

2.6.1 Validation with a simply supported beam-column subjected to axial and transverse loading

To validate the proposed model, a simply supported beam-column subjected to axial and transverse loading is considered, see Fig. 2.6. A closed-form solution of this problem, in which the uplift effect is neglected, is provided by Girhammar and Gopu [49] and Kroflič, Saje, and Planinc [30]. In order to eliminate uplifts, we consider a large vertical connection stiffness equal to 1000 kN/cm^2 (continuous connection stiffness value which will be converted later for discrete connection) for the present model. The beam is modeled with 20 elements and the penalty method with penalty parameter equal to 1000 kN/cm is adopted in the present model.

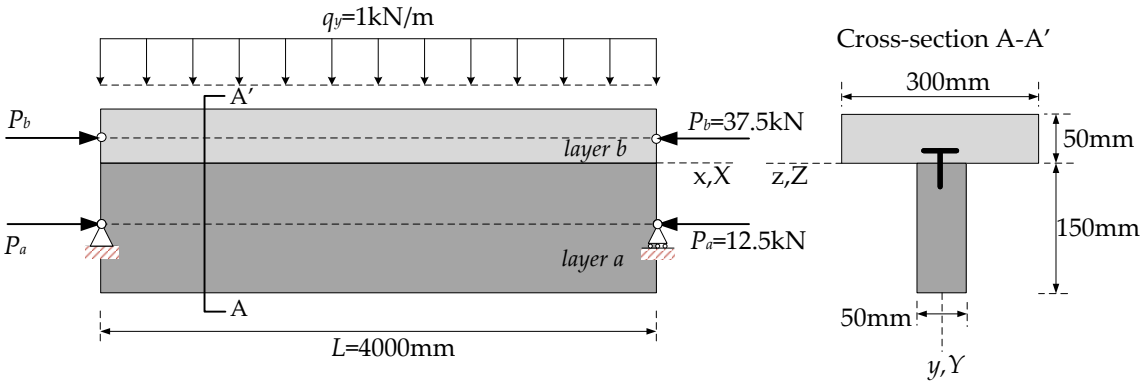

FIGURE 2.6: Two-layer composite beam under axial and transverse loads.

The elastic modulus of layer a and b are 800 kN/cm^2 and 1200 kN/cm^2, respectively. The stiffness of continuous shear connection in horizontal direction is equal to 5 kN/cm^2. Since the discrete bond is also used in the present model, the stiffness of connectors k_h and k_v are calculated by multiplying the continuous shear connection stiffness by the spacing of the connector elements.

The results obtained with the present models are compared for the absolute value of maximum vertical displacement $||v_{max}||$ and maximum slip value s_{max} with the ones found in the literature and summarized in Table 2.1. It can be seen that a very good agreement is obtained.

TABLE 2.1: Numerical results.

Result	$\|\|v_{max}\|\|$(mm)	s_{max}(mm)
Girhammar and Gopu [49]	7.560	0.2262
Kroflič, Saje, and Planinc [30]	7.560	0.2259
Present discrete model	7.586	0.2283
Present continuous model	7.559	0.2288
Comparison	**Ratio of $\|\|v_{max}\|\|$**	**Ratio of s_{max}**
Present discrete model/[49]	1.0034	1.0092
Present continuous model/[49]	0.9998	1.0114

2.6.2 Comparison between discrete and continuous bond model

This numerical model has demonstrated a high level of agreement in comparison to the results of [30] and [49] during the validation process. As a result, this model is now suitable for the use in comparing the discrete bond and continuous bond models.

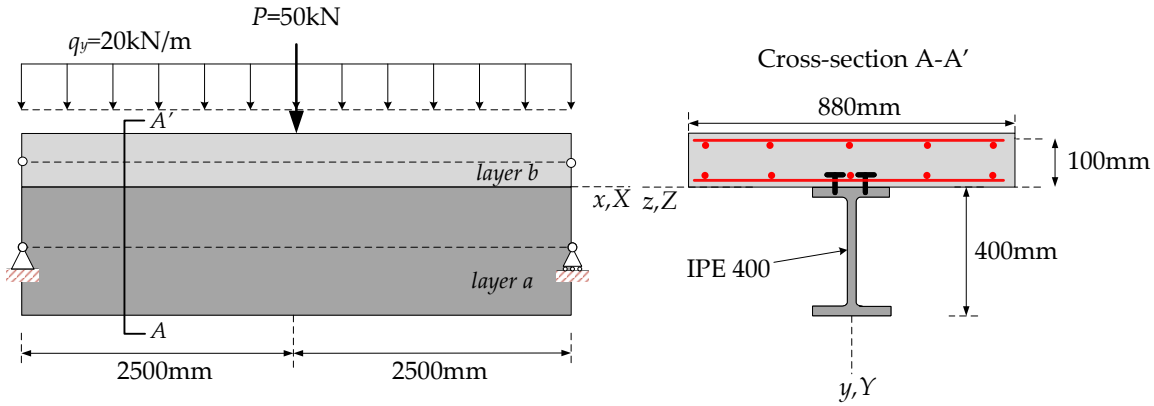

FIGURE 2.7: Two-layer composite beam under concentrated and distributed loads.

Introducing an iso-static steel-concrete composite beam supported by two simple supports, with a length of 5 meters. The beam is subjected to a distributed load of 20 kN/m and a pointed load of 50 kN applied at mid-span. The beam consists of a reinforced concrete slab with a section of 880$\times$ 100 mm^2, as well as an IPE 400 steel profile connected by 11 pairs of Nelson studs, with a height of 75 mm and a diameter of 16 mm, evenly spaced along the beam. Each pair of studs is placed in the same cross section of the beam (see Fig. 2.7). The modulus of elasticity of the steel is 210 GPa, while that of the concrete is 34 GPa. The analysis is performed with 2 elements for continuous bond model and with 10 elements for the discrete bond model. The stiffness of each stud is assumed to be 20 MN/m (assuming to equal for both direction). The horizontal stiffness of the connection device, used in the simulation with the discrete connection model, is therefore equal to 2 $\times$ 11 $\times$ 20

= 440 MN/m in total. The distribution of the connection in both directions for discrete and continuous bond, is calculated as follows:

-Continuous bond model

$$K_h = K_v = \frac{440\text{MN/m}}{5m} = 88\text{MN/m}^2 \tag{2.169}$$

-Discrete bond model

$$k_h = k_v = 20\text{MN/m} \tag{2.170}$$

for both elements at the extremities of the beam and

$$k_h = k_v = 20\text{MN/m}^2 \times 2 = 40\text{MN/m} \tag{2.171}$$

for interior elements.

Through the utilization of the two connection models, we have made observations and comparisons of the axial displacement, vertical displacement, slip, and uplift at the interface.

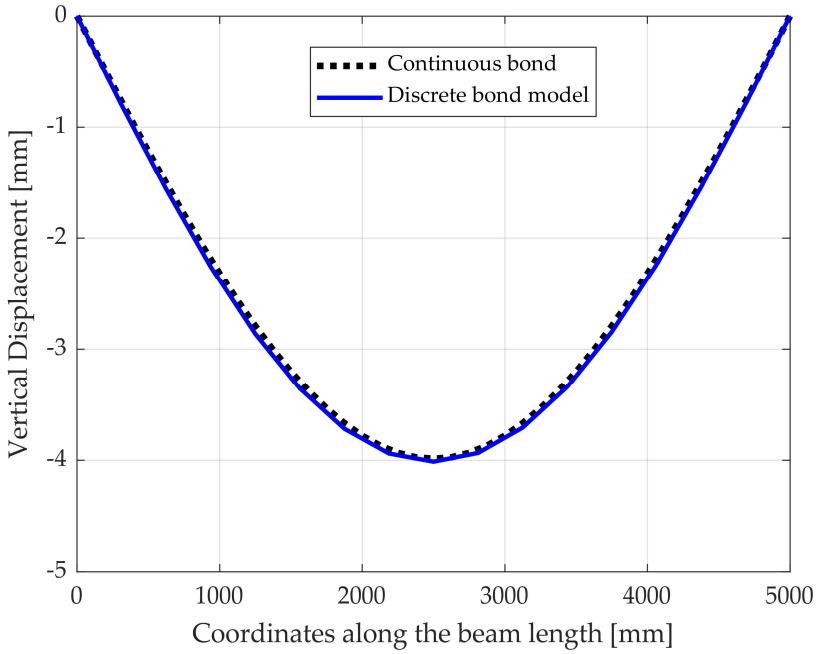

FIGURE 2.8: Vertical displacement of lower layer in discrete and continuous bond model.

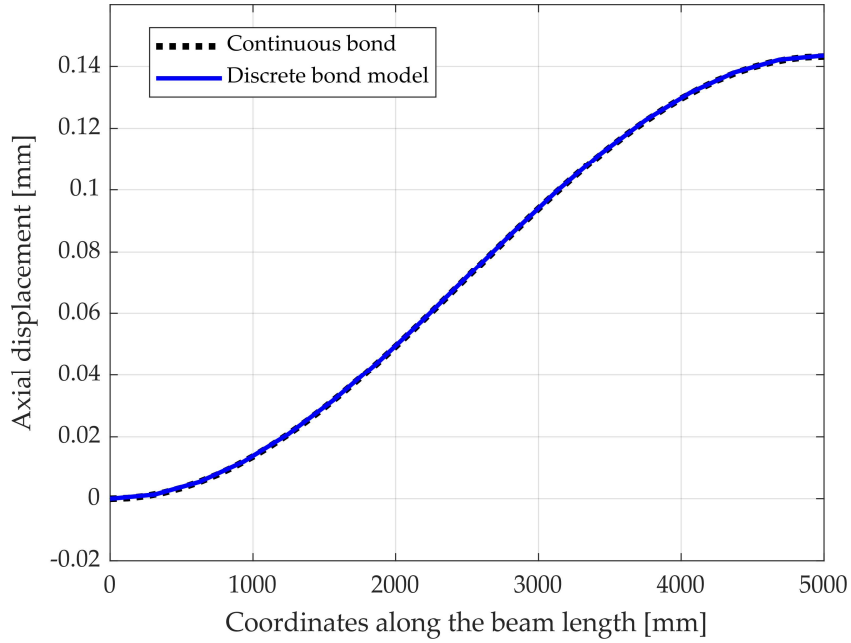

FIGURE 2.9: Axial displacement of lower layer in discrete and continuous bond model.

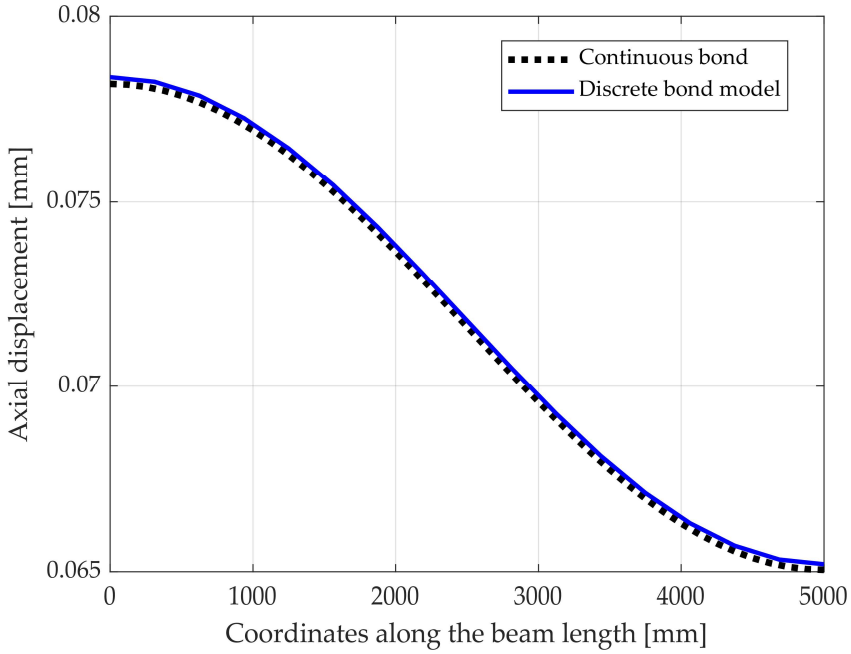

FIGURE 2.10: Axial displacement of upper layer in discrete and continuous bond model.

It is showed that the results illustrated in Figs. 2.8 to 2.12 obtained with the discrete bond and continuous bond models were identical with the tolerance less than 1%. The main observation from these results is that the continuous bond model requires only two elements,

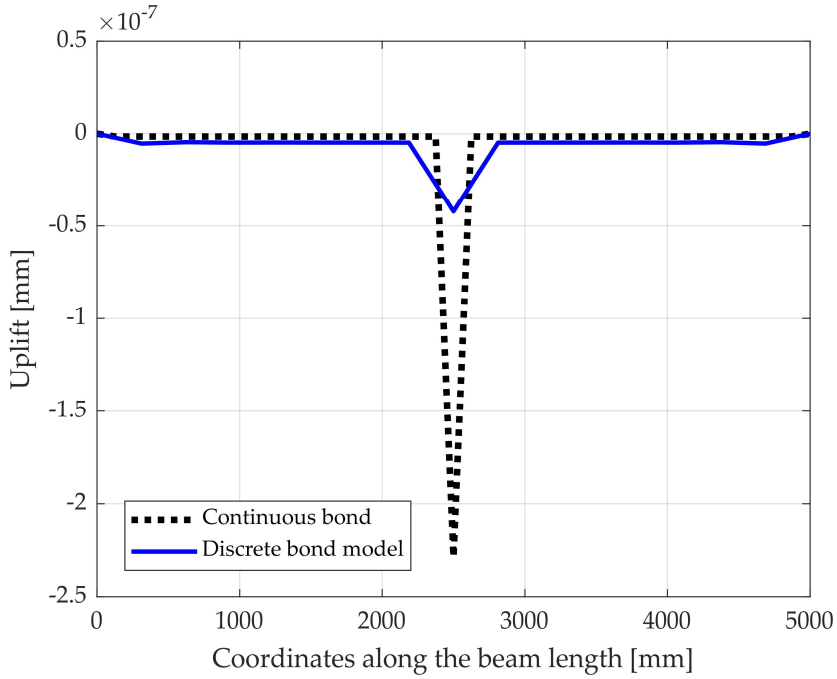

FIGURE 2.11: Uplift of beam in discrete and continuous bond model.

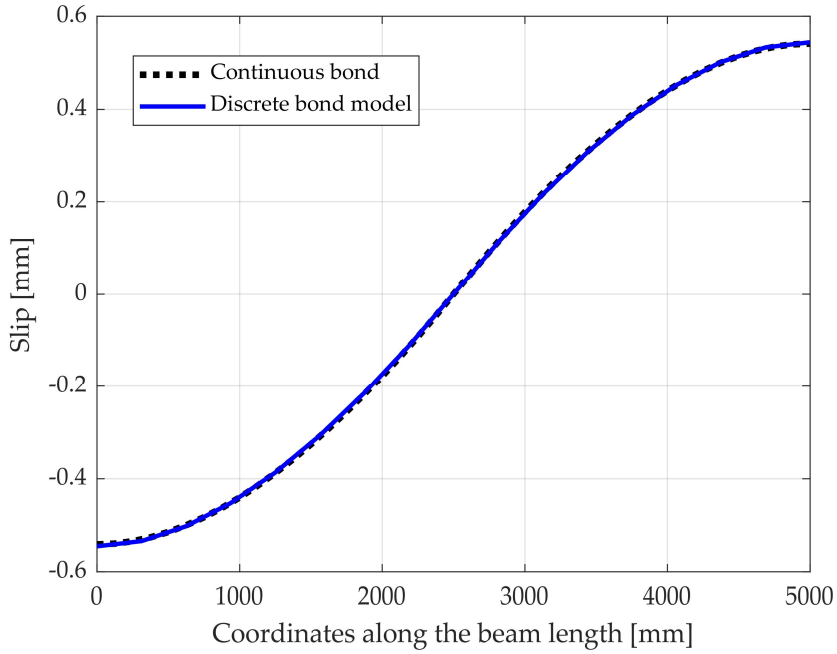

FIGURE 2.12: Slip of beam in discrete and continuous bond model.

which can save significantly computation time for this and other complex problems. As a result, we recommend using the continuous bond model to save time in calculations. Besides, with the exact solution presented in Section 2.3, the distribution of the displacement

field can be obtained, using the information of the nodal displacements.

The second point of observation concerns the uplift results shown in Fig. 2.11. Although there are some small differences in the graph between the two models, they are very small ($< 10^{-6}$ mm). It is notable that both the discrete bond and continuous bond models accurately captured the lack of penetration between layers. This indicates that both models were appropriately designed and validated for this problem.

2.6.3 Influence of vertical stiffness of the connection

In this example, the focus is on investigating the influence of the vertical stiffness of connectors on slip and uplift at the interlayer, as well as the treatment of penetration using the penalty method. A simply supported two-layered beam of length L=2800 mm is studied. As our mathematical model considers linear elastic material, its results could be realistic for the low load at mid-span (P=7624 N). The modulus of elasticity of both layers are considered to be equal ($E_a = E_b$=15000 N/m^2). The geometries of both layers are described in Fig. 2.13. In the first step of our problem, we examine the influence of transverse stiffness by keeping the horizontal stiffness of connection K_h at 27.2 MPa and varying the transverse stiffness K_v (1, 10, and 100 MPa).

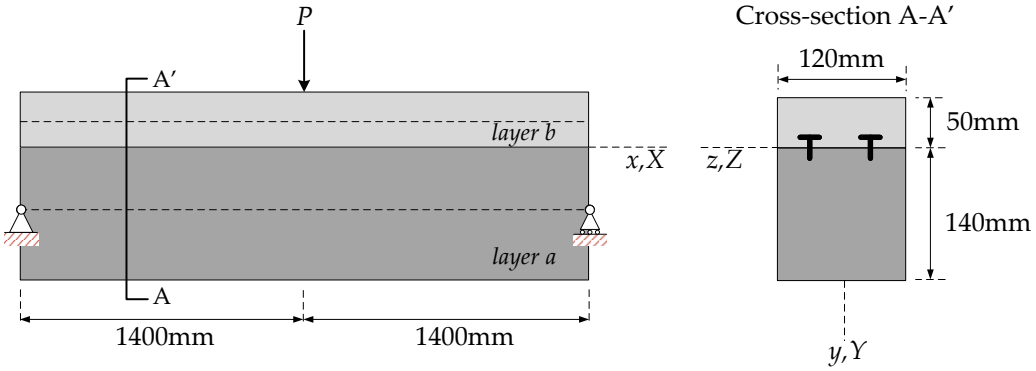

FIGURE 2.13: Two-layer composite beam under transverse loads at mid-span.

This study investigates the variation of slip and uplift along the contact surface for various transverse connection stiffness, as illustrated in Figs. 2.14 and 2.15. The analysis is performed using continuous bond model with 2 elements. The results indicate that negligible changes of slip occur at both extremities within the permissible range of tolerance (<5%), even in the case of a ten-fold difference in transverse connection stiffness, see in Fig. 2.14. Moreover, the mid-span of the simply supported beam exhibits no slip in this loading condition. In contrast to slip, the uplift demonstrates a noteworthy change in response to variations in transverse connection stiffness, as indicated in Figure 2.15.

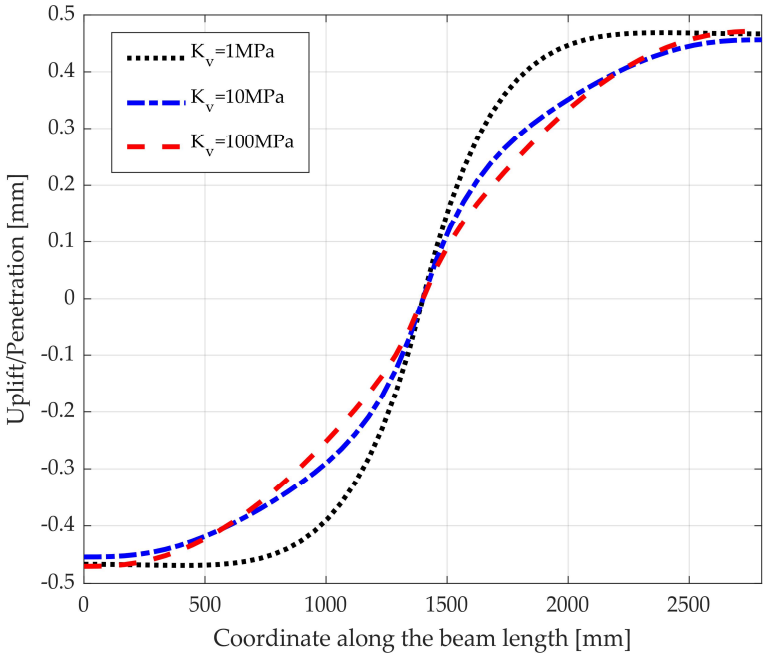

FIGURE 2.14: Slip with varied transverse spring stiffness.

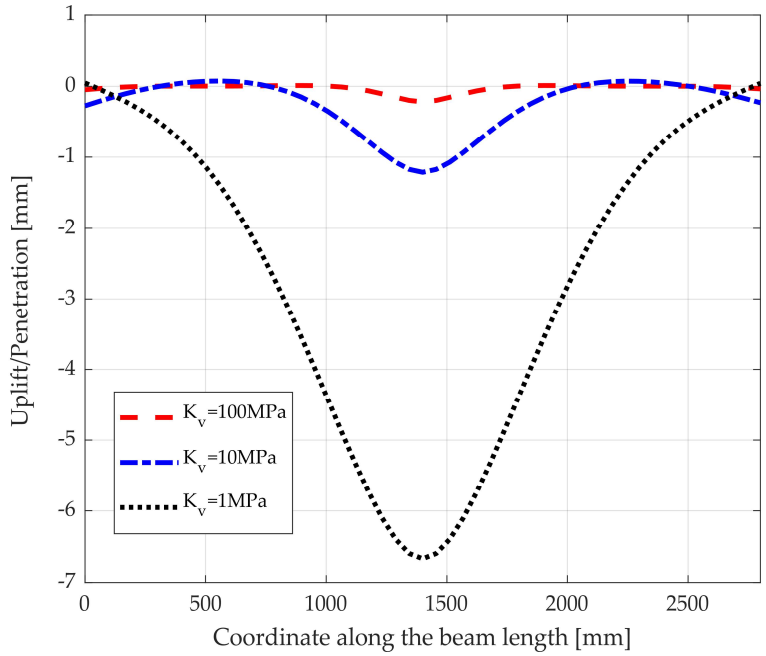

FIGURE 2.15: Uplift/Penetration with varied transverse spring stiffness.

As expected, increasing the traverse stiffness K_v result in decreasing penetration depths, see Figure 2.15. However, although the penetration depth associated with a K_v value of 100 MPa was less than 1 mm, practical applications of construction materials do not permit

such levels of penetration. To address this issue of non-penetrability, a penalty method or augmented Lagrange method described earlier might be used.

2.6.4 Non-penetration treatment

As discussed in Section 2.6.3, penetrations are not permitted in practical construction materials such as concrete, steel, timber, etc. Non-penetration is enforced by penalty method with using a penalty parameter of 10^8 MPa.

Results obtained from this method showed effective improvement in non-penetration.

TABLE 2.2: Maximum penetration results.

Traverse stiffness K_v (MPa)	1	10	100
Penetration at mid-span (mm)	-6.98×10^{-5}	-7.09×10^{-5}	-7.17×10^{-5}
Penetration at extremities (mm)	-3.91×10^{-6}	-4.09×10^{-6}	-4.09×10^{-6}

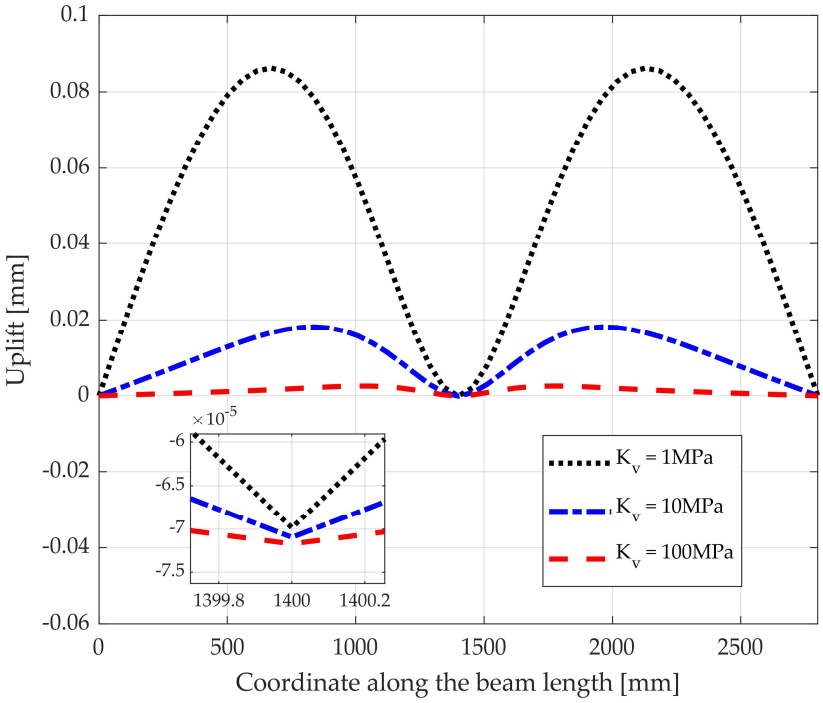

FIGURE 2.16: Uplift/Penetration distribution with contact algorithm

In Fig. 2.15, we observed notable penetration at the mid-span of the beam. This can be adjusted using the contact algorithm, as demonstrated in Fig. 2.16, where very small and negligible penetration was observed along the interface of the beam. It is reasonable to expect some uplift when treating non-penetrated conditions, as shown in Fig. 2.16. Moreover, the slip at the interface does change its form but its maximum value at the extremities does not change significantly with or without the contact algorithm, as illustrated in Fig. 2.17.

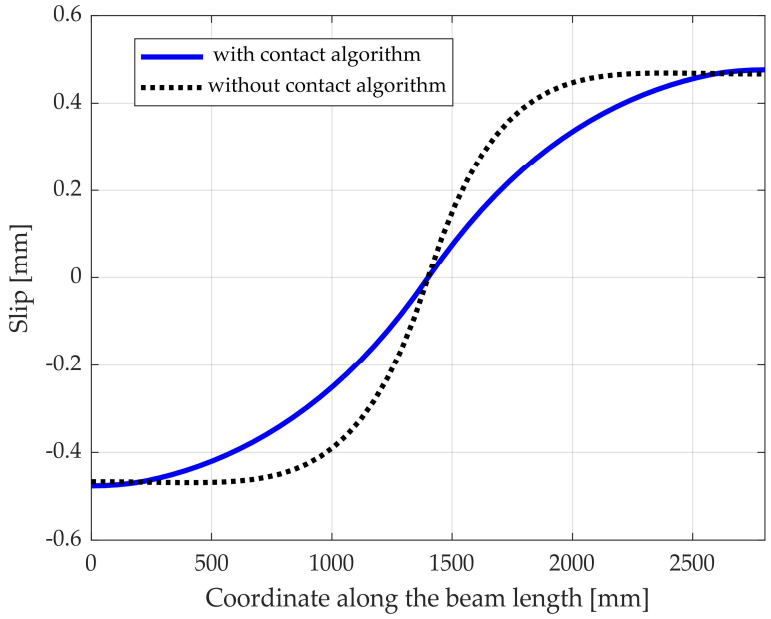

FIGURE 2.17: Slip distribution with/without contact algorithm

2.7 Conclusion

This chapter introduces the governing equations of composite steel-concrete beams, taking into account slip and uplift phenomena. These developed formulations have been formulated using both discrete bond and continuous bond models. The primary aim of this chapter is to investigate the linear elastic behavior of composite beams taking into account slip and uplift at the interface. The "exact" stiffness matrix has been derived through a closed-form solution of the governing equations. It is showed that using the same connection vertical stiffness for tension and compression results in penetration between the layers of composite beam.

The present model has been validated and has demonstrated good agreement with several research studies [49, 30]. Both discrete and continuous bond models provide accurate results. However the discrete bond model requires a larger number of elements to produce results similar to the ones obtained with the continuous bond model, which makes it a slower process during numerical calculations. Under certain load conditions, the penetration increases as the transverse stiffness of the connector weakens. To ensure that a non-penetration condition is respected, a contact algorithm such as the penalty and augmented Lagrangian method was used in this study, resulting in minimal and negligible penetration at inter-layer.

Chapter 3

Geometrically nonlinear elastic behavior of composite beams

3.1 Introduction

Geometrically linear elastic analysis of composite beams in Chapter 2 assumed that the displacement of the beam is small which is appropriate for predicting the behavior of the beam under infinitesimal rotation. In some applications, the deformation gradient of the beam can be large. In such cases, nonlinear geometrically analysis is required.

The purpose of this chapter is to present a finite element formulation for geometrically nonlinear analysis of two-layer composite beams with inter-layer slips and uplifts. To take into account geometric non-linearity, a co-rotational method is adopted. In this approach, the motion of the element is decomposed into two parts: a rigid body motion that defines a local coordinate system and a small deformational motion of the element relative to this local coordinate system. A co-rotational element formulation has several relative advantages: (1) the co-rotational formulation is accurate and has good convergence properties for problems with large displacements and large rotations but small strains; and (2) the treatment of geometric non-linearity is effectively undertaken at the level of discrete nodal variables with the transformation matrix between the local and global nodal entities, being independent of the assumptions made for the local element. Thus, many existing high-performance elements can be reused at the core of a co-rotational element formulation, and the resulting formulation can be employed to solve large displacement and large rotation problems.

The organization of this chapter is as follows. In Section 3.2, we discuss the co-rotational framework, including beam kinematics and element formulations. In Section 3.3, we provide numerical examples to evaluate the proposed formulation and support the conclusions drawn in Section 3.4.

3.2 Co-rotational framework

The co-rotational method for 2D beams is known for many years. This approach is a priory based on the kinematic assumptions that the displacements and the rotations many be arbitrarily large, but the deformation is small. However, when dealing with planar two-layer beams, it is necessary to select pertinent kinematic local and global variables. The local stiffness matrix must then be reformulated. In the following, we present the main ingredients of a co-rotational formulation for two-layer beam element:

- the choice of co-rotating frame,
- the derivation of the relationships between the local variables and the global ones,
- a variationally consistent internal force vector along with the tangent stiffness matrix.

3.2.1 Beam Kinematics

The co-rotational description of the motion of a deformable body assumes that the motion of a body can be decomposed into a rigid body motion and pure deformations. Primarily, a local rigid reference frame is defined and attached to the element so that this local frame translates and rotates with the element but does not deform with it. With respect to this moving frame, local deformational displacements are defined and the geometrical nonlinearity introduced by element large rigid-body motion is incorporated into the transformation matrix relating local and global displacements.

In our present model, the rigid reference frame (co-rotational frame) is defined by constructing a local reference system attached to the composite beam element. Its origin is taken at the node a^i which corresponds to the centroid of the lower layer cross-section, see Fig. 3.1. The x_l-axis is represented by the line connecting the end nodes of lower layer a^i and a^j while the y_l-axis is orthogonal to the x_l-axis. The decomposition of the element movement from the initially undeformed state to the actual deformed one are: the rigid motion of the local frame corresponding to the translation of the node a^i and the rigid rotation α of the x_l-axis (see Fig. 3.2), and the local deformations with respect to the local frame. The local deformations are assumed to be small and the ones defined in Chapter 2 can be used.

According to the notations defined in the co-rotating frame (Fig. 3.2), the local displacement vector $\mathbf{q}_l$ can be defined as:

$$\mathbf{q}_l = [\overline{u}_b^i, \overline{v}_b^i, \overline{\theta}_b^i, \overline{u}_a^i, \overline{v}_a^i, \overline{\theta}_a^i, \overline{u}_b^j, \overline{v}_b^j, \overline{\theta}_b^j, \overline{u}_a^j, \overline{v}_a^j, \overline{\theta}_a^j]^{\mathrm{T}}$$

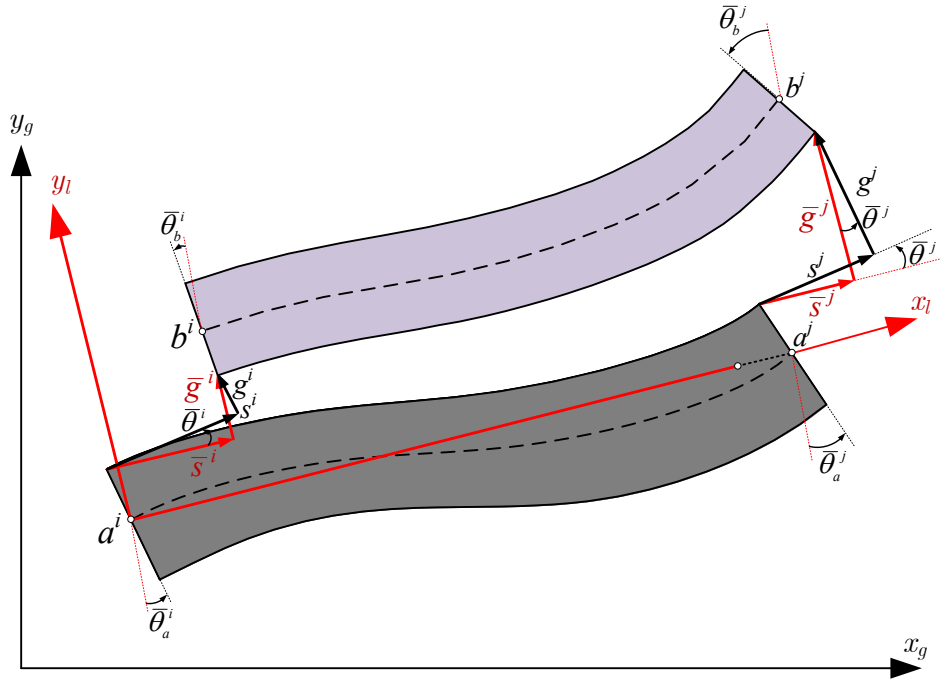

FIGURE 3.1: Co-rotational kinematics (slip and uplift)

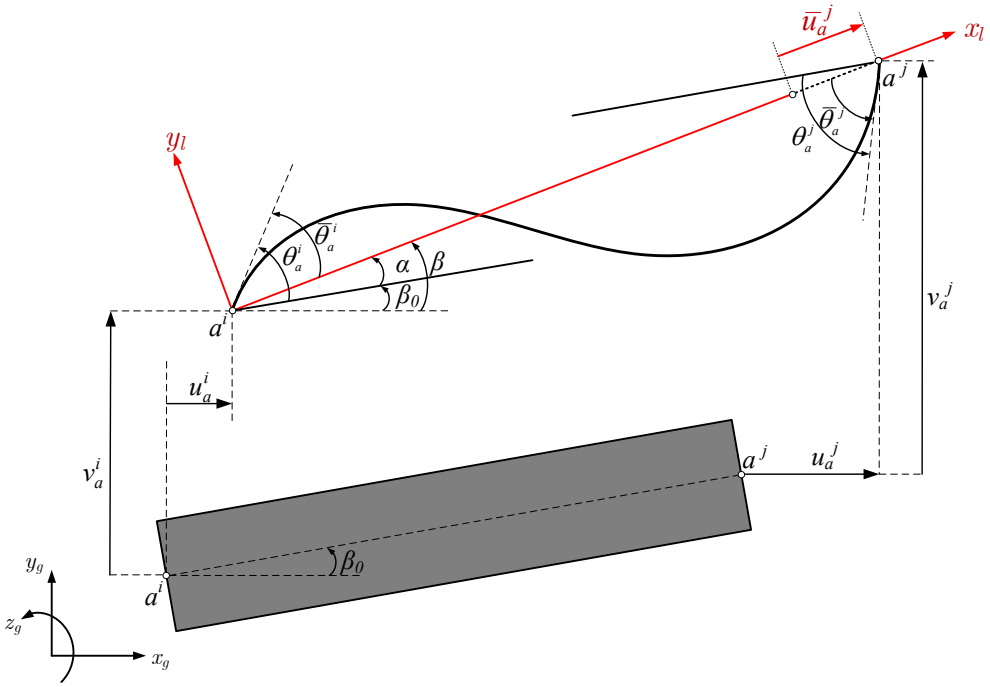

FIGURE 3.2: Initial and deformed configuration (displacements and rotations)

The bar in the displacement components indicates that it is in the local coordinate system, and its components can be computed as below:

$$\overline{u}_a^i = 0 \tag{3.1}$$
$$\overline{v}_a^i = 0 \tag{3.2}$$
$$\overline{v}_a^j = 0 \tag{3.3}$$
$$\overline{\theta}_a^i = \theta_a^i - \alpha \tag{3.4}$$
$$\overline{u}_a^j = l_n - l_0 \tag{3.5}$$
$$\overline{\theta}_a^j = \theta_a^j - \alpha \tag{3.6}$$
$$\overline{u}_b^i = \overline{s}^i - h_a\overline{\theta}_a^i - h_b\overline{\theta}_b^i \tag{3.7}$$
$$\overline{v}_b^i = \overline{g}^i + \overline{v}_a^i \tag{3.8}$$
$$\overline{\theta}_b^i = \theta_b^i - \alpha \tag{3.9}$$
$$\overline{u}_b^j = \overline{s}^j + \overline{u}_a^j - h_a\overline{\theta}_a^j - h_b\overline{\theta}_b^j \tag{3.10}$$
$$\overline{v}_b^j = \overline{g}^j + \overline{v}_a^j \tag{3.11}$$
$$\overline{\theta}_b^j = \theta_b^j - \alpha \tag{3.12}$$

where α is the rigid rotation of the x_l axis and is obtained by using the geometrical relation in Fig. 3.2:

$$\sin\alpha = \mathfrak{c}_o\,\mathfrak{s} - \mathfrak{s}_o\,\mathfrak{c} \tag{3.13}$$
$$\cos\alpha = \mathfrak{c}_o\,\mathfrak{c} + \mathfrak{s}_o\,\mathfrak{s} \tag{3.14}$$

with,

$$\mathfrak{c}_0 = \cos\beta_0 = \frac{1}{l_0}\left(x_a^j - x_a^i\right) \tag{3.15}$$
$$\mathfrak{s}_0 = \sin\beta_0 = \frac{1}{l_0}\left(y_a^j - y_a^i\right) \tag{3.16}$$
$$\mathfrak{c} = \cos\beta = \frac{1}{l_n}\left(x_a^j + u_a^j - x_a^i - u_a^i\right) \tag{3.17}$$
$$\mathfrak{s} = \sin\beta = \frac{1}{l_n}\left(y_a^j + v_a^j - y_a^i - v_a^i\right) \tag{3.18}$$

l_0 and l_n are the element's length in initial and deformed configuration, respectively.

$$l_0 = \sqrt{\left(x_a^j - x_a^i\right)^2 + \left(y_a^j - y_a^i\right)^2} \tag{3.19}$$
$$l_n = \sqrt{\left(x_a^j + u_a^j - x_a^i - u_a^i\right)^2 + \left(y_a^j + v_a^j - y_a^i - v_a^i\right)^2} \tag{3.20}$$

3.2.2 The relationships between slip and uplift in local and global coordinate system

In the local coordinate system, the inter-layer slip is measured at the extremities of the element in the direction of x_l-axis, see Figure 3.3a. In the global coordinate system, it is assumed to be measured in the direction of an axis forming an average angle $\bar{\theta}$ to local x_l-axis, with $\bar{\theta} = \frac{1}{2}(\bar{\theta}_a + \bar{\theta}_b)$. It is worth to point out that uplift will result in a rotation $\bar{\theta}_a$ different to that $\bar{\theta}_b$. Without uplift, the two components of a two-layer beam who deform according to Bernoulli kinematics will rotate equally ($\bar{\theta}_a = \bar{\theta}_b$). Besides, it is assumed that the uplifts in both local and global coordinate system are measured in the orthogonal direction to the slips, see Figure 3.3b. From the assumptions above, the relationships between slip and uplift in local and global coordinate system are given by:

$$\bar{s}^k = s^k \cos(\bar{\theta}^k) - g^k \sin(\bar{\theta}^k) \tag{3.21}$$

$$\bar{g}^k = s^k \sin(\bar{\theta}^k) + g^k \cos(\bar{\theta}^k) \tag{3.22}$$

where $\bar{\theta}^k = \dfrac{\bar{\theta}_a^k + \bar{\theta}_b^k}{2}, \qquad k = i, j.$

3.2.3 Element Formulations

Once the relationship between local and global variables is established, the rigid body motions can be removed from the element displacement field. It can be achieved by calculating the local displacements using Eqs. (3.1-3.22).

Let us consider two different coordinate systems with subscript l and g. Assume that the internal force vector $\mathbf{Q}_l$ and tangent stiffness matrix $\mathbf{K}_l$ are consistent with the displacement vector $\mathbf{q}_l$ such that:

$$\delta\mathbf{Q}_l = \mathbf{K}_l \, \delta\mathbf{q}_l \tag{3.23}$$

Consider now that $\mathbf{q}_l$ is related to the displacement vector $\mathbf{q}_g$ through:

$$\delta\mathbf{q}_l = \mathbf{B}_{lg} \, \delta\mathbf{q}_g \tag{3.24}$$

Then, by equating the virtual work in both systems, the internal force vector $\mathbf{Q}_g$ consistent with $\mathbf{q}_g$ is defined by:

$$\mathbf{Q}_g = \mathbf{B}_{lg}^{\mathrm{T}} \mathbf{Q}_l \tag{3.25}$$

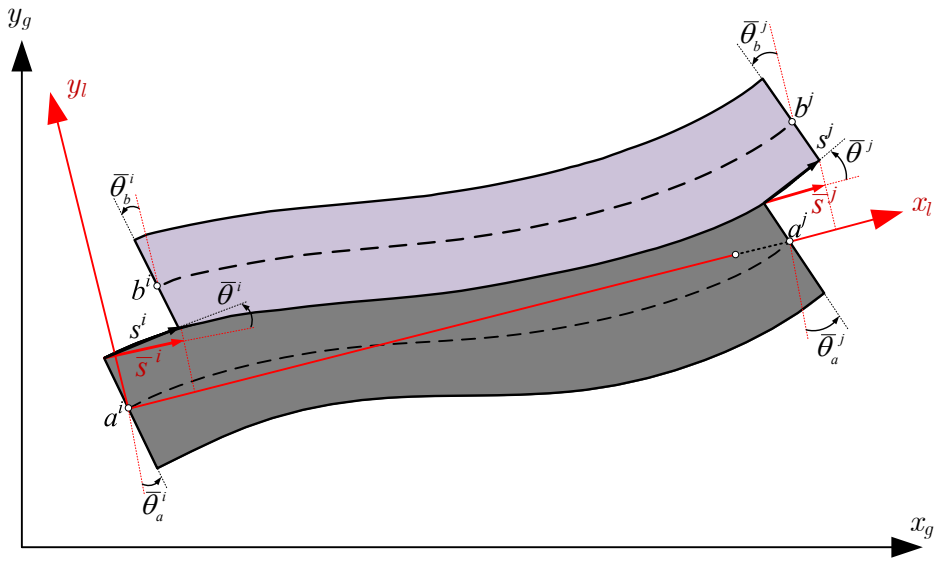

(A) slip

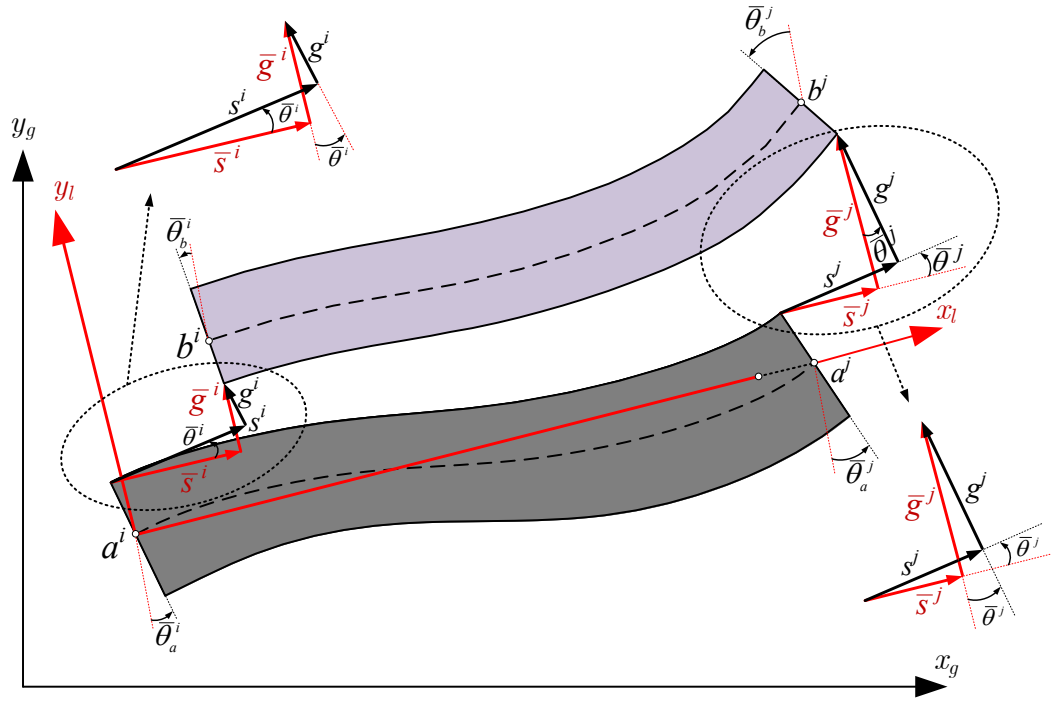

(B) Slip and uplift

FIGURE 3.3: Slip and uplift in local and global coordinate system

The expression of the tangent stiffness matrix $\mathbf{K}_g$, consistent with $\mathbf{q}_g$ is obtained by differentiating Eq. (3.25) and combining the outcome with Eq. (3.23) and Eq. (3.24):

$$\mathbf{K}_g = \mathbf{B}_{lg}^{\mathrm{T}}\,\mathbf{K}_l\,\mathbf{B}_{lg} + \mathbf{H}_{lg}, \qquad \mathbf{H}_{lg} = \left.\frac{\partial(\mathbf{B}_{lg}^{\mathrm{T}}\,\mathbf{Q}_l)}{\partial \mathbf{q}_g}\right|_{\mathbf{Q}_l} \tag{3.26}$$

From the idea described above, the element formulation can be obtained using four consecutive changes of variables:

$$\mathbf{Q}_l, \mathbf{K}_l \rightarrow \mathbf{Q}_e, \mathbf{K}_e \rightarrow \mathbf{Q}_a, \mathbf{K}_a \rightarrow \mathbf{Q}_n, \mathbf{K}_n \rightarrow \mathbf{Q}_g, \mathbf{K}_g$$

and five different displacement vectors as follows:

$$\begin{aligned}
\mathbf{q}_l &= [\overline{u}_b^i, \overline{v}_b^i, \overline{\theta}_b^i, \overline{u}_a^i, \overline{v}_a^i, \overline{\theta}_a^i, \overline{u}_b^j, \overline{v}_b^j, \overline{\theta}_b^j, \overline{u}_a^j, \overline{v}_a^j, \overline{\theta}_a^j]^{\mathrm{T}} \\
\mathbf{q}_e &= [\overline{u}_a^j, \overline{\theta}_b^i, \overline{\theta}_a^i, \overline{\theta}_b^j, \overline{\theta}_a^j, \overline{s}^i, \overline{s}^j, \overline{g}^i, \overline{g}^j]^{\mathrm{T}} \\
\mathbf{q}_a &= [\overline{u}_a^j, \overline{\theta}_b^i, \overline{\theta}_a^i, \overline{\theta}_b^j, \overline{\theta}_a^j, s^i, s^j, g^i, g^j]^{\mathrm{T}} \\
\mathbf{q}_n &= [u_a^i, v_a^i, \theta_b^i, \theta_a^i, u_a^j, v_a^j, \theta_b^j, \theta_a^j, s^i, s^j, g^i, g^j]^{\mathrm{T}} \\
\mathbf{q}_g &= [u_b^i, v_b^i, \theta_b^i, u_a^i, v_a^i, \theta_a^i, u_b^j, v_b^j, \theta_b^j, u_a^j, v_a^j, \theta_a^j]^{\mathrm{T}}
\end{aligned}$$

The matrix of transformation which transfers from the state of one displacement vector to another is given in the following, whereas the variation of global slip and uplift with respect to the displacement vector are shown in Appendix A.

3.2.4 The first change of variables from $\mathbf{q}_l$ to $\mathbf{q}_e$

By using Eqs. (3.1) to (3.3), (3.7), (3.8), (3.10) and (3.11), the transformation matrix $\mathbf{B}_{le}$ relating:

$$\mathbf{q}_l = [\overline{u}_b^i, \overline{v}_b^i, \overline{\theta}_b^i, \overline{u}_a^i, \overline{v}_a^i, \overline{\theta}_a^i, \overline{u}_b^j, \overline{v}_b^j, \overline{\theta}_b^j, \overline{u}_a^j, \overline{v}_a^j, \overline{\theta}_a^j]^{\mathrm{T}}$$

with

$$\mathbf{q}_e = [\overline{u}_a^j, \overline{\theta}_b^i, \overline{\theta}_a^i, \overline{\theta}_b^j, \overline{\theta}_a^j, \overline{s}^i, \overline{s}^j, \overline{g}^i, \overline{g}^j]^{\mathrm{T}}$$

is obtained as follow:

$$\mathbf{B}_{le} = \begin{bmatrix}
0 & -h_b & -h_a & 0 & 0 & 1 & 0 & 0 & 0 \\
0 & 0 & 0 & 0 & 0 & 0 & 0 & 1 & 0 \\
0 & 1 & 0 & 0 & 0 & 0 & 0 & 0 & 0 \\
0 & 0 & 0 & 0 & 0 & 0 & 0 & 0 & 0 \\
0 & 0 & 0 & 0 & 0 & 0 & 0 & 0 & 0 \\
0 & 0 & 1 & 0 & 0 & 0 & 0 & 0 & 0 \\
1 & 0 & 0 & -h_b & -h_b & 0 & 1 & 0 & 0 \\
0 & 0 & 0 & 0 & 0 & 0 & 0 & 0 & 1 \\
0 & 0 & 0 & 1 & 0 & 0 & 0 & 0 & 0 \\
1 & 0 & 0 & 0 & 0 & 0 & 0 & 0 & 0 \\
0 & 0 & 0 & 0 & 0 & 0 & 0 & 0 & 0 \\
0 & 0 & 0 & 0 & 1 & 0 & 0 & 0 & 0
\end{bmatrix}$$

In this case, the nonlinear geometric term of the stiffness matrix is:

$$\mathbf{H}_{le} = 0$$

3.2.5 The second change of variables from $\mathbf{q}_e$ to $\mathbf{q}_a$

By using Eqs. (3.21) and (3.22), the second change of variables from:

$$\mathbf{q}_e = [\overline{u}_a^j, \overline{\theta}_b^i, \overline{\theta}_a^i, \overline{\theta}_b^j, \overline{\theta}_a^j, \overline{s}^i, \overline{s}^j, \overline{g}^i, \overline{g}^j]^{\mathrm{T}}$$

to

$$\mathbf{q}_a = [\overline{u}_a^j, \overline{\theta}_b^i, \overline{\theta}_a^i, \overline{\theta}_b^j, \overline{\theta}_a^j, s^i, s^j, g^i, g^j]^{\mathrm{T}}$$

can be performed, in which the transformation matrix $\mathbf{B}_{ea}$ is given by:

$$\mathbf{B}_{ea} = \begin{bmatrix} 1 & 0 & 0 & 0 & 0 & 0 & 0 & 0 & 0 \\ 0 & 1 & 0 & 0 & 0 & 0 & 0 & 0 & 0 \\ 0 & 0 & 1 & 0 & 0 & 0 & 0 & 0 & 0 \\ 0 & 0 & 0 & 1 & 0 & 0 & 0 & 0 & 0 \\ 0 & 0 & 0 & 0 & 1 & 0 & 0 & 0 & 0 \\ 0 & \mathfrak{A}^i & \mathfrak{A}^i & 0 & 0 & \cos\bar{\theta}^i & 0 & -\sin\bar{\theta}^i & 0 \\ 0 & 0 & 0 & \mathfrak{A}^j & \mathfrak{A}^j & 0 & \cos\bar{\theta}^j & 0 & -\sin\bar{\theta}^j \\ 0 & \mathfrak{B}^i & \mathfrak{B}^i & 0 & 0 & \sin\bar{\theta}^i & 0 & \cos\bar{\theta}^i & 0 \\ 0 & 0 & 0 & \mathfrak{B}^j & \mathfrak{B}^j & 0 & \sin\bar{\theta}^j & 0 & \cos\bar{\theta}^j \end{bmatrix}$$

where,

$$\begin{aligned} \mathfrak{A}^i &= -\frac{g^i}{2}\cos\bar{\theta}^i - \frac{s^i}{2}\sin\bar{\theta}^i \\ \mathfrak{A}^j &= -\frac{g^j}{2}\cos\bar{\theta}^j - \frac{s^j}{2}\sin\bar{\theta}^j \\ \mathfrak{B}^i &= \frac{s^i}{2}\cos\bar{\theta}^i - \frac{g^i}{2}\sin\bar{\theta}^i \\ \mathfrak{B}^j &= \frac{s^j}{2}\cos\bar{\theta}^j - \frac{g^j}{2}\sin\bar{\theta}^j \end{aligned}$$

Accordingly, the nonlinear geometric term of the stiffness matrix is:

$$\mathbf{H}_{ea} = \frac{\partial \mathbf{B}_{ea}\mathbf{Q}_e}{\partial \mathbf{q}_a} = \mathbf{H}_{ea}(1)Q_e(6) + \mathbf{H}_{ea}(2)Q_e(7) + \mathbf{H}_{ea}(3)Q_e(8) + \mathbf{H}_{ea}(4)Q_e(9)$$

where:

$$\mathbf{H}_{ea}(1) = \begin{bmatrix} 0 & 0 & 0 & 0 & 0 & 0 & 0 & 0 & 0 \\ 0 & -\frac{1}{2}\mathfrak{B}^i & -\frac{1}{2}\mathfrak{B}^i & 0 & 0 & -\frac{1}{2}\sin(\bar{\theta}^i) & 0 & -\frac{1}{2}\cos(\bar{\theta}^i) & 0 \\ 0 & -\frac{1}{2}\mathfrak{B}^i & -\frac{1}{2}\mathfrak{B}^i & 0 & 0 & -\frac{1}{2}\sin(\bar{\theta}^i) & 0 & -\frac{1}{2}\cos(\bar{\theta}^i) & 0 \\ 0 & 0 & 0 & 0 & 0 & 0 & 0 & 0 & 0 \\ 0 & 0 & 0 & 0 & 0 & 0 & 0 & 0 & 0 \\ 0 & -\frac{1}{2}\sin(\bar{\theta}^i) & -\frac{1}{2}\sin(\bar{\theta}^i) & 0 & 0 & 0 & 0 & 0 & 0 \\ 0 & 0 & 0 & 0 & 0 & 0 & 0 & 0 & 0 \\ 0 & -\frac{1}{2}\cos(\bar{\theta}^i) & -\frac{1}{2}\cos(\bar{\theta}^i) & 0 & 0 & 0 & 0 & 0 & 0 \\ 0 & 0 & 0 & 0 & 0 & 0 & 0 & 0 & 0 \end{bmatrix},$$

$$\mathbf{H}_{ea}(2) = \begin{bmatrix} 0 & 0 & 0 & 0 & 0 & 0 & 0 & 0 & 0 \\ 0 & 0 & 0 & 0 & 0 & 0 & 0 & 0 & 0 \\ 0 & 0 & 0 & 0 & 0 & 0 & 0 & 0 & 0 \\ 0 & 0 & 0 & -\frac{1}{2}\mathfrak{B}^j & -\frac{1}{2}\mathfrak{B}^j & 0 & -\frac{1}{2}\sin(\bar{\theta}^j) & 0 & -\frac{1}{2}\cos(\bar{\theta}^j) \\ 0 & 0 & 0 & -\frac{1}{2}\mathfrak{B}^j & -\frac{1}{2}\mathfrak{B}^j & 0 & -\frac{1}{2}\sin(\bar{\theta}^j) & 0 & -\frac{1}{2}\cos(\bar{\theta}^j) \\ 0 & 0 & 0 & 0 & 0 & 0 & 0 & 0 & 0 \\ 0 & 0 & 0 & -\frac{1}{2}\sin(\bar{\theta}^j) & -\frac{1}{2}\sin(\bar{\theta}^j) & 0 & 0 & 0 & 0 \\ 0 & 0 & 0 & 0 & 0 & 0 & 0 & 0 & 0 \\ 0 & 0 & 0 & -\frac{1}{2}\cos(\bar{\theta}^j) & -\frac{1}{2}\cos(\bar{\theta}^j) & 0 & 0 & 0 & 0 \end{bmatrix},$$

$$\mathbf{H}_{ea}(3) = \begin{bmatrix} 0 & 0 & 0 & 0 & 0 & 0 & 0 & 0 & 0 \\ 0 & \frac{1}{2}\mathfrak{A}^i & \frac{1}{2}\mathfrak{A}^i & 0 & 0 & -\frac{1}{2}\cos(\bar{\theta}^i) & 0 & -\frac{1}{2}\sin(\bar{\theta}^i) & 0 \\ 0 & \frac{1}{2}\mathfrak{A}^i & \frac{1}{2}\mathfrak{A}^i & 0 & 0 & -\frac{1}{2}\cos(\bar{\theta}^i) & 0 & -\frac{1}{2}\sin(\bar{\theta}^i) & 0 \\ 0 & 0 & 0 & 0 & 0 & 0 & 0 & 0 & 0 \\ 0 & 0 & 0 & 0 & 0 & 0 & 0 & 0 & 0 \\ 0 & -\frac{1}{2}\cos(\bar{\theta}^i) & -\frac{1}{2}\cos(\bar{\theta}^i) & 0 & 0 & 0 & 0 & 0 & 0 \\ 0 & 0 & 0 & 0 & 0 & 0 & 0 & 0 & 0 \\ 0 & -\frac{1}{2}\sin(\bar{\theta}^i) & -\frac{1}{2}\sin(\bar{\theta}^i) & 0 & 0 & 0 & 0 & 0 & 0 \\ 0 & 0 & 0 & 0 & 0 & 0 & 0 & 0 & 0 \end{bmatrix},$$

and,

$$\mathbf{H}_{ea}(4) = \begin{bmatrix} 0 & 0 & 0 & 0 & 0 & 0 & 0 & 0 & 0 \\ 0 & 0 & 0 & 0 & 0 & 0 & 0 & 0 & 0 \\ 0 & 0 & 0 & 0 & 0 & 0 & 0 & 0 & 0 \\ 0 & 0 & 0 & \frac{1}{2}\mathfrak{A}^j & \frac{1}{2}\mathfrak{A}^j & 0 & -\frac{1}{2}\cos(\bar{\theta}^j) & 0 & -\frac{1}{2}\sin(\bar{\theta}^j) \\ 0 & 0 & 0 & \frac{1}{2}\mathfrak{A}^j & \frac{1}{2}\mathfrak{A}^j & 0 & -\frac{1}{2}\cos(\bar{\theta}^j) & 0 & -\frac{1}{2}\sin(\bar{\theta}^j) \\ 0 & 0 & 0 & 0 & 0 & 0 & 0 & 0 & 0 \\ 0 & 0 & 0 & -\frac{1}{2}\cos(\bar{\theta}^j) & -\frac{1}{2}\cos(\bar{\theta}^j) & 0 & 0 & 0 & 0 \\ 0 & 0 & 0 & 0 & 0 & 0 & 0 & 0 & 0 \\ 0 & 0 & 0 & -\frac{1}{2}\sin(\bar{\theta}^j) & -\frac{1}{2}\sin(\bar{\theta}^j) & 0 & 0 & 0 & 0 \end{bmatrix}$$

3.2.6 The third change of variables from $\mathbf{q}_a$ to $\mathbf{q}_n$

The displacement vector $\mathbf{q}_a$ is presented as follow:

$$\mathbf{q}_a = [\overline{u}_a^j, \overline{\theta}_b^i, \overline{\theta}_a^i, \overline{\theta}_b^j, \overline{\theta}_a^j, s^i, s^j, g^i, g^j]^{\mathrm{T}}$$

is related to the displacement vector

$$\mathbf{q}_n = [u_a^i, v_a^i, \theta_b^i, \theta_a^i, u_a^j, v_a^j, \theta_b^j, \theta_a^j, s^i, s^j, g^i, g^j]^{\mathrm{T}}$$

by the transformation matrix $\mathbf{B}_{an}$ obtained by making use of Eqs. (3.4) to (3.6), (3.9) and (3.12) :

$$\mathbf{B}_{an} = \begin{bmatrix} -\mathfrak{c} & -\mathfrak{s} & 0 & 0 & \mathfrak{c} & \mathfrak{s} & 0 & 0 & 0 & 0 & 0 & 0 \\ -\frac{\mathfrak{s}}{l_n} & -\frac{\mathfrak{c}}{l_n} & 1 & 0 & \frac{\mathfrak{s}}{l_n} & -\frac{\mathfrak{c}}{l_n} & 0 & 0 & 0 & 0 & 0 & 0 \\ -\frac{\mathfrak{s}}{l_n} & -\frac{\mathfrak{c}}{l_n} & 0 & 1 & \frac{\mathfrak{s}}{l_n} & -\frac{\mathfrak{c}}{l_n} & 0 & 0 & 0 & 0 & 0 & 0 \\ -\frac{\mathfrak{s}}{l_n} & -\frac{\mathfrak{c}}{l_n} & 0 & 0 & \frac{\mathfrak{s}}{l_n} & -\frac{\mathfrak{c}}{l_n} & 1 & 0 & 0 & 0 & 0 & 0 \\ -\frac{\mathfrak{s}}{l_n} & -\frac{\mathfrak{c}}{l_n} & 0 & 0 & \frac{\mathfrak{s}}{l_n} & -\frac{\mathfrak{c}}{l_n} & 0 & 1 & 0 & 0 & 0 & 0 \\ 0 & 0 & 0 & 0 & 0 & 0 & 0 & 0 & 1 & 0 & 0 & 0 \\ 0 & 0 & 0 & 0 & 0 & 0 & 0 & 0 & 0 & 1 & 0 & 0 \\ 0 & 0 & 0 & 0 & 0 & 0 & 0 & 0 & 0 & 0 & 1 & 0 \\ 0 & 0 & 0 & 0 & 0 & 0 & 0 & 0 & 0 & 0 & 0 & 1 \end{bmatrix}$$

In this case, after some algebraic manipulations, we get:

$$\mathbf{H}_{an} = \frac{\mathbf{z}\mathbf{z}^{\mathrm{T}}}{l_n} Q_a(1) + \frac{1}{l_n^2}\left(\mathbf{r}\mathbf{z}^{\mathrm{T}} + \mathbf{z}\mathbf{r}^{\mathrm{T}}\right)\left(Q_a(2) + Q_a(3) + Q_a(4) + Q_a(5)\right)$$

where,

$$\mathbf{r} = \begin{bmatrix} -\mathfrak{c} & -\mathfrak{s} & 0 & 0 & \mathfrak{c} & \mathfrak{s} & 0 & 0 & 0 & 0 & 0 & 0 \end{bmatrix}^{\mathrm{T}}$$
$$\mathbf{z} = \begin{bmatrix} \mathfrak{s} & -\mathfrak{c} & 0 & 0 & -\mathfrak{s} & \mathfrak{c} & 0 & 0 & 0 & 0 & 0 & 0 \end{bmatrix}^{\mathrm{T}}$$

3.2.7 The fourth change of variables from $\mathbf{q}_n$ to $\mathbf{q}_g$

The transformation matrix $\mathbf{B}_{ng}$ relating the displacement vectors:

$$\mathbf{q}_n = [u_a^i, v_a^i, \theta_b^i, \theta_a^i, u_a^j, v_a^j, \theta_b^j, \theta_a^j, s^i, s^j, g^i, g^j]^{\mathrm{T}}$$

and

$$\mathbf{q}_g = [u_b^i, v_b^i, \theta_b^i, u_a^i, v_a^i, \theta_a^i, u_b^j, v_b^j, \theta_b^j, u_a^j, v_a^j, \theta_a^j]^{\mathrm{T}}$$

is obtained by using the relationships of global slip and gap variations with respect to the displacement vector $\mathbf{q}_g$, given in Appendix A.

$$\mathbf{B}_{ng} = \begin{bmatrix} 0 & 0 & 0 & 1 & 0 & 0 & 0 & 0 & 0 & 0 & 0 & 0 \\ 0 & 0 & 0 & 0 & 1 & 0 & 0 & 0 & 0 & 0 & 0 & 0 \\ 0 & 0 & 1 & 0 & 0 & 0 & 0 & 0 & 0 & 0 & 0 & 0 \\ 0 & 0 & 0 & 0 & 0 & 1 & 0 & 0 & 0 & 0 & 0 & 0 \\ 0 & 0 & 0 & 0 & 0 & 0 & 0 & 0 & 0 & 1 & 0 & 0 \\ 0 & 0 & 0 & 0 & 0 & 0 & 0 & 0 & 0 & 0 & 1 & 0 \\ 0 & 0 & 0 & 0 & 0 & 0 & 0 & 0 & 1 & 0 & 0 & 0 \\ 0 & 0 & 0 & 0 & 0 & 0 & 0 & 0 & 0 & 0 & 0 & 1 \\ \mathfrak{C}^i & \mathfrak{S}^i & \mathfrak{M}^i & -\mathfrak{C}^i & -\mathfrak{S}^i & \mathfrak{O}^i & 0 & 0 & 0 & 0 & 0 & 0 \\ 0 & 0 & 0 & 0 & 0 & 0 & \mathfrak{C}^j & \mathfrak{S}^j & \mathfrak{M}^j & -\mathfrak{C}^j & -\mathfrak{S}^j & \mathfrak{O}^j \\ -\mathfrak{S}^i & \mathfrak{C}^i & \mathfrak{N}^i & \mathfrak{S}^i & -\mathfrak{C}^i & \mathfrak{P}^i & 0 & 0 & 0 & 0 & 0 & 0 \\ 0 & 0 & 0 & 0 & 0 & 0 & -\mathfrak{S}^j & \mathfrak{C}^j & \mathfrak{N}^j & \mathfrak{S}^j & -\mathfrak{C}^j & \mathfrak{P}^j \end{bmatrix}$$

where

$$\mathfrak{C}^i = \cos(\beta_0 + \theta^i) \quad ; \quad \mathfrak{C}^j = \cos(\beta_0 + \theta^j) \quad ;$$

$$\mathfrak{S}^i = \sin(\beta_0 + \theta^i) \quad ; \quad \mathfrak{S}^j = \sin(\beta_0 + \theta^j) \quad ;$$

$$\mathfrak{M}^i = \left[h_b \cos\left(\frac{\theta_b^i - \theta_a^i}{2}\right) + \frac{g^i}{2}\right] \quad ; \quad \mathfrak{M}^j = \left[h_b \cos\left(\frac{\theta_b^j - \theta_a^j}{2}\right) + \frac{g^j}{2}\right] \quad ;$$

$$\mathfrak{N}^i = \left[h_b \sin\left(\frac{\theta_b^i - \theta_a^i}{2}\right) - \frac{s^i}{2}\right] \quad ; \quad \mathfrak{N}^j = \left[h_b \sin\left(\frac{\theta_b^j - \theta_a^j}{2}\right) - \frac{s^j}{2}\right] \quad ;$$

$$\mathfrak{O}^i = \left[h_a \cos\left(\frac{\theta_a^i - \theta_b^i}{2}\right) + \frac{g^i}{2}\right] \quad ; \quad \mathfrak{O}^j = \left[h_a \sin\left(\frac{\theta_a^j - \theta_b^j}{2}\right) + \frac{g^j}{2}\right] \quad ;$$

$$\mathfrak{P}^i = \left[h_a \sin\left(\frac{\theta_a^i - \theta_b^i}{2}\right) - \frac{s^i}{2}\right] \quad ; \quad \mathfrak{P}^j = \left[h_a \sin\left(\frac{\theta_a^j - \theta_b^j}{2}\right) - \frac{s^j}{2}\right]$$

Accordingly, the nonlinear geometric term of the stiffness matrix is obtained as follow:

$$\mathbf{H}_{ng} = \mathbf{H}_{ng}(1)Q_n(9) + \mathbf{H}_{ng}(2)Q_n(10) + \mathbf{H}_{ng}(3)Q_n(11) + \mathbf{H}_{ng}(4)Q_n(12)$$

where

$$\mathbf{H}_{ng}(1) = \frac{1}{2}\begin{bmatrix}
0 & 0 & -\mathfrak{S}^i & 0 & 0 & -\mathfrak{S}^i & 0 & 0 & 0 & 0 & 0 & 0 \\
0 & 0 & \mathfrak{C}^i & 0 & 0 & \mathfrak{C}^i & 0 & 0 & 0 & 0 & 0 & 0 \\
-\mathfrak{S}^i & \mathfrak{C}^i & -\frac{s^i}{2} & \mathfrak{S}^i & -\mathfrak{C}^i & \frac{s^i}{2}+\mathfrak{N}^i+\mathfrak{P}^i & 0 & 0 & 0 & 0 & 0 & 0 \\
0 & 0 & \mathfrak{S}^i & 0 & 0 & \mathfrak{S}^i & 0 & 0 & 0 & 0 & 0 & 0 \\
0 & 0 & -\mathfrak{C}^i & 0 & 0 & -\mathfrak{C}^i & 0 & 0 & 0 & 0 & 0 & 0 \\
-\mathfrak{S}^i & \mathfrak{C}^i & \frac{s^i}{2}+\mathfrak{N}^i+\mathfrak{P}^i & \mathfrak{S}^i & -\mathfrak{C}^i & -\frac{s^i}{2} & 0 & 0 & 0 & 0 & 0 & 0 \\
0 & 0 & 0 & 0 & 0 & 0 & 0 & 0 & 0 & 0 & 0 & 0 \\
0 & 0 & 0 & 0 & 0 & 0 & 0 & 0 & 0 & 0 & 0 & 0 \\
0 & 0 & 0 & 0 & 0 & 0 & 0 & 0 & 0 & 0 & 0 & 0 \\
0 & 0 & 0 & 0 & 0 & 0 & 0 & 0 & 0 & 0 & 0 & 0 \\
0 & 0 & 0 & 0 & 0 & 0 & 0 & 0 & 0 & 0 & 0 & 0 \\
0 & 0 & 0 & 0 & 0 & 0 & 0 & 0 & 0 & 0 & 0 & 0
\end{bmatrix}$$

$$\mathbf{H}_{ng}(2) = \frac{1}{2}\begin{bmatrix}
0 & 0 & 0 & 0 & 0 & 0 & 0 & 0 & 0 & 0 & 0 & 0 \\
0 & 0 & 0 & 0 & 0 & 0 & 0 & 0 & 0 & 0 & 0 & 0 \\
0 & 0 & 0 & 0 & 0 & 0 & 0 & 0 & 0 & 0 & 0 & 0 \\
0 & 0 & 0 & 0 & 0 & 0 & 0 & 0 & 0 & 0 & 0 & 0 \\
0 & 0 & 0 & 0 & 0 & 0 & 0 & 0 & 0 & 0 & 0 & 0 \\
0 & 0 & 0 & 0 & 0 & 0 & 0 & 0 & 0 & 0 & 0 & 0 \\
0 & 0 & 0 & 0 & 0 & 0 & 0 & 0 & -\mathfrak{S}^j & 0 & 0 & -\mathfrak{S}^j \\
0 & 0 & 0 & 0 & 0 & 0 & 0 & 0 & \mathfrak{C}^j & 0 & 0 & \mathfrak{C}^j \\
0 & 0 & 0 & 0 & 0 & 0 & -\mathfrak{S}^j & \mathfrak{C}^j & -\frac{s^j}{2} & \mathfrak{S}^j & -\mathfrak{C}^j & \frac{s^j}{2}+\mathfrak{N}^j+\mathfrak{P}^j \\
0 & 0 & 0 & 0 & 0 & 0 & 0 & 0 & \mathfrak{S}^j & 0 & 0 & \mathfrak{S}^j \\
0 & 0 & 0 & 0 & 0 & 0 & 0 & 0 & -\mathfrak{C}^j & 0 & 0 & -\mathfrak{C}^j \\
0 & 0 & 0 & 0 & 0 & 0 & -\mathfrak{S}^j & \mathfrak{C}^j & \frac{s^j}{2}+\mathfrak{N}^i+\mathfrak{P}^j & \mathfrak{S}^j & -\mathfrak{C}^j & -\frac{s^j}{2}
\end{bmatrix}$$

$$\mathbf{H}_{ng}(3) = \frac{1}{2}\begin{bmatrix}
0 & 0 & -\mathfrak{C}^i & 0 & 0 & -\mathfrak{C}^i & 0 & 0 & 0 & 0 & 0 & 0 \\
0 & 0 & -\mathfrak{S}^i & 0 & 0 & -\mathfrak{S}^i & 0 & 0 & 0 & 0 & 0 & 0 \\
-\mathfrak{C}^i & -\mathfrak{S}^i & -\frac{g^i}{2} & \mathfrak{C}^i & \mathfrak{S}^i & \frac{g^i}{2}-\mathfrak{M}^i-\mathfrak{O}^i & 0 & 0 & 0 & 0 & 0 & 0 \\
0 & 0 & \mathfrak{C}^i & 0 & 0 & \mathfrak{C}^i & 0 & 0 & 0 & 0 & 0 & 0 \\
0 & 0 & \mathfrak{S}^i & 0 & 0 & \mathfrak{S}^i & 0 & 0 & 0 & 0 & 0 & 0 \\
-\mathfrak{C}^i & -\mathfrak{S}^i & \frac{g^i}{2}-\mathfrak{M}^i-\mathfrak{O}^i & \mathfrak{C}^i & \mathfrak{S}^i & -\frac{g^i}{2} & 0 & 0 & 0 & 0 & 0 & 0 \\
0 & 0 & 0 & 0 & 0 & 0 & 0 & 0 & 0 & 0 & 0 & 0 \\
0 & 0 & 0 & 0 & 0 & 0 & 0 & 0 & 0 & 0 & 0 & 0 \\
0 & 0 & 0 & 0 & 0 & 0 & 0 & 0 & 0 & 0 & 0 & 0 \\
0 & 0 & 0 & 0 & 0 & 0 & 0 & 0 & 0 & 0 & 0 & 0 \\
0 & 0 & 0 & 0 & 0 & 0 & 0 & 0 & 0 & 0 & 0 & 0 \\
0 & 0 & 0 & 0 & 0 & 0 & 0 & 0 & 0 & 0 & 0 & 0
\end{bmatrix}$$

$$\mathbf{H}_{ng}(4) = \frac{1}{2}\begin{bmatrix}
0 & 0 & 0 & 0 & 0 & 0 & 0 & 0 & 0 & 0 & 0 & 0 \\
0 & 0 & 0 & 0 & 0 & 0 & 0 & 0 & 0 & 0 & 0 & 0 \\
0 & 0 & 0 & 0 & 0 & 0 & 0 & 0 & 0 & 0 & 0 & 0 \\
0 & 0 & 0 & 0 & 0 & 0 & 0 & 0 & 0 & 0 & 0 & 0 \\
0 & 0 & 0 & 0 & 0 & 0 & 0 & 0 & 0 & 0 & 0 & 0 \\
0 & 0 & 0 & 0 & 0 & 0 & 0 & 0 & 0 & 0 & 0 & 0 \\
0 & 0 & 0 & 0 & 0 & 0 & 0 & 0 & -\mathfrak{C}^j & 0 & 0 & -\mathfrak{C}^j \\
0 & 0 & 0 & 0 & 0 & 0 & 0 & 0 & -\mathfrak{S}^j & 0 & 0 & -\mathfrak{S}^j \\
0 & 0 & 0 & 0 & 0 & 0 & -\mathfrak{C}^j & -\mathfrak{S}^j & -\frac{g^j}{2} & \mathfrak{C}^j & \mathfrak{S}^j & \frac{g^j}{2} - \mathfrak{M}^j - \mathfrak{O}^j \\
0 & 0 & 0 & 0 & 0 & 0 & 0 & 0 & \mathfrak{C}^j & 0 & 0 & \mathfrak{C}^j \\
0 & 0 & 0 & 0 & 0 & 0 & 0 & 0 & \mathfrak{S}^j & 0 & 0 & \mathfrak{S}^j \\
0 & 0 & 0 & 0 & 0 & 0 & -\mathfrak{C}^j & -\mathfrak{S}^j & \frac{g^j}{2} - \mathfrak{M}^j - \mathfrak{O}^j & \mathfrak{C}^j & \mathfrak{S}^j & -\frac{g^j}{2}
\end{bmatrix}$$

3.3 Numerical applications

The purpose of this section is to illustrate the capability of the proposed formulation in reproducing the nonlinear behavior of composite beam taking into account slips and uplifts. The proposed model is firstly evaluated and validated by comparing its results with the ones available in the literature. The validated model is then used to illustrate the effects of uplift in the nonlinear behavior of composite beam-column.

3.3.1 Example 1: Validation with a simply supported beam subjected to axial and transverse loading

To validate the proposed model, a simply supported beam subjected to axial and transverse loading is considered, see Fig. 3.4. For this problem, a non-linear analysis is required even for small displacements. A closed-form solution of this problem, in which the uplift effect is neglected, is provided by Girhammar and Gopu [49] and Kroflič, Saje, and Planinc [30]. In order to eliminate uplifts, we consider a large vertical connection stiffness equal to 1000 kN/cm^2 (continuous connection stiffness value which will be converted later for discrete connection) for the present model. The beam is modeled with 20 elements and the penalty method with penalty parameter equal to 1000 kN/cm is adopted in the present model. This corresponds to a continuous connection stiffness value which will be converted later for discrete connection. The beam is modeled with 20 elements and the penalty method with penalty parameter equal to 1000 kN/cm is adopted in the present model. The elastic modulus of layer a and b are 800 kN/cm^2 and 1200 kN/cm^2, respectively. The stiffness of continuous shear connection in horizontal direction is equal to 5 kN/cm^2. Since the discrete bond is also used in the present model, the stiffness of connectors k_h and k_v is calculated

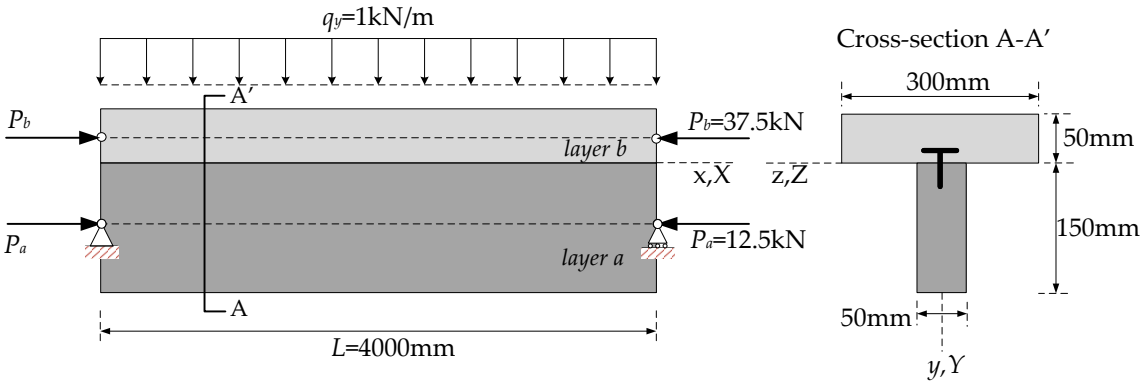

FIGURE 3.4: Two-layer composite beam under axial and transverse loads.

by multiplying the continuous shear connection stiffness by the spacing of the connector elements.

The results obtained with the present models are compared for the absolute value of maximum vertical displacement $||v_{max}||$ and maximum slip value s_{max} with the ones found in the literature and summarized in Table 2.1. It can be seen that a very good agreement is obtained.

TABLE 3.1: Numerical results.

Result	$\|\|v_{max}\|\|$(mm)	s_{max}(mm)
Girhammar and Gopu [49]	9.276	0.2776
Battini, Nguyen, and Hjiaj [26]	9.249	0.2760
Kroflič, Saje, and Planinc [30]	9.273	0.2772
Present discrete model	9.315	0.2772
Present continuous model	9.275	0.2775
Comparison	**Ratio of $\|\|v_{max}\|\|$**	**Ratio of s_{max}**
Present discrete model/[49]	1.0042	0.9985
Present continuous model/[49]	0.9998	0.9996

3.3.2 Example 2: Uplift effects on buckling load of simply supported beam-column

A simply supported two-layer beam subjected to an axial load, see Fig. 3.5, is studied in this example. The elastic modulus of layer a is 7.84 GPa and of layer b is 4.9 GPa. An incremental compression force P is applied on layer a. Due to the lack of symmetry of the structure, a small value of compression load P produces vertical displacements of the beam-column. The composite beam-column is analyzed using the discrete connection model with a mesh of 20 elements. In order to represent the shear connection stiffness independently from the number of finite elements, we provide here the equivalent stiffnesses for continuous connection. The stiffnesses of the connectors k_h and k_v used in the discrete connection model

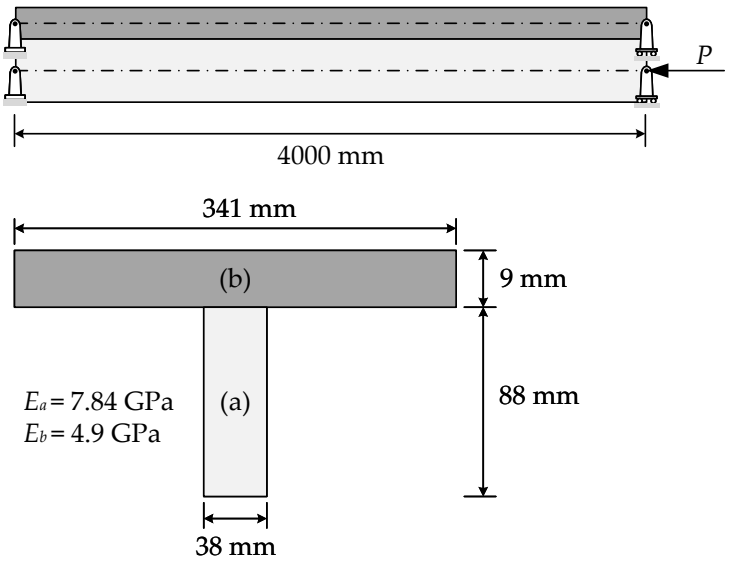

FIGURE 3.5: Two-layer composite beam under an incremental axial load.

can be then calculated correspondingly. In this example, to study the effects of uplift on the buckling behavior of the composite beam-column, various uplift moduli are considered: 10^{-6} MPa, 1 MPa and 10^{6} MPa, while the longitudinal shear connection stiffness is taken equal to 50 MPa and remains constant.

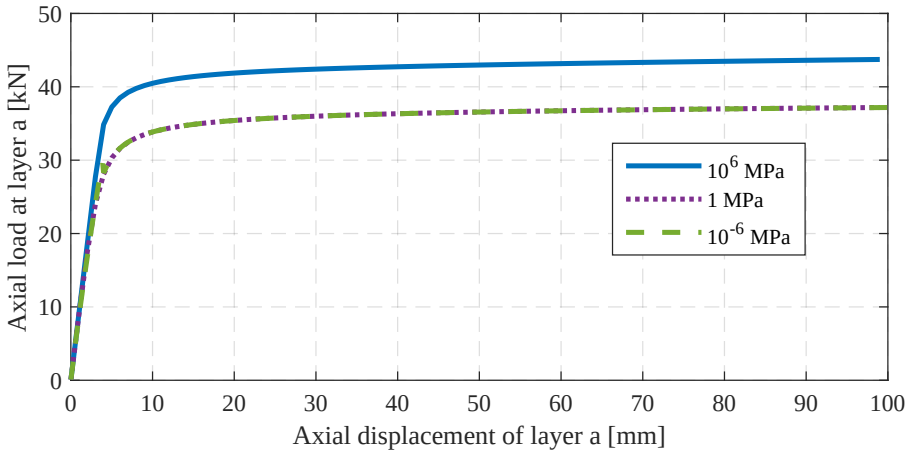

FIGURE 3.6: Load-axial displacement path for different uplift moduli

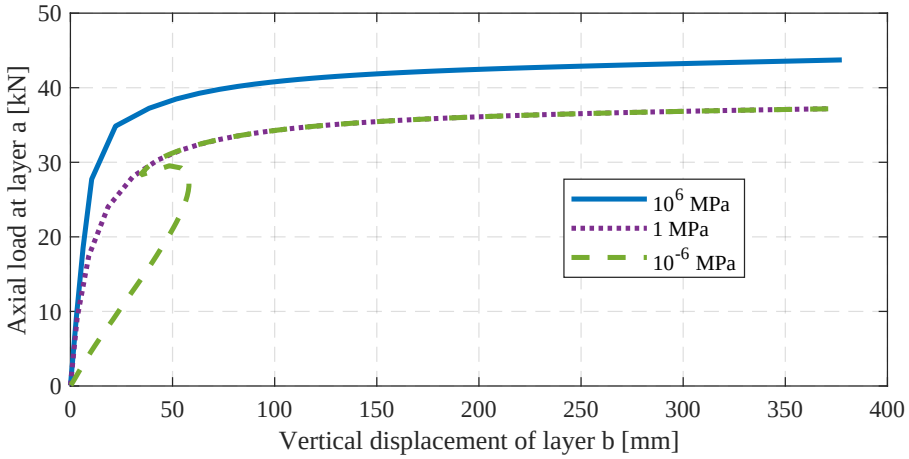

FIGURE 3.7: Load-vertical displacement path for different uplift moduli

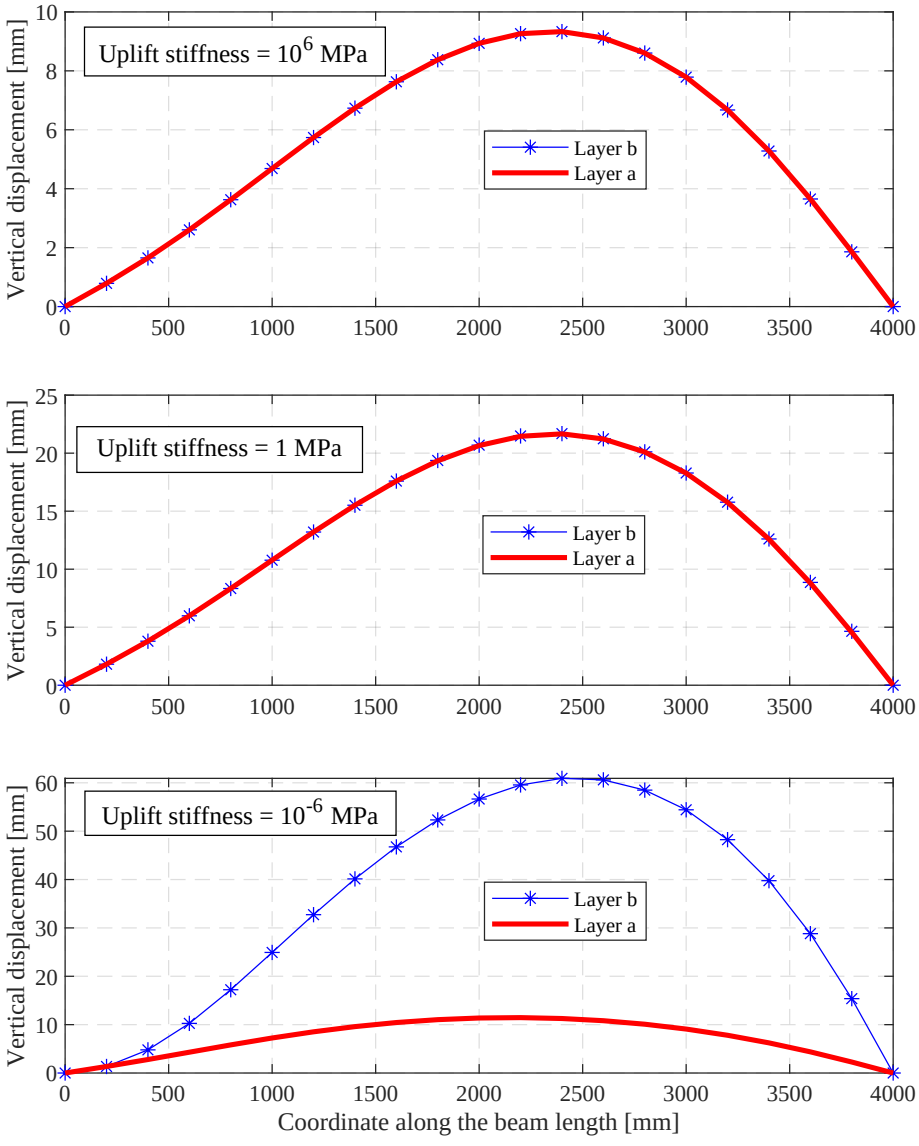

FIGURE 3.8: Vertical displacement of composite beam-column with P=25 kN and for different uplift moduli

Fig. 3.6 and Fig. 3.7 show the load-displacement curves for different uplift moduli. It can be seen that the uplift stiffness has an effect on the buckling load of the composite beam-column. For lower uplift stiffness, we have a large separation between the layers at the beginning of loading, resulting the buckling of layer b, whereas layer a experiencing moderate vertical displacement, see Fig. 3.7 and Fig. 3.8. Increasing the load produces increasingly larger vertical displacement. At some point, layer a will come into contact with layer b.

3.3.3 Example 3: Contact treatment of uniform bending of a cantilever beam

For this problem, the cantilever beam with 5 m length is composed of unconnected two identical layers, see Fig. 3.9. The elastic modulus of both layers is 3500 kN/cm^2. The height and the width of both layers are 5 cm and 10 cm, respectively. The load is applied incrementally, within 20 steps using displacement control method, at the tip of the lower layer so that the latter is deformed into a quarter circle. The analysis is performed with the present model using 10 elements. To treat the contact of the two layers, the resolution methods discussed earlier in this paper, i.e. penalty method (PM) and augmented Lagrangian method (ALM), are adopted and compared. The penalty parameter is taken equal to 10^8 kN/cm in both methods. Besides, the convergence tolerance of 0.0001 mm for non penetrability condition is considered. Table 3.2 shows the number of iterations required for convergence for each load step. It can be seen that the number of iterations in ALM is larger than the one in PM at the beginning of load step. However, they are both equal after the third load step. It is worth mentioning here that increasing the penalty parameter in both PM and ALM does not improve the convergence rate. Instead, numerical problem is occurred when the penalty parameter is larger than 10^8 kN/cm. The slip at the tip of the composite beam when the lower layer is bent into a quarter circle, obtained with PM and ALM, is 77.0690 mm and 77.0692 mm, respectively. It is worth mentioning that for vertically unseparated two-layer beam, the analytical solution of slip at the tip of the beam is 79.1665 mm, i.e. 2.65% of difference with the proposed model.

TABLE 3.2: Number of iterations for each load step

Load step	1	2	3	4	5	6	7	8	9	10
PM	12	5	5	5	5	5	5	5	5	5
ALM	14	14	5	5	5	5	5	5	5	5
Load step	11	12	13	14	15	16	17	18	19	20
PM	5	5	5	5	5	5	5	5	5	5
ALM	5	5	5	5	5	5	5	5	5	5

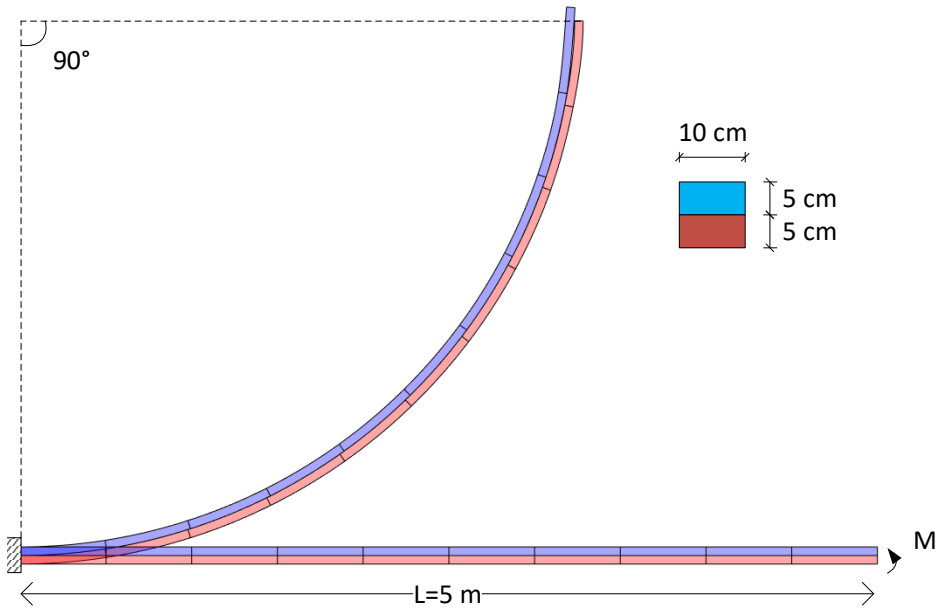

FIGURE 3.9: Uniform bending of a cantilever beam

3.3.4 Example 4: Contact treatment of continuous beam

In this example, the continuous composite steel-concrete beam subjected to a uniform load of 20 kN/m along its length and a concentrated load of 100 kN at the mid-span of the first span, see Fig. 3.10, is considered. 19 pairs of stud connectors with a spacing of 1 m along the beam length are used to connect the steel beam to the concrete slab. Each pair of connectors has a shear rigidity of 300 kN/mm. The uplift modulus of a pair of connectors is assumed equal to one-third of its shear rigidity, i.e. equal to 100 kN/mm.

The analysis is performed with the discrete connection model using 18 elements. Both the penalty (PM) and augmented Lagrangian (ALM) methods are employed. Table 3.3 shows the maximum penetration between the two materials in function of penalty parameter used in penalty method. It can be seen clearly that the penetration decreases when the penalty parameter increases. Fig. 3.11 illustrates the penetration (negative) or uplift (positive) along the beam length obtained with ALM and PM for penalty parameter equal to 10^4 N/mm and 10^{10} N/mm, respectively. As expected, small penetrations are obtained with penalty method. Meanwhile, in augmented Lagrangian method, the contact condition is fully respected. Fig. 3.12 shows the displacement of the composite beam. It can be seen that both methods give the same result.

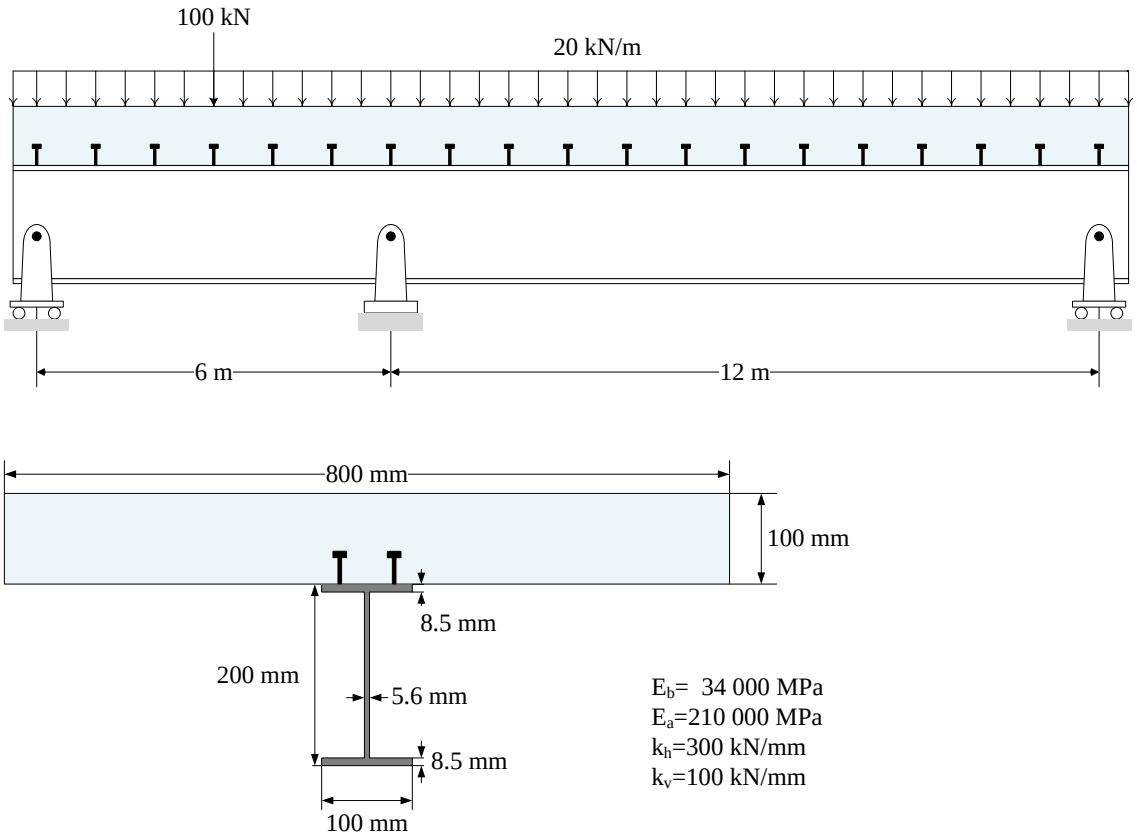

FIGURE 3.10: Continuous composite beam.

TABLE 3.3: Maximum penetration obtained with penalty method

Penalty parameter (N/mm)	10^4	10^6	10^8	10^{10}
Maximum penetration (mm)	1.0417	0.0656	$6.9362.10^{-4}$	$6.9402.10^{-6}$

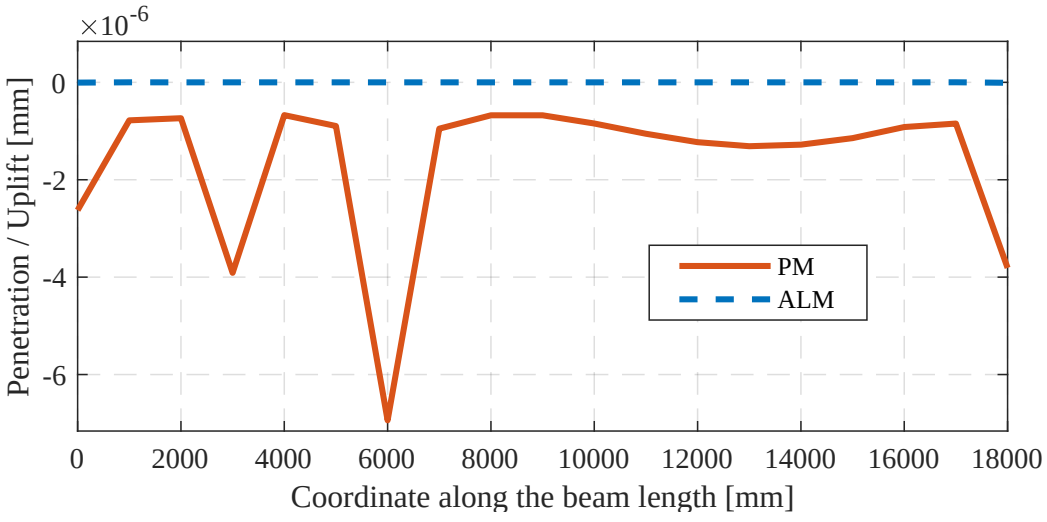

FIGURE 3.11: Penetration / Uplift obtained with ALM and PM.

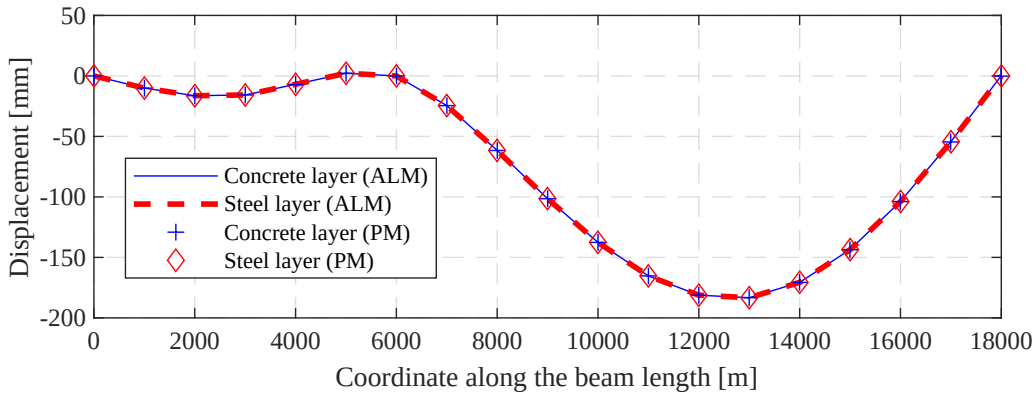

FIGURE 3.12: Displacement of the composite beam.

3.4 Conclusion

A new finite element formulation for the large displacement analysis of two-layer beam is presented in this chapter. To describe the geometrical nonlinearity, a co-rotational method is adopted in which the motion of the element is decomposed into two parts: a rigid body motion that defines a local coordinate system and a small deformational motion of the element relative to this local coordinate system. The treatment of geometrical nonlinearity is effectively undertaken at the level of discrete nodal variables with the transformation matrix between the local and global nodal entities being independent of the assumptions made for the local element.

Besides, to enforce the non penetrability between the layers, the methods generally used to solve the node-to-node contact problem, for instance the penalty method (PM) and augmented Lagrangian method (ALM), are used. Both resolution methods have been compared in the numerical applications presented in this chapter. The comparison shows that more iteration numbers are required in ALM. However, despite a low convergence rate of ALM compared to PM, the non penetrability condition is fully respected in ALM. Hence, the unrealistic penetration between the layers can be prevented by using ALM algorithm.

Furthermore, the effects of uplift on the elastic buckling behavior of simply supported two-layered beam have been studied. It is shown that the buckling load of the composite beam is largely effected by the uplift stiffness of the connectors. In composite members with a low uplift stiffness, the gap between the two layers is large and the layer with low flexural stiffness is prone to buckle before global bucking of the composite beam occurs. For a cantilever two-layer beam under an uniform bending of the lower layer, it is observed that there is a presence of a small uplift near the tip of the cantilever beam. However, comparing to the analytical solution of a vertically unseparated two-layer cantilever beam, this small uplift has little effects.

Chapter 4

Constitutive modeling

4.1 Introduction

Inelastic behavior analysis is indispensable for designing framed structures to withstand extreme loads. Two main modeling approaches, lumped plasticity and distributed plasticity, are commonly used. Lumped plasticity models use yield surfaces and flow rules based on classical plasticity theory to describe relationships between axial force, shear force, and bending moment. Distributed plasticity models consider a nonlinear interaction of internal forces along the entire element by integrating the constitutive behavior at the control section. The latter is subdivided into fibre and each fibre responds to the stress applied to it. The distributed plasticity models provide then a more accurate representation of inelastic response of the element. However, it is computationally more demanding.

This chapter presents the constitutive models that will be used to describe the nonlinear behavior for the steel-concrete composite beam. Since the Bernoulli kinematic assumptions are adopted for both layers, a uniaxial stress-strain relationship can be employed. For steel model, in addition to the bilinear and multilinear models with isotropic and kinematic hardening, the explicit 1D Armstrong-Frederick model is presented. For concrete model, the plastic-damaged model of Kent and Park, along with the return mapping algorithm, is introduced. Additionally, the interaction behavior of shear stud connectors in shear and tension actions is studied.

The organization of this chapter is as the following. In Section 4.2, the steel constitutive law is presented including explicit 1D model of steel material. In Section 4.3, the constitutive model of concrete is demonstrated with explicit 1D model of concrete. To take into account the modulus of degradation and tension stiffening, a plastic-damage model is adopted for the concrete material. Section 4.4 presents the behavior of stud connector including the push-out and pull-out test, shear and tensile stiffness of connector, load-slip relationship which involves the interaction between bond force and uplift force of connector. Lastly, it is concluded by Section 4.5.

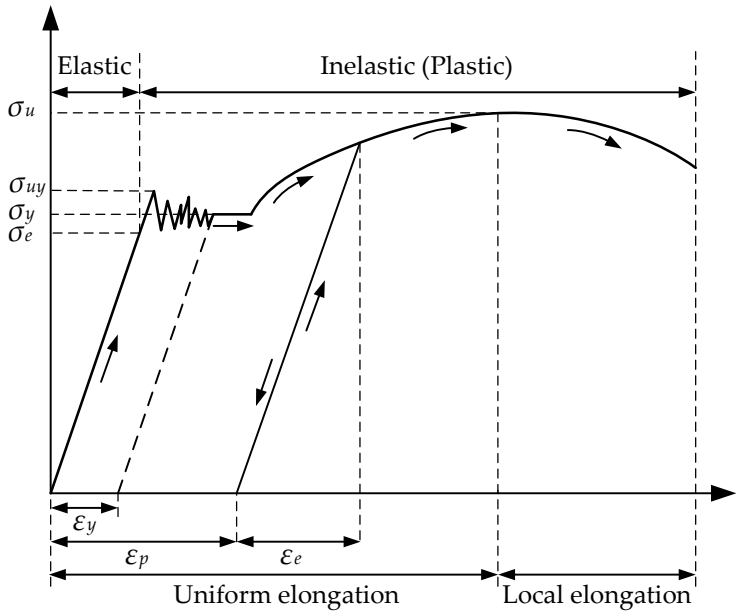

FIGURE 4.1: Stress-strain constitutive curve in tensile test results

4.2 Steel constitutive law

The behavior of steel strongly influences the response of composite steel-concrete structural elements subjected to complex loadings, particularly in tension. Therefore, it is necessary to develop an analytical model that predicts the fundamental characteristics of steel within an appropriate range of loading.

The tensile test of steel material is widely used to provide basic design information on the strength of materials and as an acceptance test for the specification of materials. In the tensile test, a specimen is subjected to a continually increasing uniaxial tensile force while simultaneous observations are made on the elongation of the specimen. The parameters, which are used to describe the stress-strain curve of steel material, are the tensile strength, yield strength or yield point, percent elongation, and reduction of area.

4.2.1 Stress-strain curve

The steel sample is subjected to an uni-axial tensile test where it is loaded along its longitudinal axis until it reaches its maximum load-bearing capacity and eventually fractures. The load applied is recorded, and the sample's deformation is measured to determine its stress and strain. This data is then utilized to plot a stress-strain curve that characterizes the material's deformation behavior under tension.

The linear elastic range

During the initial stage of loading, the stress in the material varies linearly with the strain up to the elastic limit. In this region, the stress is proportional to the strain with the constant of proportionality being the modulus of elasticity, denoted as E. As the strain is increased within the range $0 \leq \varepsilon \leq \varepsilon_y$, the steel material deviates from this linear proportionality and enters the nonlinear reversible domain up to the yield point, σ_y, where plasticity begins to develop (as shown in Fig. 4.1). Since it can be difficult to accurately determine the stress at which plastic deformation begins, the yield stress is often defined as the stress required to induce a specified amount of permanent strain, typically 0.2%.

The yield plateau

For strains greater than the yielding strain ε_y, the stress in the material remains nearly constant at the yield stress value for a moderate increase in strain. This region is referred to as the yield plateau, which is a characteristic feature of the stress-strain curve for many metals including steel. At the yield point, plastic deformation occurs through the evolution of plastic strain, also known as plastic flow. During this stage, the material undergoes significant plastic deformation while maintaining a nearly constant stress level until strain hardening begins. The yield plateau is an important region of the stress-strain curve as it indicates the material's ability to resist plastic deformation under load.

The strain-hardening region

Once the yield plateau is exceeded, the stress begins to increase again with increasing total strain. During this stage, an evolution of the yield stress is observed, a phenomenon known as hardening. This strain-hardening regime is maintained until the ultimate stress, also known as the stress peak, is reached.

4.2.2 Yielding criteria

Once the steel coupon is loaded beyond its yield limit and subsequently unloaded, the material undergoes a phenomenon known as plastic deformation, which results in a permanent deformation or strain that cannot be recovered. This unrecoverable deformation is known as plastic strain, denoted by ε_p. During the unloading state, the behavior of the steel coupon is considered to be linear elastic. The uniaxial stress corresponding to a configuration with total strain ε is given by:

$$\sigma = E\left(\varepsilon - \varepsilon_p\right) \tag{4.1}$$

It is noticeable that the difference between the total strain and the current plastic strain is fully reversible. The upon complete unloading, $\varepsilon - \varepsilon_p$ is fully recovered without further evolution of plastic strains. In this manner, the total strain, ε, can be decomposed into the sum of an elastic (or reversible) strain, ε_e, and a plastic (or permanent) strain, ε_p at restrictions to

small strains:

$$\varepsilon = \varepsilon_e + \varepsilon_p \tag{4.2}$$

where the elastic strain has been defined as

$$\varepsilon_e = \varepsilon - \varepsilon_p \tag{4.3}$$

Following the above definition of the elastic axial strain, the constitutive law for the axial stress can be expressed as

$$\sigma = E\varepsilon_e \tag{4.4}$$

The relation is also known as Hooke's law for linear elastic behavior. For plastic material behavior, no more explicit relation between stress and strain is given since the strain state is also dependent on the loading history. In spite of that, the plastic material behavior can be described by a yield condition, a flow rule and hardening law.

The elastic domain delimited by the yield stress can be expressed as:

$$|\sigma| - \sigma_y < 0 \tag{4.5}$$

where, the yield stress, σ_y is identical in the tensile and compressive regime. Eq. (4.5) denotes no change in plastic strain taking place, i.e., $\dot{\varepsilon}_p = 0$. A change in ε_p can take place only if the relevant body is under plastic loading where

$$|\sigma| - \sigma_y = 0 \tag{4.6}$$

It is worth mentioning that, at any stage, no stress level is allowed above the current yield stress, i.e. plastically admissible stresses lie either in the elastic domain or on the yield limit. The following notation is introduced to designate the set of admissible stresses:

$$\mathbb{E}_\sigma = \left\{\sigma \in \mathbb{R} \,|\, f\left(\sigma, \sigma_y\right) = |\sigma| - \sigma_y \leq 0\right\} \tag{4.7}$$

Thus, the yield condition that enables one to determine whether the relevant material suffers only elastic or also plastic strains at a certain stress state is:

$$f\left(\sigma, \sigma_y\right) = |\sigma| - \sigma_y \leq 0 \tag{4.8}$$

4.2.3 Flow rule

The flow rule relates plastic deformation to the stress state in a material, and is fundamental to develop constitutive laws for materials that exhibit plastic behavior. Incorporating the flow rule into a constitutive law allows for accurate modeling of mechanical behavior under various loading conditions.

In the plastic range, the relevant body experiences the plastic strain rate. Let $\dot{\lambda}$ denote the absolute value of the plastic strain rate (also known as plastic multiplier or consistency parameter), i.e. $\dot{\lambda} = |\dot{\varepsilon}_p|$.

Then the preceding physical assumption takes the form:

$$\dot{\varepsilon}_p = \dot{\lambda} \frac{\partial f}{\partial \sigma} \tag{4.9}$$

By applying Eq. (4.8), it can be expressed as:

$$\dot{\varepsilon}_p = \dot{\lambda} \text{sign}(\sigma)$$

where $\dot{\lambda} \geq 0$ is a hardening parameter. This form of the flow rule is called an associated flow rule and the assumption of co-directionality is called the normality condition.

The factor sign is the signum function defined as:

$$\text{sign}(\sigma) = \begin{cases} +1 & \text{if} \quad \sigma > 0 \\ 0 & \text{if} \quad \sigma = 0 \\ -1 & \text{if} \quad \sigma < 0 \end{cases} \tag{4.10}$$

4.2.4 Hardening law

The complete characterization of the uniaxial model is achieved with the introduction of the hardening law which allows the consideration of the influence of material hardening on the yield condition and the flow rule. As remarked in the experimental test of steel coupon, an evolution of the yield stress accompanies the evolution of the plastic strain in strain-hardening range. Whereas for perfect plasticity the closure of the elastic range $\mathbb{E}_\sigma$ remains unchanged, $\mathbb{E}_\sigma$ expands with the amount of plastic flow in the system for the strain hardening model. This expansion can be incorporated into the uniaxial model by simply assuming that the yield stress σ_y is given as a function:

$$\sigma_y = \sigma_y(p) \tag{4.11}$$

of the internal variable. In this case the accumulated axial plastic strain, p is defined as

$$p = \int_0^t |\dot{\varepsilon}_p| \, dt \tag{4.12}$$

It is straightforward that in a monotonic tensile test, we obtain:

$$p = |\varepsilon_p| \tag{4.13}$$

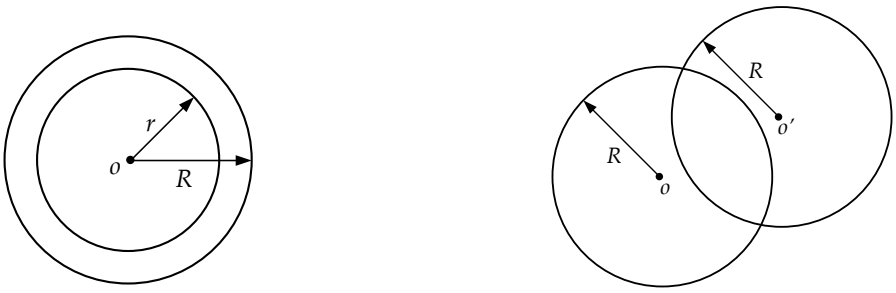

(A) Isotropic hardening (B) Kinematic hardening

FIGURE 4.2: Nature of hardening

which, in view of the plastic flow rule, gives

$$\dot{p} = \dot{\lambda} \tag{4.14}$$

Eqs. (4.11) and (4.14) define the hardening law of the material subjected to the monotonic loading. The classical theory includes two types of hardening: *isotropic* and *kinematic*. Isotropic hardening represents an uniform expansion of the yield surface, which is independent of the direction of plastic flow. Classical kinematic hardening, on the other hand, represents a translation of the locus of the yield surface in stress space, in the direction of flow. An illustration of the differences between isotropic and kinematic hardening in stress space can be seen in Fig. 4.2. In this figure, o represents the locus of the yield surface, r represents the radii, and R indicates an increment in hardening. The difference between isotropic and kinematic hardening is not evident until the loading path for the material is altered. For example, in cyclic loading from tension to compression, during the tension portion of the curve the stress-strain curve would appear identical. However, upon reverse loading into compression, the kinematic hardening material would yield at a smaller (in magnitude) loading level than the isotropic hardening material. A schematic of stress-strain behavior for isotropic and kinematic hardening, with linear hardening modulus H, can be seen in Fig. 4.3.

The multilinear isotropic hardening in the uniaxial case of loading is described by a piecewise total stress-strain curve that starts from the origin and has positive values of stress and strain (see Fig. 4.3d). Yielding in compression is considered to occur when the stress changes by twice the maximum stress reached in tension.

4.2.5 Tangent elasto-plastic modulus

The consistency condition enables us to solve explicitly for $\dot{\lambda}$ and relate stress rates to strain rates as follows. By taking the time derivative of the yield function and making use of

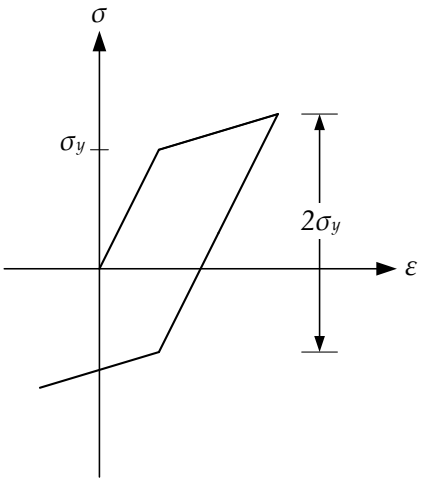

(A) Bilinear kinematic

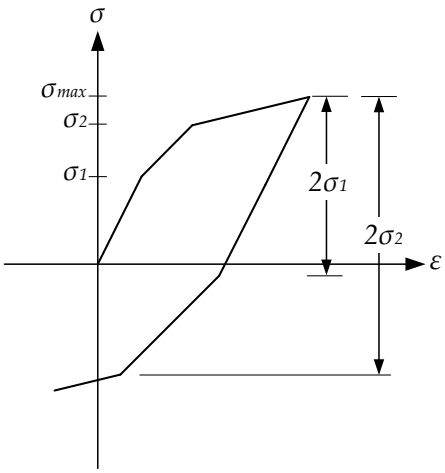

(B) Multilinear kinematic

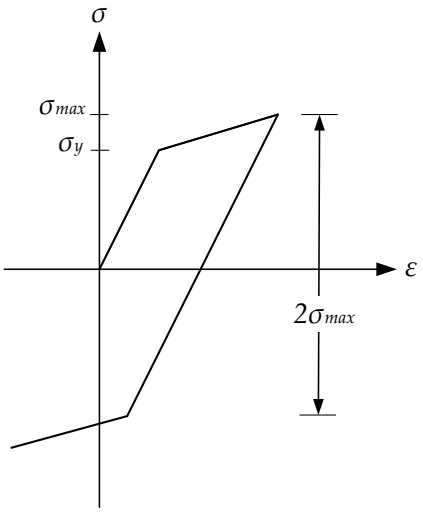

(C) Bilinear isotropic

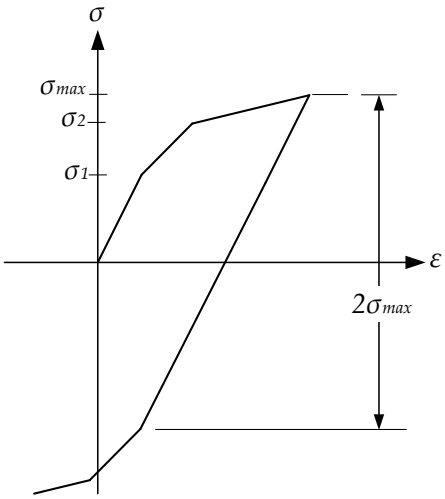

(D) Multilinear isotropic

FIGURE 4.3: Uniaxial stress-strain behavior of some of the plasticity options

Eqs. (4.8), (4.9) and (4.13), along with the elastic stress-strain relationship Eq. (4.1), we obtain:

$$\dot{f} = \frac{\partial f}{\partial \sigma}\dot{\sigma} + \frac{\partial f}{\partial p}\dot{p} \tag{4.15}$$

$$= \text{sign}(\sigma)E(\dot{\varepsilon} - \dot{\varepsilon}_p) - H\dot{\varepsilon}_p sign(\sigma) \tag{4.16}$$

$$= \text{sign}(\sigma)E\dot{\varepsilon} - \dot{\lambda}(E + H) \tag{4.17}$$

where H is called the hardening modulus, or hardening slope, and is defined as:

$$H = H(p) = \frac{d\sigma_y}{dp} \tag{4.18}$$

The consistency conditions is provided by Kuhn-Tucker condition. Thus, the consistency conditions of the elasto-plastic model are defined as follows:

$$f(\sigma,\sigma_y) \leq 0, \qquad \dot{\lambda} \geq 0, \qquad \dot{\lambda} f(\sigma,\sigma_y) = 0 \tag{4.19}$$

In addition to above conditions, $\lambda \geq 0$ satisfies the consistency requirement bolow:

$$\dot{\lambda}\dot{f}(\sigma,\sigma_y) = 0 \tag{4.20}$$

In classical literature, Eqs. (4.19) and (4.20) is also known as 'loading/unloading' and 'consistency' condition, respectively. This consistency condition implies that the rate of f vanishes when plastic yielding occurs.

The plastic multiplier, $\dot{\lambda}$, is uniquely determined during plastic yielding and can be expressed by:

$$\dot{\lambda} = \frac{E\dot{\varepsilon}}{H+E}\text{sign}(\sigma)$$

4.2.6 Steel stress-strain explicit 1D model

Armstrong Frederick 1D steel model [50] is a commonly used constitutive model to describe the mechanical behavior of steel under different loading conditions. This model assumes that steel behaves as an elasto-plastic material and is widely used.

The model consists of three parts: elastic behavior, yield behavior, and strain hardening behavior. During loading, the material will initially exhibit linear elastic behavior until it reaches the yield point, from which it begins to deform plastically. Once the material has yielded, its stress-strain behavior follows a nonlinear strain hardening curve. The rate at which the material hardens after yielding is determined by the hardening modulus, H_k.

When the material is unloaded, the stress decreases, but the material will not return to its original, undeformed state due to the plastic deformation that has occurred. Instead, the material follows a reloading path that is different from the original elastic path, see in Fig. 4.4.

The yield surface:

$$f = |\sigma - \chi| - \sigma_y \leq 0 \tag{4.21}$$

Taking into account of kinematic hardening in Armstrong-Frederick model, χ is represented as the back stress and σ_y is the yield stress.

The variation of back stress χ is shown in the Armstrong-Frederick model as follows:

$$\dot{\chi} = H_k\dot{\varepsilon}_p - H_{nl}\left|\dot{\varepsilon}_p\chi\right| \tag{4.22}$$

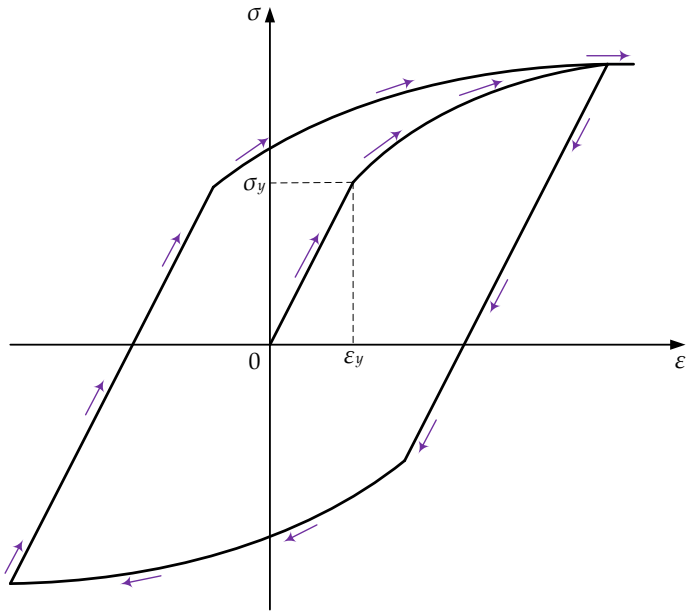

FIGURE 4.4: Armstrong-Frederick steel model [51].

Where H_k is the instant kinematic hardening parameter and H_{nl} is Armstrong-Frederick hardening parameter which plays a role as the nonlinear hardening parameter and represents the degree of nonlinearity in the strain hardening behavior after yielding.

4.2.7 Algorithm-Armstrong-Frederick steel model

The return mapping algorithm basically consists of two major steps: the formulation of the elastic trial stress σ_{trial}^{n+1}, also referred to as an elastic predictor, and the return mapping to the yield surface, which can be interpreted as a closest point projection of the trial stress onto the yield surface, also referred to as a plastic corrector. The algorithm for numerically integrating the one-dimensional kinematic hardening model with the yielding function: $f = |\sigma - \chi| - \sigma_y$ is presented in the following:

1. Given input at the time t^n: σ^n, ε^n, ε_p^n, p^n and E
2. Given variation of deformation $\Delta\varepsilon \Rightarrow \varepsilon^{n+1} = \varepsilon^n + \Delta\varepsilon$
3. Predictor (Trial state): compute elastic trial stress and test for inelastic loading

$$\sigma_{trail}^{n+1} = E\left(\varepsilon^{n+1} - \varepsilon_p^n\right)$$
$$R_{trail} = \sigma_y\left(p^n\right)$$
$$f_{trail}^{n+1} = \left|\sigma_{trail}^{n+1} - \chi^n\right| - R_{trial}$$

4. Evaluation the yield function at trial state

if $f_{trial}^{n+1} \leq 0$ **then**

$\varepsilon_p^{n+1} = \varepsilon_p^n$

$p^{n+1} = p^n$

$\sigma^{n+1} = \sigma^n$

$E_{tg}^{n+1} = E$

else

Go to step 5 for updating.

end

5. Corrector: by using the Kuhn-Tucker's conditions, compute $\Delta\lambda$ and then update the other variables:

$$\begin{aligned}
\Delta\lambda &= \Delta p = p^{n+1} - p^n \\
\varepsilon_p^{n+1} &= \varepsilon_p^n + \Delta\lambda \text{sign}(\sigma_{trail}^{n+1}) \\
\sigma^{n+1} &= \sigma_{trail}^{n+1} - E\Delta\lambda \text{sign}(\sigma_{trail}^{n+1}) \\
\chi^{n+1} &= \chi^n + \left(H_k \Delta\varepsilon_p - H_{nl} \left|\Delta\varepsilon_p\right|\right)
\end{aligned}$$

6. Compute the tangent modulus

$$E_{tg}^{n+1} = \left.\frac{\partial\sigma}{\partial\varepsilon}\right|^{n+1} = E\left(1 + \frac{E\text{sign}(\sigma^{n+1})}{(E + H_k)\text{sign}(\sigma^{n+1}) - H_{nl}\chi^{n+1}}\right)$$

4.3 Concrete constitutive law

The behavior of concrete is highly non-linear, and it is affected by several factors, including the properties of the material, the size and shape of the specimen, and the loading conditions. The concrete constitutive law is typically derived from experimental data obtained from tests on concrete specimens.

There are several types of concrete constitutive laws, each of which describes the behavior of concrete under different loading conditions, particularly in compression. Some of the most commonly used concrete constitutive laws include the linear elastic model, the nonlinear elastic model, the plasticity-based model, coupled plastic-damage model and damaged model, see Fig. 4.5.

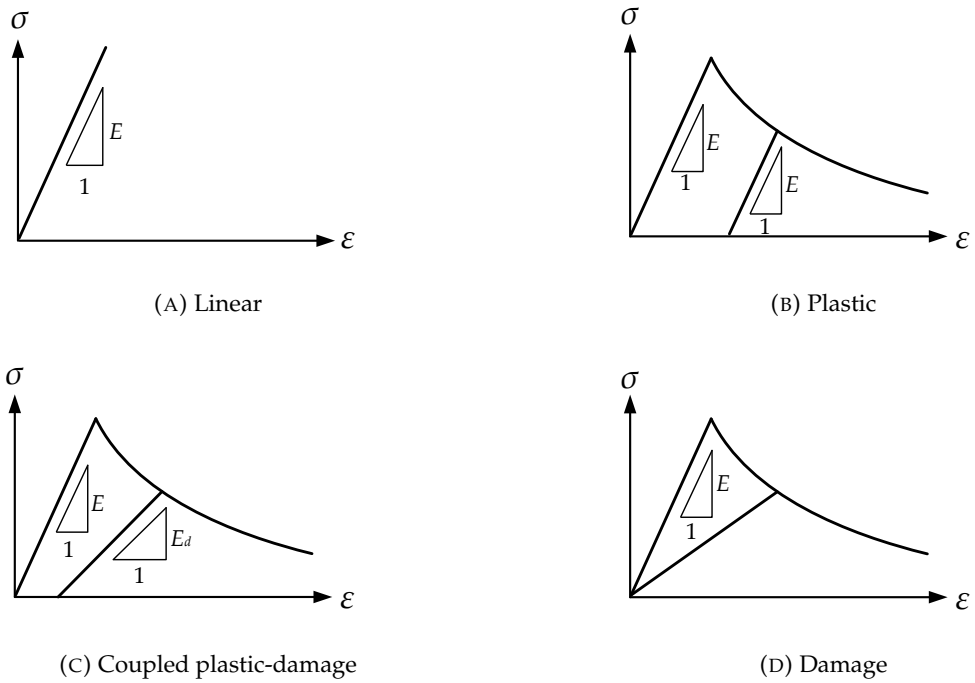

(A) Linear (B) Plastic

(C) Coupled plastic-damage (D) Damage

FIGURE 4.5: Uniaxial stress-strain behavior of constitutive model

4.3.1 Uniaxial compression of concrete material

Concrete is highly non-linear material in uniaxial compression, meaning that its response to increasing levels of compressive stress is not linearly proportional to the applied force.

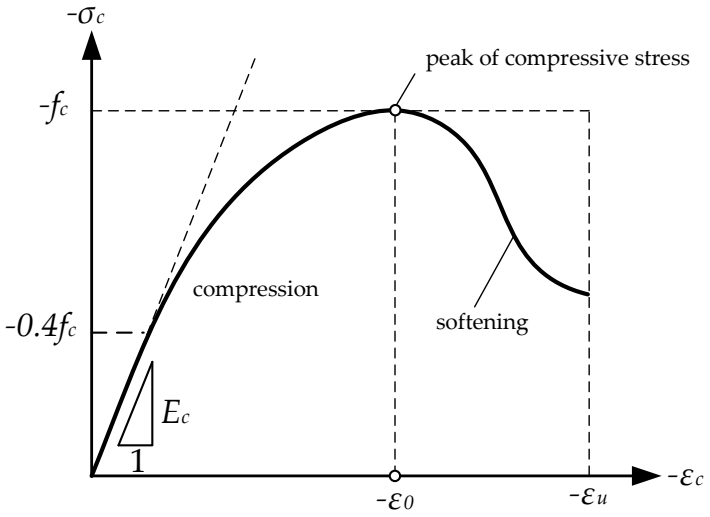

FIGURE 4.6: Uniaxial compression curve

Fig. 4.6 shows a typical uniaxial compression stress-strain curve. Concrete is a heterogeneous material, the shape and the peak of the stress-strain curve varies greatly and are dependent on the proportions and properties of the constituents, the size and shape of the

specimen, the rate of loading and also the age of concrete. In Fig. 4.6 the response of concrete may be taken to be linear-elastic up to 30% or 40% of the peak stress, f_c (often called the compressive strength of concrete).

4.3.2 Uniaxial tension of concrete

The uniaxial tension tests are important for understanding the behavior of concrete under tensile loading conditions, as well as for designing structures that can resist tensile forces. In practice, structures made of concrete are usually reinforced by steel bars to provide additional tensile strength.

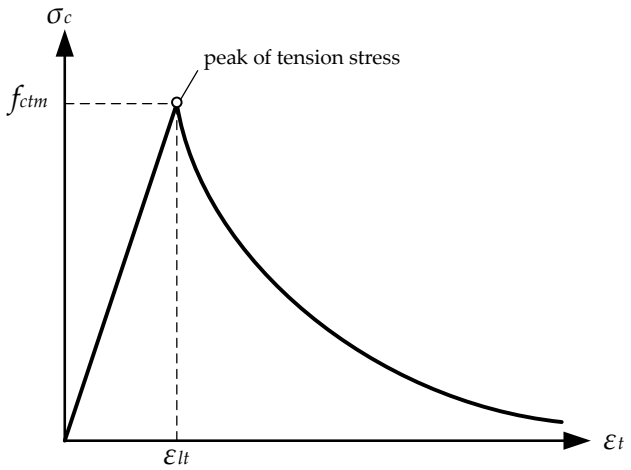

FIGURE 4.7: Uniaxial tension curve

The uniaxial stress-strain behavior of concrete in tension can be divided into two parts, see Fig. 4.7. The first part is a linear elastic behavior up to concrete tensile strength f_{ctm}. The second part corresponds to the phase where the crack is initiated and propagates in concrete material. This part is represented by a descending branch in the uniaxial tensile stress-strain diagram.

4.3.3 Concrete stress-strain explicit 1D model

In this section, we present a concrete model that can describe the concrete stress-strain relation under an arbitrary cyclic strain history. In particular, the model implemented in this study takes into account four important factors:

- the effect of concrete confinement on the monotonic envelope curve in compression.
- the successive degradation of stiffness of both unloading and reloading curves.
- the effect of tension stiffening.
- the hysteresis response under cyclic loading.

Compression

The monotonic envelope curve of concrete in compression used in this work follows the model of modified Kent and Park proposed by [52], see in Fig. 4.8, the monotonic concrete stress-strain relation in compression is described by three regions.

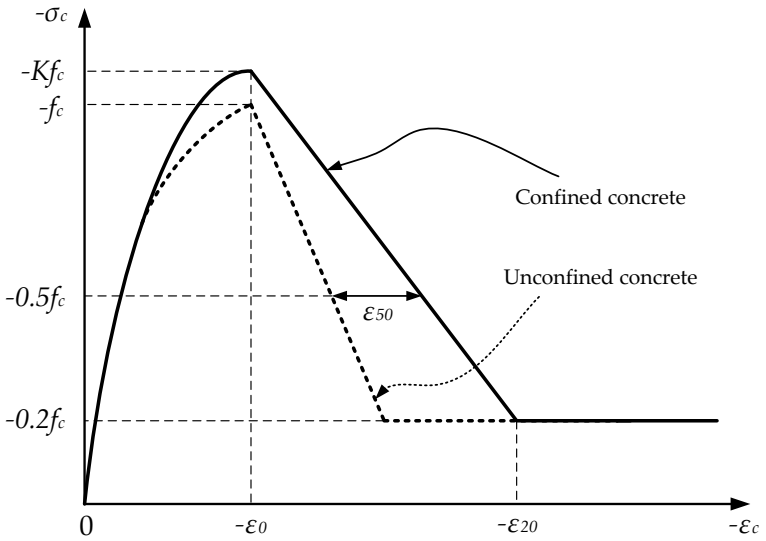

FIGURE 4.8: Modified Kent and Park model for confined and unconfinced concrete

- for $0 \leq \varepsilon_c \leq \varepsilon_0$

$$\sigma_c = Kf_c \left[2\left(\frac{\varepsilon_c}{\varepsilon_0}\right) - \left(\frac{\varepsilon_c}{\varepsilon_0}\right)^2 \right] \tag{4.23}$$

- for $\varepsilon_0 < \varepsilon_c \leq \varepsilon_{20}$

$$\sigma_c = Kf_c \left[1 - Z\left(\varepsilon_c - \varepsilon_0\right)\right] \tag{4.24}$$

- for $\varepsilon_c > \varepsilon_{20}$

$$\sigma_c = 0.2Kf_c \tag{4.25}$$

where ε_0 is the concrete strain at maximum stress (strain at peak stress), K is a factor which accounts for the strength increase due to confinement, Z is the strain softening slope, f_c is the concrete compressive cylinder strength in MPa, f_{yh} is the yield strength of stirrups in

MPa. For a low strain rate the coefficients K and Z are defined as:

$$K = 1 + \frac{\rho_s f_{yh}}{f_c} \tag{4.26}$$

$$Z = \frac{0.5}{\frac{3 + 0.29 f_c}{145 f_c - 1000} + 0.75 \rho_s \sqrt{\frac{h'}{s_h}} - 0.002K} \tag{4.27}$$

and for a high strain rate,

$$K = 1.25 \left[1 + \frac{\rho_s f_{yh}}{f_c} \right] \tag{4.28}$$

$$Z = \frac{0.625}{\varepsilon_{50c} - 0.002K} \tag{4.29}$$

where ρ_s is the ratio of volume of rectangular steel hoop to volume of concrete core measured to the outside of the peripheral hoop, h' the width of concrete core measured to the outside of the peripheral hoop, s_h the center to center spacing of hoop sets, f_{yh} the yield strength of the hoop reinforcement, ε_{50c} strain at $0.5 f_c$ on the falling branch of stress-strain curve for confined concrete, and f_c is the cylinder compressive strength in MPa.

For the unconfined concrete model, the same formulation of stress-strain will be applied with the factor $K = 1$.

Tension

In this section, we present the proposed tension stiffening model of concrete. A linear elastic behavior up to concrete tensile strength f_{ctm} is adopted. After the tensile strength is reached, the crack is initiated and the concrete tensile strength is dropped to $0.5 f_{ctm}$, see Fig. 4.9.

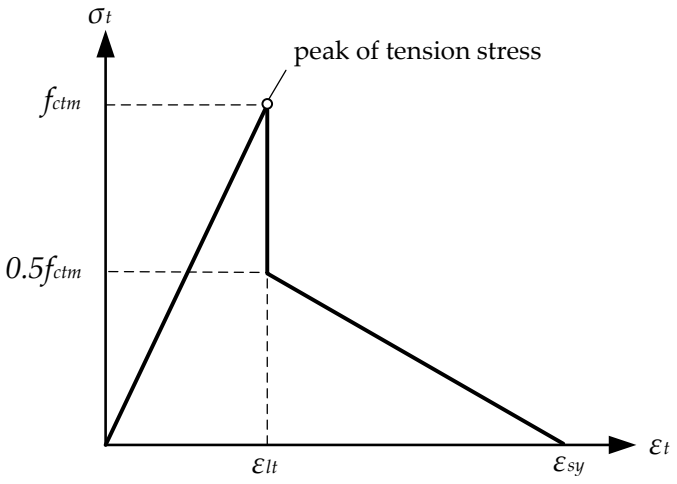

FIGURE 4.9: Proposed concrete model in tension

Beyond that, the concrete tensile strength decreases linearly to zero when the strain reaches the yield strain of the reinforcing rebar, ε_{sy}.

4.3.4 Governing equations of damaged plasticity theory

In this section, the theory of an anisotropic elasto-plastic damage 1D model for the plain concrete which incorporates both damage degradation and growth of inelastic strains is presented. It is based on a continuum formulation of damage degradation ([53], [54]). In analogy to classical plasticity, we assume that total strain ε is decomposed into an elastic part ε_e, a plastic part ε_p and a damage part ε_d:

$$\varepsilon = \varepsilon_e + \varepsilon_p + \varepsilon_d \tag{4.30}$$

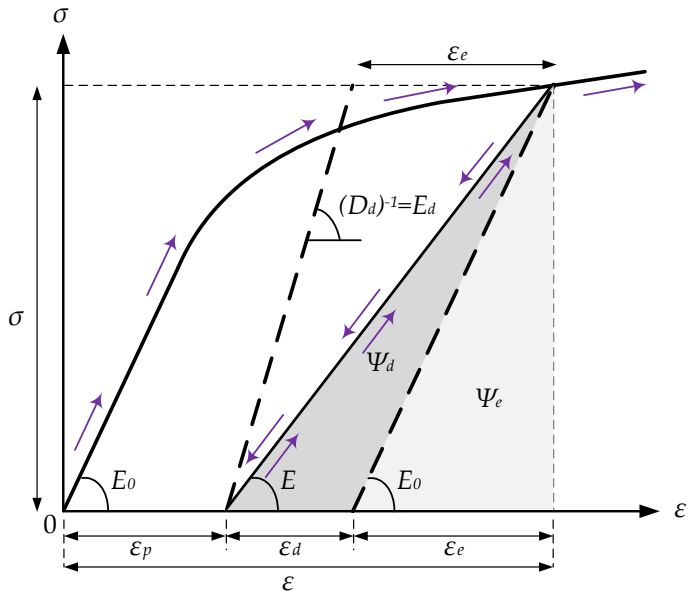

FIGURE 4.10: Stress-strain relation of a plastic damage behavior under uniaxial loading conditions

Fig. 4.10 represents the identity for the constitutive relationship under uniaxial loading condition for the damage mechanism. It shows that the damage strains ε_d can be recovered, and that the damage potential decreases when the tension is released. This is because the stored energy function takes into account the damage strains, just like it does for the elastic strain ε_e, but not for the plastic strains ε_p. The assumed decomposition Eq. (4.30) is commonly used in the context of elastoplastic theories, but are rarely considered in the context of damage models that usually employed a internal variable d to characterize the damage mechanisms. It corresponds to a decomposition of the deformation at a given point of the solid in elastic, plastic and damage mechanisms in series, referring to the usual convention in a generalized standard solid [55]. In accordance, there is a description about the decomposition of the

stored energy function, namely Helmholtz free energy, as:

$$\Psi = \Psi_e(\varepsilon_e) + \Psi_d(\varepsilon_d) + \Psi_p(p) \tag{4.31}$$

where:

- $\Psi_e(\varepsilon_e) = \frac{1}{2}E_0(\varepsilon_e)^2$ is free energy associated with elastic strains ε_e.
- $\Psi_d(\varepsilon_d) = \frac{1}{2}E_d(\varepsilon_d)^2$ is free energy associated with progressive degradation.
- $\Psi_p(p)$ is free energy associated with plastic strains.

Based on the diagram showns in Fig. 4.10, we can express the stress as:

$$\sigma = E_0\varepsilon_e = E_d\varepsilon_d = E\left(\varepsilon - \varepsilon_p\right) \tag{4.32}$$

By introducing Eq. (4.32) into Eq. (4.31), we obtain the new expression of Helmholtz free energy:

$$\Psi = \frac{1}{2}E_0(\varepsilon_e)^2 + \frac{1}{2}E_d(\varepsilon_d)^2 + \Psi_p(p) = \frac{1}{2}\left(D_0 + D_d\right)^{-1}\left(\varepsilon - \varepsilon_p\right)^2 + \Psi_p(p) \tag{4.33}$$

To ensure that the second principle of thermodynamics is satisfied, the local Clausius-Duhem's inequality requires that the reduced dissipation inequality holds

$$\Re = \sigma\dot{\varepsilon} - \dot{\Psi} = \left[\sigma - \frac{\partial\Psi}{\partial\left(\varepsilon - \varepsilon_p\right)}\right]\dot{\varepsilon} + \frac{\partial\Psi}{\partial\varepsilon_e}\dot{\varepsilon}_p - \frac{\partial\Psi}{\partial D_d}\dot{D}_d - \frac{\partial\Psi}{\partial p}\dot{p} \geq 0 \tag{4.34}$$

Since the inequality Eq. (4.34) must hold for any value of $\dot{\varepsilon}$, $\dot{\varepsilon}_p$, $\dot{D}_d$ and $\dot{p}$, the Coleman relations yield the constitutive expressions:

$$\sigma = \frac{\partial\Psi}{\partial\left(\varepsilon - \varepsilon_p\right)} = D^{-1}\left(\varepsilon - \varepsilon_p\right) \tag{4.35}$$

and the thermodynamic conjugate forces for plasticity and damage are:

$$R = \frac{\partial\Psi}{\partial p} = \frac{\partial\Psi_p}{\partial p} \tag{4.36}$$

$$\hat{Y} = \frac{\partial\Psi}{\partial D_d} = -\frac{1}{2}\sigma^2 \tag{4.37}$$

The Clausius-Duhem's inequality becomes:

$$\Re = \sigma\dot{\varepsilon}_p + \frac{1}{2}\sigma^2\dot{D}_d - R(p)\dot{p} \geq 0 \tag{4.38}$$

The interest is to introduce a coupling between plasticity and damage phenomena by introducing a single criterion that depends only on σ and R. In the absence of an explicit

criterion of $\hat{Y}$, it is able to overcome the presence of $\hat{Y}$ in the Clausius-Duhem's inequality. The reversibility convex domain C is defined in the space of thermodynamic force (σ, R). This convex domain is limited by the yield surface $f(\sigma, R) = 0$.

$$C := \{(\sigma, R) \mid f(\sigma, R) \leq 0\} \tag{4.39}$$

By assuming a normal evolution of internal variables. The flow rules of the internal variables ε_p, D_d and p are obtained from the principle of maximum dissipation Eq. (4.38):

$$\inf_{(\sigma,R)\in C} \left[-\dot{\Re}\right]$$

Hence, for giving the admissible state variables $(\sigma, R) \in C$, the rates $\dot{\varepsilon}_p$, $\dot{D}_d$ and $\dot{p}$ are those which yield a stationary point of the dissipation $\Re$. To find the solution of this constrained optimization problem, the method of Lagrange multipliers is used, introducing the Lagrangian function:

$$\sup_{\dot{\lambda}\geq 0} \inf_{(\sigma,R)\in C} \Im(\sigma, R, \dot{\lambda})$$

where,

$$\Im(\sigma, R, \dot{\lambda}) = -\Re + \dot{\lambda} f(\sigma, R) = -\sigma\dot{\varepsilon}_p - \frac{1}{2}\sigma^2 \dot{D}_d + R(p)\dot{p} + \dot{\lambda} f(\sigma, R) \tag{4.40}$$

and $\dot{\lambda} \geq 0$ is Lagrange multiplier. From the associated optimal conditions, we obtain:

$$\frac{\partial \Im}{\partial \sigma} = -\dot{\varepsilon}_p - \dot{D}_d \sigma + \dot{\lambda}\frac{\partial f}{\partial \sigma} = 0 \tag{4.41}$$

$$\frac{\partial \Im}{\partial R} = \dot{p} + \dot{\lambda}\frac{\partial f}{\partial R} = 0 \tag{4.42}$$

By defining a strain rate related to the degradation of the compliance as:

$$\dot{\varepsilon}_{da} = \dot{D}_d \sigma \tag{4.43}$$

It follows that

$$\dot{\varepsilon}_p + \dot{\varepsilon}_{da} = \dot{\lambda}\frac{\partial f}{\partial \sigma} \tag{4.44}$$

$$\dot{p} = -\dot{\lambda}\frac{\partial f}{\partial R} \tag{4.45}$$

Defining

$$\dot{\varepsilon}_{pd} = \dot{\varepsilon}_p + \dot{\varepsilon}_{da} \tag{4.46}$$

Making use Eq. (4.41), it can be rewritten in a form analogous to classical associative plasticity theory as

$$\dot{\varepsilon}_{pd} = \dot{\lambda}\frac{\partial f}{\partial \sigma} \tag{4.47}$$

Introducing a scalar parameter β with $0 \leq \beta \leq 1$, the plastic and the damage strains are given as:

$$\dot{\varepsilon}_p = (1-\beta)\dot{\lambda}\frac{\partial f}{\partial \sigma} \tag{4.48}$$

$$\dot{\varepsilon}_{da} = \beta\dot{\lambda}\frac{\partial f}{\partial \sigma} \tag{4.49}$$

The parameter β allows a simple partitioning of the effects associated with inelastic processes, resulting in an increase of inelastic strains and deterioration of the micro-structure and in an increase of the compliance moduli $D = D_0 + D^d$.

The lagrange multiplier $\dot{\lambda}$ is determined by the KUHN-TUCKER's relation:

$$\dot{\lambda} f(\sigma, R) = 0 \qquad \text{with} \qquad f(\sigma, R) \leq 0 \qquad \text{and} \qquad \dot{\lambda} \geq 0 \tag{4.50}$$

Thus, we obtain:

$$\dot{\lambda} = \frac{\dfrac{\partial f}{\partial \sigma}\varepsilon}{\left(\dfrac{\partial f}{\partial \sigma}\right)^2 + D\left(\dfrac{\partial f}{\partial R}\right)^2 \dfrac{\partial R}{\partial R}} \tag{4.51}$$

4.3.5 Concrete stress-strain explicit plastic-damaged model

The explicit concrete model proposed in Section 4.3.3 can be re-described by accounting the plastic-damaged behavior. Since the plastic and damage strain are included in the total strain, the total strain should be the sum of elastic, plastic and damage strain. By making use the integration of Eq. (4.43), the total strain is expressed by:

$$\varepsilon = \frac{\sigma}{E_0} + D_d\sigma + \varepsilon_p \tag{4.52}$$

For one-dimensional concrete stress-strain model, the yield surface can be expressed as:

$$f = |\sigma| - R \leq 0 \tag{4.53}$$

By making uses Eqs. (4.35), (4.48), (4.49) and (4.52), we obtain:

$$\varepsilon = \left(\frac{1}{E_0} + D_d\right)\sigma + \varepsilon_p \tag{4.54}$$

$$\dot{\varepsilon}_p = (1-\beta)\,\dot{\lambda}\,\mathrm{sign}(\sigma) \tag{4.55}$$

$$\dot{\varepsilon}_{da} = \dot{D}_d\sigma = \beta\dot{\lambda}\,\mathrm{sign}(\sigma) \tag{4.56}$$

$$\dot{p} = \dot{\varepsilon}_{pd}\,\mathrm{sign}(\sigma) = \dot{\lambda} \tag{4.57}$$

Replacing Eq. (4.55) and Eq. (4.56) to the derivation Eq. (4.54), one gets:

$$\dot{\varepsilon} = \frac{\dot{\sigma}}{E_0} + D_d\dot{\sigma} + \dot{\varepsilon}_{pd} \tag{4.58}$$

Assume that:

$$D_d\dot{\sigma} = \xi\dot{\varepsilon}_{pd} \tag{4.59}$$

where ξ is the constant scalar parameter. This parameter ξ will be determined by calibrating the numerical result with the experimental curve of the uni-axial compression test. Inserting Eq. (4.59) into Eq. (4.58), and making use of Eq. (4.57), we get:

$$\dot{\varepsilon} = \frac{\dot{\sigma}}{E_0} + (1+\xi)\,\dot{p}\,\text{sign}(\sigma) \tag{4.60}$$

or

$$\int_{\varepsilon_0}^{\varepsilon}\dot{\varepsilon} = \int_{\sigma_0(\varepsilon_0)}^{\sigma}\frac{\dot{\sigma}}{E_0} + (1+\xi)\,\text{sign}(\sigma)\int_{p_0}^{p}\dot{p} \tag{4.61}$$

- In case of compression, the yield surface is defined as:

$$f(\sigma_c, R_c) = -\sigma_c - R_c \leq 0 \tag{4.62}$$

where the index "c" indicates the compression criteria.

- Region 1: $0 \geq \varepsilon_c \geq \varepsilon_0$

$$\sigma_c = Kf_c\left[2\left(\frac{\varepsilon_c}{\varepsilon_0}\right) - \left(\frac{\varepsilon_c}{\varepsilon_0}\right)^2\right] \tag{4.63}$$

Internal variable: $0 \leq p_c \leq \dfrac{\sigma_c - E_0\varepsilon_0}{E\,(1+\xi)}$

$$R_c = -Kf_c\left[2\left(\frac{\varepsilon_c}{\varepsilon_0}\right) - \left(\frac{\varepsilon_c}{\varepsilon_0}\right)^2\right] \tag{4.64}$$

By replacing Eq. (4.61) to Eq. (4.64), we obtain:

$$\mathbb{A}R_c^2 + \mathbb{B}R_c + \mathbb{C} = 0 \tag{4.65}$$

where

$$\mathbb{A} = -\frac{Kf_c}{E_0\varepsilon_0^2}$$
$$\mathbb{B} = 1 - \frac{2Kf_c}{E_0\varepsilon_0} - \frac{2Kf_c p_c\,(1+\xi)}{E_0\varepsilon_0^2}$$
$$\mathbb{C} = -\frac{2Kf_c p_c\,(1+\xi)}{\varepsilon_0} - \frac{Kf_c p_c^2\,(1+\xi)^2}{\varepsilon_0^2}$$

Solve it by discriminant second order equation.

- Region 2: $\varepsilon_0 < \varepsilon_c \leq \varepsilon_{20}$

$$\sigma_c = Kf_c\,[1 - Z\,(\varepsilon_c - \varepsilon_0)] \leq 0.2Kf_c \tag{4.66}$$

Internal variable: $\dfrac{\sigma - E_0\varepsilon_{20}}{E_0\,(1+\xi)} \geq p_c > \dfrac{\sigma - E_0\varepsilon_0}{E_0\,(1+\xi)}$

$$R_c = -Kf_c\,[1 - Z\,(\varepsilon_c - \varepsilon_0)]$$
$$= -\frac{Kf_c\,[1 + Z\,(1+\xi)\,p_c - Z\varepsilon_0]}{1 + \dfrac{Kf_c Z}{E_0}} \leq 0.2Kf_c$$

- Region 3: $\varepsilon_c > \varepsilon_{20}$

$$\sigma_c = 0.2Kf_c \tag{4.67}$$

Internal variable: $p_c > \dfrac{\sigma - E_0\varepsilon_{20}}{E_0\,(1+\xi)}$

$$R_c = -0.2Kf_c \tag{4.68}$$

- In case of tension, the yield surface is defined as:

$$f(\sigma_t, R_t) = \sigma_t - R_t \leq 0 \tag{4.69}$$

where the index "t" indicates the tension criteria.

$$R_t = \sigma_t = \frac{0.5f_{ctm}\left(\varepsilon_{sy} - p_t\right)}{\varepsilon_{sy} - \varepsilon_{lt} + 0.5\dfrac{f_{ctm}}{E_0}} \tag{4.70}$$

4.3.6 Integration algorithm for plastic-damaged concrete model

This strategy involves an implicit approximation of the governing equations, leading to a nonlinear system of algebraic equations in the stresses and updated internal variables. For applications of an implicit backward Euler integration scheme on the generalized flow rule

yields the following return mapping algorithm:

$$\sigma_{trial}^{n+1} = \frac{1}{D^n}(\varepsilon^{n+1} - \varepsilon_p^n) \tag{4.71}$$

where, $D^n = \dfrac{1}{E_0} + D_d^n$

From Eq. (4.53), we are able to compute the trial yield surface as:

$$f_{trial}^{n+1} = \left|\sigma_{trial}^{n+1}\right| - R_{trial}^{n+1} \tag{4.72}$$

If the trial yield surface $f_{trial}^{n+1} \leq 0$, the stress takes place as the elastic predictor:

$$\sigma^{n+1} = \sigma_{trial}^{n+1}$$

Otherwise, we perform the return mapping algorithm. The consistent tangent operator can be determine as the following. We have:

$$D^{n+1}\sigma^{n+1} = \varepsilon^{n+1} - \varepsilon_p^{n+1} \tag{4.73}$$

Differentiating Eq. (4.73) and the incremental form of Eq. (4.55), we obtain:

$$dD^{n+1}\sigma^{n+1} + D^{n+1}d\sigma^{n+1} = d\varepsilon^{n+1} - d\varepsilon_p^{n+1} \tag{4.74}$$

and

$$d\varepsilon_p^{n+1} = d\varepsilon_p^n + d(\Delta\varepsilon_p^{n+1}) = (1-\beta)\Delta\dot{\lambda}\,\mathrm{sign}(\sigma_{trail}^{n+1}) \tag{4.75}$$

From Eq. (4.56), we have:

$$\sigma^{n+1}D_d^{n+1} = \sigma^{n+1}D_d^n + \beta\Delta\lambda\,\mathrm{sign}(\sigma_{trail}^{n+1}) \tag{4.76}$$

So,

$$d\sigma^{n+1}D_d^{n+1} + \sigma^{n+1}dD_d^{n+1} = d\sigma^{n+1}D_d^n + \beta\Delta\dot{\lambda}\,\mathrm{sign}(\sigma_{trail}^{n+1}) \tag{4.77}$$

Combining Eqs. (4.76) and (4.77) with Eq. (4.74), we get:

$$D^n d\sigma^{n+1} = d\varepsilon^{n+1} - \Delta\dot{\lambda}\,\mathrm{sign}(\sigma_{trail}^{n+1}) \tag{4.78}$$

Computing $d\dot{\lambda}$ by $df^{n+1} = 0$, we obtain

$$d\sigma^{n+1}\,\mathrm{sign}(\sigma_{trail}^{n+1}) - \left.\frac{\partial R}{\partial p}\right|^{n+1}\Delta\dot{\lambda} = 0 \tag{4.79}$$

Solving Eq. (4.79) for $\Delta\dot{\lambda}$ and replacing the result to Eq. (4.79), we obtain:

$$d\sigma^{n+1} = E_{tg}^{n+1}\,d\varepsilon^{n+1} \tag{4.80}$$

in which

$$E_{tg}^{n+1} = \frac{1}{D^n} - \frac{1}{D^n \left(1 + D^n \left.\frac{\partial R}{\partial p}\right|^{n+1}\right)} \tag{4.81}$$

is the consistent tangent operator.

Algorithm

In this study, the one-dimensional plastic damaged model developed by the constitutive relation Kent and Park described in Section 4.3.3 is used. The hardening-softening functions of this model are expressed as follows:

1. Given input at the time t^n: σ^n, ε^n, ε_p^n, p^n and D_d^n
2. Given variation of deformation $\Delta\varepsilon \Rightarrow \varepsilon^{n+1} = \varepsilon^n + \Delta\varepsilon$
3. Predictor (Trial state): compute elastic trial stress and test for inelastic loading

$$\sigma_{trail}^{n+1} = \frac{1}{D^n}\left(\varepsilon^{n+1} - \varepsilon_p^n\right)$$
$$R_{trail} = R\left(p^n\right)$$
$$f_{trail}^{n+1} = \left|\sigma_{trail}^{n+1}\right| - R_{trial}$$

4. Evaluation the yield function at trial state

if $f_{trial}^{n+1} \leq 0$ **then**

$\varepsilon_p^{n+1} = \varepsilon_p^n$

$p^{n+1} = p^n$

$D_d^{n+1} = D_d^n$

$\sigma^{n+1} = \sigma^n$

else

Go to step 5 for updating.

end

5. Corrector: by using the Kuhn-Tucker's conditions, compute $\Delta\lambda$ and then update the other variables:

$$\Delta\lambda = \Delta p = p^{n+1} - p^n$$
$$\varepsilon_p^{n+1} = \varepsilon_p^n + (1-\beta)\Delta\lambda \text{sign}(\sigma_{trail}^{n+1})$$
$$\sigma^{n+1} = \sigma_{trail}^{n+1} - \left(\frac{1}{E_0} + D_d^n\right)^{-1} \Delta\lambda \, \text{sign}(\sigma_{trail}^{n+1})$$
$$D_d^{n+1} = D_d^n + \Delta D_d = D_d^n + \beta\Delta\lambda \frac{\text{sign}(\sigma_{trail}^{n+1})}{\sigma^{n+1}}$$

6. Compute the tangent modulus

$$E_{tg}^{n+1} = \left.\frac{\partial\sigma}{\partial\varepsilon}\right|^{n+1} = \frac{1}{D^n} - \frac{1}{D^n + (D^n)^2 \left.\dfrac{\partial R}{\partial p}\right|^{n+1}}$$

4.4 Behavior of connector

Shear stud connectors are widely used in steel-concrete composite structures to resist shear and tensile loads at the steel-concrete interface. In the literature, extensive researches [56, 57, 58, 59, 60, 61, 62, 63, 64, 65, 66] have been conducted to study the behavior of connectors under static and/or fatigue loading. Most of the research works are focused on the shear response of the stud connector. The stud connectors under combined tension and shear have received more attention in the last decades due to the increase of using composite constructions. In this section, the behavior of stud connector under shear loading, tension loading and combination of both are presented.

4.4.1 Shear behavior of connector

The primary function of the shear behavior of connectors in composite beams is to transfer shear forces between the concrete slab and the steel beam, and to resist slip at the interface. The shear behavior of connectors is usually characterized by push-out test, see the represented configuration in Fig. 4.11, though which the shear strength, the shear stiffness as well as load-slip relationship can be evaluated.

Shear strength

The shear behavior of connectors, such as headed studs or welded shear connectors, depends on the cross-sectional area of the stud shank and the ultimate strength of the stud material. The larger the cross-sectional area of the stud shank, the greater the shear capacity of the connector. Additionally, connectors made of materials with higher ultimate strengths

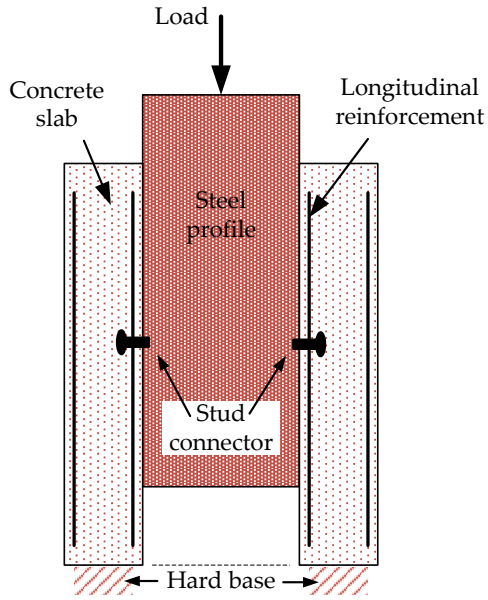

FIGURE 4.11: Details of represented push-out test

can withstand higher shear forces. These factors are to be considered when selecting connectors that are capable of transferring the necessary shear forces without failure.

Some existing shear strength formulations for a shear stud connector are evaluated herein [67, 68, 69]:

$$D_{u,Kim} = 0.725 A_{sc} f_u \tag{4.82}$$

$$D_{u,EC4} = \min\left(0.29\alpha d^2\sqrt{E_{cm} f_c}, 0.8\pi d^2 f_u/4\right) \tag{4.83}$$

$$D_{u,AASHTOLRFD} = 0.5 A_{sc}\sqrt{E_{cm} f_c} \leq A_{sc} f_u \tag{4.84}$$

where

- d the stud shank diameter [mm],
- A_{sc} is the cross area of the stud shank [mm^2],
- f_c is the concrete compressive strength [MPa],
- E_{cm} is the Young's modulus of concrete [MPa],
- f_u is the ultimate strength of the stud material [MPa].

Load-slip relationship

Experimental tests [58, 60] show that the load-slip relationship of stud connector is nearly linear up to 50% of the maximum load. Based on the test results, several load-slip relationships have been proposed. The exponential [57] and fractional [70] load-slip relation are

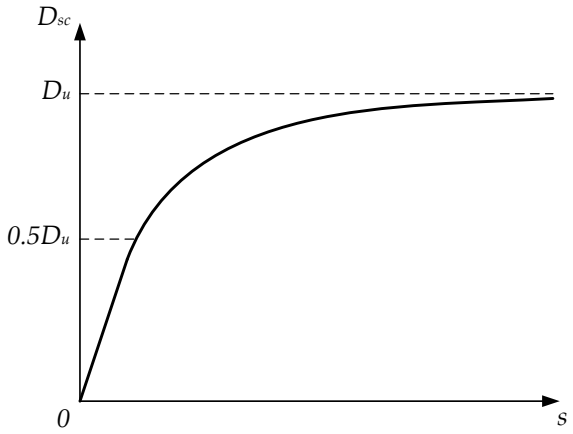

FIGURE 4.12: Load-slip relationship represented in Eq. (4.85)

widely used to simulate behavior of headed studs under pure shear loading:

$$\frac{D_{sc}}{D_u} = \left(1 - e^{-0.71s}\right)^{0.4} \tag{4.85}$$

$$\frac{D_{sc}}{D_u} = \frac{3.15s}{1 + 3.15s} \tag{4.86}$$

The shear force in studs is usually not greater than half of the maximum load under serviceability limit states. Hence, the shear stiffness (horizontal spring stiffness), k_h, is defined as the secant modulus at the point where the applied load is half of the maximum load for the lying studs in this study. The load-slip curves presented in Eqs. (4.85) and (4.86) have a similar configuration, where the curve is nearly linear up to 50% of the maximum load, as shown in Fig. 4.12.

Shear stiffness of connector

The initial shear stiffness of the shear stud connector, k_h, proposed by [58] is defined as the mean stiffness at the applied load of a half shear strength, i.e. $0.5D_u$ and is expressed by:

$$k_h = \frac{D_u}{d\,(0.16 - 0.0017 f_c)} \tag{4.87}$$

where d represents the diameter of studs and f_c is the mean compressive strength of concrete. In Eq. (4.87), the constant 0.16 should be substituted by 0.08 and 0.24 for the upper and lower characteristic stiffness, respectively. This means that there is a large variation in the shear stiffness because the measure of slips at that region are typically very small values.

4.4.2 Tensile behavior of connector

The tensile behavior of connectors plays a critical role in capturing of gaps or separations between the concrete slab and the steel beam. The pull-out test is commonly used to evaluate the uplift or tensile strength of the concrete slab-steel beam connection, see in **??**. This test determines the maximum force required to pull the steel beam out of the concrete slab and provides important information about the integrity of the connection between the two materials.

Tensile strength

The pull-out strength, also known as the tensile strength, of a stud connector represents the maximum amount of force that can be applied to the connector before it fails. It measures the connector's resistance to pull away from the anchored material. It is determined by various factors, including the material, properties and dimensions of the connector, and the method of installation [71]. For instance, steel connectors typically have higher tensile strength than plastic connectors due to their high-strength material.

It is important to choose a connector with a tensile strength that is appropriate for the specific application, to ensure that the connector provides adequate support and resistance to failure. According to [71], the pull-out failure of a shear stud connector is avoid if $d_h < 1.71d$:

$$V_{u,kips} = \Psi_{c,P} 8 A_{brg,inches^2} f_{c,ksi} \quad \text{for pull out strength (5\% fractile)} \tag{4.88}$$

$$V_{u,kips} = 13 A_{brg,inches^2} f_{c,ksi} \quad \text{for pull out strength (Average)} \tag{4.89}$$

where: $A_{brg,inches^2} = \frac{\pi}{4}(d^2_{h,inches} - d^2_{inches})$ and $\Psi_{c,P} = 1.4$

The units of forces, length and strength are in kip, inches and ksi, respectively.

Tensile stiffness of stud connector

The tensile stiffness expression for headed studs under tension proposed by Yang, Liu, and Liang [72] is shown in Eq. (4.90), in which $n = Es/Ec$. It can be seen that the tensile stiffness of headed studs k_v under tension is related to its effective embedded height h_{ef}, the elastic modulus of the stud E_s, the area of the stud A_s and the elastic modulus E_c of the concrete block.

$$k_v = \frac{E_s A_s h_{ef}}{h^2_{ef} + 11.5 n A_s} \tag{4.90}$$

Accordingly, in the prediction of the tensile stiffness for headed stud connectors, the bond force and the friction force are not taken into consideration. Thus, the tensile stiffness of headed studs under tension depends only on the elastic extension of the stud rod and the vertical displacement of the stud head in concrete block.

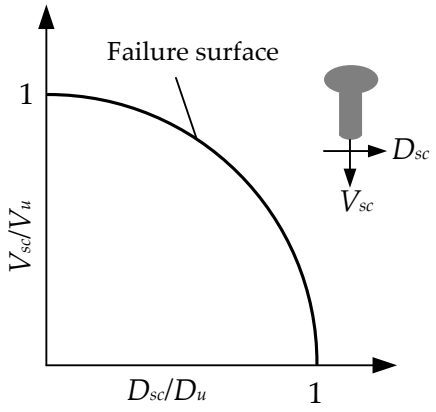

FIGURE 4.13: Interacted-forces in stud connector proposed by [65]

4.4.3 Coupled connector model

Several research works [64, 66, 65, 73] have been conducted to study the behavior of shear stud connector under combined tensile and shear loading. McMACKIN [64] and Takami, Nishi, and Hamada [65] respectively proposed an elliptical interaction relation under the form of Eq. (4.91) and a circular interaction curve Eq. (4.93). According to these interaction curves if the headed stud is subjected to combine shear and tension, no matter how small the shear and tension force is, the interaction effect should be considered. On the contrary, the tri-linear interaction under the formulation Eq. (4.92) developed by [66] suggests that if applied shear or tension force under combined loading is less than 20 % of the ultimate strength under shear or tension, the interaction effect can be neglected.

$$\left(\frac{D_{sc}}{D_u}\right)^{5/3} + \left(\frac{V_{sc}}{V_u}\right)^{5/3} \leq 1 \tag{4.91}$$

$$\left(\frac{D_{sc}}{D_u}\right) + \left(\frac{V_{sc}}{V_u}\right) \leq 1.2 \tag{4.92}$$

$$\left(\frac{D_{sc}}{D_u}\right)^{2} + \left(\frac{V_{sc}}{V_u}\right)^{2} \leq 1 \tag{4.93}$$

Moreover, in order to consider the influences of tension force and peak slip, a non-dimensional Eq. (4.94) for predicting the non-dimensional load-slip relationship is proposed by Lin, Liu, and He [73]. α_T is the coefficient which reflects the influence of applied tension force.

$$\frac{D_{sc}}{D_u} = \left[1.5(s/s_p)^{0.2} - 0.5(s/s_p)^{0.45}\right]^{\alpha_T} \tag{4.94}$$

where $\alpha_T = \frac{2}{3} + \frac{5}{3}\frac{V_{sc}}{V_u}$.

To get the dimensional load-slip curve, the calculation of peak slip s_p is critical and calculated by:

$$s_p = (0.389 - 0.0023 f_c)\, d_s$$

in which f_c is the cylinder compressive strength of concrete and d_s is the diameter of the shank of the headed stud. At this stage, the relationship between shear force and slip is not purely determined by their relation, but is also influenced by the tension force in the connector, as indicated by the coefficient α_T which characterizes the performance of the connector in terms of the interaction between forces.

In this thesis, by making use the load-slip relation and the interaction relation between shear and uplift force proposed by [65], the tangent operator of the connection can be derived. This section provides algorithm in determining the tangent operator of a stud connector in which the uplift/penetration phenomena is taken into account.

Tangent operator consistent for stud connector

In this study, we denote that the yield function is expressed by:

$$f(F, R) = F(d, d_p) - R \tag{4.95}$$

with $F = [D_{sc},\, V_{sc}]^{\mathrm{T}}$ is the force vector; $d = [s,\, g]^{\mathrm{T}}$ the displacement vector (strain-like); and $d_p = [s_p,\, g_p]^{\mathrm{T}}$ is the plastic displacement vector (plastic strain-like).

The elastic stiffness: $K = \begin{bmatrix} k_h & 0 \\ 0 & k_v \end{bmatrix}$.

The elastic stress-strain relationship and the discrete flow rule:

$$F^{n+1} = F_{trial} - K\Delta\lambda \left.\frac{\partial f}{\partial F}\right|^{n} \tag{4.96}$$

$$d_p^{n+1} = d_p^n + \Delta\lambda \left.\frac{\partial f}{\partial F}\right|^{n} \tag{4.97}$$

and

$$F^{n+1} = K\left(d^{n+1} - d_p^{n+1}\right) \tag{4.98}$$

Differentiation of the elastic stress-strain relationship Eq. (4.98):

$$\Delta F^{n+1} = K\left(\Delta d^{n+1} - \Delta d_p^{n+1}\right) \tag{4.99}$$

The variation of flow rule:

$$\Delta d_p^{n+1} = \Delta d_p^n + \Delta(\Delta d_p^{n+1}) = \Delta\dot{\lambda} \left.\frac{\partial f}{\partial F}\right|^{n+1} + \Delta\lambda \frac{\partial}{\partial F}\left(\frac{\partial f}{\partial F}\right)\Bigg|^{n+1}$$

The yield surface of the behavior of the connector, as represented by Eq. (4.93), is depicted in terms of its first and second variations as follows:

$$\left.\frac{\partial f}{\partial F}\right|^{n+1} = \dot{F} = \begin{Bmatrix} 2D_{sc}/D_u^2 \\ 2V_{sc}/V_u^2 \end{Bmatrix}^{n+1}$$

$$\left.\frac{\partial}{\partial F}\left(\frac{\partial f}{\partial F}\right)\right|^{n+1} = \ddot{F} = \begin{bmatrix} 2/D_u^2 & 0 \\ 0 & 2/V_u^2 \end{bmatrix}$$

Thus

$$\Delta F^{n+1} = K\left(\Delta d^{n+1} - \Delta\dot{\lambda}\dot{F}^{n+1} - \Delta\lambda\ddot{F}^{n+1}\Delta F^{n+1}\right) \tag{4.100}$$

$$\Delta F^{n+1}\left(\mathbb{I} + K\Delta\lambda\ddot{F}^{n+1}\right) = K\left(\Delta d^{n+1} - \Delta\dot{\lambda}\dot{F}^{n+1}\right) \tag{4.101}$$

$$\Delta F^{n+1} = \mathbb{C}\left(\Delta d^{n+1} - \Delta\dot{\lambda}\dot{F}^{n+1}\right) \tag{4.102}$$

where

$$\mathbb{C}^{n+1} = \left(\mathbb{I} + \Delta\lambda K\ddot{F}^{n+1}\right)^{-1} K$$

Find $\Delta\dot{\lambda}$ by $\Delta f^{n+1} = 0$,

$$\Delta f^{n+1} = \Delta f^{n+1}(F,p) = \dot{F}^{n+1}\Delta F^{n+1} - \left.\frac{\partial R}{\partial p}\right|^{n+1}\Delta\lambda = 0 \tag{4.103}$$

Making use of Eq. (4.102) and replacing the results in Eq. (4.103), once gets:

$$\Delta\dot{\lambda} = \frac{(\dot{F}^{n+1})^T\mathbb{C}^{n+1}\Delta d^{n+1} - \left.\frac{\partial R}{\partial p}\right|^{n+1}\Delta\lambda}{(\dot{F}^{n+1})^T\mathbb{C}^{n+1}\dot{F}^{n+1}} \tag{4.104}$$

Replacing back Eq. (4.104) to Eq. (4.102), we obtain:

$$\Delta F^{n+1} = \left(\mathbb{C}^{n+1} - \frac{\mathbb{C}^{n+1}\dot{F}_{n+1}\otimes(\dot{F}^{n+1})^T\mathbb{C}^{n+1}}{(\dot{F}^{n+1})^T\mathbb{C}^{n+1}\dot{F}^{n+1}}\right)\Delta d^{n+1} + \frac{\mathbb{C}^{n+1}\left.\frac{\partial R}{\partial p}\right|^{n+1}\Delta\lambda\dot{F}^{n+1}}{(\dot{F}^{n+1})^T\mathbb{C}^{n+1}\dot{F}^{n+1}} \tag{4.105}$$

By making use of Eq. (4.99), we are also to express

$$\Delta\lambda\dot{F}^{n+1} = \Delta d^{n+1} - K^{-1}\dot{F}^{n+1} \tag{4.106}$$

Using Eq. (4.106) turn back to replace into Eq. (4.105), we get

$$\Delta F^{n+1} = \mathbf{K}_{sc}^{n+1}\Delta d^{n+1} \tag{4.107}$$

where,

$$\mathbf{K}_{sc}^{n+1} = \left(\mathbb{I} + \frac{\mathbb{C}^{n+1} \left. \frac{\partial R}{\partial p} \right|^{n+1} K^{-1}}{(\dot{F}^{n+1})^T \mathbb{C}^{n+1} \dot{F}^{n+1}} \right)^{-1} \left(\mathbb{D}^{n+1} + \frac{\mathbb{C}^{n+1} \left. \frac{\partial R}{\partial p} \right|^{n+1}}{(\dot{F}^{n+1})^T \mathbb{C}^{n+1} \dot{F}^{n+1}} \right) \tag{4.108}$$

$$\mathbb{D}^{n+1} = \mathbb{C}^{n+1} - \frac{\mathbb{C}^{n+1} \dot{F}_{n+1} \otimes (\dot{F}^{n+1})^T \mathbb{C}^{n+1}}{(\dot{F}^{n+1})^T \mathbb{C}^{n+1} \dot{F}^{n+1}} \tag{4.109}$$

Algorithm

At this stage, the algorithm of numerical modeling the behavior of interaction between forces in connector performs in two cases separately (the case of uplift and penetration). Making uses the load-slip relation in Eq. (4.85) and Eq. (4.93), including the connector properties which was shown in Eqs. (4.82), (4.87), (4.88) and (4.90) provided the algorithm following plasticity of connector as below:

1. Given input at the time t_n: s^n, g^n, s_p^n, g_p^n and p^n and the connector properties k_h, k_v, D_u and V_u.

2. Given the variation of deformation

$$\Delta s \Rightarrow s^{n+1} = s^n + \Delta s$$
$$\Delta g \Rightarrow g^{n+1} = g^n + \Delta g$$

- **Uplift case**: $g \geq 0$

3. Predictor (Trial state): compute elastic trial slip, gap and trail function by assuming no gap for this trail state:

$$D_{trial}^{n+1} = k_h \left(s^{n+1} - s_p^n \right)$$
$$V_{trial}^{n+1} = k_v \left(g^{n+1} - g_p^n \right)$$
$$f_{trial}^{n+1} = \left(\frac{D_{trial}^{n+1}}{D_u} \right)^2 + \left(\frac{V_{trial}^{n+1}}{V_u} \right)^2 - R_{trial}^{n+1}$$

4. Evaluation the yield function at trial state

5. Corrector: by using the Kuhn-Tucker's conditions, compute $\Delta\lambda$ and then update the other variables:

if $f_{trial}^{n+1} \leq 0$ **then**

$D_{sc}^{n+1} = D_{trial}^{n+1}$

$V_{sc}^{n+1} = V_{trial}^{n+1}$

$s_p^{n+1} = s_p^n$

$g_p^{n+1} = g_p^n$

$p^{n+1} = p^n$

Tangent operator: $\mathbf{K}_{sc}^{n+1} = \begin{bmatrix} k_h & 0 \\ 0 & k_v \end{bmatrix}$

else

Go to step 5 for updating.

end

$$\Delta\lambda = \Delta p = p^{n+1} - p^n$$

$$D_{sc}^{n+1} = D_{trial}^{n+1} - k_h \Delta\lambda \left.\frac{\partial f}{\partial D_{sc}}\right|^n$$

$$V_{sc}^{n+1} = V_{trial}^{n+1} - k_v \Delta\lambda \left.\frac{\partial f}{\partial V_{sc}}\right|^n$$

$$s_p^{n+1} = s_p^n + \Delta\lambda \left.\frac{\partial f}{\partial D_{sc}}\right|^n$$

$$g_p^{n+1} = g_p^n + \Delta\lambda \left.\frac{\partial f}{\partial V_{sc}}\right|^n$$

6. Compute the tangent modulus following Eq. (4.108):

$$\mathbf{K}_{sc}^{n+1} = \left.\frac{\partial F}{\partial d}\right|_{n+1} = \left(\mathbb{I} + \frac{\mathbb{C}^{n+1} \left.\frac{\partial R}{\partial p}\right|^{n+1} K^{-1}}{(\dot{F}^{n+1})^T \mathbb{C}^{n+1} \dot{F}^{n+1}} \right)^{-1} \left(\mathbb{D}^{n+1} + \frac{\mathbb{C}^{n+1} \left.\frac{\partial R}{\partial p}\right|^{n+1}}{(\dot{F}^{n+1})^T \mathbb{C}^{n+1} \dot{F}^{n+1}} \right)$$

- **Penetration case**: $g < 0$

3. Predictor (Trial state): compute elastic trial bond force, the trail function by assuming new expression as:

$$D_{trial}^{n+1} = k_h \left(s^{n+1} - s_p^n \right)$$
$$f_{trial}^{n+1} = \left| \frac{D_{trial}^{n+1}}{D_u} \right| - R_{trial}^{n+1}$$

4. Evaluation the yield function at trial state

if $f_{trial}^{n+1} \leq 0$ **then**

$D_{sc}^{n+1} = D_{trial}^{n+1}$

$V_{sc}^{n+1} = k_v g^n$

$s_p^{n+1} = s_p^n$

$g_p^{n+1} = g_p^n$

$p^{n+1} = p^n$

Tangent operator: $\mathbf{K}_{sc}^{n+1} = \begin{bmatrix} k_h & 0 \\ 0 & k_v \end{bmatrix}$

else

Go to step 5 for updating.

end

5. Corrector: by using the Kuhn-Tucker's conditions, compute $\Delta\lambda$ and then update the other variables:

$$\Delta\lambda = \Delta p = p^{n+1} - p^n$$
$$D_{sc}^{n+1} = D_{trial}^{n+1} - k_h \Delta\lambda \left. \frac{\partial f}{\partial D_{sc}} \right|^n$$
$$V_{sc}^{n+1} = k_v g^n$$
$$s_p^{n+1} = s_p^n + \Delta\lambda \left. \frac{\partial f}{\partial D_{sc}} \right|^n$$
$$g_p^{n+1} = g_p^n$$

6. Compute the tangent modulus following Eq. (4.108):

$$\mathbb{K}_h^{n+1} = \frac{\left.\frac{\partial R}{\partial p}\right|^{n+1} D_u^2 k_h}{\left.\frac{\partial R}{\partial p}\right|^{n+1} D_u^2 + k_h}$$

and,

$$\mathbf{K}_{sc}^{n+1} = \begin{bmatrix} \mathbb{K}_h^{n+1} & 0 \\ 0 & k_v \end{bmatrix}$$

4.4.4 Uncoupled connector model

The shear and tensile strength, denoted as D_u and V_u, as well as the shear and tensile stiffness of the connector, denoted as k_h and k_v, are used to study the behavior of the uncoupled model of the connector in this section. This stage, we will separately show the corresponding yield functions for the shear and tensile behavior of the connector using the following functions:

$$\left|\frac{D_{sc}}{D_u}\right| \leq 1 \qquad \text{for shear behavior of connector} \tag{4.110}$$

$$\left|\frac{V_{sc}}{V_u}\right| \leq 1 \qquad \text{for tensile behavior of connector} \tag{4.111}$$

Algorithm

The algorithm for the uncoupled connector model is activated only in the case of uplift ($g \geq 0$). For the penetrated case ($g < 0$), the algorithm will follow the one described in Section 4.4.3. In this process, we will firstly derive the tangent modulus in shear, tensile behavior, respectively. Next, the combination of shear and tensile tangent modulus is used to determine the one for the uncoupled model connector.

1. Given input at the time t_n: s^n, s_p^n, and p_s^n and the connector properties k_h and D_u.
2. Given the variation of deformation

$$\Delta s \Rightarrow s^{n+1} = s^n + \Delta s$$

3. Predictor (Trial state): compute elastic trial slip and trail function:

$$D_{trial}^{n+1} = k_h \left(s^{n+1} - s_p^n\right)$$

$$f_{trial}^{n+1} = \left|\frac{D_{trial}^{n+1}}{D_u}\right| - R_{trial}^{n+1}$$

4. Evaluation the yield function at trial state

if $f_{trial}^{n+1} \leq 0$ **then**

$D_{sc}^{n+1} = D_{trial}^{n+1}$

$s_p^{n+1} = s_p^n$

$p_s^{n+1} = p^n$

Tangent operator: $K_{sc,h}^{n+1} = k_h$

else

Go to step 5 for updating.

end

5. Corrector: by using the Kuhn-Tucker's conditions, compute $\Delta\lambda$ and then update the other variables:

$$\Delta\lambda = \Delta p = p^{n+1} - p^n$$
$$D_{sc}^{n+1} = D_{trial}^{n+1} - k_h \Delta\lambda \left.\frac{\partial f}{\partial D_{sc}}\right|^n$$
$$s_p^{n+1} = s_p^n + \Delta\lambda \left.\frac{\partial f}{\partial D_{sc}}\right|^n$$

6. Compute the tangent modulus following Eq. (4.108):

$$K_{sc,h}^{n+1} = \frac{\left.\frac{\partial R}{\partial p}\right|^{n+1} D_u^2 k_h}{\left.\frac{\partial R}{\partial p}\right|^{n+1} D_u^2 + k_h} \tag{4.112}$$

7. Analogously to the shear behavior process, the computation is performed for the tensile part of connector by redoing steps 1 to 5, providing inputs at time t_n such as g^n, g_p^n, p_g^n, and the connector properties k_v and V_u. This step aims to update $\Delta\lambda$, V_{sc}^{n+1} and g_p^{n+1} for tensile behavior the connector.

8. Compute the tangent modulus following Eq. (4.108):

$$K_{sc,v}^{n+1} = \frac{\left.\frac{\partial R}{\partial p}\right|^{n+1} V_u^2 k_v}{\left.\frac{\partial R}{\partial p}\right|^{n+1} V_u^2 + k_v} \tag{4.113}$$

9. The combination of Eqs. (4.112) and (4.113) is used to build the tangent modulus for the uncoupled model of the connector, which is depicted below:

$$\mathbf{K}_{sc}^{n+1} = \begin{bmatrix} K_{sc,h}^{n+1} & 0 \\ 0 & K_{sc,v}^{n+1} \end{bmatrix} \tag{4.114}$$

4.5 Conclusion

This chapter provides comprehensive knowledge focused on the nonlinear behavior of materials. The behavior of materials is often described using uniaxial stress-strain relationships, also known as constitutive laws. In this chapter, bi-linear, multi linear isotropic and kinematic hardening models are presented for steel materials. The Armstrong-Frederick kinematic hardening model is also employed for the steel material, while the plastic-damage model of Kent and Park [52], is adopted for the concrete material. For the connector model, the load-slip relationships are presented, and the coupled behavior of the connection in shear and tension is considered using the curve reported in Takami, Nishi, and Hamada [65]. The tangent operator of each material is also provided with the return-mapping algorithm in each case, which is essential for studying nonlinear finite element analysis in Chapter 5.

Chapter 5

Nonlinear finite element analysis of composite beams

5.1 Introduction

In Chapter 2, an analytical solution of a composite beam subjected to any loading within the elastic range using both the continuous and discrete models of connection was presented. If the material behavior becomes nonlinear, it is necessary to solve the system of equations incrementally and iteratively. To do this, some approximations have to be made and the finite element method based on the so-called "displacement-based formulation" is commonly adopted. The displacement-based (DB) method is based on the interpolation functions of the displacement fields. However, due to this interpolation method, it can lead to curvature locking issues when the shear connection stiffness is high and the continuous connection model is used. Consequently, it may limit its applicability. To overcome these problems, one solution is to use the discrete connection model although this approach requires a higher number of degrees of freedom (more number of elements). Another solution is to adopt the force-based or mixed formulations, which have been shown to be beneficial for highly nonlinear problems.

The nonlinear finite element formulation involves the division of the solution domain into discrete elements, in which each element has its own set of governing differential equations. These equations are then linearized to obtain the element stiffness matrix and the resisting load vector. The stiffness matrix and the load vector for the entire structure are obtained by assembling the element contributions. The resulting system of equations is solved using an iterative solution strategy, typically of the Newton-Raphson type, where linearized equations of the current state of the structure are solved for the unknown increments of the primary variables. The iteration continues until the convergence is achieved within a specified tolerance, at which point the solution advances to the next load step.

In this chapter, two finite element formulations have been developed for steel-concrete composite beams: a displacement-based formulation and a mixed formulation. The algorithms

including the non-penetrated condition for both formulations have been derived. The fiber discretization is used to characterize the behavior of the sections and a distributed spring element (continuous connection model) is adopted to model the force transfer mechanism at the interface. This chapter is organized as follows: firstly, the element kinematics are presented in Section 5.2 according to the assumptions made in the formulation. Subsequently, the equilibrium equation is developed in Section 5.3 using the total potential energy. Section 5.4 highlights the development of the displacement-based formulation using the variational principle. The mixed-formulation, including its resolution method and algorithm, is presented in Section 5.5. Numerical applications are presented in Section 5.6 to assess and illustrate the performance of the developed formulations, and to support the conclusions drawn in Section 5.7.

5.2 Model assumptions

Using the compatibility in Section 2.2.1, as the consideration of Euler-Bernoulli beam kinematics, the displacement vector $\mathbf{d}$ collecting the displacement field can be written as:

$$\mathbf{d}(x) = \Big[u_b(x,y), \quad v_b(x,y), \quad u_a(x,y), \quad v_a(x,y)\Big]^{\mathrm{T}} \tag{5.1}$$

Since fiber discretization will be applied in the nonlinear formulation, we must evaluate the axial strain at any position y in terms of the axial strain ϵ and the curvature κ at the reference axis, which corresponds to the cross-section centroid. Therefore, the axial strain can be evaluated using this displacement field as follows:

$$\varepsilon_i(\mathbf{d}) = u_{i,x} - y_i v_{,xx} \tag{5.2}$$

The axial strain can also be expressed in function of generalized strains as:

$$\hat{\varepsilon}_i(x,y_i) = \epsilon_i(x) - y_i\kappa_i(x) = \mathbf{a}_s^{\mathrm{T}}(y_i)\mathbf{e}_i(x) \tag{5.3}$$

where $i = a,b$ and the subscript $(\bullet)_{,x}$ denotes derivation with respect to x. We also denote:

$\mathbf{a}_s(y_i) = [1,-y_i]^{\mathrm{T}}$ and $\mathbf{e}_i(x) = [\epsilon_i(x),\kappa_i(x)]^{\mathrm{T}}$.

The kinematic of the connection between the two components of the composite beam are described by slip and uplift. The slip s and uplift g are measured in Section 2.2.1 shown as:

$$s(\mathbf{d}) = u_b(x) - u_a(x) + h_b v_{b,x}(x) + h_a v_{a,x}(x) \tag{5.4}$$

$$g(\mathbf{d}) = v_b(x) - v_a(x) \tag{5.5}$$

The kinematic relationships can be cast in the compact form as:

$$\tilde{\boldsymbol{\partial}}\mathbf{d} - \mathbf{e} = \mathbf{0} \tag{5.6}$$

where,

$$\tilde{\boldsymbol{\partial}} = \begin{bmatrix} \dfrac{\mathrm{d}}{\mathrm{d}x} & 0 & 0 & 0 \\ 0 & \dfrac{\mathrm{d}^2}{\mathrm{d}x^2} & 0 & 0 \\ 0 & 0 & \dfrac{\mathrm{d}}{\mathrm{d}x} & 0 \\ 0 & 0 & 0 & \dfrac{\mathrm{d}^2}{\mathrm{d}x^2} \\ 1 & h_b \dfrac{\mathrm{d}}{\mathrm{d}x} & -1 & h_a \dfrac{\mathrm{d}}{\mathrm{d}x} \\ 0 & 1 & 0 & -1 \end{bmatrix}$$

and $\mathbf{e}$ is the vector collecting the generalized deformations, given by:

$$\mathbf{e}(x) = \begin{bmatrix} \epsilon_b(x) & \kappa_b(x) & \epsilon_a(x) & \kappa_a(x) & s(x) & g(x) \end{bmatrix}^{\mathrm{T}} \tag{5.7}$$

5.3 Equilibrium equation

To develop a finite element formulation for the static analysis of composite beam under the above assumptions, the virtual work principle will be employed. For an isolated element of length L, the internal virtual work is given by the sum of the contributions of the two components plus the interface connection:

$$\delta\Pi_{int} = \int_{\Omega_a} \sigma_a \delta\varepsilon_a d\Omega_a + \int_{\Omega_b} \sigma_b \delta\varepsilon_b d\Omega_b + \int_L D_{sc}\delta s dx + \int_L V_{sc}\delta g dx \tag{5.8}$$

and the external virtual work comes from the contribution of the surface and body loads:

$$\delta\Pi_{ext} = \int_L \left(\delta u_a p_{ax} + \delta v_a p_{ay}\right) dx + \int_L \left(\delta u_b p_{bx} + \delta v_b p_{by}\right) dx + \delta\mathbf{q}^T \mathbf{Q}_{ext} \tag{5.9}$$

in which p_{ix} and p_{iy} are applied distributed load on the layer i in x and y-axis, and $\mathbf{Q}_{ext}$ is external nodal force. The total virtual work is the difference of the internal and external virtual work as follows:

$$\delta\Pi = \delta\Pi_{int} - \delta\Pi_{ext} \tag{5.10}$$

Introducing Eqs. (5.2), (5.4) and (5.5) into Eq. (5.10) and performing intergration by part, one gets:

$$\delta\Pi = -\int_L \delta\mathbf{d}^{\mathrm{T}}\left(\boldsymbol{\partial}\mathbf{D}+\mathbf{P}_y\right)\mathrm{d}x + \left(\begin{bmatrix}\delta u_b\\ \delta v_b\\ \delta\theta_b\\ \delta u_b\\ \delta v_b\\ \delta\theta_b\end{bmatrix}^{\mathrm{T}}\begin{bmatrix}N_b\\ -M_{b,x}+h_b D_{sc}\\ M_b\\ N_a\\ -M_{a,x}+h_a D_{sc}\\ M_a\end{bmatrix}\right)_0^L - \delta\mathbf{q}^{\mathrm{T}}\mathbf{Q}_{ext} = 0 \tag{5.11}$$

where:

$$\boldsymbol{\partial} = \begin{bmatrix}\frac{\mathrm{d}}{\mathrm{d}x} & 0 & 0 & 0 & -1 & 0\\ 0 & -\frac{\mathrm{d}^2}{\mathrm{d}x^2} & 0 & 0 & h_b\frac{\mathrm{d}}{\mathrm{d}x} & -1\\ 0 & 0 & \frac{\mathrm{d}}{\mathrm{d}x} & 0 & 1 & 0\\ 0 & 0 & 0 & -\frac{\mathrm{d}^2}{\mathrm{d}x^2} & h_a\frac{\mathrm{d}}{\mathrm{d}x} & 1\end{bmatrix} \tag{5.12}$$

$$\mathbf{P}_y = \begin{bmatrix}p_{bx}, & p_{by}, & p_{ax}, & p_{ay}\end{bmatrix}^{\mathrm{T}} \tag{5.13}$$

$$\mathbf{D}(x) = \begin{bmatrix}N_b(x), & M_b(x), & N_a(x), & M_a(x), & D_{sc}(x), & V_{sc}(x)\end{bmatrix}^{\mathrm{T}} \tag{5.14}$$

Eq. (5.11) being satisfied for all admissible variations, the following equilibrium equations can be then deduced:

$$\boldsymbol{\partial}\mathbf{D} + \mathbf{P}_y = \mathbf{0} \tag{5.15}$$

which can be expanded as:

$$N_{b,x} - D_{sc} + p_{bx} = 0 \tag{5.16}$$

$$-M_{b,xx} + h_b D_{sc,x} - V_{sc} + p_{by} = 0 \tag{5.17}$$

$$N_{a,x} + D_{sc} + p_{ax} = 0 \tag{5.18}$$

$$-M_{a,xx} + h_a D_{sc,x} - V_{sc} + p_{ay} = 0 \tag{5.19}$$

The beam under consideration is assumed to be simply supported and subjected to external distributed forces in both layers. The internal forces in the two-layered beam are represented by 12 nodal forces corresponding to nodal displacements.

However, due to the support conditions, it is necessary to exclude three nodal forces (in the horizontal and vertical directions of layer a, and in the vertical direction of layer b). To

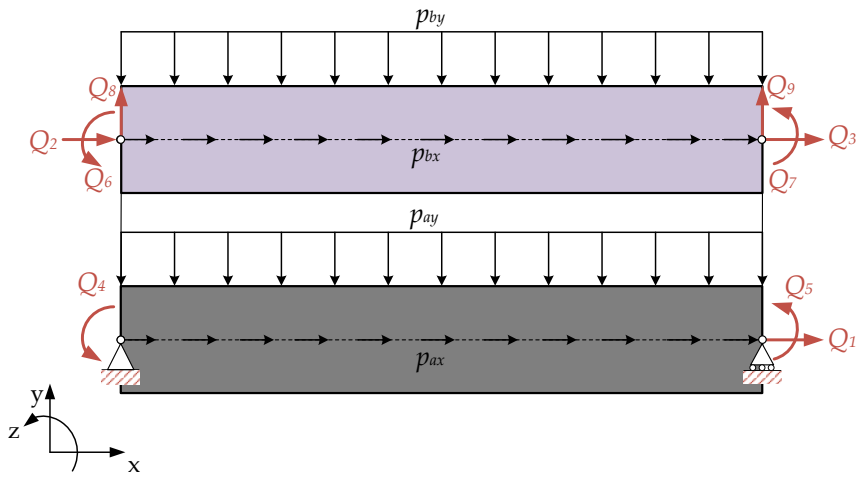

FIGURE 5.1: Nodal forces in beam element with simply supported condition

address this, the nodal forces from $Q_1 \dots Q_9$, as depicted in the Fig. 5.1, are considered. The natural boundary conditions are then as the following:

$$\begin{cases} N_a(L) = Q_1 \\ N_b(0) = -Q_2 + p_{bx}\dfrac{L}{2} \\ N_b(L) = Q_3 - p_{bx}\dfrac{L}{2} \\ M_a(0) = -Q_4 \\ M_a(L) = Q_5 \\ M_b(0) = -Q_6 \\ M_b(L) = Q_7 \\ -M_{b,x}(0) + h_b D_{sc}(0) = -Q_8 + p_{by}\dfrac{L}{2} \\ -M_{b,x}(L) + h_b D_{sc}(L) = Q_9 - p_{by}\dfrac{L}{2} \end{cases}$$

5.4 Displacement-based formulation

In a standard displacement-based (DB) formulation, the state of determination is a strain-driven process, i.e., the stresses are obtained from the strains. The strains are computed from the displacements. Another way to describe the displacement-based formulation is that it is based on interpolation functions of displacement, specifically the axial and transverse displacements of the element. The commonly used functions for beam elements are quadratic functions for the axial displacements and cubic Hermitian polynomials for the transverse displacements.

In the context of the displacement-based approach, the system's equilibrium is established by minimizing the total virtual work, which requires calculating the variation of the total virtual work with respect to the displacement field $\mathbf{d}$.

5.4.1 Interpolation of displacement fields

The analytical solution, as presented in Section 2.3.3, indicates the exact displacement fields in linear elasticity. In nonlinear finite element analysis, Dall'Asta and Zona [40] developed a displacement-based model that accounts for interlayer slip using distinct degrees of freedom (DOF): 8DOF, 10DOF, and 18DOF. The comparison of these models revealed poor performance of the 8 DOF element due to numerical locking issues (curvature locking), as mentioned earlier, and superior performance of the 16 DOF element, despite its more complex implementation. They chose to use 10DOF element in which additional nodes are added for axial displacement at the mid-length of the element for both layers. For the two-layered beam model that considers slip and uplift, additional nodes should be added for axial and vertical displacement, as well as rotation, as shown in Fig. 5.2.

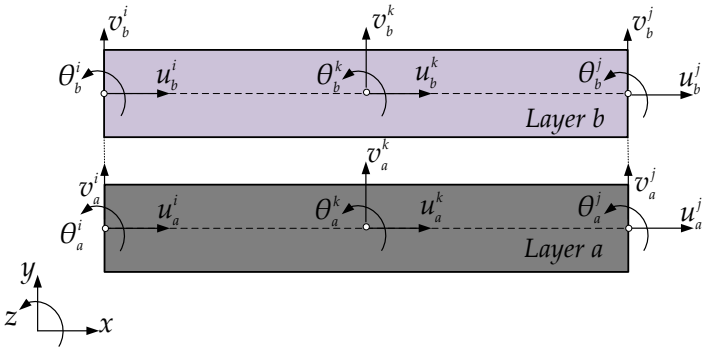

FIGURE 5.2: Displacement field by adding nodes at middle of elements

In this study, we focus on the interpolation of displacement fields $\mathbf{d}(x)$ which is described in Eq. (5.1) for a composite beam. We use quadratic functions for the axial displacements u_a and u_b, and Hermite polynomials for the transverse displacement v_a and v_b.

For a quadratic function of axial displacement $u(x)$ is given by:

$$u(x) = a_0 + a_1 x + a_2 x^2 \tag{5.20}$$

For the Hermite interpolation function of vertical displacement $v(x)$ is given by:

$$v(x) = a_3 v^i + a_4 \theta^i + a_5 v^j + a_6 \theta^j + a_7 v^k + a_8 \theta^k \tag{5.21}$$

where, the constants $a_1, a_2 \ldots a_8$ will be detailed in Appendix B.

By employing these interpolation methods, we can achieve a more accurate representation of the displacement fields $\mathbf{q}$ in the composite beam. This is performed by selecting appropriate displacement interpolation functions $\mathbf{a}(x)$ as follows:

$$\mathbf{d}(x) = \mathbf{a}(x)\mathbf{q} \tag{5.22}$$

where $\mathbf{a}(x) = \left[\mathbf{a}_{u_b}(x), \quad \mathbf{a}_{v_b}(x), \quad \mathbf{a}_{u_a}(x), \quad \mathbf{a}_{v_a}(x)\right]^{\mathrm{T}}$ is the shape function matrix.

- $\mathbf{a}_{u_b}(x)$ and $\mathbf{a}_{u_a}(x)$ are derived by using quadratic functions.
- $\mathbf{a}_{v_b}(x)$ and $\mathbf{a}_{v_a}(x)$ are derived by using Hermite interpolation functions.

In this section, we note that the displacement fields $\mathbf{q}$ account for the middle node of the element and are expressed as follows:

$$\mathbf{q} = \left[u_b^i, v_b^i, \theta_b^i, u_a^i, v_a^i, \theta_a^i, u_b^j, v_b^j, \theta_b^j, u_a^j, v_a^j, \theta_a^j, u_b^k, v_b^k, \theta_b^k, u_a^k, v_a^k, \theta_a^k\right]^{\mathrm{T}}$$

By the derived formulation in Appendix B, as a result, $\mathbf{a}_{u_b}(x)$, $\mathbf{a}_{u_a}(x)$, $\mathbf{a}_{v_b}(x)$ and $\mathbf{a}_{a_a}(x)$ shown as follows:

$$\mathbf{a}_{u_b}(x) = \begin{bmatrix} a_u^i & 0 & 0 & 0 & 0 & 0 & a_u^j & 0 & 0 & 0 & 0 & 0 & a_u^k & 0 & 0 & 0 & 0 & 0 \end{bmatrix}$$

$$\mathbf{a}_{u_a}(x) = \begin{bmatrix} 0 & 0 & 0 & a_u^i & 0 & 0 & 0 & 0 & 0 & a_u^j & 0 & 0 & 0 & 0 & 0 & a_u^k & 0 & 0 \end{bmatrix}$$

$$\mathbf{a}_{v_b}(x) = \begin{bmatrix} 0 & a_v^i & a_\theta^i & 0 & 0 & 0 & 0 & a_v^j & a_\theta^j & 0 & 0 & 0 & 0 & a_v^k & a_\theta^k & 0 & 0 & 0 \end{bmatrix}$$

$$\mathbf{a}_{v_a}(x) = \begin{bmatrix} 0 & 0 & 0 & 0 & a_v^i & a_\theta^i & 0 & 0 & 0 & 0 & a_v^j & a_\theta^j & 0 & 0 & 0 & 0 & a_v^k & a_\theta^k \end{bmatrix}$$

in which

$$a_u^i = 1 - \frac{3x}{L} + \frac{2x^2}{L^2}; \qquad a_u^j = \frac{2x^2}{L^2} - \frac{x}{L}; \qquad a_u^k = \frac{4x}{L} - \frac{4x^2}{L^2}$$

$$a_v^i = \frac{66x^3}{L^3} - \frac{23x^2}{L^2} - \frac{68x^4}{L^4} + \frac{25x^5}{L^5} + 1; \quad a_v^j = \frac{7x^2}{L^2} - \frac{34x^3}{L^3} + \frac{52x^4}{L^4} - \frac{25x^5}{L^5};$$

$$a_v^k = \frac{16x^2}{L^2} - \frac{32x^3}{L^3} + \frac{16x^4}{L^4}; \qquad a_\theta^i = x - \frac{6x^2}{L} + \frac{13x^3}{L^2} - \frac{12x^4}{L^3} + \frac{4x^5}{L^4};$$

$$a_\theta^j = \frac{5x^3}{L^2} - \frac{x^2}{L} - \frac{8x^4}{L^3} + \frac{4x^5}{L^4}; \qquad a_\theta^k = \frac{32x^3}{L^2} - \frac{8x^2}{L} - \frac{40x^4}{L^3} + \frac{16x^5}{L^4}$$

The section deformation vector $\mathbf{e}(x)$ in Eq. (5.7), is related to the nodal displacements by:

$$\mathbf{e}(x) = \mathbf{a}'(x)\mathbf{q} \tag{5.23}$$

The matrix $\mathbf{a}'(x)$ contains the first derivative of the axial displacement shape function, and the second derivatives of the transverse displacement shape functions.

5.4.2 Non-penetration condition

The two layers of the composite beam element initially in contact within the element length may partially separate (vertical uplift) or bear (contact) from one to another under a certain loading condition. When adopting a node-to-node contact algorithm in the displacement based formulation, the contact between the two layers of composite beam element can be evaluated only at the nodes of the element. The continuous contact condition along the element length beside those nodes are not verified. But it can be done by considering the discretized form of contact condition using the interpolated displacement field.

The non-penetrated condition between the layers imposes that:

$$g(x) = v_b(x) - v_a(x) \geq 0 \tag{5.24}$$

or by using interpolation function from Eq. (5.22), we have:

$$\mathbf{a}_g(x)\mathbf{q} \geq 0 \tag{5.25}$$

where $\mathbf{a}_g(x) = \mathbf{a}_{v_b}(x) - \mathbf{a}_{v_a}(x)$.

To take into account the non-penetration condition, the augmented Lagrangian term is added to the system as:

$$\delta\bar{\Pi}(\mathbf{q}) = \delta\Pi(\mathbf{q}) + \delta\mathbf{q}^{\mathrm{T}}\left[\bar{\lambda}\mathbf{a}_g^{\mathrm{T}}(x) + p\mathbf{a}_g^{\mathrm{T}}(x)\mathbf{a}_g(x)\mathbf{q}\right] = 0 \tag{5.26}$$

where $\bar{\lambda}$ is the so-called Lagrangian multiplier and p is a penalty parameter. Newton-Raphson method may be used to solve nonlinear equation (5.26) for a fixed known Lagrange multiplier $\bar{\lambda}$ by following the so-called Uzawa updating scheme. The solution of Eq. (5.51) is then used to verified the positiveness of the uplift $(g(x) \geq 0)$. If this condition is violated, the Lagrange multiplier can be updated using:

$$\bar{\lambda}_{k+1} = \bar{\lambda}_k + p\, g(x) \tag{5.27}$$

It is worth mentioning that the node-to-node contact condition will be evaluated at the integration points, i.e. at $x = \bar{x}$.

5.4.3 Element stiffness matrix

In the equilibrium state, Eq. (5.15) is satisfied. The variational formulations of equilibrium equations are then as follow:

$$\delta\Pi(\mathbf{q}) = \int_L \delta\mathbf{e}^{\mathrm{T}}\hat{\mathbf{D}}dx - \delta\mathbf{q}^{\mathrm{T}}\mathbf{Q}_{ext} = 0 \tag{5.28}$$

in which $\hat{\mathbf{D}}$ is the vector collecting the internal force derived from the constitutive relations.

Then, Eq. (5.26) can be rewritten as:

$$\delta\bar{\Pi}(\mathbf{q}) = \int_L \delta\mathbf{e}^{\mathrm{T}}\hat{\mathbf{D}}dx + \delta\mathbf{q}^{\mathrm{T}}\left[\bar{\lambda}\mathbf{a}_g^{\mathrm{T}}(\bar{x}) + p\mathbf{a}_g^{\mathrm{T}}(\bar{x})\mathbf{a}_g(\bar{x})\mathbf{q}\right] - \delta\mathbf{q}^{\mathrm{T}}\mathbf{Q}_{ext} = 0 \tag{5.29}$$

The consistent matrix formulations are obtained by utilizing the Newton-Raphson iterative procedure. In the interval from the $(i-1)^{th}$ to the i^{th} iteration, a linear behavior is assumed, which results in:

$$\hat{\mathbf{D}}^i = \hat{\mathbf{D}}^{i-1} + \mathbf{k}^{i-1}\Delta\mathbf{e} \tag{5.30}$$

where $\mathbf{k}^{i-1}$ is the tangent stiffness matrix of the section at the $(i-1)^{th}$ iteration.

At the i^{th}, by using Eq. (5.30), Eq. (5.29) is rewritten as:

$$\int_L \delta\mathbf{e}^T\left(\hat{\mathbf{D}}^{i-1} + \mathbf{k}^{i-1}\Delta\mathbf{e}\right)dx + \delta\mathbf{q}^{\mathrm{T}}\left[\bar{\lambda}\mathbf{a}_g^{\mathrm{T}}(\bar{x}) + p\mathbf{a}_g^{\mathrm{T}}(\bar{x})\mathbf{a}_g(\bar{x})\left(\mathbf{q}^{i-1} + \Delta\mathbf{q}\right)\right] = \delta\mathbf{q}^{\mathrm{T}}\mathbf{Q}_{ext} \tag{5.31}$$

Inserting Eq. (5.23) to Eq. (5.31), one obtains:

$$\begin{aligned}&\delta\mathbf{q}^{\mathrm{T}}\int_L\left[\mathbf{a}'^{\mathrm{T}}(x)\left(\hat{\mathbf{D}}^{i-1} + \mathbf{k}^{i-1}\mathbf{a}'(x)\Delta\mathbf{q}\right)\right]dx \\ &+\delta\mathbf{q}^{\mathrm{T}}\left[\bar{\lambda}\mathbf{a}_g^{\mathrm{T}}(\bar{x}) + p\mathbf{a}_g^{\mathrm{T}}(\bar{x})\mathbf{a}_g(\bar{x})\left(\mathbf{q}^{i-1} + \Delta\mathbf{q}\right)\right] = \delta\mathbf{q}^{\mathrm{T}}\mathbf{Q}_{ext}\end{aligned} \tag{5.32}$$

which must hold for any kinematically admissible variations $\delta\mathbf{q}$. Therefore, this equation may be simplified in the following form,

$$\int_L\left[\mathbf{a}'^{\mathrm{T}}(x)\left(\hat{\mathbf{D}}^{i-1} + \mathbf{k}^{i-1}\mathbf{a}'(x)\Delta\mathbf{q}\right)\right]dx + \bar{\lambda}\mathbf{a}_g^{\mathrm{T}}(\bar{x}) + p\mathbf{a}_g^{\mathrm{T}}(\bar{x})\mathbf{a}_g(\bar{x})\left(\mathbf{q}^{i-1} + \Delta\mathbf{q}\right) = \mathbf{Q}_{ext} \tag{5.33}$$

In short, it can be written as:

$$\mathbf{K}^{i-1}\Delta\mathbf{q} = \mathbf{Q}_{ext} - \mathbf{Q}_R^{i-1} \tag{5.34}$$

where

$$\mathbf{K}^{i-1} = \int_L \mathbf{a}'^{\mathrm{T}}(x)\mathbf{k}^{i-1}\mathbf{a}'(x)dx + p\mathbf{a}_g^{\mathrm{T}}(\bar{x})\mathbf{a}_g(\bar{x})$$

is the element tangent stiffness matrix, and

$$\mathbf{Q}_R^{i-1} = \int_L \mathbf{a}'^{\mathrm{T}}(x)\mathbf{D}^{i-1}dx + \bar{\lambda}\mathbf{a}_g^{\mathrm{T}}(\bar{x}) + p\mathbf{a}_g^{\mathrm{T}}(\bar{x})\mathbf{a}_g(\bar{x})\mathbf{q}^{i-1}$$

is the nodal forces due to the lack of equilibrium at the element level.

5.5 Mixed Formulation

In a mixed formulation approach, it is assumed that there are two separate resultant stress fields (internal forces) and two distinct strain fields. One of the resultant stress fields is determined from the sectional integration of the the stress derived from the constitutive relations. Another resultant stress field is obtained from the approximation of the force fields.

Likewise, the deformation of the composite beam can be described using the displacement field or obtained from the approximation of the strain fields.

5.5.1 Variational formulation

The Hu-Washizu functional with three independent fields (displacement, strain and stress) over the composite element volume Ω (domain of the solid) is chosen for the developed finite element formulation. The latter is based on the combination of variational forms of equilibrium equations (virtual work principal), compatibility relations and constitutive relationships, i.e.:

$$\delta\Pi_{hw} = \delta\Pi + \delta_\sigma\Pi_{hw} + \delta_\varepsilon\Pi_{hw} \tag{5.35}$$

where

- $\delta\Pi$ is the virtual work principle for the composite beam element written as:

$$\begin{aligned}\delta\Pi = &\int_{\Omega_a} \sigma_a \delta\varepsilon_a d\Omega_a + \int_{\Omega_b} \sigma_b \delta\varepsilon_b d\Omega_b + \int_L D_{sc}\delta s dx + \int_L V_{sc}\delta g dx \\ &- \int_L \left(\delta u_a p_{ax} + \delta v_a p_{ay}\right) dx - \int_L \left(\delta u_b p_{bx} + \delta v_b p_{by}\right) dx - \delta\mathbf{q}^T\mathbf{Q}_{ext}\end{aligned}$$

- $\delta_\varepsilon\Pi_{hw}$ is the variational form of the constitutive relations:

$$\delta_\varepsilon\Pi_{hw} = \int_L \delta\mathbf{e}^T\left(\hat{\mathbf{D}} - \mathbf{D}\right) dx = 0 \tag{5.36}$$

  in which $\hat{\mathbf{D}}$ is the vector collecting the internal forces derived from the constitutive relations.

- $\delta_\sigma\Pi_{hw}$ is the variational form of compatibility relations:

$$\delta_\sigma\Pi_{hw} = \int_L \delta\mathbf{D}^T\left(\tilde{\partial}\mathbf{d} - \mathbf{e}\right) dx = 0 \tag{5.37}$$

Performing integration by part on Eq. (5.37), one gets:

$$\delta_\sigma\Pi_{\mathrm{hw}} = -\int_L \boldsymbol{\partial}\left(\delta\mathbf{D}\right)^{\mathrm{T}}\mathbf{d}\,\mathrm{d}x + \left(\begin{bmatrix} \delta N_b \\ -\delta M_{b,x} + h_b\delta D_{sc} \\ \delta M_b \\ \delta N_a \\ -\delta M_{a,x} + h_a\delta D_{sc} \\ \delta M_a \end{bmatrix}^{\mathrm{T}} \begin{bmatrix} u_b \\ v_b \\ \theta_b \\ u_a \\ v_a \\ \theta_a \end{bmatrix}\right)_0^L - \int_L \delta\mathbf{D}^{\mathrm{T}}\mathbf{e}\,\mathrm{d}x = 0 \tag{5.38}$$

5.5.2 Force interpolation function

It can be observed that in Eqs. (5.11) and (5.38), if the exact internal force distributions are used, the first terms of both equations are vanished. The formulation can be then developed without approximating the displacement fields. For a statically determinate beam, we can basically derive the exact internal force distributions from the equilibrium equations. However, they are available only for a linear elastic composite beam since with continuous connection, it is an internally indeterminate beam. The exact solution for a linear elastic composite beam shows that the distribution of the internal forces are highly non-linear (hyperbolic functions). Nevertheless, if the shear and uplift force distributions in the connection are supposed to be known, all other internal forces can be obtained through equilibrium. In the present formulation, the shear and uplift forces are treated as redundant forces and are approximated by interpolating them using the ones defined at a finite number of reference points along the element, i.e.:

$$D_{sc} = \mathbf{N}_s \tilde{\mathbf{D}}_{sc}$$
$$V_{sc} = \mathbf{N}_g \tilde{\mathbf{V}}_{sc}$$

where

$\mathbf{N}_s(x) = \left[N_{s1}(x), \ldots, N_{sip}(x)\right]$ and $\mathbf{N}_g(x) = \left[N_{g1}(x), \ldots, N_{gip}(x)\right]$ are interpolation functions. $\tilde{\mathbf{D}}_{sc} = \left[\tilde{D}_{sc1}, \ldots, \tilde{D}_{scip}\right]^{\mathrm{T}}$ and $\tilde{\mathbf{V}}_{sc} = \left[\tilde{V}_{sc1}, \ldots, \tilde{V}_{scip}\right]^{\mathrm{T}}$ are the vectors collecting the shear and uplift forces evaluated at the reference points, respectively.

Furthermore, the bond and uplift forces at the reference points are related to the nodal forces through equilibrium. These relations are obtained by enforcing equilibrium in the x- and y-direction, respectively, of the top beam component of the composite beam element. It follows that:

$$\int_0^L D_{sc}(x)dx = Q_2 + Q_3$$
$$\int_0^L V_{sc}(x)dx = Q_8 + Q_9$$

or,

$$\int_0^L \mathbf{N}_s \tilde{\mathbf{D}}_{sc} dx = Q_2 + Q_3 \tag{5.39}$$
$$\int_0^L \mathbf{N}_g \tilde{\mathbf{V}}_{sc} dx = Q_8 + Q_9 \tag{5.40}$$

in which ${}^x\mathbf{N}_s = \int \mathbf{N}_s dx$, ${}^x\mathbf{N}_g = \int \mathbf{N}_g dx$, ${}^x\mathbf{N}_s(0) = 0$ and ${}^x\mathbf{N}_g(0) = 0$. Another interesting relation between the distributed uplift force and nodal forces is obtained with the bending moment equilibrium of the top beam component of the composite beam. Integrating twice

of Eq. (5.17), we obtain:

$$-\int_0^L \left(\int_0^x M_{b,xx}dx\right)dx + h_b\int_0^L \left(\int_0^x D_{sc,x}dx\right)dx - \int_0^L \left(\int_0^x V_{sc}dx\right)dx + \int_0^L p_{by}xdx = 0$$

Subsequently, we obtain:

$${}^{xx}\mathbf{N}_g(L)\tilde{\mathbf{V}}_{sc} = -Q_6 - Q_7 + h_b(Q_2+Q_3) + LQ_8 \tag{5.41}$$

where Eq. (5.39) and the natural boundary conditions have been used, and ${}^{xx}\mathbf{N}_g = \int\int \mathbf{N}_g dx$.

It can be seen that from Eq. (5.39), we can express one of the bond reference forces, said $\tilde{\mathbf{D}}_{scip} = D_{sc}(L)$, as a function of nodal forces and other bond reference forces as:

$$D_{sc}(L) = \frac{Q_2+Q_3}{{}^{x}N_{sip}(L)} - \frac{{}^{x}\bar{\mathbf{N}}_s(L)}{{}^{x}N_{sip}(L)}\bar{\mathbf{D}}_{sc} \tag{5.42}$$

where:

$$\bar{\mathbf{D}}_{sc} = \left[\tilde{D}_{sc1},\ldots,\tilde{D}_{scip-1}\right]^{\mathrm{T}}$$
$${}^{x}\bar{\mathbf{N}}_s(L) = \left[{}^{x}N_{s1}(L),\ldots,{}^{x}N_{sip-1}(L)\right]$$

In the same way from Eqs. (5.40) and (5.41), two of the uplift reference forces, said $\tilde{V}_{sc1} = V_{sc}(0)$ and $\tilde{V}_{scip} = V_{sc}(L)$, can be expressed in function of nodal forces and other bond reference forces $\bar{\mathbf{V}}_{sc}$ as:

$$\begin{aligned}V_{sc}(0) = {} & \frac{-h_b{}^{x}N_{gip}(L)(Q_2+Q_3) + {}^{x}N_{gip}(L)(Q_6+Q_7)}{{}^{x}N_{g1}(L){}^{xx}N_{gip}(L) - {}^{x}N_{gip}(L){}^{xx}N_{g1}(L)} \\ & + \frac{\left[{}^{xx}N_{gip}(L) - L{}^{x}N_{gip}(L)\right]Q_8 + {}^{xx}N_{gip}(L)Q_9}{{}^{x}N_{g1}(L){}^{xx}N_{gip}(L) - {}^{x}N_{gip}(L){}^{xx}N_{g1}(L)} \\ & + \frac{{}^{x}N_{gip}(L){}^{xx}\bar{\mathbf{N}}_{gip}(L) - {}^{x}\bar{\mathbf{N}}_g(L){}^{xx}N_{gip}(L)}{{}^{x}N_{g1}(L){}^{xx}N_{gip}(L) - {}^{x}N_{gip}(L){}^{xx}N_{g1}(L)}\bar{\mathbf{V}}_{sc}\end{aligned}$$

$$\begin{aligned}V_{sc}(L) = {} & \frac{h_b{}^{x}N_{g1}(L)(Q_2+Q_3) + {}^{x}N_{g1}(L)(Q_6+Q_7)}{{}^{x}N_{g1}(L){}^{xx}N_{gip}(L) - {}^{x}N_{gip}(L){}^{xx}N_{g1}(L)} \\ & - \frac{\left[{}^{xx}N_{g1}(L) - L{}^{x}N_{g1}(L)\right]Q_8 + {}^{xx}N_{g1}(L)Q_9}{{}^{x}N_{g1}(L){}^{xx}N_{gip}(L) - {}^{x}N_{gip}(L){}^{xx}N_{g1}(L)} \\ & - \frac{{}^{x}N_{g1}(L){}^{xx}\bar{\mathbf{N}}_g(L) - {}^{x}\bar{\mathbf{N}}_g(L){}^{xx}N_{g1}(L)}{{}^{x}N_{g1}(L){}^{xx}N_{gip}(L) - {}^{x}N_{gip}(L){}^{xx}N_{g1}(L)}\bar{\mathbf{V}}_{sc}\end{aligned}$$

Finally, we can write the bond and uplift forces as:

$$D_{sc}(x) = \mathbf{b}_{D_{sc}}(x)\,\mathbf{Q} + \left[\bar{\mathbf{N}}_s(x) - \frac{N_{sip}(x)}{{}^{x}N_{sip}(L)}\,{}^{x}\bar{\mathbf{N}}_s(L)\right]\bar{\mathbf{D}}_{sc} \tag{5.43}$$

$$V_{sc}(x) = \mathbf{b}_{V_{sc}}(x)\,\mathbf{Q} + \mathbf{b}^{g}_{V_{sc}}(x)\,\bar{\mathbf{V}}_{sc} \tag{5.44}$$

where

$$\mathbf{Q} = \begin{bmatrix} Q_1 & Q_2 & Q_3 & Q_4 & Q_5 & Q_6 & Q_7 & Q_8 & Q_9 \end{bmatrix}^T$$

and $\mathbf{b}_{D_{sc}}(x)$, $\mathbf{b}_{V_{sc}}(x)$ and $\mathbf{b}^{g}_{V_{sc}}(x)$ are given in the Appendix D.

The generalized forces $\mathbf{D}$, the bond force $\bar{\mathbf{D}}_{sc}$ and uplift force $\bar{\mathbf{V}}_{sc}$ are interpolated using polynomial function (shape functions) that must satisfy the equilibrium along beam element. Inserting Eqs. (5.43) and (5.44) into Eq. (5.15) and solving for the remaining internal forces, one obtains the following sectional resultant forces written in the compact form as:

$$\mathbf{D} = \mathbf{b}(x)\mathbf{Q} + \mathbf{b}_s(x)\bar{\mathbf{D}}_{sc} + \mathbf{b}_g(x)\bar{\mathbf{V}}_{sc} + \mathbf{D}_p(x) \tag{5.45}$$

It is noticeable that $\mathbf{b}(x)$, $\mathbf{b}_s(x)$ and $\mathbf{b}_g(x)$ are polynomial interpolation functions. The matrix $\mathbf{b}(x)$,$\mathbf{b}_s(x)$ and $\mathbf{b}_g(x)$ are constructed to satisfy the homogeneous equilibrium equations beforehand, regardless of $\mathbf{Q}$, $\bar{\mathbf{D}}_{sc}$ and $\bar{\mathbf{V}}_{sc}$ and given in Appendix D.

$\mathbf{D}_p(x)$ is a particular solution of differential equations that allows for the consideration of the distributed load p_{bx}, p_{by}, p_{ax} and p_{ay}.

$$\mathbf{D}_p(x) = \begin{bmatrix} p_{bx}\left(\frac{L}{2} - x\right) & p_{by}\frac{x(x-L)}{2} & p_{ax}(L-x) & p_{ay}\frac{x(x-L)}{2} & 0 & 0 \end{bmatrix}^T$$

In this study, the connection uplift and shear forces along the element is approximated by quadratic and cubic polynomials, i.e. three and four reference uplift and shear forces, respectively. From equilibrium equations, these approximations results in fourth-order distributions for the bending moment and the axial force along each layer of the composite beam.

5.5.3 Generalized strain interpolation

The same order of polynomial functions as the ones for force fields are adopted for strain fields. It is in accordant to de Veubeke's principle of limitation [74] which states that there is no improvement of the analysis accuracy by increasing the order of the force field beyond the one of the strain field that complies with the compatibility condition. Hence, the

generalized strains can be approximated by:

$$\mathbf{e}(x) = \begin{bmatrix} \epsilon_b(x) \\ \kappa_b(x) \\ \epsilon_a(x) \\ \kappa_a(x) \\ s(x) \\ g(x) \end{bmatrix} = \begin{bmatrix} \sum_{i=1}^{e_{ip}} N_e^{(i)}(x)\epsilon_b^{(i)} \\ \sum_{i=1}^{k_{ip}} N_k^{(i)}(x)\kappa_b^{(i)} \\ \sum_{i=1}^{e_{ip}} N_e^{(i)}(x)\epsilon_a^{(i)} \\ \sum_{i=1}^{k_{ip}} N_k^{(i)}(x)\kappa_a^{(i)} \\ \sum_{i=1}^{s_{ip}} N_s^{(i)}(x)s^{(i)} \\ \sum_{i=1}^{g_{ip}} N_g^{(i)}(x)g^{(i)} \end{bmatrix} = \mathbf{N}_e(x)\tilde{\mathbf{e}} \tag{5.46}$$

in which $N_e^{(i)}(x)$, $N_k^{(i)}(x)$, $N_s^{(i)}(x)$ and $N_g^{(i)}(x)$ are Lagrange interpolation polynomials, and $s^{(i)}$, $g^{(i)}$, $\epsilon_j^{(i)}$, and $\kappa_j^{(i)}$, $j = a, b$, are generalized strains evaluated at reference points (i) while $e_{ip} = 5$, $k_{ip} = 5$, $s_{ip} = 4$ and $g_{ip} = 3$.

$\mathbf{N}_e(x)$ denotes a matrix assembling the interpolation functions and $\tilde{\mathbf{e}}$ is a vector collecting reference generalized strains.

5.5.4 Mixed variational formulation

The form of Hu-Washizu functional can be obtained by introducing Eqs. (5.45) and (5.46) back into Eqs. (5.11), (5.36) and (5.38) and substituting the results into Eq. (5.35). One gets:

$$\delta\Pi_{hw} = \begin{Bmatrix} \delta\mathbf{q} \\ \delta\tilde{\mathbf{e}} \\ \delta\mathbf{Q} \\ \delta\bar{\mathbf{D}}_{sc} \\ \delta\bar{\mathbf{V}}_{sc} \end{Bmatrix}^T \begin{bmatrix} \mathbf{H}^T\mathbf{Q} - \mathbf{Q}_p - \mathbf{Q}_{ext} \\ \int_L \mathbf{N}_e^T\hat{\mathbf{D}}dx - \int_L \mathbf{N}_e^T\left(\mathbf{b}\mathbf{Q} + \mathbf{b}_s\bar{\mathbf{D}}_{sc} + \mathbf{b}_g\bar{\mathbf{V}}_{sc} + \mathbf{D}_p\right)dx \\ \mathbf{H}\mathbf{q} - \int_L \mathbf{b}^T\mathbf{N}_e\tilde{\mathbf{e}}dx \\ \int_L \mathbf{b}_s^T\mathbf{N}_e\tilde{\mathbf{e}}dx \\ \int_L \mathbf{b}_g^T\mathbf{N}_e\tilde{\mathbf{e}}dx \end{bmatrix} = 0 \tag{5.47}$$

in which is valid for all virtual variables.

The vector $\mathbf{Q}_p$ is associated to the distributed load p_y and expressed as:

$$\mathbf{Q}_p^{\mathrm{T}} = \begin{bmatrix} p_{bx}\frac{L}{2} & p_{by}\frac{L}{2} & 0 & p_{ax}\frac{L}{2} & p_{ay}\frac{L}{2} & 0 & p_{bx}\frac{L}{2} & p_{by}\frac{L}{2} & 0 & 0 & p_{ay}\frac{L}{2} & 0 \end{bmatrix}$$

and the expression of $\mathbf{H}$ is written as follows:

$$\mathbf{H}^{\mathrm{T}} = \begin{bmatrix} 0 & 1 & 0 & 0 & 0 & 0 & 0 & 0 & 0 \\ 0 & 0 & 0 & 0 & 0 & 0 & 0 & 1 & 0 \\ 0 & 0 & 0 & 0 & 0 & 1 & 0 & 0 & 0 \\ -1 & -1 & -1 & 0 & 0 & 0 & 0 & 0 & 0 \\ 0 & -\dfrac{h_a+h_b}{L} & -\dfrac{h_a+h_b}{L} & \dfrac{1}{L} & \dfrac{1}{L} & \dfrac{1}{L} & \dfrac{1}{L} & -1 & 0 \\ 0 & 0 & 0 & 1 & 0 & 0 & 0 & 0 & 0 \\ 0 & 0 & 1 & 0 & 0 & 0 & 0 & 0 & 0 \\ 0 & 0 & 0 & 0 & 0 & 0 & 0 & 0 & 1 \\ 0 & 0 & 0 & 0 & 0 & 0 & 1 & 0 & 0 \\ 1 & 0 & 0 & 0 & 0 & 0 & 0 & 0 & 0 \\ 0 & \dfrac{h_a+h_b}{L} & \dfrac{h_a+h_b}{L} & -\dfrac{1}{L} & -\dfrac{1}{L} & -\dfrac{1}{L} & -\dfrac{1}{L} & 0 & -1 \\ 0 & 0 & 0 & 0 & 1 & 0 & 0 & 0 & 0 \end{bmatrix}$$

5.5.5 Non-penetration condition

The non-penetration condition between the layers imposes that:

$$g(x) \geq 0 \tag{5.48}$$

or by using interpolation functions, we have:

$$\mathbf{N}^{g}(x)\mathbf{G} \geq 0 \tag{5.49}$$

where $\mathbf{G}$ is a vector collecting all uplifts $g^{(i)}$ evaluated at the reference points and $\mathbf{G}$ can be expressed in function of $\tilde{\mathbf{e}}$ as:

$$\mathbf{G} = \bar{\mathbf{A}}^{\mathrm{T}}\tilde{\mathbf{e}} \tag{5.50}$$

in which:

$$\bar{\mathbf{A}}^{\mathrm{T}} = \begin{bmatrix} \mathbf{0}_{\tilde{\epsilon}_1}^{\mathrm{T}} & \mathbf{0}_{\tilde{\kappa}_1}^{\mathrm{T}} & \mathbf{0}_{\tilde{\epsilon}_2}^{\mathrm{T}} & \mathbf{0}_{\tilde{\kappa}_2}^{\mathrm{T}} & \mathbf{0}_{\tilde{s}}^{\mathrm{T}} & 1 & 0 & \dots & 0 \\ \mathbf{0}_{\tilde{\epsilon}_1}^{\mathrm{T}} & \mathbf{0}_{\tilde{\kappa}_1}^{\mathrm{T}} & \mathbf{0}_{\tilde{\epsilon}_2}^{\mathrm{T}} & \mathbf{0}_{\tilde{\kappa}_2}^{\mathrm{T}} & \mathbf{0}_{\tilde{s}}^{\mathrm{T}} & 0 & 1 & \dots & 0 \\ \vdots & \vdots & \vdots & \vdots & \vdots & \vdots & 0 & \ddots & 0 \\ \mathbf{0}_{\tilde{\epsilon}_1}^{\mathrm{T}} & \mathbf{0}_{\tilde{\kappa}_1}^{\mathrm{T}} & \mathbf{0}_{\tilde{\epsilon}_2}^{\mathrm{T}} & \mathbf{0}_{\tilde{\kappa}_2}^{\mathrm{T}} & \mathbf{0}_{\tilde{s}}^{\mathrm{T}} & 0 & 0 & \dots & 1 \end{bmatrix}$$

To take into account the non-penetration condition, the augmented Lagrangian therms are added to the system as:

$$\delta\bar{\Pi}_{\mathrm{hw}} = \delta\Pi_{\mathrm{hw}} + \delta\tilde{\mathbf{e}}^{\mathrm{T}}\left(\mathbf{A}\bar{\boldsymbol{\lambda}} + p\mathbf{A}\mathbf{A}^{\mathrm{T}}\tilde{\mathbf{e}}\right) = 0 \tag{5.51}$$

where $\mathbf{A} = \mathbf{N}^g(x)\,\bar{\mathbf{A}}$ and $\bar{\boldsymbol{\lambda}}$ is the so-called Lagrangian multiplier vector and p is a penalty parameter. Newton-Raphson method may be used to solve nonlinear equation (5.51) for a fixed known Lagrange multiplier $\bar{\boldsymbol{\lambda}}$ by following the so-called Uzawa updating scheme. The solution of Eq. (5.51) is then used to verified the positiveness of the uplift ($g^{(ip)} \geq 0$, evaluated at the integration point x_{ip}). If this condition is violated, the Lagrange multiplier can be updated at iteration $k+1$ using:

$$\bar{\lambda}_{k+1}^{(ip)} = \bar{\lambda}_{k}^{(ip)} + p\, g_k^{(ip)} \tag{5.52}$$

5.5.6 Resolution

In this section, the system of equations represented by Eq. (5.51) will be derived, and demonstrations of the solution and integration algorithms will be shown. Applying linearization of Eq. (5.51) gives the incremental form for a Newton solution process as:

$$\begin{bmatrix} \mathbf{0} & \mathbf{0} & \mathbf{H}^T & \mathbf{0} & \mathbf{0} \\ \mathbf{0} & \mathbf{K}_s & -\int_L \mathbf{N}_e^T \mathbf{b} dx & -\int_L \mathbf{N}_e^T \mathbf{b}_s dx & -\int_L \mathbf{N}_e^T \mathbf{b}_g dx \\ \mathbf{H} & -\int_L \mathbf{b}^T \mathbf{N}_e dx & \mathbf{0} & \mathbf{0} & \mathbf{0} \\ \mathbf{0} & -\int_L \mathbf{b}_s^T \mathbf{N}_e dx & \mathbf{0} & \mathbf{0} & \mathbf{0} \\ \mathbf{0} & -\int_L \mathbf{b}_g^T \mathbf{N}_e dx & \mathbf{0} & \mathbf{0} & \mathbf{0} \end{bmatrix} \begin{Bmatrix} \Delta\mathbf{q} \\ \Delta\tilde{\mathbf{e}} \\ \Delta\mathbf{Q} \\ \Delta\bar{\mathbf{D}}_{sc} \\ \Delta\bar{\mathbf{V}}_{sc} \end{Bmatrix} = \begin{Bmatrix} \mathbf{R}_q \\ \mathbf{R}_{\tilde{e}} \\ \mathbf{R}_Q \\ \mathbf{R}_s \\ \mathbf{R}_g \end{Bmatrix} \tag{5.53}$$

where:

$$\mathbf{K}_s = \int_L \mathbf{N}_e^T \mathbf{K}_m \mathbf{N}_e dx + p\mathbf{A}\mathbf{A}^{\mathrm{T}} \tag{5.54}$$

and

$$\mathbf{K}_m = \begin{bmatrix} \mathbf{K}_{ab} & \mathbf{0} \\ \mathbf{0} & \mathbf{K}_{sc} \end{bmatrix} \tag{5.55}$$

in which

$$\mathbf{K}_{ab} = \begin{bmatrix} \int_{A_b} E_b^t dA_b & -\int_{A_b} y E_b^t dA_b & 0 & 0 \\ -\int_{A_b} y E_b^t dA_b & -\int_{A_b} y^2 E_b^t dA_b & 0 & 0 \\ 0 & 0 & \int_{A_a} E_a^t dA_a & -\int_{A_a} y E_a^t dA_a \\ 0 & 0 & -\int_{A_a} y E_a^t dA_a & -\int_{A_a} y^2 E_a^t dA_a \end{bmatrix}$$

In the coupled-plastic connector model, $\mathbf{K}_{sc}$ is a matrix provided by the tangent operator consistent with the connector and found in Section 4.4.3. For the uncoupled model of the connector, $\mathbf{K}_{sc}$ is presented as Section 4.4.4.

The residuals are presented as follows:

$$
\begin{aligned}
\mathbf{R}_q &= -\mathbf{H}^T\mathbf{Q} + \mathbf{Q}_p + \mathbf{Q}_{ext} \\
\mathbf{R}_{\tilde{e}} &= \int_L \mathbf{N}_e^T \left(\mathbf{D} - \hat{\mathbf{D}}\right) dx - \mathbf{A}\bar{\boldsymbol{\lambda}} - p\mathbf{A}\mathbf{A}^{\mathrm{T}}\tilde{\mathbf{e}} \\
\mathbf{R}_Q &= -\mathbf{H}\mathbf{q} + \int_L \mathbf{b}^T\mathbf{N}_e\tilde{\mathbf{e}}dx \\
\mathbf{R}_s &= \int_L \mathbf{b}_s^T\mathbf{N}_e\tilde{\mathbf{e}}dx \\
\mathbf{R}_g &= \int_L \mathbf{b}_g^T\mathbf{N}_e\tilde{\mathbf{e}}dx
\end{aligned}
$$

The stiffness matrix of the element can be determined by eliminating the generalized strain, the reference uplift force, the reference bond force and the nodal force increments as follows. From Eq. (5.53)b, calculate the generalized strain increment:

$$
\begin{aligned}
\Delta\tilde{\mathbf{e}} &= \mathbf{K}_s^{-1}\left[\mathbf{R}_{\tilde{e}} + \left(\int_L \mathbf{N}_e^T\mathbf{b}dx\right)\Delta\mathbf{Q} + \left(\int_L \mathbf{N}_e^T\mathbf{b}_s dx\right)\Delta\bar{\mathbf{D}}_{sc} + \left(\int_L \mathbf{N}_e^T\mathbf{b}_g dx\right)\Delta\bar{\mathbf{V}}_{sc}\right] \\
&= \mathbf{K}_s^{-1}\left(\mathbf{R}_{\tilde{e}} + \mathbf{b}_e\Delta\mathbf{Q} + \mathbf{b}_{se}\Delta\bar{\mathbf{D}}_{sc} + \mathbf{b}_{ge}\Delta\bar{\mathbf{V}}_{sc}\right)
\end{aligned}
\tag{5.56}
$$

Introducing Eq. (5.56) into Eq. (5.53)c, Eq. (5.53)d and Eq. (5.53)e, one gets:

$$\mathbf{F}_{QQ}\Delta\mathbf{Q} + \mathbf{F}_{Qs}\Delta\bar{\mathbf{D}}_{sc} + \mathbf{F}_{Qg}\Delta\bar{\mathbf{V}}_{sc} = -\bar{\mathbf{R}}_Q + \mathbf{H}\Delta\mathbf{q} \tag{5.57}$$

$$\mathbf{F}_{sQ}\Delta\mathbf{Q} + \mathbf{F}_{ss}\Delta\bar{\mathbf{D}}_{sc} + \mathbf{F}_{sg}\Delta\bar{\mathbf{V}}_{sc} = -\bar{\mathbf{R}}_s \tag{5.58}$$

$$\mathbf{F}_{gQ}\Delta\mathbf{Q} + \mathbf{F}_{gs}\Delta\bar{\mathbf{D}}_{sc} + \mathbf{F}_{gg}\Delta\bar{\mathbf{V}}_{sc} = -\bar{\mathbf{R}}_g \tag{5.59}$$

where:

$$
\begin{aligned}
&\mathbf{F}_{ss} = \mathbf{b}_{se}^T\mathbf{K}_s^{-1}\mathbf{b}_{se} && \mathbf{F}_{gg} = \mathbf{b}_{ge}^T\mathbf{K}_s^{-1}\mathbf{b}_{ge} && \mathbf{F}_{QQ} = \mathbf{b}_e^T\mathbf{K}_s^{-1}\mathbf{b}_e \\
&\mathbf{F}_{sQ} = \mathbf{b}_{se}^T\mathbf{K}_s^{-1}\mathbf{b}_e && \mathbf{F}_{gQ} = \mathbf{b}_{ge}^T\mathbf{K}_s^{-1}\mathbf{b}_e && \mathbf{F}_{Qs} = \mathbf{b}_e^T\mathbf{K}_s^{-1}\mathbf{b}_{se} \\
&\mathbf{F}_{sg} = \mathbf{b}_{se}^T\mathbf{K}_s^{-1}\mathbf{b}_{ge} && \mathbf{F}_{gs} = \mathbf{b}_{ge}^T\mathbf{K}_s^{-1}\mathbf{b}_{se} && \mathbf{F}_{Qg} = \mathbf{b}_e^T\mathbf{K}_s^{-1}\mathbf{b}_{ge} \\
&\bar{\mathbf{R}}_s = \mathbf{R}_s + \mathbf{b}_{se}^T\mathbf{K}_s^{-1}\mathbf{R}_{\tilde{e}} && \bar{\mathbf{R}}_g = \mathbf{R}_g + \mathbf{b}_{ge}^T\mathbf{K}_s^{-1}\mathbf{R}_{\tilde{e}} && \bar{\mathbf{R}}_Q = \mathbf{R}_Q + \mathbf{b}_e^T\mathbf{K}_s^{-1}\mathbf{R}_{\tilde{e}}
\end{aligned}
$$

Solve Eqs. (5.57-5.59) for $\Delta\bar{\mathbf{D}}_{sc}$ and $\Delta\bar{\mathbf{V}}_{sc}$, we get:

$$\begin{Bmatrix}\Delta\bar{\mathbf{D}}_{sc} \\ \Delta\bar{\mathbf{V}}_{sc}\end{Bmatrix} = -\mathbf{F}_{ssgg}^{-1}\left[\bar{\mathbf{R}}_{sg} + \begin{Bmatrix}\mathbf{F}_{sQ} \\ \mathbf{F}_{gQ}\end{Bmatrix}\Delta\mathbf{Q}\right] \tag{5.60}$$

where:

$$\mathbf{F}_{ssgg} = \begin{bmatrix}\mathbf{F}_{ss} & \mathbf{F}_{sg} \\ \mathbf{F}_{gs} & \mathbf{F}_{gg}\end{bmatrix} \quad , \quad \bar{\mathbf{R}}_{sg} = \begin{Bmatrix}\bar{\mathbf{R}}_s \\ \bar{\mathbf{R}}_g\end{Bmatrix} \tag{5.61}$$

Substituting the result back into Eq. (5.57), we obtain:

$$\Delta\mathbf{Q} = \mathbf{f}^{-1}\left(\mathbf{H}\Delta q - \hat{\mathbf{R}}_Q\right) \tag{5.62}$$

where:

$$\mathbf{f} = \mathbf{F}_{QQ} - \begin{bmatrix} \mathbf{F}_{Qs} & \mathbf{F}_{Qg} \end{bmatrix} \mathbf{F}_{ssgg}^{-1} \begin{Bmatrix} \mathbf{F}_{sQ} \\ \mathbf{F}_{gQ} \end{Bmatrix} \tag{5.63}$$

and:

$$\hat{\mathbf{R}}_Q = \bar{\mathbf{R}}_Q - \begin{bmatrix} \mathbf{F}_{Qs} & \mathbf{F}_{Qg} \end{bmatrix} \mathbf{F}_{ssgg}^{-1} \bar{\mathbf{R}}_{sg} \tag{5.64}$$

Finally, substituting Eq. (5.62) back into Eq. (5.53)a, one gets:

$$\mathbf{K}\Delta\mathbf{q} = \mathbf{R}_q + \mathbf{H}^T \mathbf{f}^{-1} \hat{\mathbf{R}}_Q \tag{5.65}$$

where $\mathbf{K} = \mathbf{H}^T \mathbf{f}^{-1} \mathbf{H}$ is the stiffness matrix of the element and $\bar{\mathbf{R}}_q = \mathbf{R}_q + \mathbf{H}^T \mathbf{f}^{-1} \hat{\mathbf{R}}_Q$ is the modified force residual. The element stiffness matrix and force residual can be now assembled into the global system in an identical manner to any displacement-based formulation. The modified elemental internal force can be expressed as:

$$\mathbf{Q}_R = \mathbf{H}^T \mathbf{Q} - \mathbf{H}^T \mathbf{f}^{-1} \hat{\mathbf{R}}_Q \tag{5.66}$$

5.5.7 Integration Algorithms

NEWTON-RAPHSON equilibrium iteration: Loop i:

Iteration NEWTON-RAPHSON (i) is organized step by step:

(1) Solve the global system of equations and update the structural displacements.

At iteration NEWTON-RAPHSON (i), the stiffness matrix $\mathbf{K}_g^{i-1}$ of iteration $(i-1)$ is used to calculate displacement increments $\Delta\mathbf{q}_g^i$ corresponding with load increments given $\bar{\mathbf{R}}_{qg}^{i-1}$ which is forces out of balance relative with iteration before.

$$\mathbf{K}_g^{i-1} \Delta\mathbf{q}_g^i = \bar{\mathbf{R}}_{qg}^{i-1} \tag{5.67}$$

$$\mathbf{q}_g^i = \mathbf{q}_g^{i-1} + \Delta\mathbf{q}_g^i \tag{5.68}$$

(2) For each element, extract the displacements and increments of displacement.

Nodal displacement increments of element $\Delta\mathbf{q}^i$ are extracted from the one of structure $\Delta\mathbf{q}_g^i$.

$$\mathbf{q}^i = \mathbf{q}^{i-1} + \Delta\mathbf{q}^i \tag{5.69}$$

Start local equilibrium state

Update internal forces: Loop j:

(3) For each element, doing these following steps from (3) to (18).

Displacements $\mathbf{q}^i$ are now used at the element level to determine the internal forces that satisfy local equilibrium equations and constitutive relationships. For this purpose, an iterative process, identified by j, is used. The index of the first iteration is $j = 1$.

(4) Calculate the increments of element forces without rigid body mode.

$$\Delta\mathbf{Q}^j = [\mathbf{f}^{j-1}]^{-1}\left(\mathbf{H}\Delta\mathbf{q}^j - \hat{\mathbf{R}}_Q^{j-1}\right) \tag{5.70}$$

$$\begin{Bmatrix}\Delta\bar{\mathbf{D}}_{sc}^j \\ \Delta\bar{\mathbf{V}}_{sc}^j\end{Bmatrix} = -\left[\mathbf{F}_{ssgg}^{j-1}\right]^{-1}\left[\bar{\mathbf{R}}_{sg}^{j-1} + \begin{Bmatrix}\mathbf{F}_{sQ}^{j-1} \\ \mathbf{F}_{gQ}^{j-1}\end{Bmatrix}\Delta\mathbf{Q}^j\right] \tag{5.71}$$

where

for $j = 0$, $\mathbf{f}^0 = \mathbf{f}^{i-1}$, $\Delta\mathbf{q}^1 = \Delta\mathbf{q}^i$, $\hat{\mathbf{R}}_Q^0 = \mathbf{0}$, $\mathbf{F}_{ssgg}^0 = \mathbf{F}_{ssgg}^{i-1}$, $\mathbf{F}_{sQ}^0 = \mathbf{F}_{sQ}^{i-1}$, $\mathbf{F}_{gQ}^0 = \mathbf{F}_{gQ}^{i-1}$ and $\bar{\mathbf{R}}_{sg}^0 = \mathbf{0}$

for $j > 1$, $\Delta\mathbf{q}^j = 0$ and $\mathbf{f}^{j-1}$, $\hat{\mathbf{R}}_Q^{j-1}$, $\mathbf{F}_{ssgg}^{j-1}$, $\bar{\mathbf{R}}_{sg}^{j-1}$, $\mathbf{F}_{sQ}^{j-1}$, $\mathbf{F}_{gQ}^{j-1}$ are determined at step (16).

(5) Update element forces.

$$\mathbf{Q}^j = \mathbf{Q}^{j-1} + \Delta\mathbf{Q}^j \tag{5.72}$$

with $\mathbf{Q}^0 = \mathbf{Q}^{i-1}$

(6) Calculate the increments of sectional resultant forces at each integration point x_{ip}.

$$\Delta\mathbf{D}^j(x_{ip}) = \mathbf{b}(x_{ip})\Delta\mathbf{Q}^j + \mathbf{b}_s(x_{ip})\Delta\bar{\mathbf{D}}_{sc}^j + \mathbf{b}_g(x_{ip})\Delta\bar{\mathbf{V}}_{sc}^j \tag{5.73}$$

(7) Update sectional resultant forces at each integration point x_{ip}.

$$\mathbf{D}^j(x_{ip}) = \mathbf{D}^{j-1}(x_{ip}) + \Delta\mathbf{D}^j(x_{ip}) \tag{5.74}$$

with $\mathbf{D}^0 = \mathbf{D}^{i-1}$

(8) Calculate the increments of generalized deformations at all integration points.

$$\Delta\tilde{\mathbf{e}}^j = \left[\mathbf{K}_s^{j-1}\right]^{-1}\left(\mathbf{R}_{\tilde{e}}^{j-1} + \mathbf{b}_e\Delta\mathbf{Q}^j + \mathbf{b}_{se}\Delta\bar{\mathbf{D}}_{sc}^j + \mathbf{b}_{ge}\Delta\bar{\mathbf{V}}_{sc}^j\right) \tag{5.75}$$

where

- for $j=1$, $\mathbf{K}_s^0 = \mathbf{K}_s^{i-1}$, $R_{\tilde{e}}^0 = 0$
- for $j>1$, $\mathbf{K}_s^{j-1} = \int_L \mathbf{N}_e^T \mathbf{K}_m^{j-1} \mathbf{N}_e dx$ determined at step (12) and $R_{\tilde{e}}^{j-1}$ is determined at step (14).

(9) Update the generalized deformations at all integration points.

$$\tilde{\mathbf{e}}^j = \tilde{\mathbf{e}}^{j-1} + \Delta\tilde{\mathbf{e}}^j \tag{5.76}$$

(10) For each fiber, calculate the deformation at each integration point $\mathbf{x}_{ip}$

- Layer a:

$$\varepsilon_a^j(x_{ip}, y_a) = \tilde{\epsilon}_a^j(x_{ip}) - y_a \tilde{\kappa}_a^j(x_{ip}) \tag{5.77}$$

- Layer b:

$$\varepsilon_b^j(x_{ip}, y_b) = \tilde{\epsilon}_b^j(x_{ip}) - y_b \tilde{\kappa}_b^j(x_{ip}) \tag{5.78}$$

(11) For each fiber, calculate the stress field and the tangent modulus at each integration point.

The stress field at each fiber $\left(\hat{\sigma}_a^j(x_{ip}, y_a), \hat{\sigma}_b^j(x_{ip}, y_b), \hat{D}_{sc}^j(x_{ip}) \text{and} \hat{V}_{sc}^j(x_{ip})\right)$ and the tangent operator $\left(\left(E_a^t(x_{ip}, y_a)\right)^j, \left(E_b^t(x_{ip}, y_a)\right)^j, \left(k_{sc}^h\right)^j \text{and} \left(k_{sc}^v\right)^j\right)$ corresponding to the deformation $\left(\varepsilon_a^j(x_{ip}, y_a), \varepsilon_b^j(x_{ip}, y_b), s^j \text{and} g^j\right)$.

(12) Calculate the sectional stiffness matrix.

$$\mathbf{K}_m^j(x_{ip}) = \begin{bmatrix} \mathbf{K}_{ab}^j(x_{ip}) & \mathbf{0} \\ \mathbf{0} & \mathbf{K}_{sc}^j(x_{ip}) \end{bmatrix} \tag{5.79}$$

where:

$$\mathbf{K}_{ab}^j(x_{ip}) = \begin{bmatrix} (EA)_b^j & -(ES)_b^j & 0 & 0 \\ -(ES)_b^j & (EI)_b^j & 0 & 0 \\ 0 & 0 & (EA)_a^j & -(ES)_a^j \\ 0 & 0 & -(ES)_a^j & (EI)_a^j \end{bmatrix}$$

$\mathbf{K}_{sc}^j(x_{ip})$ can be found in Section 4.4.3 for coupled model of connector and in Section 4.4.4 for uncoupled model of connector.

and

$$\mathbf{K}_s^j = \sum_{ip} \omega(x_{ip}) \mathbf{N}_e^T(x_{ip}) \mathbf{K}_m^j(x_{ip}) \mathbf{N}_e(x_{ip}) + p\mathbf{A}\mathbf{A}^{\mathrm{T}} \tag{5.80}$$

where:

$$\begin{aligned}
(EA)_a^j &= \int_{A_a} \left(E_a^t(x_{ip}, y_a)\right)^j dA_a \\
(ES)_a^j &= \int_{A_a} y_a \left(E_a^t(x_{ip}, y_a)\right)^j dA_a \\
(EI)_a^j &= \int_{A_a} y_a^2 \left(E_a^t(x_{ip}, y_a)\right)^j dA_a \\
(EA)_b^j &= \int_{A_b} \left(E_b^t(x_{ip}, y_b)\right)^j dA_b \\
(ES)_b^j &= \int_{A_b} y_b \left(E_b^t(x_{ip}, y_b)\right)^j dA_b \\
(EI)_b^j &= \int_{A_b} y_b^2 \left(E_b^t(x_{ip}, y_b)\right)^j dA_b
\end{aligned}$$

and $\omega(x_{ip})$ is the weight function of Gauss integration.

(13) Calculate the resisting sectional forces at each integration point.

$$\hat{\mathbf{D}}^j(x_{ip}) = \begin{bmatrix} \int_{A_b} \hat{\sigma}_b^j(x_{ip}, y_b) dA_b \\ -\int_{A_b} y_b \hat{\sigma}_b^j y_b(x_{ip}, y_b) dA_b \\ \int_{A_a} \hat{\sigma}_a^j(x_{ip}, y_a) dA_a \\ -\int_{A_a} y_a \hat{\sigma}_a^j y_a(x_{ip}, y_a) dA_a \\ \hat{D}_{sc}^j(x_{ip}) \\ \hat{V}_{sc}^j(x_{ip}) \end{bmatrix} \tag{5.81}$$

where $\hat{D}_{sc}^j(x_{ip})$ and $\hat{V}_{sc}^j(x_{ip})$ are determined at step (11).

(14) Calculate the stress residual.

$$\mathbf{R}_{\tilde{e}}^j = \Sigma_{ip} \omega(x_{ip}) \left[\mathbf{N}_e^T(x_{ip}) \left(\mathbf{D}^j(x_{ip}) - \hat{\mathbf{D}}^j(x_{ip})\right)\right] - \mathbf{A}\bar{\boldsymbol{\lambda}}^j - p\mathbf{A}\mathbf{A}^{\mathrm{T}}\tilde{\mathbf{e}}^j \tag{5.82}$$

(15) Calculate the displacement residual.

$$\begin{aligned}
\mathbf{R}_Q^j &= \mathbf{b}_e^{\mathrm{T}}\tilde{\mathbf{e}}^j - \mathbf{H}\mathbf{q}^j \\
\mathbf{R}_s^j &= \mathbf{b}_{se}^{\mathrm{T}}\tilde{\mathbf{e}}^j \\
\mathbf{R}_g^j &= \mathbf{b}_{ge}^{\mathrm{T}}\tilde{\mathbf{e}}^j
\end{aligned}$$

(16) Calculate the element flexibility matrix and the modified displacement residual.

$$
\begin{aligned}
\mathbf{F}^j_{ss} &= \mathbf{b}^{\mathrm{T}}_{se}[\mathbf{K}^j_s]^{-1}\mathbf{b}_{se}\\
\mathbf{F}^j_{gg} &= \mathbf{b}^{\mathrm{T}}_{ge}[\mathbf{K}^j_s]^{-1}\mathbf{b}_{ge}\\
\mathbf{F}^j_{QQ} &= \mathbf{b}^{\mathrm{T}}_{e}[\mathbf{K}^j_s]^{-1}\mathbf{b}_{e}\\
\mathbf{F}^j_{sQ} &= \mathbf{b}^{\mathrm{T}}_{se}[\mathbf{K}^j_s]^{-1}\mathbf{b}_{e}\\
\mathbf{F}^j_{gQ} &= \mathbf{b}^{\mathrm{T}}_{ge}[\mathbf{K}^j_s]^{-1}\mathbf{b}_{e}\\
\mathbf{F}^j_{sg} &= \mathbf{b}^{\mathrm{T}}_{se}[\mathbf{K}^j_s]^{-1}\mathbf{b}_{ge}\\
\mathbf{F}^j_{gs} &= \mathbf{b}^{\mathrm{T}}_{ge}[\mathbf{K}^j_s]^{-1}\mathbf{b}_{se}\\
\mathbf{F}^j_{Qs} &= \mathbf{b}^{\mathrm{T}}_{e}[\mathbf{K}^j_s]^{-1}\mathbf{b}_{se}\\
\mathbf{F}^j_{Qg} &= \mathbf{b}^{\mathrm{T}}_{e}[\mathbf{K}^j_s]^{-1}\mathbf{b}_{ge}\\
\bar{\mathbf{R}}^j_s &= \mathbf{R}^j_s + \mathbf{b}^{\mathrm{T}}_{se}[\mathbf{K}^j_s]^{-1}\mathbf{R}^j_{\tilde{e}}\\
\bar{\mathbf{R}}^j_g &= \mathbf{R}^j_g + \mathbf{b}^{\mathrm{T}}_{ge}[\mathbf{K}^j_s]^{-1}\mathbf{R}^j_{\tilde{e}}\\
\bar{\mathbf{R}}^j_Q &= \mathbf{R}^j_Q + \mathbf{b}^{\mathrm{T}}_{e}[\mathbf{K}^j_s]^{-1}\mathbf{R}^j_{\tilde{e}}\\
\mathbf{F}^j_{ssgg} &= \begin{bmatrix} \mathbf{F}^j_{ss} & \mathbf{F}^j_{sg} \\ \mathbf{F}^j_{gs} & \mathbf{F}^j_{gg} \end{bmatrix}\\
\bar{\mathbf{R}}^j_{sg} &= \begin{Bmatrix} \bar{\mathbf{R}}^j_s & \bar{\mathbf{R}}^j_g \end{Bmatrix}\\
\mathbf{f}^j &= \mathbf{F}^j_{QQ} - \begin{bmatrix} \mathbf{F}^j_{Qs} & \mathbf{F}^j_{Qg} \end{bmatrix}\left[\mathbf{F}^j_{ssgg}\right]^{-1}\begin{Bmatrix} \mathbf{F}_{sQ} \\ \mathbf{F}_{gQ} \end{Bmatrix}\\
\hat{\mathbf{R}}^j_Q &= \bar{\mathbf{R}}^j_Q - \begin{bmatrix} \mathbf{F}^j_{Qs} & \mathbf{F}^j_{Qg} \end{bmatrix}\left[\mathbf{F}^j_{ssgg}\right]^{-1}\bar{\mathbf{R}}^j_{sg}
\end{aligned}
$$

(17) Check convergence at the element level.

- If $\|\hat{\mathbf{R}}^j_Q\|$ less than or equal to tolerance set for the accuracy of the calculation, convergence at the element level is reached. Skip to step (18).
- Else, convergence at the element level is not reached. Go to step (4).

(18) Calculate the force residual.

$$\mathbf{R}^j_q = \mathbf{Q}_{ext} + \mathbf{Q}_p - \mathbf{H}^T\mathbf{Q}^j \tag{5.83}$$

.....**End local equilibrium**.....

(19) Calculate the structural nodal force and update the global stiffness matrix.

When the convergence is reached for all elements, Newton-Raphson iteration (i) is complete. Nodal forces and stiffness matrices of all elements are assembled in order to update

the global stiffness matrix and the vector of nodal forces of the structure:

$$\bar{\mathbf{R}}^i_{qg} = \text{assembly}\left(\mathbf{R}^i_q + \mathbf{H}^T[\mathbf{f}^i]^{-1}\hat{\mathbf{R}}^i_Q\right) \tag{5.84}$$

$$\bar{\mathbf{K}}^i_g = \text{assembly}\left(\mathbf{H}^T[\mathbf{f}^i]^{-1}\mathbf{H}\right) \tag{5.85}$$

(20) Check convergence at the structural level.

- If $\|\bar{\mathbf{R}}^i_{qg}\|$ less than or equal to tolerance set for the accuracy of the calculation, convergence at the element level is reached. Proceed to next load increment.
- Else, convergence at the element level is not reached. Go to step (1).

5.6 Numerical Applications

The developed finite element models including the nonlinear behavior of concrete, steel, and connectors will be assessed by comparing their results with the experimental test. Moreover, the effects of concrete with/without couple-plastic damage model are discussed. Furthermore, the influence of coupled /uncoupled connector model is illustrated. The constitutive model of steel, concrete and connector adopted in the following applications are shown as follows:

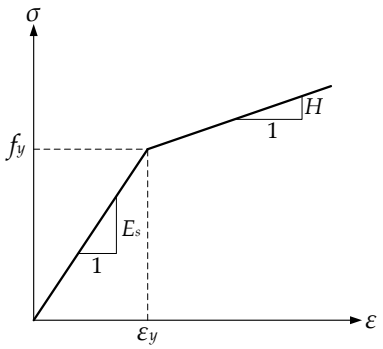

(A) Steel

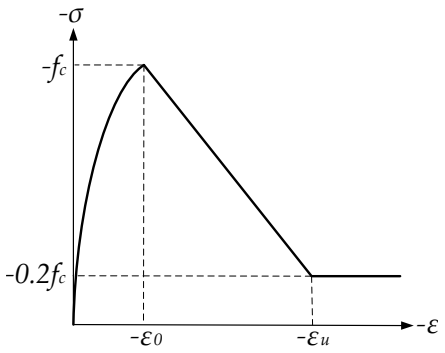

(B) Concrete in compression

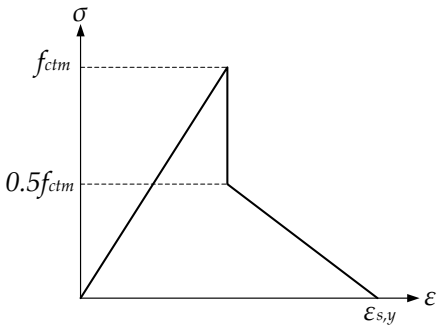

(C) Concrete in tension

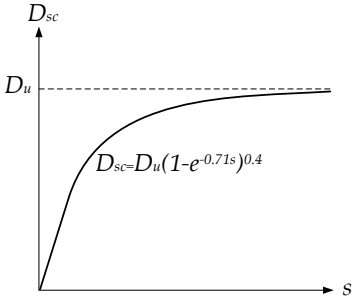

(D) Load-slip relationship

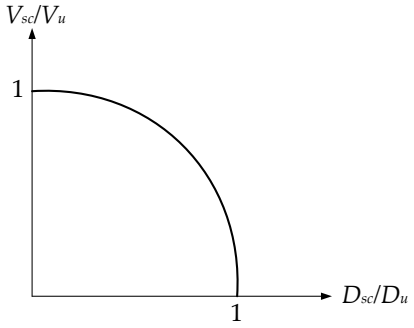

(E) Interaction shear and tensile force of connector

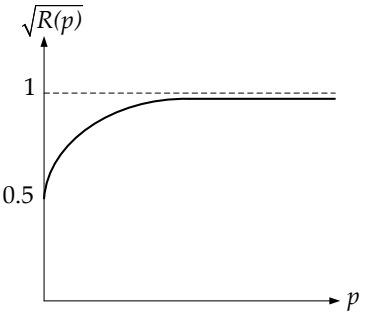

(F) Relation between p and R_p

FIGURE 5.3: Constitutive relationship of materials

5.6.1 Simply supported beam

The composite beam PI4, which was studied by Abdel Aziz [75] has 5m length with a simply supported condition. This composite beam is constructed by 800 mm×100 mm concrete slab and IPE400 steel beam with the geometrical details in Fig. 5.4. For this loading case, a concentrated load P is applied at mid-span of beam.

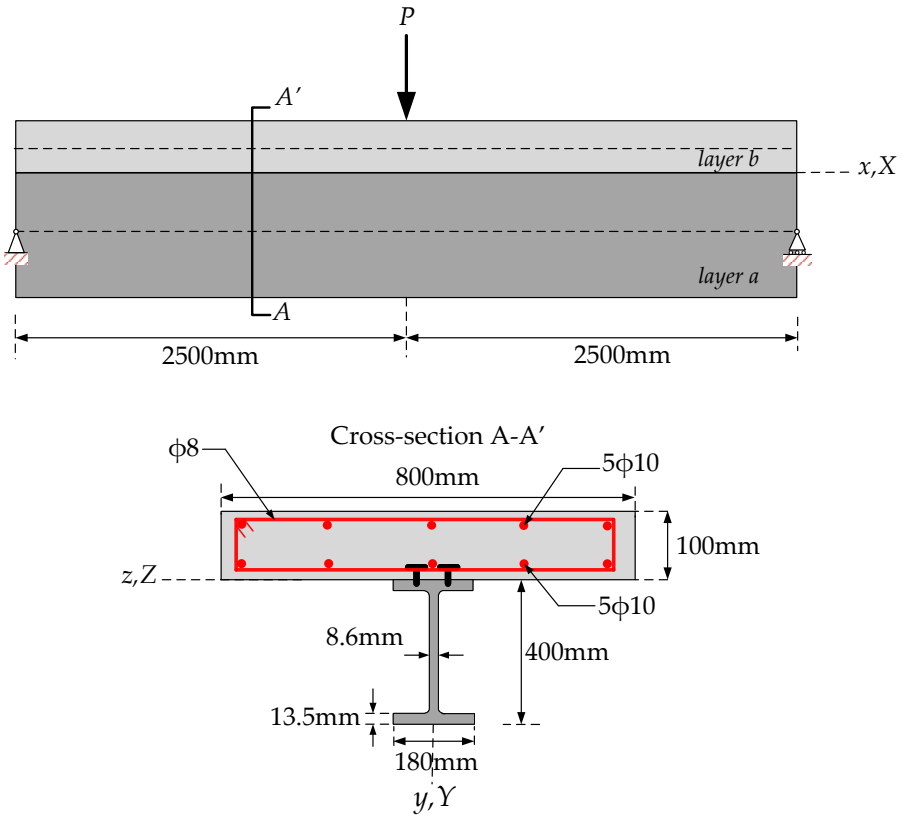

FIGURE 5.4: Simply supported composite beam PI4 [75]

The spacing between the connectors is 650 mm. We propose to calculate the shear and tensile strength of connector by using Eqs. (4.83) and (4.89), respectively. The shear and tensile stiffness of connector are calculated by Eqs. (4.87) and (4.90). The materials properties are shown in Table 5.1. The displacement based and mixed formulation are presented in this chapter and implemented into co-rotational framework (see Chapter 3). The analysis of beam PI4 is performed using the displacement-based with various number of elements: 2, 4, 8 and 12 elements and mixed formulation approach with 2 elements. It is worth noting that the continuous connection model is adopted. Figure 5.5 presents the relationship of applied force-vertical displacements at mid-span of composite beam with different computations as follows:

- EXP-PI4: results by experimental data of Abdel Aziz [75].

TABLE 5.1: Materials properties details (PI4) Abdel Aziz [75]

Material	Parameter	Value
Steel	Elastic mod. E_s	210 GPa
	Hard. mod. H	1.05 GPa
	Yield stress:	
	- Flange	245 MPa
	- Web	260 MPa
	- Reinforcement	370 MPa
	Ultimate stress:	
	- Flange	361 MPa
	- Web	372 MPa
	- Reinforcement	375 MPa
	Yield strain $\varepsilon_{s,y}$	0.0025

Material	Parameter	Value
Concrete	Compressive str. f_c	34.7 MPa
	Elastic mod. E_c	33.3 GPa
	Tensile str. f_{ctm}	3.02 MPa
	Initial strain ε_0	0.0026
	Ultimate strain ε_u	0.0040
Connector	Stud diameter d_s	19 mm
	Stud length l_s	80 mm
	Shear strength D_u	126 N/mm
	Tensile strength V_u	161 N/mm
	Shear stiffness K_h	66 MPa
	Tensile stiffness K_v	27.1 MPa

- FE1-PI4-2E, FE1-PI4-4E, FE1-PI4-8E, FE1-PI4-12E: results by displacement-based formulation using 2, 4, 8, 12 elements, respectively.
- FE2-PI4: results by mixed formulation.

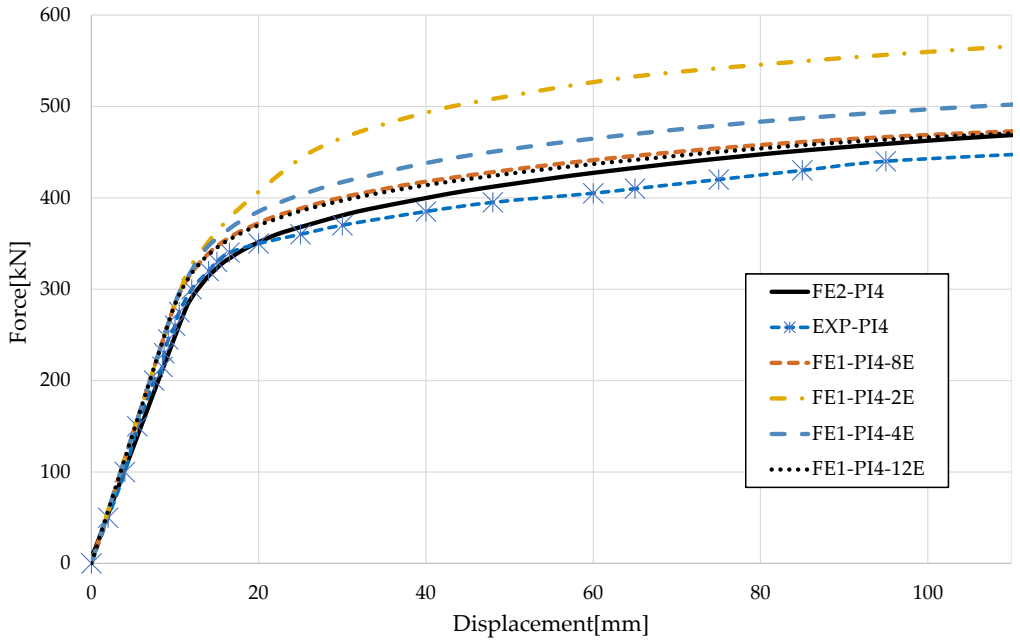

FIGURE 5.5: Comparison of load-vertical displacement

It can be seen that all formulations give essentially the same force-displacement curve in elastic range. Exceed that, we observe that more elements are required when the displacement-based formulation is used. In the results shown by Fig. 5.5, it requires 8 or 12 elements for displacement-based formulation to get a satisfactory result. On the other hand, the use of 2 elements in mixed formulation gives a good agreement to the experimental results.

Next, in Fig. 5.6, a symmetrical slip distributions in both methods are pretty similar and accurate compared to the experiment [75].

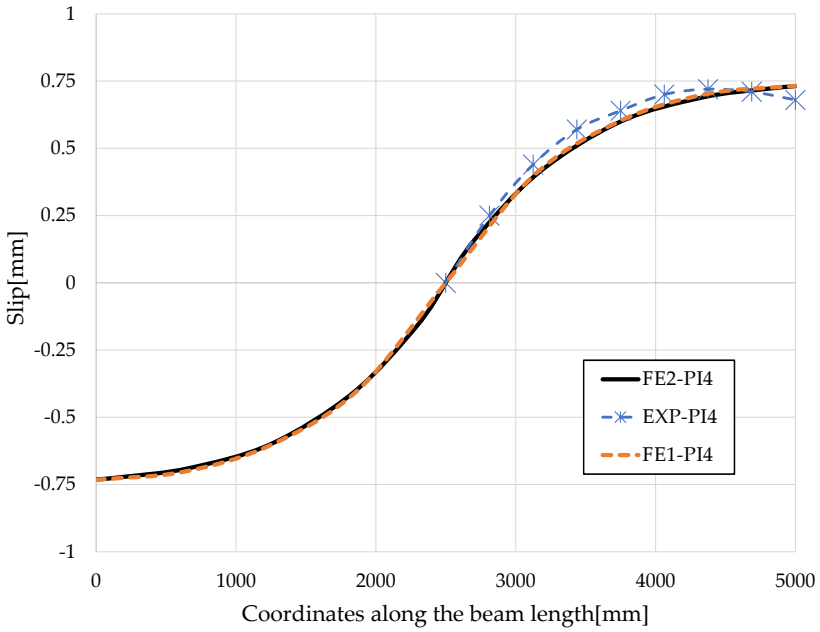

FIGURE 5.6: Slip distribution of beam PI4 at P=297 kN

The axial force and moment of layer b at P=297 kN are depicted in Figs. 5.7 and 5.8, respectively. It is worth noting that, similar to the vertical displacement and slip distribution, the results obtained using only 2 elements in the mixed formulation exhibit similarity to those obtained using 8 elements in the displacement-based formulation.

5.6.2 Continuous composite beam CTB1

In this example, we will consider the two-span-continuous composite beam CTB1 (4m and 5m long) designed and tested by Ansourian [76]. We denote the 4m and 5m span of the beam by short and long span, respectively. The beam is subjected to a single concentrated load P at the middle of the short span, as depicted in Fig. 5.9.

The cross-section of CTB1 consisted of an IPE200 steel beam and a concrete slab 800mm $\times$ 100mm (details are given in Fig. 5.9). The connection is made of 66 welded studs (19mm

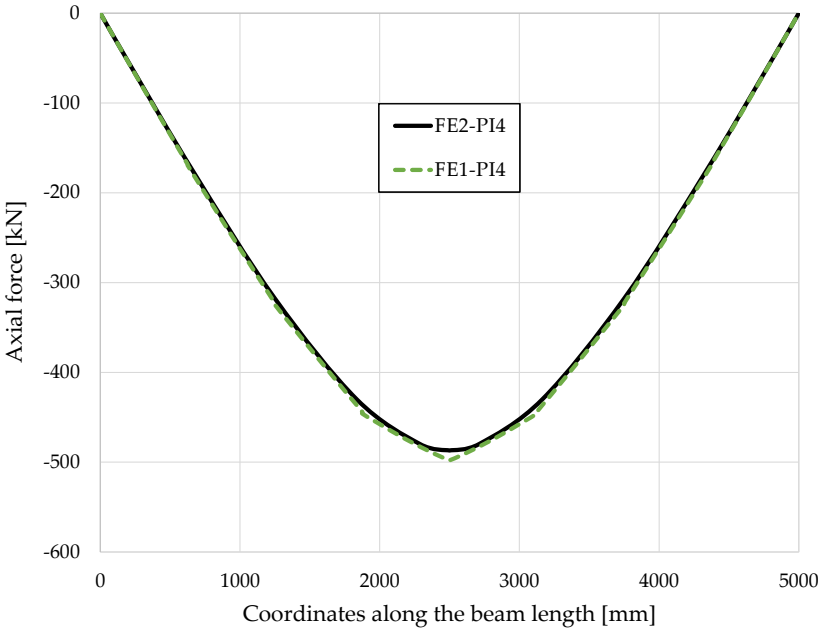

FIGURE 5.7: Axial force of layer *b* of beam PI4 at *P*=297 kN

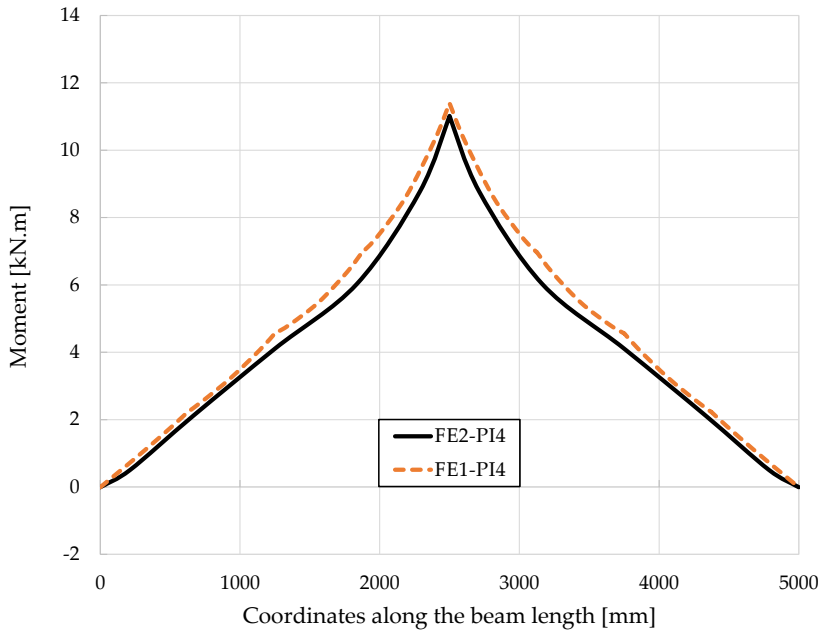

FIGURE 5.8: Moment of layer *b* of beam PI4 at *P*=297 kN

$\times$ 75mm), resulting in a degree of shear connection of 150% in positive bending and 160% in negative bending. The shear and tensile strength as well as the stiffness are calculated by Eqs. (4.82), (4.87), (4.88) and (4.90). For hogging region, the longitudinal reinforcement areas at the top and bottom of the cross-section are 800 mm^2 and 316 mm^2, respectively. The sagging cross-section contains also 160 mm^2 of reinforcement.

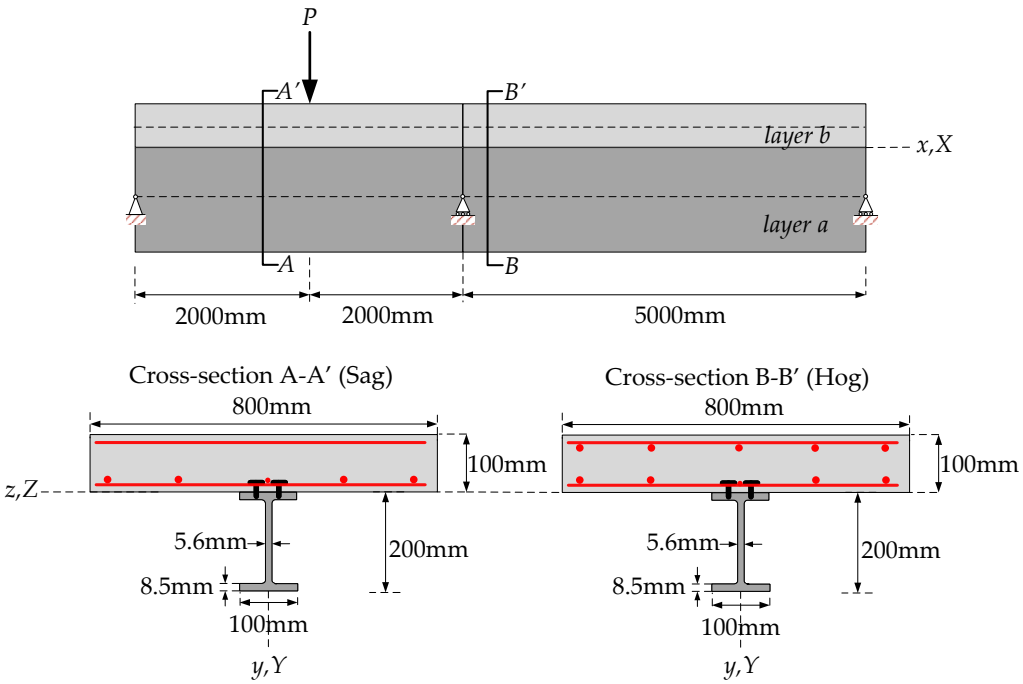

FIGURE 5.9: Continuous composite beam CTB1

In this section, we will focus on the behavior of concrete, a key material in the numerical analysis of composite beam CTB1. Specifically, we intend to explore the influence of the concrete damage in simulating the behavior of composite beam. For this purpose, we will compare the performance of two different concrete models: the Kent and Park plasticity model and Kent and Park plastic-damage model. The materials properties are presented in Table 5.2. The mixed formulation presented in this chapter and implemented into co-rotational framework (see Chapter 3) with 8 elements is used. Figure 5.10 presents a comparison of force-displacement curves obtained with experimental test and the proposed finite element model. In Fig. 5.10, the vertical displacements at the middle of short and long span are indicated by Sag and Hog, respectively. The FE model considering concrete damage is denoted by FE3 and FE2 corresponds to FE model without considering concrete damage. For incorporating the damage effect, the algorithm in Section 4.3.5 is adopted.

It can be seen that both FE models give a good agreement with the experimental results of [76] and there is little variation between both FE models. It is what is expected since the

TABLE 5.2: Materials properties details (CTB1)

Material	Parameter	Value
Steel	Elastic mod. E_s	210 GPa
	Hard. mod. H	1.05 GPa
	Yield stress:	
	- Flange	277 MPa
	- Web	340 MPa
	- Reinforcement	430 MPa
	Ultimate stress:	
	- Flange	421 MPa
	- Web	440 MPa
	- Reinforcement	533 MPa
	Yield strain $\varepsilon_{s,y}$	0.0025

Material	Parameter	Value
Concrete	Compressive str. f_c	24.6 MPa
	Elastic mod.E_c	29.69 GPa
	Tensile str.f_{ctm}	2.55 MPa
	Initial strain ε_0	0.0021
	Ultimate strain ε_u	0.0035
Connector	Stud diameter d_s	19 mm
	Stud length l_s	109 mm
	Shear strength D_u	656 N/mm
	Tensile strength V_u	543 N/mm
	Shear stiffness K_h	293 MPa
	Tensile stiffness K_v	134 MPa

composite beam is subjected to monotonic loading and the local unloading on the monitored cross-sections is very limited.

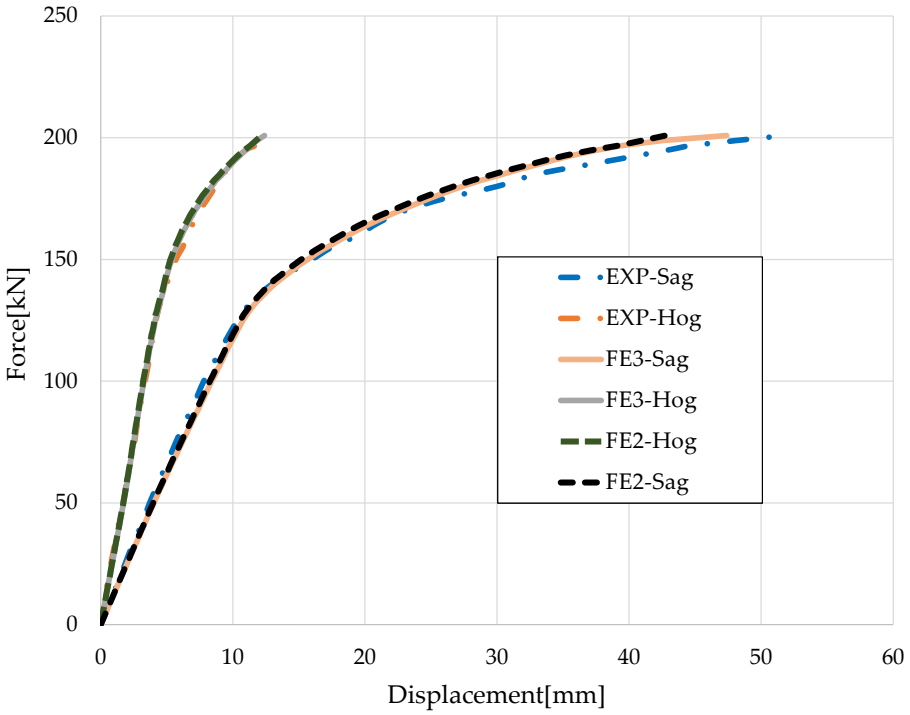

FIGURE 5.10: Force-displacement curve in plastic concrete model with/without damage

5.6.3 Influence of interaction behavior of connectors in continuous composite beam

For this example, the behaviors of the coupled and uncoupled connector models are examined. To do this, the continuous composite beam CTB1 is reanalysed using the displacement-based formulation. However, the partial interaction i.e. a very low degree of shear connection is considered. In FE model, the beam is meshed with 8 elements. The material properties outlined in Section 5.6.2 are used, except the ones of the connector. To facilitate the observation of distinct behaviors between computations employing the coupled and uncoupled connector models, the strengths and stiffnesses of the connector (D_u, V_u, K_h and K_v) are divided by a factor of 10. Figure 5.11 presents the comparison between FE results with both connector models (FE4 for the results with coupled connector model and FE5 for the ones with uncoupled connector model). We observe that both models provide an ultimate

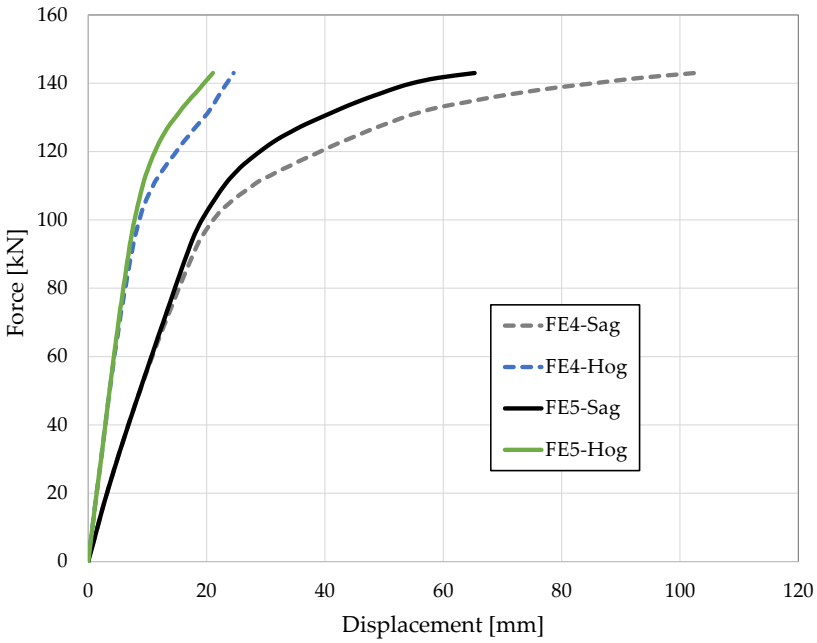

FIGURE 5.11: Force-displacement curve by coupled/uncoupled connector model

load of 143 kN. At this load level, we observe a significant difference between the vertical displacements obtained with the coupled and uncoupled models. This can be explained by the distribution of slip and uplift at P = 143 kN depicted in Figs. 5.12 and 5.13. As expected, in Fig. 5.12, the coupled connector model provided larger slip value than the uncoupled one. This is because the strength of the connector is reduced in the coupled model. Besides, as illustrated in Fig. 5.13, the contact algorithm handled the non-penetrated condition very well, resulting in a maximum penetration of 0.0015mm which is very small and negligible.

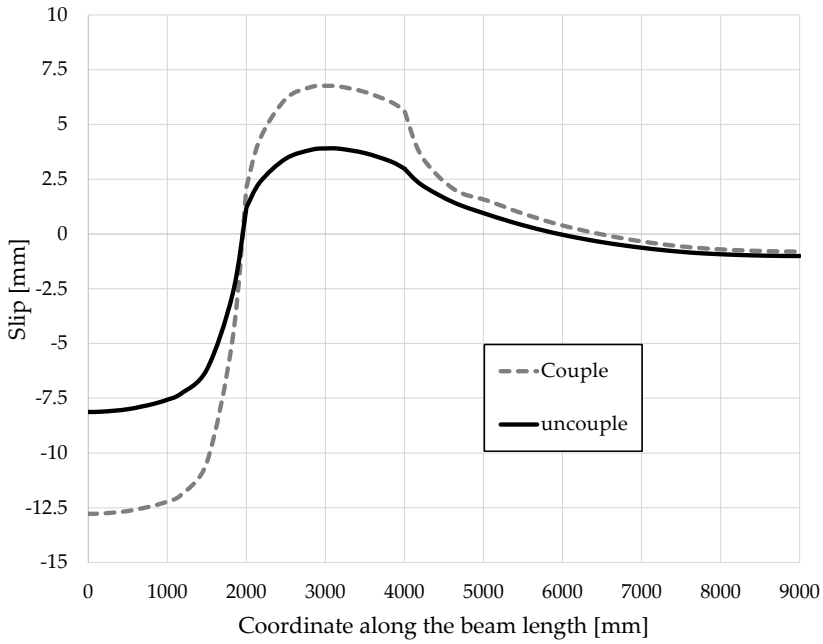

FIGURE 5.12: Slip distribution at P=143 kN.

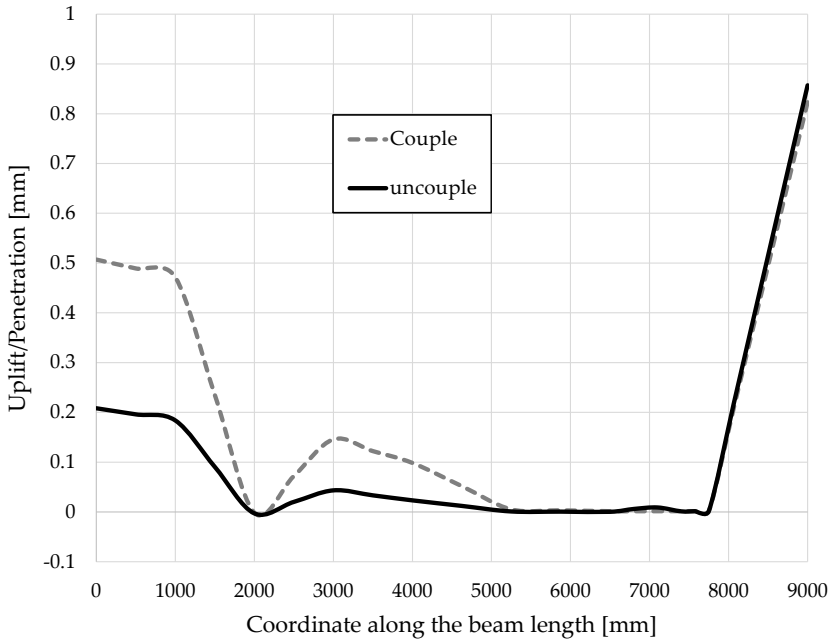

FIGURE 5.13: Uplift distribution at P=143 kN.

Moreover, for both Fig. 5.12 and Fig. 5.13, the values of slip and uplift at the starting extremity ($x = 0$) are significantly different, and we will continuously observe their evolution at the starting extremity with the imposed load from the initial stage ($P = 0$ kN) until reaching 143

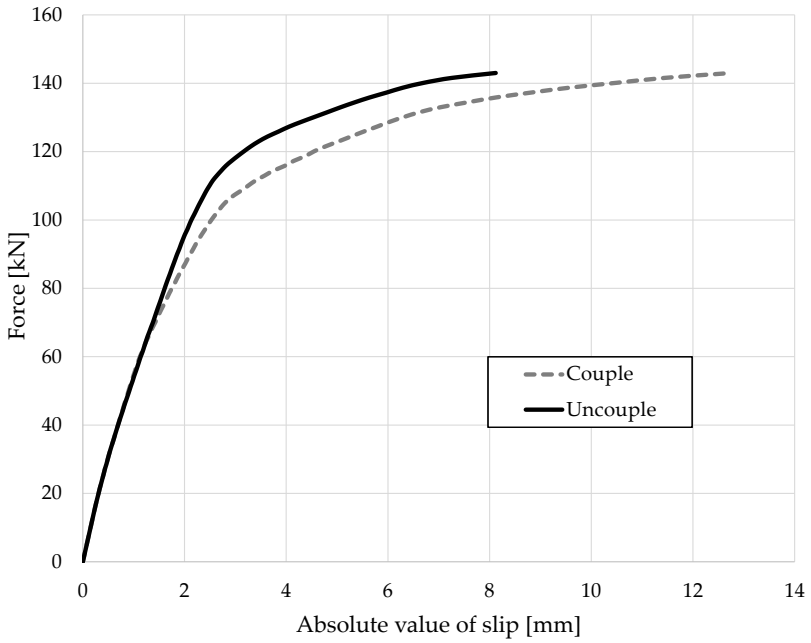

FIGURE 5.14: Force-slip curve in coupled/uncoupled connector model

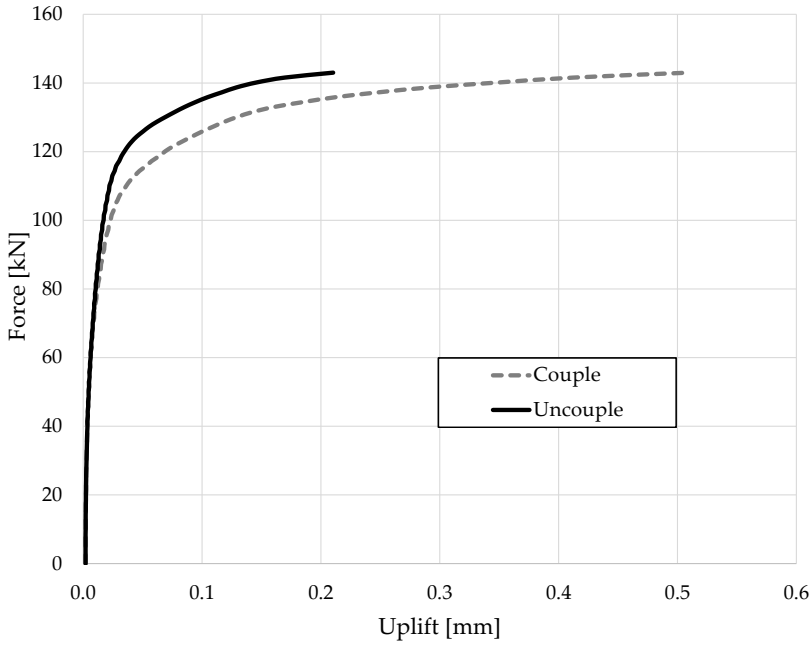

FIGURE 5.15: Force-uplift curve in coupled/uncoupled connector model

kN. Fig. 5.14 and Fig. 5.15 illustrate the force-slip and force-uplift curves, respectively. The results indicate that there is no difference in slip and uplift when the imposed load is within the elastic range. However, they become significantly different in plastic domain.

5.7 Conclusion

This chapter presents the development of displacement-based and mixed formulations for nonlinear analysis of two-layered beams taking into account slip and uplift. The continuous bond model considering two-directional spring distributed along the interface to represent the force transfer mechanisms is adopted in both formulations. The node-to-node contact conditions are imposed by augmented Lagrangian method in these models. As demonstrated in numerical applications, the computation employed displacement-based and mixed formulations with geometrical linearity yielded a good agreement with experimental results. However, unlike the mixed formulation, the displacement-based formulation required more number of elements to obtain satisfactory results. Another key aspect is the importance of the concrete material, particularly in compression. By incorporating the plastic-damage model, the FE model yielded more accurate results.

In the model of the connector, the coupled and uncoupled models exhibit a good agreement during the elastic deformation stage. However, beyond that stage, the connector behaves more stiff with the uncoupled connector model.

Chapter 6

General conclusions and perspectives

6.1 Summary

This thesis presented a new composite two-layered beam formulation taking into account slip and uplift at the inter-layer interface. The connector elements were represented by two-directional springs (horizontal and vertical directions). The horizontal spring parallel to the layer interface captured the slip, while the vertical spring orthogonal to the interface captured the uplift. Two connection models (discrete and continuous bond model) were considered. For both connection models, the governing equations of composite steel-concrete beams were derived and solved to obtain a closed-form solution. As a result, the "exact" stiffness matrix could be obtained. To ensure the satisfaction of the non-penetrated condition, the "Contact algorithm" was used. To account for geometrical non-linearity, a co-rotational method was adopted. The nonlinear finite element analysis was performed using displacement-based and mixed formulations. The fiber discretization for the sections of the composite beam was adopted. A plastic flow rule considering the coupling between slip and uplift was use to model of the interaction between longitudinal shear forces and the tensile force of the connector. For both formulations, a corresponding algorithm was proposed to solve the penetrated problem. Finally, the numerical applications have demonstrated the robustness of the proposed formulations.

6.2 Concluding remarks

It was observed that both discrete and continuous bond models provided accurate results, with the exception that the discrete bond model required a larger number of elements to produce results similar to the continuous bond model. For the uplift/penetration problems in both bond models, under certain load conditions, penetration increased as the transverse stiffness of the connector weakened. However, the slip at the interface was not significantly affected by the value of the transverse stiffness. In practical construction applications, penetration was not permitted. The contact algorithm such as the penalty and augmented Lagrangian method should be used to address this issue, resulting in minimal and negligible

penetration during contact situations. Furthermore, the slip distribution may change its form before and after applying the contact algorithm, while its extremities do not exhibit significant changes.

The comparison of penalty method (PM) and augmented Lagrangian method (ALM) used to deal with the non-penetrability between the layers was made. The results has indicated that ALM required more iterations to converge compared to PM. However, despite its slower convergence rate, ALM has fulfilled the non-penetrability condition, thereby preventing unrealistic penetration between the layers. Moreover, the impact of uplift on the elastic buckling behavior of a simply supported two-layer beam has been investigated. It was found that the buckling load of the composite beam was significantly influenced by the uplift stiffness of the connectors. For composite members with low uplift stiffness, the uplift between the layers was large, and the layer with low flexural stiffness was susceptible to buckling before global buckling of the composite beam took place. Furthermore, when considering the cantilever beam under uniform bending of the lower layer, a small uplift was observed near the tip of the beam. However, compared to the analytical solution of a vertically unseparated two-layer cantilever beam, this small uplift had minimal effects.

In nonlinear analysis, it has been demonstrated that the computations with displacement-based formulation was simple, but it required more numbers of elements to obtain accurate results. Besides, the mixed formulation required fewer elements to have a good agreement with experimental tests. It has been shown that considering the uncoupled behavior of the connector under combined tension and shear may over estimate the stiffness of the composite beam, specifically at the plastic range and when uplift occurs.

6.3 Perspectives

In the context of the forthcoming research, the two key perspectives for observation will be identified. Firstly, the extension of this model will be considered in three-dimensional analysis, based on the assumption that our composite beam will undergo a deformation in the (x,y,z) plan. This consideration will also impact the constraints of the non-penetrated condition, as the gaps will exist in two directions. Secondly, the complexity of the 3D material model will be taken into account.

For the analysis in 3D approach, besides u_i, v_i and $\theta_{z,i}$ as mentioned in Section 2.2.1, other component of displacement fields are presented as: transverse displacement, twist angle and out-plan rotation denoted by $w_{b,i}$, $\theta_{x,i}$ and $\theta_{z,i}$, respectively, see figure Fig. 6.1.

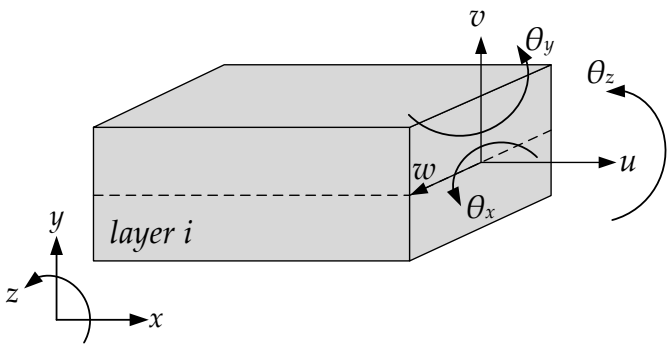

FIGURE 6.1: Configuration of beam i in 3D

In this configuration, the twist angle $\theta_{x,i}$ and out-of-plane rotation $\theta_{z,i}$ will be considered to develop new slip and gap functions that are associated with the constraints imposed by the non-penetration condition. The computational process will be more complicated and will allow us to study the behavior of the composite beam using three-dimensional approach.

Beside the methods for treating the penetration between layers as mentioned in Section 2.5, there exist alternative methods that can be employed to mitigate the issue of penetration between composite layers. These methods include:

- The Penalty-Contact Algorithm (PCA): an extension of the Penalty Method that can be used to model contact behavior between two surfaces. This method involves solving the governing equations subject to a set of inequality constraints that ensure that the two surfaces do not penetrate each other.
- The Smoothed Particle Hydrodynamics (SPH) Method: a mesh-free method that can be used to model contact behavior between two surfaces. This method involves representing the surfaces using a set of particles and then solving the governing equations subject to a set of constraints that ensure that the two surfaces do not penetrate each other.

Both of these methods are recognized approaches for addressing surface penetration issues. A comparative analysis of the advantages of these methods in comparison to our current study methodology would be highly beneficial.

Appendix A

Derivation of the global inter-layer slip and uplift variations

Let us consider the case where the prescribed displacements or rotation are applied at the nodes c^i which is located at the interface of the two layers as illustrated in Figure A.0.1. From point a^i to c^i, it requires a rigid link and a change of the degrees of freedom. From

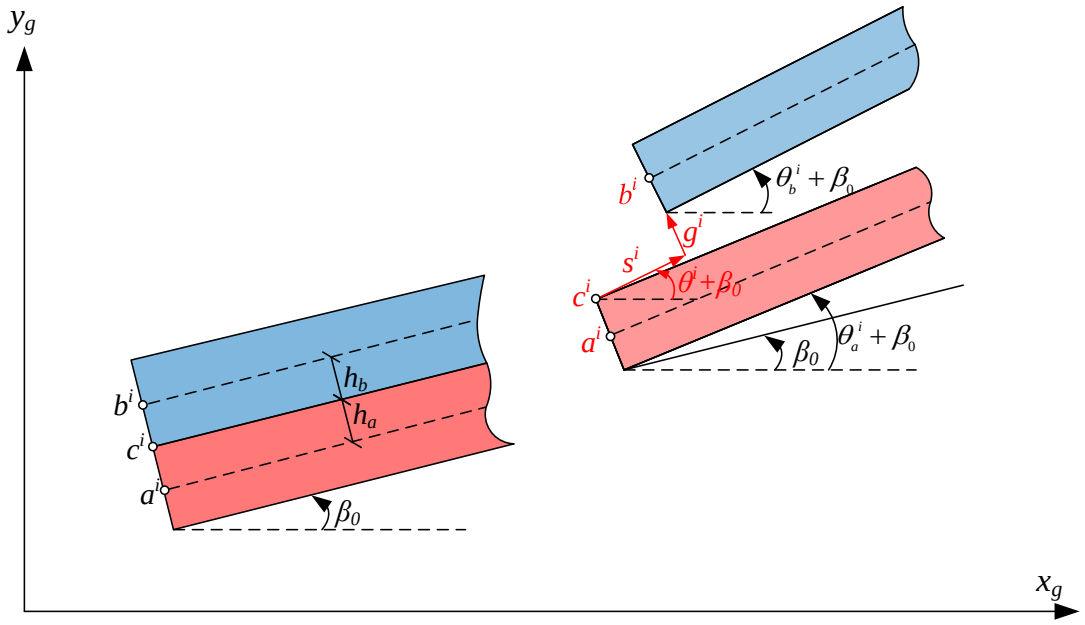

FIGURE A.0.1: Configuration of global inter-layer slip and uplift

Figure A.0.1, the position of point c^i in the deformed configuration is given by:

$$\begin{bmatrix} u_c^i \\ v_c^i \end{bmatrix} + \begin{bmatrix} x_c^i \\ y_c^i \end{bmatrix} = \begin{bmatrix} u_a^i \\ v_a^i \end{bmatrix} + \begin{bmatrix} x_a^i \\ y_a^i \end{bmatrix} + \begin{bmatrix} -\sin(\beta_0 + \theta_a^i)h_a \\ \cos(\beta_0 + \theta_a^i)h_a \end{bmatrix} \tag{A.1}$$

Or,

$$\begin{bmatrix} \delta u_c^i \\ \delta v_c^i \end{bmatrix} = \begin{bmatrix} \delta u_a^i \\ \delta v_a^i \end{bmatrix} + \begin{bmatrix} -\cos(\beta_0 + \theta_a^i) h_a \\ -\sin(\beta_0 + \theta_a^i) h_a \end{bmatrix} \delta\theta_a^i \tag{A.2}$$

On the other hand, the position of point c^i in the deformed configuration can be expressed in function of slip and uplift as:

$$\begin{bmatrix} u_c^i \\ v_c^i \end{bmatrix} + \begin{bmatrix} x_c^i \\ y_c^i \end{bmatrix} = \begin{bmatrix} u_b^i \\ v_b^i \end{bmatrix} + \begin{bmatrix} x_b^i \\ y_b^i \end{bmatrix} + \begin{bmatrix} \sin(\beta_0 + \theta_b^i) h_b \\ -\cos(\beta_0 + \theta_b^i) h_b \end{bmatrix} + \begin{bmatrix} \sin(\beta_0 + \theta^i) g^i \\ -\cos(\beta_0 + \theta^i) g^i \end{bmatrix} + \begin{bmatrix} -\cos(\beta_0 + \theta^i) s^i \\ -\sin(\beta_0 + \theta^i) s^i \end{bmatrix} \tag{A.3}$$

Replacing Equation A.2 into the variation of Equation A.3 and rearranging, we obtain a system of equations as follow:

$$\begin{bmatrix} \delta u_a^i \\ \delta v_a^i \end{bmatrix} - \begin{bmatrix} \delta u_b^i \\ \delta v_b^i \end{bmatrix} - \begin{bmatrix} A \\ B \end{bmatrix} \delta\theta_a^i - \begin{bmatrix} C \\ D \end{bmatrix} \delta\theta_b^i + \begin{bmatrix} \cos(\beta_0 + \theta_b^i) \\ \sin(\beta_0 + \theta_b^i) \end{bmatrix} \delta s^i - \begin{bmatrix} \sin(\beta_0 + \theta^i) \\ -\cos(\beta_0 + \theta^i) \end{bmatrix} \delta g^i = 0 \tag{A.4}$$

where,

$$A = h_a \cos(\beta_0 + \theta_a^i) + \frac{g^i}{2} \cos(\beta_0 + \theta^i) + \frac{s^i}{2} \sin(\beta_0 + \theta^i)$$

$$B = h_a \sin(\beta_0 + \theta_a^i) + \frac{g^i}{2} \sin(\beta_0 + \theta^i) - \frac{s^i}{2} \cos(\beta_0 + \theta^i)$$

$$C = h_b \cos(\beta_0 + \theta_b^i) + \frac{g^i}{2} \cos(\beta_0 + \theta^i) + \frac{s^i}{2} \sin(\beta_0 + \theta^i)$$

$$D = h_b \sin(\beta_0 + \theta_b^i) + \frac{g^i}{2} \sin(\beta_0 + \theta^i) - \frac{s^i}{2} \cos(\beta_0 + \theta^i)$$

From Equation A.4, we can compute the relation of the variation of global inter-layer slip and uplift in terms of displacements and rotations at the centroid of the cross-section of both layer a^i and b^i as follow:

$$\begin{aligned} \delta s^i =& \delta u_b^i \cos\left(\beta_0 + \theta^i\right) + \delta v_b^i \sin\left(\beta_0 + \theta^i\right) - \delta u_a^i \cos\left(\beta_0 + \theta^i\right) - \delta v_a^i \sin\left(\beta_0 + \theta^i\right) \\ &+ \left[h_a \cos\left(\frac{\theta_a^i - \theta_b^i}{2} \right) + \frac{g^i}{2} \right] \delta\theta_a^i + \left[h_b \cos\left(\frac{\theta_b^i - \theta_a^i}{2} \right) + \frac{g^i}{2} \right] \delta\theta_b^i \end{aligned} \tag{A.5}$$

$$\begin{aligned} \delta g^i =& -\delta u_b^i \sin\left(\beta_0 + \theta^i\right) + \delta v_b^i \cos\left(\beta_0 + \theta^i\right) + \delta u_a^i \sin\left(\beta_0 + \theta^i\right) - \delta v_a^i \cos\left(\beta_0 + \theta^i\right) \\ &+ \left[h_a \sin\left(\frac{\theta_a^i - \theta_b^i}{2} \right) - \frac{s^i}{2} \right] \delta\theta_a^i + \left[h_b \sin\left(\frac{\theta_b^i - \theta_a^i}{2} \right) - \frac{s^i}{2} \right] \delta\theta_b^i \end{aligned} \tag{A.6}$$

Appendix B

Interpolation of displacement fields

The interpolation of axial displacement fields through the use of quadratic functions and Hermite interpolation functions for vertical displacement is a commonly employed technique in the context of finite element analysis. In Section 5.4, the selection of only the nodes at the two extremities, i.e., utilizing solely the first degree of the quadratic function, can lead to issues with curvature locking. This concern may be resolved by introducing an additional node at the midpoint of the element. The accuracy of the resulting approximation is contingent upon the number of nodes utilized in the interpolation, with a greater number of nodes resulting in improved accuracy. Upon obtaining the approximation, it may be employed to determine the stress and strain fields within the element. This approach is frequently applied in the field of structural analysis and has demonstrated effectiveness in a wide range of applications.

Recalling the configuration with the 18 DOF by adding the middle note of element as Fig. B.0.1:

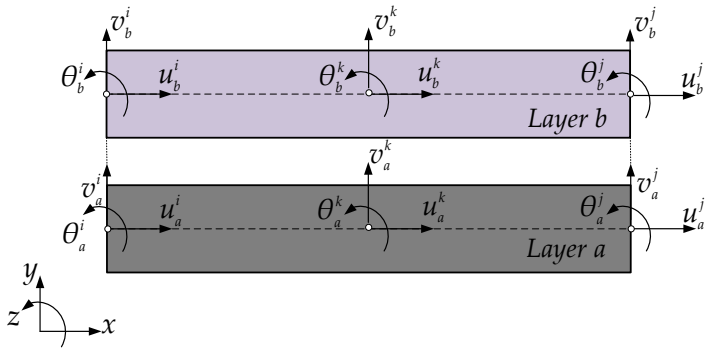

FIGURE B.0.1: Displacement field by adding nodes at middle of elements

B.1 Axial displacement u

The quadratic interpolation is a method of approximating a function using a quadratic polynomial. It is a simple and commonly used technique for interpolating data points that lie on a smooth curve.

Let us presume that the axial displacement, denoted by $u(x)$, is a quadratic function of the position along the beam, x. Specifically, we may express $u(x)$ as a second degree polynomial, i.e.,

$$u(x) = a_0 + a_1 x + a_2 x^2 \tag{B.1}$$

where a_0, a_1, and a_2 are constants that we need to determine based on the boundary conditions.

Using boundary conditions, we can solve for the constants a_0, a_1, and a_2:

$$\begin{aligned} u(x=0) = u_0 \quad &\Rightarrow \quad a_0 = u_0 \\ u(x=L) = u_L \quad &\Rightarrow \quad a_0 + a_1 L + a_2 L^2 = u_L \\ u\left(x = L/2\right) = u_{L/2} \quad &\Rightarrow \quad a_0 + \frac{a_1 L}{2} + \frac{a_2 L^2}{4} = u_{L/2} \end{aligned}$$

Solving for a_0, a_1, and a_2, we get:

$$\begin{aligned} a_0 &= u_0 \\ a_1 &= \frac{u_L - u_0 - a_2 L^2}{L} \\ a_2 &= \frac{2(u_0 - u_{L/2} + u_L)}{L^2} \end{aligned}$$

Substituting these values back into the original equation, we get:

$$u(x) = \left(\frac{2x^2}{L^2} - \frac{2x}{L}\right) u_L + \left(1 - \frac{3x^2}{L^2} + \frac{2x^3}{L^3}\right) u_0 + \left(\frac{4x}{L} - \frac{4x^2}{L^2}\right) u_{L/2}$$

B.2 Vertical displacement v

Hermite interpolation is a widely used method for interpolation in displacement fields, especially in the case of vertical displacement and rotation. The method involves interpolating a function and its derivative simultaneously. The Hermite interpolation function is constructed by letting the function be a linear combination of basis functions such as the displacement and rotation of neighboring points. The coefficients of the basis functions are then determined by solving a system of linear equations.

The vertical displacement in function of x is presented as follows:

$$v(x) = a_3 + a_4 x + a_5 x^2 + a_6 x^3 + a_7 x^4 + a_8 x^5 \tag{B.2}$$

where $a_3, \ldots, a_8$ are constants that we need to figure out with the boundary conditions:

$$\begin{aligned}
v(x = 0) &= v_0 \\
v(x = L) &= v_L \\
v(x = L/2) &= v_{L/2} \\
v'(x = 0) &= \theta_0 \\
v'(x = L) &= \theta_L \\
v'(x = L/2) &= \theta_{L/2}
\end{aligned}$$

Making uses all boundary conditions and insert to Eq. (B.2), we can obtain:

$$\begin{aligned}
a_3 &= v_0 \\
a_4 &= \theta_0 \\
a_5 &= \frac{7v_L}{L^2} - \frac{\theta_L}{L} + \frac{8\theta_{L/2}}{L} - \frac{23v_0}{L^2} - \frac{6\theta_0}{L} + \frac{16v_{L/2}}{L^2} \\
a_6 &= -\frac{34v_L}{L^3} + \frac{5\theta_L}{L^2} + \frac{32\theta_{L/2}}{L^2} - \frac{66v_0}{L^3} + \frac{13\theta_0}{L^2} - \frac{32v_{L/2}}{L^3} \\
a_7 &= \frac{52v_L}{L^4} - \frac{8\theta_L}{L^3} - \frac{40\theta_{L/2}}{L^3} - \frac{68v_0}{L^4} - \frac{12\theta_0}{L^3} + \frac{16v_{L/2}}{L^4} \\
a_8 &= -\frac{24v_L}{L^5} + \frac{4\theta_L}{L^4} + \frac{16\theta_{L/2}}{L^4} + \frac{24v_0}{L^5} + \frac{4\theta_0}{L^4}
\end{aligned}$$

Replacing all constants $a_3, \ldots, a_8$ back to Eq. (B.2), we can express it in simplify as:

$$\begin{aligned}
v(x) = &\left(\frac{66x^3}{L^3} - \frac{23x^2}{L^2} - \frac{68x^4}{L^4} + \frac{25x^5}{L^5} + 1\right) v_0 + \left(x - \frac{6x^2}{L} + \frac{13x^3}{L^2} - \frac{12x^4}{L^3} + \frac{4x^5}{L^4}\right) \theta_0 \\
&+ \left(\frac{7x^2}{L^2} - \frac{34x^3}{L^3} + \frac{52x^4}{L^4} - \frac{25x^5}{L^5}\right) v_l + \left(\frac{5x^3}{L^2} - \frac{x^2}{L} - \frac{8x^4}{L^3} + \frac{4x^5}{L^4}\right) \theta_l \\
&+ \left(\frac{16x^2}{L^2} - \frac{32x^3}{L^3} + \frac{16x^4}{L^4}\right) v_{L/2} + \left(\frac{32x^3}{L^2} - \frac{8x^2}{L} - \frac{40x^4}{L^3} + \frac{16x^5}{L^4}\right) \theta_{L/2}
\end{aligned}$$

Appendix C

Approaches to Numerical Integration

This section demonstrates the approaches aided in numerical integration in the context of the nonlinear finite element method, as described in Chapter 5. The materials are organized in order to explain 2D Gaussian quadrature, Gauss-Lobatto rules, and Lagrange interpolating polynomials.

C.1 2D Gaussian quadrature

The basic idea of Gaussian quadrature is to approximate the integral by a weighted sum of function values at a set of predetermined points within the interval. The Gaussian quadrature for a square domain ($[-1,+1] \times [-1,+1]$) can be conducted as the unit interval.

$$\int_{-1}^{1}\int_{-1}^{1} g(\gamma,\eta)d\gamma d\eta \approx \sum_{i=1}^{n}\sum_{j=1}^{n} g(\gamma_i,\eta_i)\omega_i\omega_j \tag{C.1}$$

where γ and η denotes the coordinate in horizontal and vertical direction, respectively. Theoretically, the number of integration points may be chosen different for γ and η direction. However it is more convenient in practice to select the same n number of integration points in each direction.

TABLE C.1: Coordinates and weights of the Gauss points

Point	γ	η	Weight
$1(i=1,j=1)$	$-\frac{\sqrt{3}}{3}$	$-\frac{\sqrt{3}}{3}$	$1(1\times 1)$
$2(i=1,j=2)$	$-\frac{\sqrt{3}}{3}$	$\frac{\sqrt{3}}{3}$	$1(1\times 1)$
$3(i=2,j=1)$	$\frac{\sqrt{3}}{3}$	$-\frac{\sqrt{3}}{3}$	$1(1\times 1)$
$4(i=2,j=2)$	$\frac{\sqrt{3}}{3}$	$\frac{\sqrt{3}}{3}$	$1(1\times 1)$

Integration on a convex quadrilateral domain can be easily transformed into integration on the square domain.

$$\int_{\Omega} f(x,y)d\Omega = \int_{-1}^{1}\int_{-1}^{1} f(\gamma,\eta)\,|J|\,d\gamma d\eta \tag{C.2}$$

where $|J|$ is the determinant of Jacobian matrix J, which simply contains the derivatives of x and y with respect to γ and η.

C.2 Gauss-Labatto rules

Lagrange quadrature, also known as Gauss-Lagrange quadrature, is a numerical integration method used to approximate the definite integral of a function over a given interval. It involves the use of a weighted sum of function values at specific points within the integration interval, with the weights and points determined by the properties of a Lagrange polynomial. Lobatto quadrature is a numerical integration method. It is named after Dutch

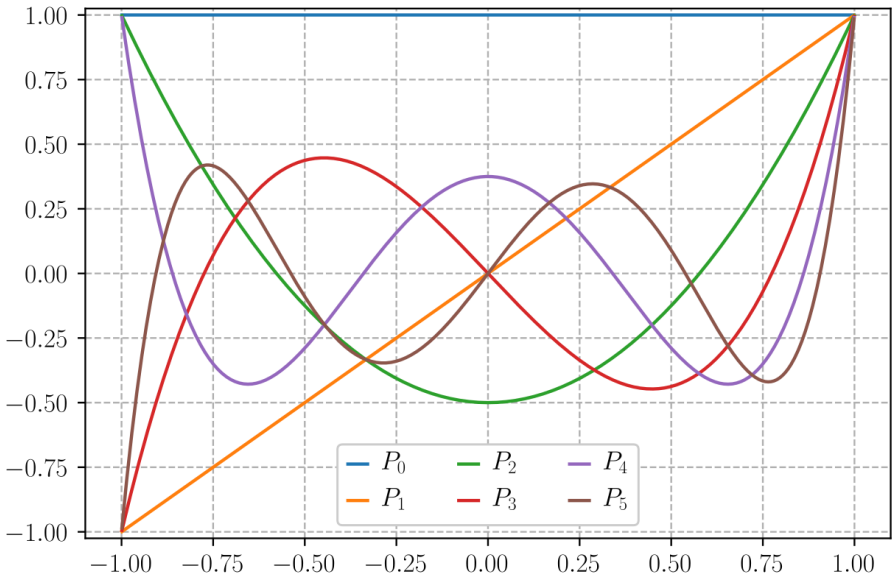

FIGURE C.2.1: Graph of Legendre polynomials (up to n =5)

mathematician, see in [77], and has important applications in various fields. It is similar to Gaussian quadrature with the following differences:

1. The intergration points include the end points of the integration interval.
2. That is accurate for polynomial up to degree $2n-3$, where n is the number of integration points, see the detail in [78]. Labatto quadrature of function $f(x)$ on interval $[-1,+1]$:

$$\int_{-1}^{+1} f(x)dx = \frac{2}{n(n-1)}\left[f(1)+f(-1)\right] + \sum_{i=2}^{n-1} w_i f(x_i) \tag{C.3}$$

Weights:

$$w_i = \frac{2}{n(n-1)[P_{n-1}(x_i)]^2} \quad \text{for} \quad x_i \neq -1, +1$$

where, $P_i(x)$ varies depending on the number of points used in the integration, denoted by 'i' and is expressed as follows:

$$\begin{aligned}
P_0(x) &= 1 \\
P_1(x) &= x \\
P_2(x) &= \frac{1}{2}(3x^2-1) \\
P_3(x) &= \frac{1}{2}(5x^3-3x) \\
P_4(x) &= \frac{1}{8}(35x^4-30x^2+3) \\
P_5(x) &= \frac{1}{8}(65x^5-70x^3+15x)
\end{aligned}$$

The following is a summary of the commonly used number of points for integration, along with their corresponding values of abscissas and weights:

TABLE C.2: Lobatto quadrature with various points and weights

Number of points n	Points x_i	Weights w_i
3	0	$\frac{4}{3}$
	± 1	$\frac{1}{3}$
4	$\pm\sqrt{\frac{1}{5}}$	$\frac{5}{6}$
	± 1	$\frac{1}{6}$
5	0	$\frac{32}{45}$
	$\pm\sqrt{\frac{3}{7}}$	$\frac{49}{90}$
	± 1	$\frac{1}{10}$

C.3 Lagrange interpolating polynomial

The Lagrange interpolating polynomial is a polynomial function of degree n that can approximate a function at any point within a given interval based on a set of given data points. In numerical analysis, it is the unique polynomial of lowest degree that interpolates a given set of data. It is derived by constructing a set of Lagrange basis polynomials that satisfy certain conditions and taking a weighted sum of these basis polynomial.

Given a set of $n+1$ nodes $x_0, x_1, \ldots, x_n$, which must all be distinct, $x_i \neq x_m$ for indices $i \neq m$, the Lagrange basis for polynomials of degree $\leq k$ for those nodes is the set of polynomial $\ell_0(x), \ell_1(x), \ldots, \ell_n(x)$ each of degree n which take value $\ell_i(x_m) = 0$ if $m \neq i$ and $\ell_i(x_i) = 1$. Each basis polynomial can be explicitly described by the product:

$$\ell_i(x) = \frac{(x - x_0)}{(x_i - x_0)} \cdots \frac{(x - x_{i-1})(x - x_{i+1})}{(x_i - x_{i-1})(x_i - x_{i+1})} \cdots \frac{(x - x_n)}{(x_i - x_n)} \tag{C.4}$$

For example: Assuming that we have 4 integrated points with abscissa values denoted by $x_{ip}(1), x_{ip}(2), x_{ip}(3)$, and $x_{ip}(4)$, thus, the Lagrange interpolation polynomials can be expressed as follows:

$$\ell_1(x) = \frac{(x - x_{ip}(2))(x - x_{ip}(3))(x - x_{ip}(4))}{(x_{ip}(1) - x_{ip}(2))(x_{ip}(1) - x_{ip}(3))(x_{ip}(1) - x_{ip}(4))}$$

$$\ell_2(x) = \frac{(x - x_{ip}(1))(x - x_{ip}(3))(x - x_{ip}(4))}{(x_{ip}(2) - x_{ip}(1))(x_{ip}(2) - x_{ip}(3))(x_{ip}(2) - x_{ip}(4))}$$

$$\ell_3(x) = \frac{(x - x_{ip}(1))(x - x_{ip}(2))(x - x_{ip}(4))}{(x_{ip}(3) - x_{ip}(1))(x_{ip}(3) - x_{ip}(2))(x_{ip}(3) - x_{ip}(4))}$$

$$\ell_4(x) = \frac{(x - x_{ip}(1))(x - x_{ip}(2))(x - x_{ip}(3))}{(x_{ip}(4) - x_{ip}(1))(x_{ip}(4) - x_{ip}(1))(x_{ip}(4) - x_{ip}(3))}$$

Appendix D

Auxiliary matrix

The below complex matrices and vectors serve the nonlinear formulation in Chapter 5:

$$\mathbf{b}(x) = \begin{bmatrix} \mathbf{b}_{N_b}(x) \\ \mathbf{b}_{M_b}(x) \\ \mathbf{b}_{N_a}(x) \\ \mathbf{b}_{M_a}(x) \\ \mathbf{b}_{D_{sc}}(x) \\ \mathbf{b}_{V_{sc}}(x) \end{bmatrix}$$

$$\mathbf{b}_s(x) = \begin{bmatrix} {}^x\bar{\mathbf{N}}_s(x) - \dfrac{{}^x\mathbf{N}_{sip}(x)}{{}^x\mathbf{N}_{sip}(L)}\bar{\mathbf{N}}_s(L) \\ h_b\left[{}^x\bar{\mathbf{N}}_s(x) - \dfrac{{}^x\mathbf{N}_{sip}(x)}{{}^x\mathbf{N}_{sip}(L)}\bar{\mathbf{N}}_s(L)\right] \\ -{}^x\bar{\mathbf{N}}_s(x) + \dfrac{{}^x\mathbf{N}_{sip}(x)}{{}^x\mathbf{N}_{sip}(L)}\bar{\mathbf{N}}_s(L) \\ h_a\left[{}^x\bar{\mathbf{N}}_s(x) - \dfrac{{}^x\mathbf{N}_{sip}(x)}{{}^x\mathbf{N}_{sip}(L)}\bar{\mathbf{N}}_s(L)\right] \\ \bar{\mathbf{N}}_s(x) - \dfrac{{}^x\mathbf{N}_{sip}(x)}{{}^x\mathbf{N}_{sip}(L)}\bar{\mathbf{N}}_s(L) \\ \mathbf{0} \end{bmatrix} \quad ; \quad \mathbf{b}_g(x) = \begin{bmatrix} \mathbf{0} \\ \mathbf{b}^g_{M_b}(x) \\ \mathbf{0} \\ \mathbf{b}^g_{M_a}(x) \\ \mathbf{0} \\ \mathbf{b}^g_{V_{sc}} \end{bmatrix}$$

where:

$$\mathbf{b}^{g}_{M_b}(x) = -{}^{xx}\bar{\mathbf{N}}_g(x) + \frac{{}^{xx}N_{gip}(x)\left[{}^{x}N_{g1}(L){}^{xx}\bar{\mathbf{N}}_g(L) - {}^{x}\bar{\mathbf{N}}_g(L){}^{xx}N_{g1}(L)\right]}{{}^{x}N_{g1}(L){}^{xx}N_{gip}(L) - {}^{x}N_{gip}(L){}^{xx}N_{g1}(L)}$$

$$- \frac{{}^{xx}N_{g1}(x)\left[{}^{x}N_{gip}(L){}^{xx}\bar{\mathbf{N}}_g(L) - {}^{x}\bar{\mathbf{N}}_g(L){}^{xx}N_{gip}(L)\right]}{{}^{x}N_{gip}(L){}^{xx}N_{gip}(L) - {}^{x}N_{gip}(L){}^{xx}N_{gip}(L)}$$

$$\mathbf{b}^{g}_{M_a}(x) = {}^{xx}\bar{\mathbf{N}}_g(x) - \frac{{}^{xx}N_{gip}(x)\left[{}^{x}N_{g1}(L){}^{xx}\bar{\mathbf{N}}_g(L) - {}^{x}\bar{\mathbf{N}}_g(L){}^{xx}N_{g1}(L)\right]}{{}^{x}N_{g1}(L){}^{xx}N_{gip}(L) - {}^{x}N_{gip}(L){}^{xx}N_{g1}(L)}$$

$$+ \frac{{}^{xx}N_{g1}(x)\left[{}^{x}N_{gip}(L){}^{xx}\bar{\mathbf{N}}_g(L) - {}^{x}\bar{\mathbf{N}}_g(L){}^{xx}N_{gip}(L)\right]}{{}^{x}N_{gip}(L){}^{xx}N_{gip}(L) - {}^{x}N_{gip}(L){}^{xx}N_{gip}(L)}$$

$$\mathbf{b}^{g}_{V_{sc}}(x) = \bar{\mathbf{N}}_g(x) - \frac{N_{gip}(x)\left[{}^{x}N_{g1}(L){}^{xx}\bar{\mathbf{N}}_g(L) - {}^{x}\bar{\mathbf{N}}_g(L){}^{xx}N_{g1}(L)\right]}{{}^{x}N_{g1}(L){}^{xx}N_{gip}(L) - {}^{x}N_{gip}(L){}^{xx}N_{g1}(L)}$$

$$+ \frac{N_{g1}(x)\left[{}^{x}N_{gip}(L){}^{xx}\bar{\mathbf{N}}_g(L) - {}^{x}\bar{\mathbf{N}}_g(L){}^{xx}N_{gip}(L)\right]}{{}^{x}N_{gip}(L){}^{xx}N_{gip}(L) - {}^{x}N_{gip}(L){}^{xx}N_{gip}(L)}$$

and,

$$\mathbf{b}_{N_a}(x) = \begin{bmatrix} 1 & 1 - \dfrac{{}^{x}N_{sip}(x)}{{}^{x}N_{sip}(L)} & 1 - \dfrac{{}^{x}N_{sip}(x)}{{}^{x}N_{sip}(L)} & 0 & 0 & 0 & 0 & 0 & 0 \end{bmatrix}$$

$$\mathbf{b}_{M_a}(x) = \begin{bmatrix} 0 & b^{(2)}_{M_a} & b^{(3)}_{M_a} & \dfrac{x}{L} - 1 & \dfrac{x}{L} & b^{(6)}_{M_a} & b^{(7)}_{M_a} & b^{(8)}_{M_a} & b^{(9)}_{M_a} \end{bmatrix}$$

$$\mathbf{b}_{N_b}(x) = \begin{bmatrix} 0 & \dfrac{{}^{x}N_{sip}(x)}{{}^{x}N_{sip}(L)} - 1 & \dfrac{{}^{x}N_{sip}(x)}{{}^{x}N_{sip}(L)} & 0 & 0 & 0 & 0 & 0 & 0 \end{bmatrix}$$

$$\mathbf{b}_{M_b}(x) = \begin{bmatrix} 0 & b^{(2)}_{M_b} & b^{(3)}_{M_b} & 0 & 0 & b^{(6)}_{M_b} & b^{(7)}_{M_b} & b^{(8)}_{M_b} & b^{(9)}_{M_b} \end{bmatrix}$$

$$\mathbf{b}_{D_{sc}}(x) = \begin{bmatrix} 0 & \dfrac{N_{sip}(x)}{{}^{x}N_{sip}(L)} & \dfrac{N_{sip}(x)}{{}^{x}N_{sip}(L)} & 0 & 0 & 0 & 0 & 0 & 0 \end{bmatrix}$$

$$\mathbf{b}_{V_{sc}}(x) = \begin{bmatrix} 0 & b^{(2)}_{V_{sc}} & b^{(3)}_{V_{sc}} & 0 & 0 & b^{(6)}_{V_{sc}} & b^{(7)}_{V_{sc}} & b^{(8)}_{V_{sc}} & b^{(9)}_{V_{sc}} \end{bmatrix}$$

where:

$$b_{M_a}^{(2)} = -\left(h_a + h_b\right)\frac{x}{L} + h_a\frac{{}^{x}N_{sip}(x)}{{}^{x}N_{sip}(L)} + h_b\frac{{}^{x}N_{g1}(L)^{xx}N_{gip}(x) - {}^{x}N_{gip}(L)^{xx}N_{g1}(x)}{{}^{x}N_{g1}(L)^{xx}N_{gip}(L) - {}^{x}N_{gip}(L)^{xx}N_{g1}(L)}$$

$$b_{M_a}^{(3)} = b_{M_a}^{(2)}$$

$$b_{M_a}^{(6)} = \frac{x}{L}\frac{{}^{x}N_{g1}(L)^{xx}N_{gip}(x) - {}^{x}N_{gip}(L)^{xx}N_{g1}(x)}{{}^{x}N_{g1}(L)^{xx}N_{gip}(L) - {}^{x}N_{gip}(L)^{xx}N_{g1}(L)}$$

$$b_{M_a}^{(7)} = b_{M_a}^{(6)}$$

$$b_{M_a}^{(8)} = \frac{{}^{xx}N_{g1}(x)\left[{}^{xx}N_{gip}(L) - L.{}^{x}N_{gip}(L)\right] - {}^{xx}N_{gip}(x)\left[{}^{xx}N_{g1}(L) - L.{}^{x}N_{g1}(L)\right]}{{}^{x}N_{g1}(L)^{xx}N_{gip}(L) - {}^{x}N_{gip}(L)^{xx}N_{g1}(L)} - x$$

$$b_{M_a}^{(9)} = \frac{{}^{xx}N_{g1}(x)^{xx}N_{gip}(L) - {}^{xx}N_{gip}(x)^{xx}N_{g1}(L)}{{}^{x}N_{g1}(L)^{xx}N_{gip}(L) - {}^{x}N_{gip}(L)^{xx}N_{g1}(L)}$$

$$b_{M_b}^{(2)} = h_b\frac{{}^{x}N_{sip}(x)}{{}^{x}N_{sip}(L)} - h_b\frac{{}^{x}N_{g1}(L)^{xx}N_{gip}(x) - {}^{x}N_{gip}(L)^{xx}N_{g1}(x)}{{}^{x}N_{g1}(L)^{xx}N_{gip}(L) - {}^{x}N_{gip}(L)^{xx}N_{g1}(L)}$$

$$b_{M_b}^{(3)} = b_{M_b}^{(2)}$$

$$b_{M_b}^{(6)} = \frac{{}^{x}N_{g1}(L)^{xx}N_{gip}(x) - {}^{x}N_{gip}(L)^{xx}N_{g1}(x)}{{}^{x}N_{g1}(L)^{xx}N_{gip}(L) - {}^{x}N_{gip}(L)^{xx}N_{g1}(L)} - 1$$

$$b_{M_b}^{(7)} = \frac{{}^{x}N_{g1}(L)^{xx}N_{gip}(x) - {}^{x}N_{gip}(L)^{xx}N_{g1}(x)}{{}^{x}N_{g1}(L)^{xx}N_{gip}(L) - {}^{x}N_{gip}(L)^{xx}N_{g1}(L)}$$

$$b_{M_b}^{(8)} = \frac{{}^{xx}N_{gip}(x)\left[{}^{xx}N_{g1}(L) - L.{}^{x}N_{g1}(L)\right] - {}^{xx}N_{g1}(x)\left[{}^{xx}N_{gip}(L) - L.{}^{x}N_{gip}(L)\right]}{{}^{x}N_{g1}(L)^{xx}N_{gip}(L) - {}^{x}N_{gip}(L)^{xx}N_{g1}(L)} + x$$

$$b_{M_b}^{(9)} = \frac{{}^{xx}N_{g1}(L)^{xx}N_{gip}(x) - {}^{xx}N_{g1}(x)^{xx}N_{gip}(L)}{{}^{x}N_{g1}(L)^{xx}N_{gip}(L) - {}^{x}N_{gip}(L)^{xx}N_{g1}(L)}$$

$$b_{V_{sc}}^{(2)} = h_b\frac{{}^{x}N_{g1}(L)N_{gip}(x) - {}^{x}N_{gip}(L)N_{g1}(x)}{{}^{x}N_{g1}(L)^{xx}N_{gip}(L) - {}^{x}N_{gip}(L)^{xx}N_{g1}(L)}$$

$$b_{V_{sc}}^{(3)} = b_{V_{sc}}^{(2)}$$

$$b_{V_{sc}}^{(6)} = \frac{N_{g1}(x)^{x}N_{gip}(L) - N_{gip}(x)^{x}N_{g1}(L)}{{}^{x}N_{g1}(L)^{xx}N_{gip}(L) - {}^{x}N_{gip}(L)^{xx}N_{g1}(L)}$$

$$b_{V_{sc}}^{(7)} = b_{V_{sc}}^{(6)}$$

$$b_{V_{sc}}^{(8)} = \frac{N_{g1}(x)\left[{}^{xx}N_{gip}(L) - L.{}^{x}N_{gip}(L)\right] - N_{gip}(x)\left[{}^{xx}N_{g1}(L) - L.{}^{x}N_{g1}(L)\right]}{{}^{x}N_{g1}(L)^{xx}N_{gip}(L) - {}^{x}N_{gip}(L)^{xx}N_{g1}(L)}$$

$$b_{V_{sc}}^{(9)} = \frac{N_{g1}(x)^{xx}N_{gip}(L) - N_{gip}(x)^{xx}N_{g1}(L)}{{}^{x}N_{g1}(L)^{xx}N_{gip}(L) - {}^{x}N_{gip}(L)^{xx}N_{g1}(L)}$$

$$\mathbf{N}_e^T(x) = \begin{bmatrix}
N_1^e(x) & 0 & 0 & 0 & 0 & 0 \\
N_2^e(x) & 0 & 0 & 0 & 0 & 0 \\
\vdots & \vdots & \vdots & \vdots & \vdots & \vdots \\
N_{ip}^e(x) & 0 & 0 & 0 & 0 & 0 \\
0 & N_1^e(x) & 0 & 0 & 0 & 0 \\
0 & N_2^e(x) & 0 & 0 & 0 & 0 \\
\vdots & \vdots & \vdots & \vdots & \vdots & \vdots \\
0 & N_{ip}^e(x) & 0 & 0 & 0 & 0 \\
0 & 0 & N_1^e(x) & 0 & 0 & 0 \\
0 & 0 & N_2^e(x) & 0 & 0 & 0 \\
\vdots & \vdots & \vdots & \vdots & \vdots & \vdots \\
0 & 0 & N_{ip}^e(x) & 0 & 0 & 0 \\
0 & 0 & 0 & N_1^e(x) & 0 & 0 \\
0 & 0 & 0 & N_2^e(x) & 0 & 0 \\
\vdots & \vdots & \vdots & \vdots & \vdots & \vdots \\
0 & 0 & 0 & N_{ip}^e(x) & 0 & 0 \\
0 & 0 & 0 & 0 & N_1^e(x) & 0 \\
0 & 0 & 0 & 0 & N_2^e(x) & 0 \\
\vdots & \vdots & \vdots & \vdots & \vdots & \vdots \\
0 & 0 & 0 & 0 & N_{ip}^e(x) & 0 \\
0 & 0 & 0 & 0 & 0 & N_1^e(x) \\
0 & 0 & 0 & 0 & 0 & N_2^e(x \\
\vdots & \vdots & \vdots & \vdots & \vdots & \vdots \\
0 & 0 & 0 & 0 & 0 & N_{ip}^e(x)
\end{bmatrix}, \quad \tilde{\mathbf{e}} = \begin{bmatrix}
\epsilon_1^{(1)} \\ \epsilon_1^{(2)} \\ \vdots \\ \epsilon_1^{(ip)} \\ \kappa_1^{(1)} \\ \kappa_1^{(2)} \\ \vdots \\ \kappa_1^{(ip)} \\ \epsilon_2^{(1)} \\ \epsilon_2^{(2)} \\ \vdots \\ \epsilon_2^{(ip)} \\ \kappa_2^{(1)} \\ \kappa_2^{(2)} \\ \vdots \\ \kappa_2^{(ip)} \\ s^{(1)} \\ s^{(2)} \\ \vdots \\ s^{(ip)} \\ g^{(1)} \\ g^{(2)} \\ \vdots \\ g^{(ip)}
\end{bmatrix}$$

Bibliography

[1] A Heidarpour and MA Bradford. "Generic non-linear modelling of a bi-material composite beam with partial shear interaction". In: *International Journal of Non-Linear Mechanics* 44.3 (2009), pp. 290–297.

[2] J-M ARIBERT, E Ragneau, and H Xu. "Développement d'un élément fini de poutre mixte acier-béton intégrant les phénomènes de glissement et de semi-continuité avec éventuellement voilement local". In: *Construction métallique* 30.2 (1993), pp. 31–49.

[3] Samy Guezouli and Anas Alhasawi. "A new concept for the contact at the interface of steel–concrete composite beams". In: *Finite Elements in Analysis and Design* 87 (Sept. 2014), 32–42. DOI: 10.1016/j.finel.2014.01.007.

[4] Quang-Huy Nguyen, Mohammed Hjiaj, and Samy Guezouli. "Exact finite element model for shear-deformable two-layer beams with discrete shear connection". In: *Finite elements in analysis and design* 47.7 (2011), pp. 718–727.

[5] Nathan M Newmark, Chester P Siess, IvanM Viest, et al. "Tests and analysis of composite beams with incomplete interaction". In: *Proc. Soc. Exp. Stress Anal* 9.1 (1951), pp. 75–92. URL: http://refhub.elsevier.com/S0045-7949(13)00110-7/h0005.

[6] Jianying Chen, Guojing He, Xiaodong Alice Wang, Jiejun Wang, Jin Yi, and Chuanjian Yang. "Theoretical and experimental research on slip and uplift of the timber-concrete composite beam". In: *BioResources* 15.3 (2020), pp. 7079–7099.

[7] Ulf Arne Girhammar and Vijaya KA Gopu. "Composite beam-columns with interlayer slip—exact analysis". In: *Journal of Structural Engineering* 119.4 (1993), pp. 1265–1282.

[8] YF Wu, DJ Oehlers, and MC Griffith. "Partial-interaction analysis of composite beam/column members". In: *Mechanics of Structures and Machines* (2007).

[9] Ciro Faella, Enzo Martinelli, and Emidio Nigro. "Steel and concrete composite beams with flexible shear connection: exact analytical expression of the stiffness matrix and applications". In: *Computers & Structures* 80.11 (2002), pp. 1001 –1009. ISSN: 0045-7949.

[10] Gianluca Ranzi, MA Bradford, and Brian Uy. "A direct stiffness analysis of a composite beam with partial interaction". In: *International Journal for Numerical Methods in Engineering* 61.5 (2004), pp. 657–672.

[11] Ulf Arne Girhammar and Dan H Pan. "Exact static analysis of partially composite beams and beam-columns". In: *International Journal of Mechanical Sciences* 49.2 (2007), pp. 239–255.

[12] Rongqiao Xu and Yufei Wu. "Static, dynamic, and buckling analysis of partial interaction composite members using Timoshenko's beam theory". In: *International Journal of Mechanical Sciences* 49.10 (2007), pp. 1139–1155.

[13] Simon Schnabl, Miran Saje, Goran Turk, and Igor Planinc. "Analytical solution of two-layer beam taking into account interlayer slip and shear deformation". In: *Journal of structural engineering* 133.6 (2007), pp. 886–894.

[14] Quang-Huy Nguyen, Enzo Martinelli, and Mohammed Hjiaj. "Derivation of the exact stiffness matrix for a two-layer Timoshenko beam element with partial interaction". In: *Engineering Structures* 33.2 (2011), pp. 298–307. URL: http://dx.doi.org/10.1016/j.engstruct.2010.10.006.

[15] Rongqiao Xu and Guannan Wang. "Variational principle of partial-interaction composite beams using Timoshenko's beam theory". In: *International Journal of Mechanical Sciences* 60.1 (2012), pp. 72–83.

[16] Gianluca Ranzi. "Locking problems in the partial interaction analysis of multi-layered composite beams". In: *Engineering Structures* 30.10 (2008), pp. 2900–2911.

[17] Andrea Dall'Asta and Alessandro Zona. "Slip locking in finite elements for composite beams with deformable shear connection". In: *Finite Elements in Analysis and Design* 40.13-14 (2004), pp. 1907–1930.

[18] Simon Schnabl, Miran Saje, Goran Turk, and Igor Planinc. "Locking-free two-layer Timoshenko beam element with interlayer slip". In: *Finite Elements in Analysis and Design* 43.9 (2007), pp. 705–714.

[19] M Heinisuo. "An exact finite element technique for layered beams". In: *Computers & Structures* 30.3 (1988), pp. 615–622.

[20] João Batista M Sousa Jr, Claudio EM Oliveira, and Amilton R da Silva. "Displacement-based nonlinear finite element analysis of composite beam–columns with partial interaction". In: *Journal of Constructional Steel Research* 66.6 (2010), pp. 772–779.

[21] João Batista M Sousa Jr. "Exact finite elements for multilayered composite beam-columns with partial interaction". In: *Computers & Structures* 123 (2013), pp. 48–57.

[22] AO Adekola. "Partial interaction between elastically connected elements of a composite beam". In: *International Journal of Solids and Structures* 4.11 (1968), pp. 1125–1135.

[23] H Robinson and KS Naraine. "Slip and uplift effects in composite beams." In: *International conference on composite construction in steel and concrete. Proceedings of an engineering foundation conference ASCE*. Amer Society of Civil Engineers, 1988, pp. 487–497.

[24] Jean-Marie Aribert and K. Abdel Aziz. "Ultimate state analysis of composite beam taking into account uplift effects at the steel-concrete interface". In: *Revue Construction Métallique* 4 (1985), pp. 3–36.

[25] F Gara, G Ranzi, and G Leoni. "Displacement-based formulations for composite beams with longitudinal slip and vertical uplift". In: *International journal for numerical methods in engineering* 65.8 (2006), pp. 1197–1220.

[26] Jean-Marc Battini, Quang-Huy Nguyen, and Mohammed Hjiaj. "Non-linear finite element analysis of composite beams with interlayer slips". In: *Computers & structures* 87.13-14 (2009), pp. 904–912.

[27] Gianluca Ranzi, Andrea Dall'Asta, Laura Ragni, and Alessandro Zona. "A geometric nonlinear model for composite beams with partial interaction". In: *Engineering Structures* 32.5 (2010), pp. 1384–1396.

[28] Mohammed Hjiaj, Jean-Marc Battini, and Quang-Huy Nguyen. "Large displacement analysis of shear deformable composite beams with interlayer slips". In: *International Journal of Non-Linear Mechanics* 47.8 (2012), pp. 895–904.

[29] Pisey Keo, Quang-Huy Nguyen, Hugues Somja, and Mohammed Hjiaj. "Geometrically nonlinear analysis of hybrid beam-column with several encased steel profiles in partial interaction". In: *Engineering Structures* 100 (2015), pp. 66–78.

[30] Aleš Kroflič, Miran Saje, and Igor Planinc. "Non-linear analysis of two-layer beams with interlayer slip and uplift". In: *Computers & structures* 89.23-24 (2011), pp. 2414–2424.

[31] S. Schnabl and I. Planinc. "Exact buckling loads of two-layer composite Reissner's columns with interlayer slip and uplift". In: *International Journal of Solids and Structures* 50.1 (2013), pp. 30–37. ISSN: 0020-7683.

[32] FC Filippou. "Lecture notes from CE221 Nonlinear Structural Analysis". In: *University of California, Berkeley* (2013).

[33] Michael H Scott and Gregory L Fenves. "Plastic hinge integration methods for force-based beam–column elements". In: *Journal of Structural Engineering* 132.2 (2006), pp. 244–252.

[34] Michael H Scott and Keri L Ryan. "Moment-rotation behavior of force-based plastic hinge elements". In: *Earthquake Spectra* 29.2 (2013), pp. 597–607.

[35] SA Mirza and BW Skrabek. "Reliability of short composite beam-column strength interaction". In: *Journal of Structural Engineering* 117.8 (1991), pp. 2320–2339.

[36] S El-Tawil, CF Sanz-Picon, and GG Deierlein. "Evaluation of ACI 318 and AISC (LRFD) strength provisions for composite beam-columns". In: *Journal of Constructional Steel Research* 34.1 (1995), pp. 103–123.

[37] V Ciampi and L Carlesimo. "A nonlinear beam element for seismic analysis of structures". In: *8th European Conference on Earthquake Engineering*. Vol. 3. 1986, pp. 6–3.

[38] Ashraf Ayoub and Filip C Filippou. "Mixed formulation of bond-slip problems under cyclic loads". In: *Journal of Structural Engineering* 125.6 (1999), pp. 661–671.

[39] R Emre Erkmen and Mark A Bradford. "Treatment of slip locking for displacement-based finite element analysis of composite beam–columns". In: *International journal for numerical methods in engineering* 85.7 (2011), pp. 805–826.

[40] Andrea Dall'Asta and Alessandro Zona. "Non-linear analysis of composite beams by a displacement approach". In: *Computers & structures* 80.27-30 (2002), pp. 2217–2228.

[41] Andrea Dall'Asta and Alessandro Zona. "Three-field mixed formulation for the nonlinear analysis of composite beams with deformable shear connection". In: *Finite Elements in Analysis and Design* 40.4 (2004), pp. 425–448.

[42] Phani Kumar VV Nukala. *Three-dimensional second-order inelastic analysis of steel frames*. Purdue University, 1997.

[43] M Reza Salari, Enrico Spacone, P Benson Shing, and Dan M Frangopol. "Nonlinear analysis of composite beams with deformable shear connectors". In: *Journal of Structural Engineering* 124.10 (1998), pp. 1148–1158.

[44] Ashraf Ayoub and Filip C Filippou. "Mixed formulation of nonlinear steel-concrete composite beam element". In: *Journal of Structural Engineering* 126.3 (2000), pp. 371–381.

[45] Phani Kumar VV Nukala and Donald W White. "Variationally consistent state determination algorithms for nonlinear mixed beam finite elements". In: *Computer Methods in Applied Mechanics and Engineering* 193.33-35 (2004), pp. 3647–3666.

[46] Phani Kumar VV Nukala and Donald W White. "A mixed finite element for three-dimensional nonlinear analysis of steel frames". In: *Computer Methods in Applied Mechanics and Engineering* 193.23-26 (2004), pp. 2507–2545.

[47] Thaileng Oeng, Pisey Keo, Samy Guezouli, and Mohammed Hjiaj. "Large displacement analysis of two-layer beam-columns taking into account slip and uplift". In: *Engineering Computations* 40.1 (2023), pp. 265–295.

[48] Joseph A Landers and Robert L Taylor. *An Augmented lagrangian formulation for the finite element solution of contact problems.* Tech. rep. California University Berkeley, Department of Civil Engineering, 1986.

[49] U. Girhammar and V. Gopu. "Composite beam-columns with interlayer slip-exact analysis". In: *Journal of Structural Engineering* 119.4 (1993), pp. 1265–1282.

[50] Yanyao Jiang and Peter Kurath. "Characteristics of the Armstrong-Frederick type plasticity models". In: *International Journal of Plasticity* 12.3 (1996), pp. 387–415.

[51] GE Varelis. "Application of the Armstrong-Frederick Cyclic Plasticity Model for Simulating Structural Steel Member Behavior". In: *MDE Thesis* (2010).

[52] Dudley Charles Kent and Robert Park. "Flexural members with confined concrete". In: *Journal of the structural division* 97.7 (1971), pp. 1969–1990.

[53] JUAN CARLOS Simo, JAVIER Oliver, and Francisco Armero. "An analysis of strong discontinuities induced by strain-softening in rate-independent inelastic solids". In: *Computational mechanics* 12.5 (1993), pp. 277–296.

[54] Sanjay Govindjee, Gregory J Kay, and Juan C Simo. "Anisotropic modelling and numerical simulation of brittle damage in concrete". In: *International journal for numerical methods in engineering* 38.21 (1995), pp. 3611–3633.

[55] Francisco Armero and Sergio Oller. "A general framework for continuum damage models. I. Infinitesimal plastic damage models in stress space". In: *International Journal of Solids and Structures* 37.48-50 (2000), pp. 7409–7436.

[56] Bruno Thurlimann. "Fatigue and static strength of stud shear connectors". In: *Journal Proceedings*. Vol. 55. 6. 1959, pp. 1287–1302.

[57] JG Ollgaard, RG Slutter, and JW Fisher. "Shear strength of stud connectors in lightweight and normal weight concrete, AISC Eng'g Jr., April 1971 (71-10)". In: *AISC Engineering journal* (1971), pp. 55–34.

[58] DJ Oehlers and CG Coughlan. "The shear stiffness of stud shear connections in composite beams". In: *Journal of Constructional Steel Research* 6.4 (1986), pp. 273–284.

[59] N Okubo, A Kurita, K Komatsu, and Y Ishihara. "Experimental study on static and fatigue characteristics of grouped stud". In: *J. Structural Eng., JSCE* 48 (2002), pp. 1391–1397.

[60] Chang-Su Shim, Pil-Goo Lee, and Tae-Yang Yoon. "Static behavior of large stud shear connectors". In: *Engineering structures* 26.12 (2004), pp. 1853–1860.

[61] Jawed Qureshi, Dennis Lam, and Jianqiao Ye. "Effect of shear connector spacing and layout on the shear connector capacity in composite beams". In: *Journal of constructional steel research* 67.4 (2011), pp. 706–719.

[62] Dongyan Xue, Yuqing Liu, Zhen Yu, and Jun He. "Static behavior of multi-stud shear connectors for steel-concrete composite bridge". In: *Journal of Constructional Steel Research* 74 (2012), pp. 1–7.

[63] Samy Guezouli, Alain Lachal, and Quang-Huy Nguyen. "Numerical investigation of internal force transfer mechanism in push-out tests". In: *Engineering Structures* 52 (2013), pp. 140–152.

[64] Patrick J McMACKIN. "Headed steel anchors under combined loading". In: *AISC Engineering Journal* (1973), pp. 43–52.

[65] K Takami, K Nishi, and S Hamada. "Shear strength of headed stud shear connector subjected to tensile load". In: *J Constr Steel* 7 (2000), pp. 233–240.

[66] Helmut Bode and Karlheinz Roik. "Headed Studs–Embedded in Concrete and Loaded in Tension". In: *Special Publication* 103 (1987), pp. 61–88.

[67] ChangSu Shim, JongHee Kim, SP Chang, and CH Chung. "The behaviour of shear connections in a composite beam with a full-depth precast slab". In: *Proceedings of the Institution of Civil Engineers-Structures and Buildings* 140.1 (2000), pp. 101–110.

[68] EN1994-1-1. *Design of Composite Steel and Concrete Structures, Part 1.1, General rules and rules for building*. 2004.

[69] Toorak AASHTO-LRFD Zokaie. "AASHTO-LRFD live load distribution specifications". In: *Journal of bridge engineering* 5.2 (2000), pp. 131–138.

[70] Kenneth Edward Buttry. "Behavior of stud shear connectors in lightweight and normal-weight concrete". PhD thesis. University of Missouri–Columbia, 1965.

[71] ACI318. *Building code requirements for structural concrete (ACI 318-08) and commentary*. 2008.

[72] Fei Yang, Yuqing Liu, and Chen Liang. "Analytical study on the tensile stiffness of headed stud connectors". In: *Advances in Structural Engineering* 22.5 (2019), pp. 1149–1160.

[73] Zhaofei Lin, Yuqing Liu, and Jun He. "Behavior of stud connectors under combined shear and tension loads". In: *Engineering structures* 81 (2014), pp. 362–376.

[74] Baudouin Fraeijs de Veubeke. "Displacement and equilibrium models in the finite element method". In: (1965).

[75] K Abdel Aziz. "Numerical modeling and experimental study of composite beams with partial or spaced shear connection". PhD thesis. INSA Rennes Rennes, France, 1986.

[76] P Ansourian. "Experiments on continuous composite beams." In: *Proceedings of the Institution of Civil Engineers* 73.1 (1982), pp. 26–51.

[77] Rehuel Lobatto. *Lessen over de differentiaal-en integraal-rekening...* Vol. 2. De Gebroeders Van Cleef, 1852.

[78] Alfio Quarteroni, Riccardo Sacco, and Fausto Saleri. *Numerical mathematics*. Vol. 37. Springer Science & Business Media, 2010.

COLLEGE DOCTORAL BRETAGNE SCIENCES POUR L'INGENIEUR

INSA INSTITUT NATIONAL DES SCIENCES APPLIQUÉES RENNES

Titre : Analyse des poutres mixtes prise en compte glissement et soulèvement à l'interface

Mot clés : poutres mixtes, glissement, soulèvement, pénalité, Lagrangien augmentée

Résumé : Dans ce travail, nous proposons une approche éléments finis pour l'analyse de poutres mixtes (bicouches) intégrant les phénomènes de glissement et le soulèvement à l'interface de la poutre bicouche. Deux modèles de connexion à l'interface sont considérés : connexion discrète et connexion continue. L'élément connecteur corresponds à 2 ressorts couplés. Dans le cas pénétration, une force de contact se développe. Deux méthodes classiques de résolutions du problème de contact sont évaluées : la méthode pénalité, et la méthode Lagrangienne augmentée. Une solution semi-analytique est proposée pour le cas géométriquement et matériellement linéaire. Dans cette formulation, les variables cinématiques sont interpolées de manière exacte et les conditions de contact sont imposées aux nœuds pour les deux modèles de connexion. Dans une seconde phase, les méthodes de résolutions du problème de contact sont évaluées dans un contexte géométriquement non-linéaire (approche co-rotationnelle). Enfin, une formulation en déplacement et une formulation mixte à deux champs du problème géométriquement et matériellement non-linéaire sont également proposées. Nous adoptons la discrétisation par fibres pour les sections de la poutre mixte. Pour ces deux formulations, on propose un algorithme ad hoc pour le traitement du problème du contact. Les exemples traités démontrent la robustesse des formulations proposées.

Title: Analysis of composite beam by taking into account inter-layer slip and uplift

Keywords: composite beam, slip, uplift, penalty, augmented Lagrangian

Abstract: This thesis presents a finite element approach for the analysis of composite (two-layers) beams taking into account slip and uplift at the interface of the layers. Two models of connection are considered: the discrete bond and continuous bond model. The connector element consists of two-directional coupled springs. In case of penetration, the contact forces exist. Two classical methods for solving the contact problem are evaluated: the penalty method and the augmented Lagrangian method. Besides, it is assumed that both slip and uplift are small, which corresponds to the observations made on composite beams. A semi-analytical solution is proposed for the geometrically and materially linear case. In this formulation, the kinematic variables are interpolated exactly, and the node-to-node contact conditions are imposed for both connection models. In the second task, the resolution methods of the contact problem are evaluated in geometrical nonlinearity (co-rotational approach). In nonlinear finite element analysis, displacement-based and two-field mixed formulations for the problem of geometrical and material nonlinearity are proposed. We adopt fiber discretization for the sections of the composite beam. For both formulations, a corresponding algorithm is proposed to solve the contact problem. The treated numerical examples demonstrate the robustness of the proposed formulations.